

Real-Time Control of Sawteeth and NTMs in TCV and ITER

THÈSE N° 6539 (2015)

PRÉSENTÉE LE 20 FÉVRIER 2015
À LA FACULTÉ DES SCIENCES DE BASE
CRPP - THÉORIE
PROGRAMME DOCTORAL EN PHYSIQUE

ÉCOLE POLYTECHNIQUE FÉDÉRALE DE LAUSANNE

POUR L'OBTENTION DU GRADE DE DOCTEUR ÈS SCIENCES

PAR

Doohyun KIM

acceptée sur proposition du jury:

Prof. V. Savona, président du jury
Dr O. Sauter, Dr T. Goodman, directeurs de thèse
Dr I. Chapman, rapporteur
Dr I. Furno, rapporteur
Dr E. Poli, rapporteur



ÉCOLE POLYTECHNIQUE
FÉDÉRALE DE LAUSANNE

Suisse
2015

e-mail: doohyun.kim@epfl.ch, doohyun.kim83@gmail.com

This document was created using L^AT_EX.

Document version: Final.

Lausanne, February 9, 2015



ÉCOLE POLYTECHNIQUE
FÉDÉRALE DE LAUSANNE



People plan their path, but the Lord secures their steps.

Proverbs 16:9

Abstract

The main goal of this thesis is to demonstrate the capability of magneto-hydrodynamic (MHD) instability control, particularly sawteeth and neoclassical tearing modes (NTMs), in order to achieve high performance operation. Experiments and simulations have been carried out to pursue this purpose on different tokamaks: TCV (in Switzerland), KSTAR (in Korea), AUG (in Germany) and ITER (in construction in France).

Each tokamak has different features such as machine size, heating systems, operation scenarios and energy confinement time scale, all the tokamaks are equipped or will be equipped with an electron cyclotron heating/current drive (ECH/ECCD) system for plasma heating/current drive and control of MHD instabilities. Therefore, this work focusses on the feasibility of using the localised ECH/ECCD beams to control the instabilities; sawteeth and NTMs.

For the experimental part, sawtooth and NTM control experiments have been carried out. In TCV, novel ways of sawtooth period control - sawtooth pacing and locking - have experimentally been demonstrated using the TCV real-time control system. Based on the successful application of these methods to sawtooth control in TCV, we have next focussed on the extension of these new sawtooth period control methods to other tokamaks: KSTAR and AUG. In the 2013 KSTAR experimental campaign, the applicability of sawtooth locking using EC power modulation has been tested for sawtooth period control in the presence of fast particles generated by neutral beam injection (NBI). The KSTAR real-time control system was not ready for sawtooth pacing thus only locking has been examined. These preliminary KSTAR experimental results have shown the possibility of sawtooth period control using sawtooth locking, although proper locking was not obtained yet. The locking parameters would still need to be adjusted for single period locking to occur. In order for the investigation of the capability of sawtooth locking on KSTAR tokamak to be complete, more experiments with different locking parameters should be carried out. The sawtooth locking technique has also been applied to AUG plasmas. As in the KSTAR tokamak, the real-time control for sawtooth pacing was not available, thus sawtooth locking has been tested. The AUG plasmas were more complicated compared to TCV and KSTAR cases due to the fast particles effect on the evolution of sawtooth from both NBI and ion cyclotron heating (ICH). Sawteeth did not lock to the EC modulation in AUG experiments, though in some discharges they became somewhat more regular. However, the application of sawtooth locking to the AUG tokamak has been well initiated and more experiments will follow to understand better the behaviour of sawteeth and to determine the sawtooth locking range. In addition, sawtooth control was demonstrated and used in other experiments studying the role of sawteeth on impurity transport.

Concerning the NTM control experiments, we have focussed on the enhancement of

the NTM control strategy, which has been achieved in two ways. In previous TCV experiments, NTM stabilisation was obtained as ECH/ECCD deposition was swept in one direction until the mode disappeared. In order to ameliorate the control of NTMs, as a first improvement, a real-time version of the equilibrium reconstruction code LIUQE (RT-LIUQE) has been implemented in the TCV real-time control system. Using RT-LIUQE, the safety factor q can be estimated in real-time and from pre-calculated ray-tracing and an assumption on which mode is to be controlled, a target q is converted to a requested EC launcher angle. In this way, the EC launcher can track the location of NTMs in real-time to stabilise the mode or to prevent the onset of the mode. In recent TCV experiments, the capability of NTM stabilisation and pre-emption using RT-LIUQE has been successfully demonstrated. Although the mode location can be estimated by RT-LIUQE, there are still uncertainties; for example an intrinsic offset exists in the estimated q profile. In order to ensure the suppression of NTMs, these difficulties need to be resolved. Therefore, as a second improvement, we have introduced a new simple and robust technique to control NTMs. By adding a sinusoidal variation on the target position estimated by RT-LIUQE, the EC launcher sweeps around the estimated position and can have a higher probability to stabilise the NTMs. In the series of experiments, several discharges have been devoted to demonstrating the capability of this new technique to control NTMs. The application of this technique has been extended to other tokamaks and aims at the projection to ITER.

As with the experiments, simulation works have aimed for a predictive simulation of the control of MHD instabilities, in particular the sawtooth instability. Prior to performing sawtooth simulations, we have introduced a simple transport model to evaluate electron temperature and density profiles during sawtooth cycles (i.e. over a sawtooth period time-scale). Since the aim of this simulation is to estimate reliable profiles within a short calculation time, a simplified ad-hoc model has been developed. It has been developed to rely on a few easy-to-check free parameters, such as the confinement time scaling factor and the profiles' averaged scale-lengths. Due to the simplicity and short calculation time of the model, it is expected that this model can also be applied to real-time transport simulations. We show that it works well for ohmic and EC heated L- and H-modes. In addition, from previous TCV experiments, we have observed that the confinement time is affected by the deposition position of the EC beams. Since this effect has not been considered in the scaling law, as a preliminary test we have introduced a new scaling factor that takes into account the effect of the heating deposition position. These models have been applied to the sawtooth simulation; TCV sawtooth control experiments have been reproduced. For the sawtooth pacing, the calculated delay between EC power off and sawtooth crash agree well with the experimental results. The map of possible locking range has also been well reproduced by the simulation. Based on the TCV sawtooth simulation, we have performed a predictive simulation for the sawtooth control on ITER and with the result of this simulation, the capability of sawtooth control using the present design of ITER EC launcher has been investigated and confirmed.

Keywords: nuclear fusion, tokamak, TCV, KSTAR, AUG, ITER, transport modelling, predictive simulation, MHD instability control, real-time control, sawteeth, sawtooth pacing, sawtooth locking, ECH, ECCD, NTMs, RT-LIUQE

Résumé

L'objectif principal de cette thèse est de démontrer la capacité de contrôle des instabilités magnéto-hydrodynamiques (MHD), en particulier les dents-de-scie et les modes de cisaillement néoclassiques (NTMs), afin d'obtenir une opération à performance élevée. A cet effet, des expériences et des simulations ont été effectuées sur différents tokamaks: TCV (Suisse), KSTAR (Corée), AUG (Allemagne) et ITER (en construction en France).

Chaque tokamak présente différentes caractéristiques, telles que la taille de la machine, le système de chauffage, le scénario d'opération et le temps de confinement énergétique. Ils sont toutefois tous équipés, ou vont l'être, d'un système de chauffage et de génération de courant électron cyclotron (ECH/ECCD) pour le contrôle des instabilités MHD. C'est pourquoi nous nous sommes concentrés dans ce travail sur la faisabilité d'utiliser des faisceaux ECH/ECCD pour contrôler ces instabilités: dents-de-scie et NTMs.

En ce qui concerne la partie expérimentale, des expériences de contrôle de la dent-de-scie et NTM ont été effectuées. Dans le cas de TCV, de nouvelles techniques de contrôle des périodes de la dent-de-scie, en régulant celles-ci par "pacing" et "locking", ont été démontrées à l'aide du système de contrôle en temps réel de TCV. Etant donné la réussite de l'application de ces méthodes de contrôle des dents-de-scie à TCV, nous nous sommes ensuite concentrés sur l'utilisation de ces méthodes sur KSTAR et AUG.

Dans la campagne expérimentale de KSTAR en 2013, l'applicabilité de la méthode de locking, utilisant la modulation EC, a été testée pour le contrôle des périodes des dents-de-scie en présence de particules rapides générées par l'injection de neutres (NBI). Ces premiers résultats ont montré la possibilité de contrôler la dent-de-scie en se servant du locking. D'autres expériences sont toutefois nécessaires afin de terminer l'étude de la capacité de la régulation par locking des dents-de-scie sur KSTAR.

La technique de locking a également été appliquée aux plasmas de AUG. Les plasmas de AUG étaient plus compliqués que ceux de TCV et KSTAR en raison de l'effet des particules rapides sur l'évolution de la dent-de-scie par le chauffage NBI et ion cyclotron (ICH) et la présence d'impuretés. Les dents-de-scie ne se verrouillaient pas clairement sur la modulation EC dans les expériences conduites à AUG. Toutefois, l'application de la régulation par locking sur le tokamak AUG a bien débuté et plus d'expériences vont suivre afin de mieux comprendre le comportement des dents-de-scie et d'avoir l'étendue entière des possibilités de cette méthode. Le contrôle des dents-de-scie a pu être utilisé pour d'autres expériences liées aux effets de transport des impuretés.

En ce qui concerne les expériences de contrôle des NTMs, nous nous sommes concentrés sur l'amélioration de la stratégie de contrôle des NTMs, qui a été accomplie de deux façons. Dans des expériences précédentes conduites à TCV, la stabilisation NTM a été obtenue quand le dépôt ECH/ECCD était balayé dans une direction jusqu'à la disparition du

mode. Afin d'améliorer le contrôle des NTMs, premièrement, une version en temps réel du code de reconstruction de l'équilibre LIUQE (RT-LIUQE) a été implémentée dans le système de contrôle en temps réel de TCV. En utilisant RT-LIUQE, le facteur de sécurité q peut être estimé en temps réel, et la position radiale d'un q cible est transformée en un angle EC du lanceur requis, à l'aide d'un ray-tracing précalculé ainsi que d'une hypothèse du mode rationnel à traiter. De cette façon, le lanceur EC peut suivre la localisation des NTMs en temps réel afin de stabiliser le mode ou d'empêcher son apparition. Dans des expériences récentes conduites à TCV, la capacité de la stabilisation des NTMs et de leur prévention a été démontrée grâce à RT-LIUQE.

Bien que la localisation du mode puisse être estimée grâce à RT-LIUQE, il reste des incertitudes, principalement l'offset intrinsèque de la valeur estimée. Afin de s'assurer de la suppression des NTMs, cette difficulté doit être résolue. C'est pourquoi nous avons introduit une nouvelle technique simple et robuste pour contrôler les NTMs ; c'est notre deuxième amélioration. En ajoutant une variation sinusoidale à la position cible estimée par RT-LIUQE, le lanceur EC balaie le faisceau ECCD autour de la position estimée et donne plus de possibilités de stabiliser les NTMs. Dans la série d'expériences présentées, nous avons pu démontrer la capacité de cette nouvelle technique pour le contrôle des NTMs. Cette méthode a été appliquée à d'autres tokamaks et vise la projection à ITER.

Comme pour les expériences, les simulations effectuées avaient comme objectif une simulation prédictive du contrôle des instabilités MHD, en particulier l'instabilité de la dent-de-scie. Avant la simulation de la dent-de-scie, nous avons introduit un modèle simple de transport afin d'évaluer les profils de température et de densité des électrons pendant les cycles de la dent-de-scie. Etant donné que le but de cette simulation est d'estimer des profils fiables dans un temps de calcul limité, les modèles de transports actuellement existants ne sont pas adéquats. Le nouveau modèle est basé sur un petit nombre de paramètres libres, ces derniers étant facilement identifiables et vérifiables. Grâce à la simplicité et rapidité de calcul de ce modèle, il est attendu qu'il peut aussi être appliqué à la simulation du transport en temps réel. Nous avons montré que ce nouveau modèle ad-hoc fonctionne bien dans les cas ohmiques et chauffés, ainsi que les modes de bas et haut confinements. De plus, à travers de précédentes expériences conduites à TCV, nous avons observé que le temps de confinement est affecté par la position de dépôt du faisceau EC. Comme cet effet n'a pas été pris en considération dans la loi d'échelle, nous avons introduit un nouveau facteur, qui prend en compte l'effet de la position radiale du chauffage. Ces modèles ont été appliqués à la simulation de la dent-de-scie; l'expérience de contrôle de la dent-de-scie sur TCV a été reproduite. Pour la régulation par pacing de la dent-de-scie, le délai calculé entre l'arrêt de l'EC et la chute de la dent-de-scie a bien correspondu aux résultats expérimentaux. Le schéma de l'étendue possible de régulation par locking a également bien été reproduite par la simulation. Basé sur cette validation de nos résultats, nous avons effectué une simulation prédictive du contrôle de la dent-de-scie pour le cas de ITER et, avec le résultat de cette simulation, nous avons étudié et confirmé la capacité de contrôle de la dent-de-scie en utilisant la conception actuelle du lanceur EC de ITER.

Mots clés: la fusion nucléaire, tokamak, TCV, KSTAR, AUG, ITER, la modélisation du transport, la simulation prédictive, le contrôle de l'instabilité MHD, le contrôle en temps réel, les dents de scie, pacing de la dent de scie, locking de la dent de scie, ECH, ECCD, NTMs, RT-LIUQE

Contents

Abstract	v
Résumé	vii
Contents	ix
1 Introduction	1
1.1 Nuclear fusion reaction	2
1.1.1 Plasma: the fourth state of matter	2
1.1.2 Conditions for fusion reaction	3
1.2 Tokamak: The device for plasma confinement	4
1.2.1 The configuration	4
1.2.2 Important parameters	5
1.2.3 Auxiliary heating and current drive systems	6
1.3 Control of plasma instabilities	7
1.4 Thesis motivation	8
1.5 Outline of this dissertation	9
2 Tokamaks	11
2.1 TCV: Tokamak à Configuration Variable	11
2.1.1 Overview	11
2.1.2 Electron cyclotron wave system	14
2.1.3 Real-time control system	15
2.2 KSTAR: Korea Superconducting Tokamak Advanced Research	16
2.3 ASDEX Upgrade: Axially Symmetric Divertor EXperiment Upgrade	18
2.4 ITER	19
2.4.1 Overview	19
2.4.2 ITER EC launcher system	21
3 Predictive electron transport model for L-mode plasmas	25
3.1 Introduction	25
3.1.1 Overview	25
3.1.2 Transport equations	27
3.2 Simplified transport model for a predictive simulation	30
3.2.1 Power balance heat transport coefficient	30
3.2.2 Ad-hoc model for electron heat diffusivity χ_e	31

CONTENTS

3.2.3	Constraints of the model	36
3.2.4	Determination of transport coefficients for density profile	41
3.2.5	Simulation results using simplified ad-hoc models for T_e and n_e	42
3.3	Effect of heating deposition position on confinement time	45
3.3.1	A new scaling factor for the heating deposition location	46
3.3.2	A test case using the new scaling factor	47
3.4	Application to H-mode	51
3.4.1	Comparison of the shape of the T_e profiles in L- and H-mode plasmas	51
3.4.2	H-mode T_e and n_e profile simulations using the same ad-hoc model as in L-mode	53
3.5	Summary	59
4	Control of sawtooth instability	61
4.1	Introduction	61
4.2	Model for sawtooth simulation	63
4.2.1	Criteria for sawtooth crash triggering	63
4.2.2	Modification of profiles after sawtooth crash	67
4.3	Control of sawtooth period using localised EC injection	71
4.3.1	Effect of EC beam on shear evolution	71
4.3.2	Sawtooth period pacing and locking	72
4.4	Control of sawtooth period on TCV	74
4.4.1	Experimental demonstration	74
4.4.2	Simulation of sawtooth pacing and locking	75
4.5	Sawtooth period control experiment on KSTAR	80
4.5.1	Experimental set up	80
4.5.2	Results of sawtooth locking experiments	81
4.6	Experiment and simulation of sawtooth locking on AUG	87
4.6.1	Preparation of sawtooth locking experiment	87
4.6.2	Experimental results of sawtooth locking	90
4.7	Predictive sawtooth control simulation for ITER	95
4.7.1	Preparation of ITER simulation	96
4.7.2	Description of the EC beams	99
4.7.3	Simulation results	101
4.8	Summary	117
5	Real-time control of neoclassical tearing mode	121
5.1	Introduction	121
5.2	Physics of neoclassical tearing modes	122
5.2.1	The formation of magnetic islands	122
5.2.2	Modified Rutherford equation	123
5.2.3	Trigger and control of NTMs	126
5.3	NTM control experiment using real-time equilibrium reconstruction	127
5.3.1	Real-time LIUQE	129
5.3.2	Operation scenarios for NTM control experiment	133
5.3.3	Mode stabilisation using RT-LIUQE with a fixed q_{target}	134
5.3.4	Destabilisation/trigging condition	137

5.3.5	Preemption of the mode	140
5.4	Robust NTM control	144
5.4.1	Application of robust control: Mode stabilisation	145
5.4.2	Application of robust control: Mode preemption	148
5.5	Summary	149
6	Conclusions	151
6.1	Predictive electron transport modelling	151
6.2	Control of sawtooth instability	152
6.3	Real-time control of neoclassical tearing mode	154
	Bibliography	155
	Acknowledgements	173
	Curriculum Vitae	175

Chapter 1

Introduction

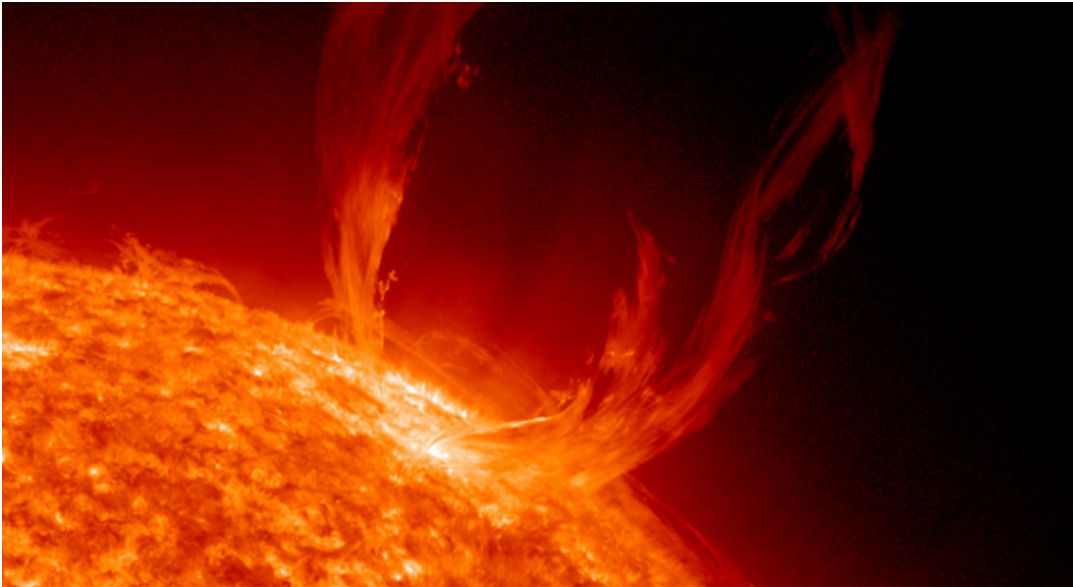


Figure 1.1: The Sun produces its energy from nuclear fusion reaction. *Image: Solar Dynamics Observatory*

Stars in the universe, such as our Sun, produce their energy from nuclear fusion reactions. Nuclear fusion is the basic process which governs the energy production of stars and it is the process whereby light nuclei, such as hydrogen, fuse into new heavier elements, such as helium. During this process, large amounts of energy are released. Hence, the purpose of nuclear fusion research is to imitate this process on earth to harness this energy source.

Compared to other energy sources, nuclear fusion has several advantageous aspects [Freidberg:PlasmaPhysics]. For instance, isotopes of hydrogen can be used as the ingredients for this process and they are obtained from water, which is abundant on earth. Furthermore, no greenhouse gases or long-lived nuclear waste are created from fusion reactions. For a power plant, a higher safety level is assured than in a fission plant. When the operation suffers a large excursion from the nominal operation point, no fusion reac-

tion happens and therefore, no explosive event can occur. Consequently, once harnessed, fusion power will be a nearly unlimited, safe and climate friendly energy source. In the following discussion, we will focus on how we can enable the nuclear fusion reaction on earth, where conditions are very different from those of the Sun.

1.1 Nuclear fusion reaction

1.1.1 Plasma: the fourth state of matter

A fusion reaction occurs between two light nuclei, such as hydrogen. Therefore, in order for the nuclear fusion reaction to occur, the nuclei should first be extracted from the atoms by separating their electrons. This requirement is naturally satisfied when a gas is heated and its temperature is beyond the ionisation limit. Once ionisation takes place, the gas is not neutral anymore but consists of ions (nuclei), electrons and neutral particles. This state of matter is called *plasma*. A plasma is almost entirely neutral but is not necessarily locally neutral. Thus it is also called a *quasi-neutral* gas of charged particles. The motion of charged particles generates currents and corresponding magnetic fields. These fields affect the motion of other particles over some distance and as a result, the charged particles in a plasma exhibit collective behaviour. The change of the state of matter is shown in Fig. 1.2.

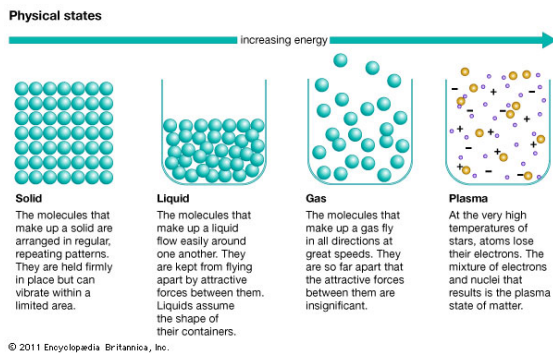


Figure 1.2: By increasing the temperature, the state of matter changes from solid to plasma. *Image: www.britannica.com*

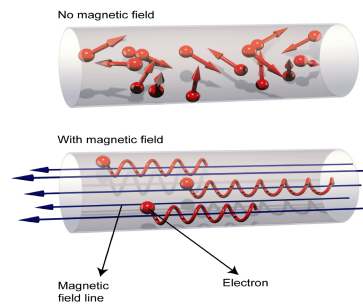


Figure 1.3: The motion of charged particles follows the electromagnetic fields and the direction of the motion is dependent on their charge. *Image: http://iter.rma.ac.be*

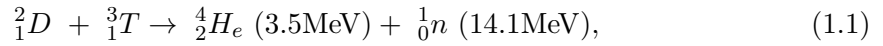
In a plasma, the motion of the charged particles is random, as seen in the top of Fig. 1.3. However, if electromagnetic fields are applied to the plasma, due to the nature of the charged particles, the behaviour of charged particles can be influenced by the applied external fields. The behaviour of the charged particle in the presence of the electromagnetic fields is shown in the bottom of Fig. 1.3. Being governed by the Lorentz force $\mathbf{F} = q(\mathbf{E} + \mathbf{v} \times \mathbf{B})$, where q is the charge of the particle, \mathbf{v} the velocity and \mathbf{E} , \mathbf{B} the electric and magnetic fields, the charged particles have a helical trajectory around the magnetic field lines. The directions of the motion parallel and perpendicular to the field lines are dependent on the charge of the particle, i.e. electrons and ions have a different direction of motion. Using this characteristic, the charged particles can be guided by the

external fields in a plasma and have opportunities to collide with other particles if the charged particles are confined by the magnetic fields.

1.1.2 Conditions for fusion reaction

Inside a plasma, positive ions move along the field lines and there are lots of possibilities to see other ions. However, between two ions there is a strong repulsive force due to their charge. They cannot exceed the Coulomb potential between them and therefore cannot create fusion reaction. In order to overcome this restriction, very high energy is demanded. In certain situations, two ions come close enough and have a sufficiently high temperature, which happens to be less than the energy required to overcome the Coulomb potential. In this situation, because of quantum mechanical tunnelling, the strong nuclear force becomes dominant and two ions fuse into a heavier element.

The probability or cross-section of fusion reaction is dependent on the ion temperature. Among the possible fusion reactions, the reaction between deuterium (${}^2_1\text{D}$) and tritium (${}^3_1\text{T}$), two isotopes of hydrogen which have one proton and respectively one and two neutrons, has the largest reaction cross-section [Freidberg:PlasmaPhysics, Wesson:Tokamaks]. From the fusion reaction between D and T, helium (${}^4_2\text{He}$) and a neutron (${}^1_0\text{n}$) are produced carrying high kinetic energies. The reaction process occurs in the following form



and it is visualised in Fig. 1.4.

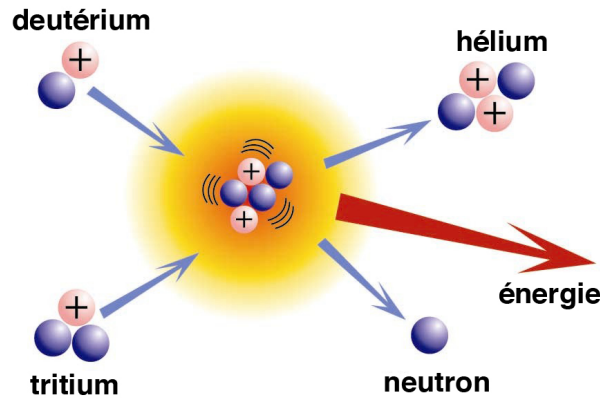


Figure 1.4: Two ions of hydrogen isotopes D, T fuse into He and n . Due to the change in the total mass, energy is released during the fusion process and each fusion product shares the energy. *Image: www.iter.org*

Along with the large cross-section (probability of fusion reaction), it is also necessary to confine the stored energy for a sufficiently long time. This time is called energy confinement time τ_E , which is the ratio of plasma stored energy to power loss. A long τ_E indicates that small power is needed to maintain the required plasma energy, which is proportional to the product of temperature and density.

In D-T fusion reactions, the H_e and the neutron share the resultant energy. Since the neutron is not a charged particle, its motion cannot be controlled by an external field. On the other hand, with a positive charge, the H_e ion moves together with D and T along the field lines and transfers its energy to other particles through collisions. This is why the fusion reaction can be self-sustained by the energy of the H_e and no additional energy would be demanded from outside. This state is called *ignition*. In order to achieve ignition, the following condition should be satisfied [Wesson:Tokamaks].

$$nT\tau_E > 3 \times 10^{21} \text{ m}^{-3} \text{ keV s}, \quad (1.2)$$

where n and T in the triple product $nT\tau_E$ are the plasma density and temperature, respectively. Therefore, in order for the plasma to be self-sustained, the fusion research should aim at having the triple product beyond the minimum value. In ITER, for instance, T aims higher than 10keV and τ_E will be of the order of seconds. Then, if $T = 10\text{keV}$ and $\tau_E = 3\text{s}$, the ignition can be reached when $n > 10^{20} \text{ m}^{-3}$. Note that we took an example from a prediction of ITER plasma but ITER does not aim the ignition.

1.2 Tokamak: The device for plasma confinement

In order to achieve the ignition condition, two approaches have been developed in the fusion research field. The first one is *inertial* confinement fusion (ICF) [Lindl:PoP2014]. The aim of this approach is to acquire the ignition by compressing small capsules to very high density using lasers. The confinement time is relatively short but with high density, the ignition condition can be satisfied. Another approach is the use of magnetic fields to confine the plasma. This approach is therefore called *magnetic* confinement fusion (MCF). In this approach, the confinement time can be longer and a relatively lower density is needed. There are several different concepts of using a magnetic field to confine fusion plasmas, such as the magnetic mirror [Burdakov:PPCF2010] and stellarator [Lyon:PPCF1990]. Among those concepts we will focus on the tokamak concept [Artsimovich:NF1972], which is the most-researched candidate for producing controlled nuclear fusion power.

1.2.1 The configuration

A tokamak is a device using helical magnetic fields to confine a plasma in the shape of a torus. The helical field can be generated by adding magnetic fields in the toroidal direction (toroidal field, traveling around the torus in circles) and other fields in the poloidal direction (poloidal field, traveling orthogonal to the toroidal field). The configuration of a tokamak is shown in Fig. 1.5. The pink coloured donut shape represents the confined plasma on the surface with same poloidal flux values (flux surface). A blue arrow inside the plasma and green arrows around the plasma indicate the toroidal and poloidal magnetic fields, respectively. The toroidal field is induced by toroidal field coils (blue coils arranged in the poloidal plane) and the poloidal field is created by the plasma current (green arrow inside the plasma), which is generated by the primary transformer coil (or central solenoid). The combination of the toroidal and poloidal fields results in helical field lines, and charged particles in a plasma are confined by following these field lines. In

1.2. Tokamak: The device for plasma confinement

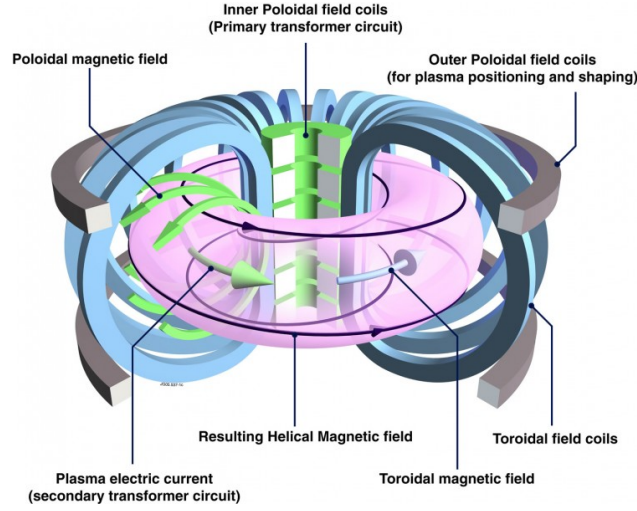


Figure 1.5: A schematic view of a tokamak device. A plasma is confined by the helical magnetic field, a combination of toroidal and poloidal magnetic fields. Using an additional field from poloidal field coils, poloidal position and shape of plasma can be controlled. *Image: www.iopblog.org*

order for a stable plasma equilibrium to be maintained, there is an additional set of coils, the poloidal field coils. Using these coils, additional fields are provided to the poloidal field and can control the plasma position in the poloidal plane and plasma shape.

1.2.2 Important parameters

A tokamak plasma is defined by a number of quantities such as geometry and magnetic field intensity. Among these quantities, some important parameters will be introduced here. The total plasma current I_P is one of the most important operational parameters. Another parameter is the normalised plasma pressure β which represents the efficiency of confinement of plasma pressure by the magnetic field. β is defined as the ratio of kinetic pressure to magnetic pressure in the following form

$$\beta = \frac{\langle p \rangle}{B_0^2/2\mu_0}, \quad (1.3)$$

where $\langle p \rangle$ is the volume averaged pressure (nT) and B_0 is the vacuum toroidal field. Similarly, the poloidal β is defined by normalising the pressure by the poloidal magnetic field B_p rather than B_0

$$\beta_p = \frac{\langle p \rangle}{B_p^2/2\mu_0}. \quad (1.4)$$

Another normalised form of β indicating how close the plasma is to reaching the operational or stability limits is defined in the form of

$$\beta_N = \frac{\beta[\%]}{I_P[\text{MA}]/(a[\text{m}]B_0[\text{T}])}, \quad (1.5)$$

where a is the plasma minor radius. Typically, the maximum value of β_N before the onset of deleterious macro-instability is around 3.4 [Troyon:PPCF1984].

A safety factor q is another important parameter in a tokamak plasma as defined below

$$q = \frac{\partial\phi}{\partial\psi}, \quad (1.6)$$

where ϕ and ψ are the toroidal and poloidal magnetic fluxes. q indicates how many toroidal turns a field line requires to make one complete poloidal turn. This parameter is called *safety factor* because it plays a role in determining the magnetohydrodynamic (MHD) stability and with high q configurations, plasmas tend to be more stable [Wesson:Tokamaks, Freidberg:PlasmaPhysics] albeit at smaller β as indicated by β_N .

1.2.3 Auxiliary heating and current drive systems

In order to have a sufficiently high plasma temperature for the fusion reaction to occur, a plasma has to be heated. By ohmic heating, the plasma current can heat the plasma as the current increases and the ohmic heating power density is given by

$$P_{ohmic} = \eta j_p^2, \quad (1.7)$$

where η is the plasma resistivity and j_p is the plasma current density. However, η is inversely proportional to the electron temperature T_e as $\eta \sim T_e^{-3/2}$ so that the ohmic heating power decreases as temperature increases. Furthermore, the maximum value of the current density itself is limited by MHD stability [Troyon:PPCF1984]. Therefore, by ohmic heating alone, the plasma itself cannot have a sufficient temperature level for fusion reactions and additional heating is required. The possible heating methods including ohmic heating are presented in Fig. 1.6.

Neutral beam injection (NBI) is one way to heat the plasma. A high-energy beam of neutral atoms (typically a hydrogen isotope such as deuterium) are injected into the core of the plasma. As the injected atoms are neutral, they are not affected by the magnetic field until they are ionised when colliding with plasma particles. During the collisions, the energetic particles transfer their energy to plasma particles, which results in an increase of the overall plasma temperature. NBI can drive a current depending on the direction of injection and it can also inject momentum causing plasma rotation.

Another way of additional heating is the injection of electromagnetic waves into the plasma. The waves couple to the plasma particles depending on the wave frequency. With low-frequency, the waves couple to ion species in the plasma and heat the ion (ion cyclotron resonance heating, ICRH). While the high-frequency waves resonate with the electron cyclotron frequency and the energy of waves is absorbed by electrons (electron cyclotron resonance heating, ECRH). In addition to plasma heating, the waves can induce currents in the ion cyclotron frequency range (ion cyclotron current drive, ICCD), electron cyclotron frequency range (electron cyclotron current drive, ECCD) and lower hybrid frequency range (lower hybrid current drive, LHCD).

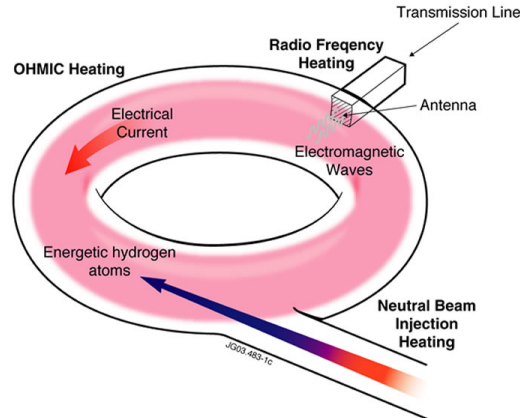


Figure 1.6: A plasma has an intrinsic heating mechanism, the ohmic heating by the plasma current. However, it is not sufficient to reach a high temperature for fusion reaction. As additional heating methods, high energy particle and electromagnetic wave injections can be applied to the plasma for heating and current drive. *Image: www.euro-fusion.org*

1.3 Control of plasma instabilities

As a plasma is confined in a tokamak and the temperature increases with heating powers, it seems that the ignition condition can be easily satisfied. Unfortunately, several obstacles still remain. One of the obstacles is plasma instabilities, in particular MHD instabilities, which can degrade the plasma performance and limit the operation regime. The MHD instabilities can be triggered by an increase in plasma current or pressure. As a result, it is difficult to get a significant value of the fusion triple product $nT\tau_E$. Therefore, the understanding and control of these instabilities are essential in order for the plasma performance to be optimised. Among the many existing MHD modes, two instabilities, which are relevant to this thesis work, and their control will be briefly discussed.

The first one is the **sawtooth** instability [VonGoeler:PRL1974], which is a periodic fast relaxation (crash) with a slower recovery of the plasma parameters in the central region that occurs where the safety factor decreases below one. As it takes place in the plasma centre, far from the edge, the plasma confinement is not much affected and moreover, the sawtooth crash has a beneficial effect since it can remove the impurities from the central region. Despite these favourable features, a sawtooth crash should be controlled as it can trigger neoclassical tearing modes (NTMs) [Sauter:PRL2002], which are detrimental in plasma confinement. Sawtoothing can be avoided in some operation scenarios, such as the hybrid scenario, but mostly exists in tokamak plasmas. Therefore, control of the sawtooth instability is required to avoid triggering NTMs.

The sawtooth instability is controlled by modifying the period between crashes using electron cyclotron (EC) wave injection [Angioni:NF2003]. By shortening a period, the magnitude of the magnetic perturbation is reduced and is not enough to trigger NTMs. On the other hand, in the case of lengthened sawtooth period, NTMs triggering is anticipated, so an action for preventing NTM triggers should be envisaged. Thanks to recent control strategies, it has been possible to control the individual sawtooth period to match a given period. The control of sawtooth will be discussed in depth in Chap. 4.

The second instabilities which will be discussed are **Neoclassical Tearing Modes** (NTMs) [LaHaye:PoP2006]. These modes cause the modification of a magnetic field configuration to form magnetic islands (magnetic reconnection). The plasma pressure becomes flat inside the island thus plasma energy decreases globally. NTM growth is driven by the plasma pressure and are triggered in high β conditions; this has the effect of limiting the achievable β value. Furthermore, in some cases, NTMs may lead to a plasma disruption, which terminates the plasma current in a short time and causes stresses on machine components. Therefore, in order to obtain the optimum performance, NTMs must be controlled.

NTMs are triggered in high β plasmas thus one way to avoid NTMs is to have a low β plasma. However, this is not acceptable since we have to aim at a high β operation for the sustainable fusion reaction. Note that even with a low β , NTMs can be triggered by a long sawtooth [Canal:NF2013], as mentioned above. Hence more active ways to control NTMs are demanded. When NTMs appear, they can be reduced in size or suppressed by using localised ECCD [Gantenbein:PRL2000]. The triggering of NTMs can also be prevented by ECCD injection when the timing of the NTM onset is predictable. The control of these instabilities using the TCV real-time control system will be discussed in Chap. 5.

1.4 Thesis motivation

In this thesis, we have focused on the control of sawteeth and neoclassical tearing modes (NTMs) using ECH/ECCD.

It is well known that ECH/ECCD can affect the evolution of magnetic shear at $q = 1$ surface and modify the sawtooth period depending on the deposition position [Angioni:NF2003]. Using this feature, active sawtooth period control methods, sawtooth pacing and locking, have been demonstrated in recent TCV experiment [Goodman:PRL2011, Lauret:NF2012]. The successful TCV experiments allow us to apply these methods to other tokamaks. Due to different factors among tokamaks such as machine size, heating system, operation scenario and energy confinement time scale, the evolution of the sawtooth instability is different for each machine. Therefore, carrying out the sawtooth control experiment on different tokamaks can provide both the information of sawtooth behaviour on each machine and show the applicability of sawtooth pacing and locking as active sawtooth period control methods. Furthermore, results from the inter-tokamak experiments can serve as a database for sawtooth control which can then be projected to ITER.

Along with the experiments, simulations are needed to help understand the behaviour of sawteeth. For sawtooth simulations, a conventional sawtooth model [Porcelli:PPCF1996] has been combined to a transport simulation code. The main objective of the simulation is to estimate the electron temperature and density profiles during the sawtooth cycle in order to examine the sawtooth period, taking into account the modification of the profiles. There have been several transport models for electron temperature and density which bring a precise result, but require relatively long calculation times. Here, however, we aim to simulate the profiles in a short calculation time; thus, a simple and fast model to estimate the profiles has been developed. Although temperature and density profiles from the new model may not have the same as predictive capabilities as those

from existing first principles models, the new model brings reliable profiles which can be used to estimate the behaviour of sawteeth. It also provides a new model for density profile evolution. Our models are constructed to have few free parameters that are easy to check. In addition, we have carried out simulations for a new scaling factor which takes into account the effect of the EC heating deposition position. As seen from the previous TCV experiments [Kirneva:PPCF2012], the plasma confinement degrades with off-axis EC heating while there is only the effect of total input power in cross-machine scaling laws [Yushmanov:NF1990, ITER-PhysicsBasis:NF1999]. Therefore, in order for the deposition position effect to be included in the scaling law, we have introduced a new scaling factor. In this thesis, we have not considered the simulation of NTMs themselves; but for the next step this factor should be taken into account on the transport modelling for NTM simulations, since the position of NTMs are usually outside the $q = 1$ surface and a modification of the scaling law is demanded while EC power is used to heal any eventual NTMs.

In previous TCV experiments, NTM stabilisation relied on the ECH/ECCD deposition sweeping without the exact information of the mode location [Felici:Thesis]. For the pre-emption of NTMs, the target position was estimated by analysing previous experiments. In this way, though it is possible to stabilise/pre-empt NTMs, a pre-estimation is required for each new experimental condition. To make experiments more efficient, the target position of EC beam should be calculated taking into account the plasma parameters in real-time. The control of NTMs has been enhanced using a real-time equilibrium reconstruction code (RT-LIUQE) [Moret:FED2015] implemented in the TCV real-time control system. Due to an intrinsic offset in the calculation of the q -profile in RT-LIUQE, the stabilisation of NTMs is affected by the ability to estimate the offset. Therefore, in order to enable the stabilisation of NTMs regardless of the offset value, we have introduced a new simple and robust technique to control NTMs. Based on the target position estimated by RT-LIUQE, the EC beam sweeps around the estimated position to increase the probability to stabilise NTMs. This technique can be used for NTM stabilisation and pre-emption. As with sawtooth control methods, the application of this technique can be extended to other tokamak and cross-tokamak experiments will lead to a better operating scenario for NTM stabilisation in ITER.

1.5 Outline of this dissertation

In this first chapter, a brief introduction of nuclear fusion, the tokamak concept and the need for instability control has been presented. The discussion of the rest of this thesis is organised as follows:

- Chapter 2 describes TCV, KSTAR, AUG and ITER tokamaks, on which all the experimental and simulation works have been carried out. The specifications and the heating systems of each machine are described. In particular, in the case of TCV, the real-time control system, which has been used for the experiments described in Chap. 5 is introduced. In the case of ITER, the possible EC beam deposition with the present design of EC launcher system is expounded.
- Chapter 3 introduces the **transport model** used for modelling in this work. A simple way to define electron temperature and density is described and the test cases

for different I_P and heating power are presented. Furthermore, a new scaling factor which takes into account the effect of heat deposition position on the confinement time is introduced and added to the confinement scaling law. The preliminary simulation result of the application of the scaling factor compared to the experimental results is presented. At the end of the chapter, the application of the transport model extended to H-mode plasmas is shown.

- Chapter 4 discusses the experimental and simulation results of **sawtooth control** using modulated EC injection on TCV, KSTAR, AUG and ITER. The recent TCV experiments are briefly reviewed. With simulations, the experiments are reproduced and the details of shear evolution during sawtooth crashes are discussed. For KSTAR and AUG, sawtooth locking experimental results are presented. Based on the experimental results, the feasibility of sawtooth period control using EC injection is discussed. A predictive simulation for ITER follows. Using the present EC launcher system and reference inductive H-mode scenario, the feasibility of sawtooth pacing and locking for sawtooth period control is demonstrated. Furthermore, the possibility of using one launcher for both sawtooth control and NTM pre-emption is examined.
- Chapter 5 presents the enhanced **NTM control** experiments using the real-time equilibrium reconstruction code RT-LIUQE. A brief introduction of RT-LIUQE, recently implemented in the TCV real-time control system, is first described and then the experimental results of NTM stabilisation, destabilisation and pre-emption using the mode location estimated by RT-LIUQE follow. A simple and robust way to compensate the intrinsic uncertainties of RT-LIUQE and to improve the control of NTMs is presented at the end of the chapter.
- Chapter 6 concludes this thesis summarising the results and providing a brief outlook for future investigations.

Chapter 2

Tokamaks

In this thesis, simulations and experiments of sawtooth and NTM control have been carried out on different tokamaks: TCV, KSTAR, AUG and ITER. In this chapter, a brief description of the main characteristics of these tokamaks will be presented.

2.1 TCV: Tokamak à Configuration Variable

2.1.1 Overview

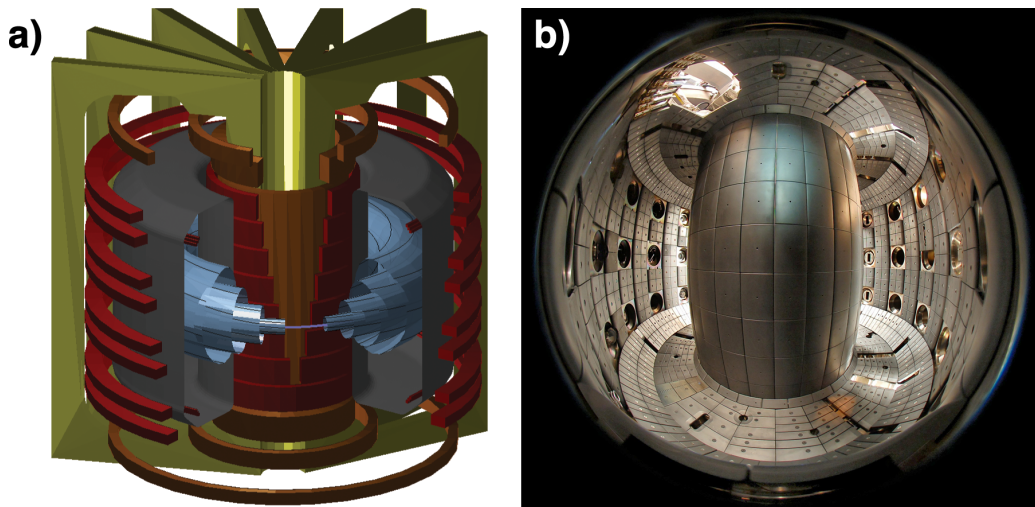


Figure 2.1: (a) cutaway view of TCV tokamak shows toroidal and poloidal magnetic coils, central solenoid, vacuum vessel with plasma inside. (b) Interior of TCV tokamak covered with carbon tiles. Numerous access ports for heating and diagnostics are cut in the vacuum vessel.

The TCV (*Tokamak à Configuration Variable*) tokamak [Hofmann:PPCF1994], located in Lausanne, Switzerland, is one of the european medium size tokamaks. The mission of the TCV tokamak is to investigate the effect of plasma shaping and heating on confinement and stability for the exploration of the physics of magnetically confined plasmas, partly in direct support of the ITER project. A highly elongated and rectangular vacuum vessel allows various plasma shapes to fit in the torus. The vacuum vessel is

Plasma parameter	Value
Major radius	0.88m
Minor radius	0.25m
Aspect ratio	3.5
Vacuum vessel height	1.54m
Vacuum vessel width	0.56m
Plasma elongation	0.9 ~ 2.8
Plasma triangularity	-0.8 ~ 0.9
Maximum plasma current	1.2MA
Maximum toroidal field on axis	1.54T
Plasma heating power	ohmic: up to 1MW ECH: 4.5MW (6 X2 + 3 X3)
Core electron density	$1 \sim 20 \times 10^{19} \text{m}^{-3}$
Core electron temperature	$\leq 1\text{keV}$ (ohmic) $\leq 15\text{keV}$ (ECH)
Core ion temperature	$\leq 1\text{keV}$
Maximum discharge duration	2.6s (ohmic), 4s (ECH/CD)

Table 2.1: Basic parameters of TCV plasma and tokamak device.

made of stainless steel and the interior is covered (90%) with carbon tiles. The cutaway view and the inside of the TCV tokamak are shown in Fig. 2.1. The basic TCV plasma and tokamak parameters are listed in Table 2.1.

The toroidal magnetic fields are induced by 16 toroidal field coils (gold rectangular coils in Fig. 2.1(a)) and a set of 7 ohmic coils (brown circular coils), as the primary transformer coil produces the plasma current. The TCV tokamak has 16 poloidal coils (red circular coils), which have independent power sources, for plasma shaping. These coils are located on both sides at the outside of the vacuum vessel. In addition, inside the vacuum vessel, there are two sets of in-vessel coils in the outer corners, protected by tiles, to control the vertical stability.

Using the poloidal coils, high degree of flexibility is achieved in creating plasma shapes with a wide range of elongation and triangularity. Examples for this are shown in Fig. 2.2. Using the various combination of the poloidal coils, limited and single/double null divertor shapes, pear and doublet shapes, highly elongated shape and high positive and negative triangularity shapes are attainable. Recently, innovative concepts of plasma shaping have also been developed and demonstrated in TCV, such as the snowflake divertor [Piras:PPCF2009, Piras:PRL2010] and X-divertor concept [Vijvers:APS2013, Vijvers:NFSUB].

For the plasma source, deuterium, hydrogen and helium are used as the main ion component. Due to the graphite tiles inside the vacuum vessel, the main impurity in TCV plasmas is carbon. In order to remove the impurities with cleaning, a helium glow discharge is applied between each discharge. The machine is also periodically boronised. In addition to ohmic heating, TCV plasmas are heated by an Electron Cyclotron Resonance Heating (ECRH) system [Goodman:NF2008, Alberti:NF2005, Arnoux:PPCF2005] which has the nominal power of 4.5MW in total, distributed over second and third harmonics of the electron cyclotron frequency through seven real-time-controllable launchers.

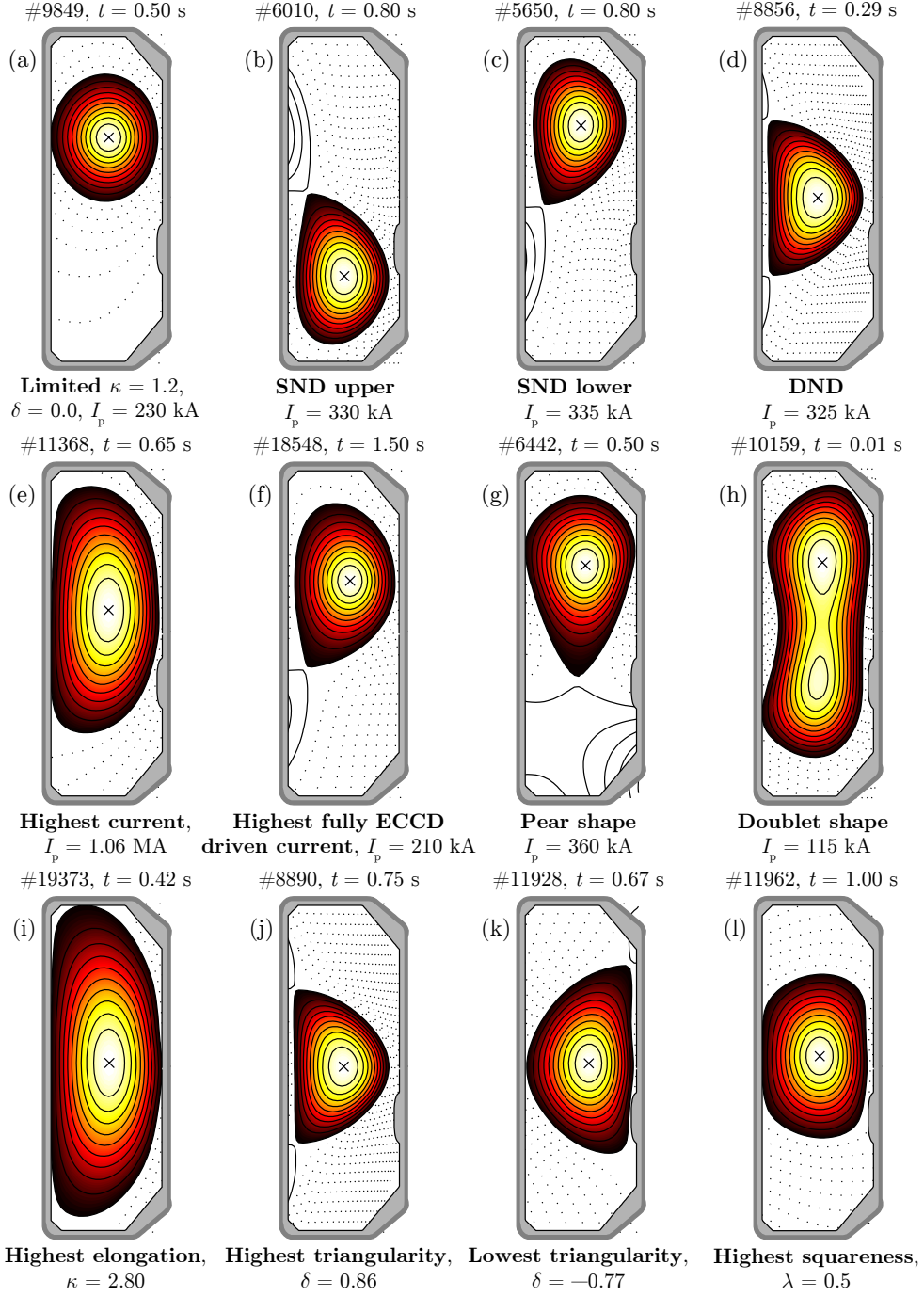


Figure 2.2: Examples of TCV plasma shapes from conventional limited and divertor shape plasmas to extremely shaped (high elongation or triangularity) plasmas.

The TCV tokamak has a large variety of diagnostics for measuring plasma parameters. These include: **magnetic diagnostics** (magnetic probes, flux loops, diamagnetic loops) [Moret:RSI1998, Rossel:Thesis] for the time derivative of magnetic fluxes and fields which can be used for plasma shape and position control, equilibrium reconstruction and MHD mode analysis; **Thomson scattering** [Franke:Thesis] for local electron temperature and density; **Far InfraRed interferometer (FIR)** [Barry:LAPD1997] for line integrated electron density; **Charge eXchange Recombination Spectroscopy (CXRS)** [Bortolon:Thesis, Bosshard:Thesis] for local measurement of impurity temperature, density and toroidal and poloidal rotation; and a **Duplex Multiwire Proportional X-ray detector (DMPX)** [Sushkov:RSI2008] for measuring the soft X-ray emissions and for the MHD instability control.

Using the measured data from diagnostics, the plasma magnetic equilibrium is reconstructed by the LIUQE code (EQUIL spelled backwards) [Hofmann:NF1988] after each discharge. By solving the Grad-Shafranov equation, LIUQE finds a poloidal flux which minimises the least-squares error to the measurements. The reconstruction can be constrained by the measured toroidal flux (from diamagnetic loops) and the pressure profile (from Thomson scattering). In addition, for the EC beam injection, the deposited power and current drive densities, the beam trajectory and absorption rate can be calculated by the ray-tracing code TORAY-GA [Matsuda:IEEE1989]. TORAY takes the plasma description from the kinetic measurements (temperature and density from Thomson scattering) and is coupled to an MHD equilibrium from the LIUQE results using the CHEASE code [Lutjens:CPC1996].

2.1.2 Electron cyclotron wave system

The versatile Electron Cyclotron (EC) wave system [Goodman:NF2008, Alberti:NF2005, Arnoux:PPCF2005] can provide localised EC heating (ECH) and current drive (ECCD) capabilities in a wide accessible operation range. The EC wave system consists of six gyrotrons for heating at the second harmonic resonance (82.7GHz) of the electron cyclotron frequency and three other gyrotrons for third harmonic (118GHz) heating. Three gyrotrons are grouped in three independently powered clusters (two for the second and one for the third harmonics). From each gyrotrons, the nominal power of 0.5MW (4.5MW in total) is provided to the plasma. The delivered EC wave can be polarised to couple to the ordinary (O-) or the extraordinary (X-) mode in the TCV plasma. In TCV, the second and third harmonic X-mode waves, X2 and X3, respectively, are usually used; mainly for bulk plasma heating and current drive, but also for other objectives such as MHD instability control. The TCV EC system for X2 and X3 wave beams are shown in Fig. 2.3.

The X2 waves are delivered through two launchers (L1, L4) at an equatorial level ($z = 0$) and four launchers (L2, L3, L5, L6) from the upper ports ($z = 0.46\text{m}$). Each launcher consists of four mirrors. Of these, the last one, facing the plasma, can be moved during a discharge, following either a pre-determined motion or a real-time control command. The X2 system is mainly used for plasma heating and current drive and can also be applied for ECH-assisted start up study and for MHD instability control, e.g. sawtooth and/or NTM controls.

Since the operation range of X2 system is restricted due to the cutoff density of about

$4 \times 10^{19} \text{m}^{-3}$, X3 waves can be used to centrally heat high density plasma (e.g. H-mode plasmas) up to somewhat below the cutoff density, approximately $11 \times 10^{19} \text{m}^{-3}$. X3 waves are delivered from a single launcher located at the top of the vessel. In order to increase the absorption path through out the plasma, X3 waves are injected nearly tangentially to the resonant surface. The absorption of X3 wave can be optimised by moving the major-radial position and the steering angle of the mirror of the X3 launcher, the latter during a discharge.

Up to the time of writing, the EC system is the only auxiliary heating and current drive system in TCV; however, upgrades of the TCV auxiliary heating system are planned. We will install a 1MW Neutral Beam Injection (NBI) heating system and increase the X3 power with an additional 2MW generated by two new multi-frequency gyrotrons (operating in the X2 or X3 range).

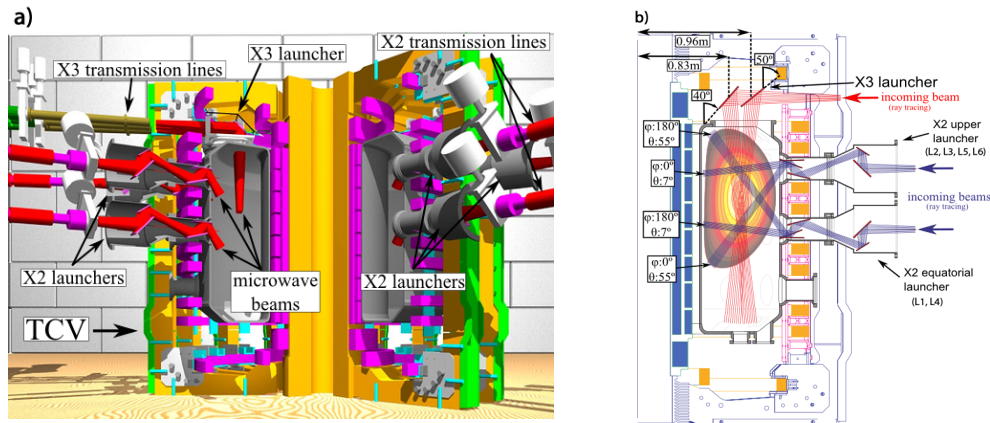


Figure 2.3: (a) The 3D view and (b) poloidal view of TCV EC system. The X2 launchers are installed at equatorial (L1, L4) and upper ports (L2, L3, L5, L6). By steering the mirror close to the plasma, X2 waves can access a wide range inside plasma (blue lines) for heating and current drive. The X3 waves injected from the top of the vessel pass the plasma vertically and deliver heating power to the plasma.

2.1.3 Real-time control system

Two control systems currently exist in TCV. The first one is the original control system [Lister:FT1997]. This system is referred to as a **hybrid** control system due to the hybrid combination of analog and digital processes in the system. The second is a new, fully digital, distributed control system which is called **SCD** (Système de Contrôle Distribué) [Paley:RTC2010, Le:FED2014]. This new system is envisioned to replace the hybrid system and is able to carry out readily-adaptable advanced control such as real-time control of the EC system. The SCD system consists of four inter communicating nodes, which share information via reflective memory. The first and second nodes are connected to different diagnostics and actuators. The third node serves only to run the real-time equilibrium reconstruction code and the last node is used as a backup. The diagram of the SCD control system is shown in Fig. 2.4 with several examples of connected diagnostics and actuators.

The main actuator used for the application of real-time control in this work is the EC system. The gyrotron powers and launcher angles are controlled by the SCD system in real-time, making real-time MHD instability control possible with the EC system. For instance, controlling of EC power allows us to apply sawtooth pacing (see chapter 4 for the detail). Using the DMPX signal, a sawtooth crash is detected in real-time and the detection triggers the EC power pulse. For more detail about real-time sawtooth crash detection and EC power control see Refs. [Felici:FED2014, Felici:Thesis]. In the real-time node 3, the real-time version of LIUQE (RT-LIUQE) has been implemented and provides the location of MHD instabilities ($q = m/n$ surfaces). By applying this transmitted information to node 1, the target launcher angle is calculated and the EC launcher (X2) can change its deposition position to follow changes in the plasma, for example. This technique has been applied for NTM stabilisation, as described in Chap. 5.

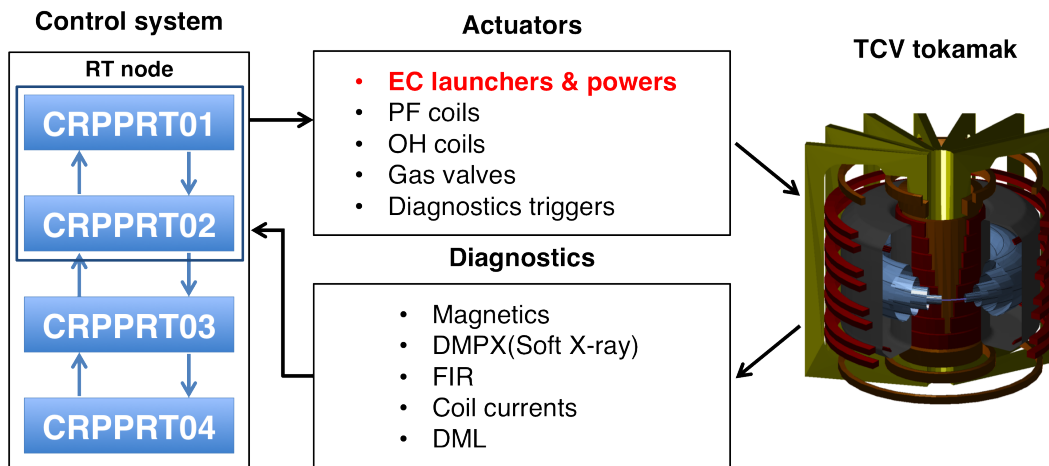


Figure 2.4: A diagram of the TCV SCD control system. Real-time control node 1 and 2 are connected to diagnostics and actuators while node 3 is allocated for RT-LIUQE.

2.2 KSTAR: Korea Superconducting Tokamak Advanced Research

The KSTAR (*Korea Superconducting Tokamak Advanced Research*) tokamak [Lee:NF2000] is a medium size magnetic fusion experimental device, located in Daejeon, South Korea. KSTAR’s aim is to develop a steady-state-capable advanced superconducting tokamak which can establish the scientific and technological base for the fusion power based reactor. KSTAR is one of the first tokamaks to be equipped with fully superconducting magnets for toroidal and poloidal magnetic field coils. This feature is an aspect relevant to ITER as superconducting magnets will be installed in ITER. The basic parameters of a KSTAR tokamak plasma are listed in Table 2.2.

The KSTAR superconducting magnet system consists of 16 toroidal field (TF) coils which use Nb₃Sn and 14 poloidal field (PF) coils, which use Nb₃Sn and NbTi. A toroidal magnetic field of 3.5T is provided by the TF coil systems at a plasma centre. Eight coils in the central solenoid and six outer PF coils compose the PF coil system and the plasma

2.2. KSTAR: Korea Superconducting Tokamak Advanced Research

Plasma parameter	Value
Major radius	1.8m
Minor radius	0.5m
Plasma elongation	2.0
Plasma triangularity	0.8
Maximum plasma current	2.0MA
Maximum toroidal field on axis	3.5T
Auxiliary heating power	~28MW
Normalised beta β_N	~5.0
Maximum pulse length	300s
Plasma shape	Single/double null divertor shape
Plasma fuel	hydrogen, deuterium
Superconductor material	Nb ₃ Sn, NbTi

Table 2.2: KSTAR parameters.

current of 2MA is induced by the PF coil system. With the superconducting magnet system, the KSTAR tokamak is able to study long plasma pulses. In 2012, the KSTAR established a flat top of H-mode plasma for 17s. The envisaged target pulse length is 300s with fully upgraded heating and control systems.

The KSTAR heating and current drive system consists of neutral beam injection (NBI) [Bae:FED2012], ion cyclotron resonance heating (ICRH) [Kwak:FED2010], lower hybrid current drive (LHCD) [Park:FST2013], and electron cyclotron resonance heating (ECRH) [Bae:FST2014] subsystems. The heating power of 8MW is delivered to the plasma from three ion sources of NBI, and 2MW from ICRH. 0.5MW of 5GHz LHCD is expected to drive non-inductive current in the plasma with high efficiency. KSTAR is equipped with ECH/ECCD systems at 84GHz with 0.5MW, 110GHz with 0.7MW and 170GHz with 3.0MW. The second harmonic (X2) 84GHz EC system is mainly for ECH-assisted start-up and the X2 110GHz EC system is for electron heating and MHD instability control. The 170GHz EC system is an ITER pre-prototype gyrotron and serves as a main electron heating and local current drive tool for the control of MHD instabilities.

Various diagnostic systems have been installed in KSTAR [Lee:RSI2010] such as magnetic diagnostics (Rogowski coils, flux loop, magnetic probe, diamagnetic loop), H_α monitor, Thomson scattering and reflectometer. Among the diagnostics, electron cyclotron emission (ECE) [JeongSH:RSI2010] is used for measuring electron temperature and providing 1D radial profile. In addition, the KSTAR tokamak is equipped with ECE imaging (ECEI) [Yun:RSI2010] systems for 2D localised electron temperature measurement. In KSTAR, the ECEI system is used for measuring the fluctuation of electron temperature and edge density and for investigating the details of MHD instabilities, e.g. sawteeth, NTMs and ELMs. The installation of diagnostics and heating and current drive systems is shown in Fig. 2.5, along with the access port view inside the vacuum vessel.

Plasma parameter	Value
Major radius	1.6m
Minor radius	0.5m
Plasma elongation	1.6
Plasma triangularity	0.5
Maximum plasma current	2.0MA
Maximum toroidal field on axis	3.9T
Auxiliary heating power	27MW
Discharge duration	10s
Plasma shape	Single null divertor shape
Plasma fuel	hydrogen, deuterium

Table 2.3: Technical data of AUG tokamak plasma.

ing/current drive (ICRH/ICCD) [Faugel:FED2005] waves are coupled to the plasma by four antennas and provide the total power of 8MW. The electron cyclotron resonance heating/current drive (ECRH/ECCD) [Stober:EPJ2012] system is comprised of ECRH-1 with four 140GHz gyrotrons which provide EC power of 0.5MW each for 2s and ECRH-2 with four 105/140GHzs gyrotrons which inject 1.0MW power each during 10s. All the EC beams are routinely operated for X2-, O2- and X3-mode resonant absorption; in an ITER-like scheme, O1-mode heating can also be applied with a toroidal magnetic field of 3.2T and a frequency of 105GHz. The EC system is used for tungsten accumulation avoidance by central heating, for transport study (e.g. ITG and TEM) and for MHD instability control such as NTM stabilisation.

After a discharge, the AUG plasma is examined using data collected from 40 diagnostics such as bolometry, CXRS, Divertor Spectroscopy, Magnetic measurements, ECE diagnostics, MSE diagnostic, Reflectometry, Soft X-Ray measurements and Thomson scattering. The measurement results are also partly available for feedback control of the plasma during a discharge. The real-time (RT) feedback control system [Treutterer:SOF2013] consists of data acquisition, RT equilibrium reconstruction, RT ray tracing code TOR-BEAM [Poli:CPC2001] and EC control system. One example of the application of the RT control system is NTM stabilisation. The RT equilibrium code takes data from the diagnostics and transfer the equilibrium data to the RT beam tracing code. Combining the real-time analysis to EC control system, EC power and deposition position are determined to stabilise NTMs. More details are discussed in Ref. [Treutterer:SOF2013].

2.4 ITER

2.4.1 Overview

ITER [Shimada:NF2007] is an international collaborative research and development project for an experimental fusion reactor. The name ITER refers to *way* in Latin which conveys an additional meaning as “the path to fusion power generation”. The ITER tokamak is now being constructed in Saint-Paul-lez-Durance, France, and the first plasma is anticipated in the second decade of this new millennium. The main objective of the ITER

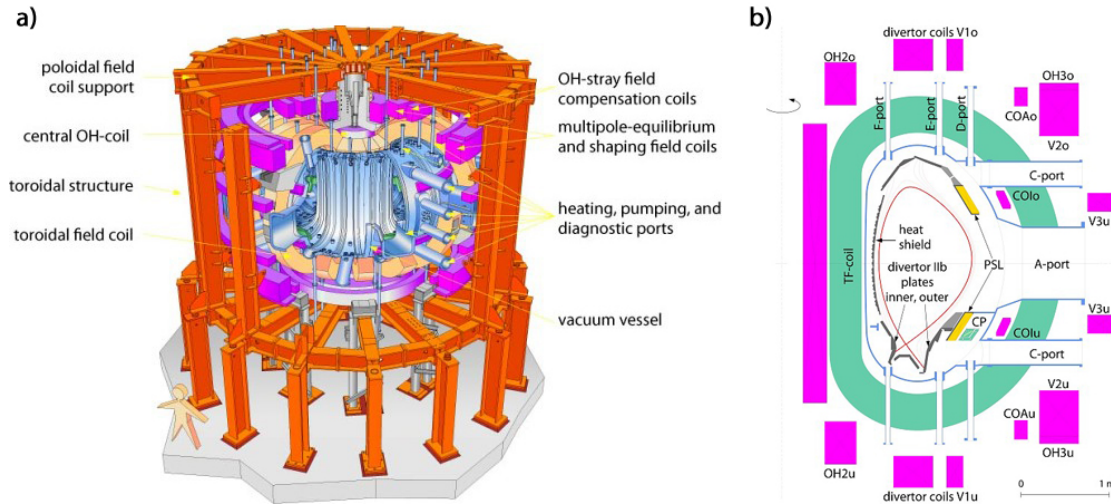


Figure 2.6: (a) The coil structures of the AUG tokamak are shown with the vacuum vessel and its ports for heating and diagnostics. (b) A divertor shape of AUG plasma is presented with TF and PF coils, vacuum vessel and divertor configuration in a poloidal plane. *Images: AUG intranet.*

tokamak is to scientifically and technologically demonstrate the feasibility of producing more nuclear fusion energy than the externally given energy. In ITER, it is envisaged to produce fusion power of $\sim 500\text{MW}$ from the input power of $\sim 50\text{MW}$ which gives the fusion energy gain factor $Q \sim 10$ (with the inductive operation scenario during 300-500s; the expected Q value is around 5 for non-inductive steady-state operation scenario). The main fusion reaction of the ITER plasma will be the deuterium and tritium (D-T) reaction in Eq. 1.1. Note that for the first phase deuterium and hydrogen will be used thus high fusion rates and substantial self-heating by α -particles (He) will not be tested. Furthermore, ITER will test technical and scientific issues such as tritium breeding, neutron shielding and heat conversion technologies for the next step, the demonstration fusion power plant. The basic parameters of an ITER plasma, such as the size of the plasma and equilibrium parameters, are listed in Table 2.4.

The ITER magnet system consists of sets of superconducting magnets (Nb_3Sn , NbTi): a central solenoid which induces the plasma current and contributes to the plasma shaping and vertical stability control, 18 toroidal field (TF) coils which produce the maximum toroidal magnetic field of 5.3T, 6 poloidal field (PF) and a set of correction coils for maintaining the plasma shaping and stability.

One of the most challenging tasks of the ITER tokamak is to test the blanket module. The D-T fusion reaction results in high energy neutrons (14.1MeV) which are not confined by the magnetic fields. The blanket shields the interior surfaces of the vacuum vessel and the superconducting magnets from the neutron fluxes and the heat from the plasma. Inside the blanket, the energy of neutrons is transformed into heat energy which can be used for electrical power production in a commercial fusion power plant. Another important feature of the blanket is tritium breeding during the fusion reaction. Although the natural supply of tritium is almost non-existent and present world production of tritium make it exceeding less abundant than deuterium, it is possible to produce tritium during the fusion reaction through the reaction between high energy neutrons and lithium isotopes in the



Figure 2.7: The schematic view of the ITER tokamak. *Image: iter.org*

blanket. The blanket module in ITER will test these tasks and the successful development of neutron shielding, energy conversion and tritium breeding provides essential techniques for the future of fusion energy.

An extensive diagnostic system, which will be installed on the ITER tokamak, consists of about 50 individual systems for measuring parameters including plasma current, plasma energy, particle and energy confinement times, loop voltage, electron temperature and density, neutron flux, plasma rotation, and MHD instabilities [Donne:NF2007]. The measured data from the diagnostic system will be provided for plasma control, and for evaluating and optimising plasma performance.

The ITER tokamak will be equipped with three external heating and current drive sources, neutral beam injection (NBI) [Hemsworth:RSI2008], ion and electron cyclotron resonance heating and current drive (ICRH/ICCD, ECRH/ECDD) [WilsonJ:PoP2015, Strauss:FED2013, Farina:NF2012] to achieve a sufficiently high temperature for abundant fusion reactions. Two NB injectors with deuterium ion sources are foreseen and each injector will deliver 16.5MW to the plasma. The ICRF/ICCD system with a frequency of 40 to 55MHz will transfer the energy to the ions in the plasma. Two antennas will be installed for the IC system and each antenna injects 20MW into the plasma. The energy from the ECRH/ECDD system with a frequency of 170GHz and a total power of 20MW is absorbed by the electrons in the plasma. Since the EC system is the main concern of this work, it will be discussed in more details in the following section.

2.4.2 ITER EC launcher system

ITER will be equipped with one equatorial launcher (EL) [Farina:NF2012] with 24 inputs and four upper launchers (ULs) [Henderson:NF2008, Strauss:FED2013] with 8 inputs each. The twenty-four 1.0MW gyrotron sources installed in the ITER RF building can be switched between the 56 transmission lines of the tokamak building to deliver 20MW of EC power to the plasma in various ways.

The EL will be used for heating and q -profile control in the central plasma region.

Plasma parameter	Value
Major radius	6.2m
Minor radius	2.0m
Plasma elongation	1.7
Plasma triangularity	0.33
Maximum plasma current	15MA
Maximum toroidal field on axis	5.3T
Auxiliary heating power	73MW
Normalised beta β_N	1.8
Maximum pulse length	1000s
Plasma shape	Single null divertor shape
Plasma fuel	hydrogen, deuterium-tritium
Superconductor material	Nb ₃ Sn, NbTi

Table 2.4: Foreseen operation parameters of ITER plasma.

It consists of three independent mirrors (upper, middle and lower) actuating 8 beams each. The top mirror directs the beams for central counter-ECCD (opposite direction to plasma current), while the other two mirrors provide co-ECCD (same direction to plasma current). Therefore using up to 16 inputs for pure central heating is possible, by combining two different mirror sets (co- plus counter-ECCD) [Farina:NF2012].

The ULs will be used for MHD instability control - in particular for NTMs and sawteeth [Henderson:EC2006]. Each launcher has an Upper and Lower Steering Mirror (USM, LSM). Each of these mirrors can direct as many as four beams simultaneously between $\rho_{tor} = 0.3$ to near the plasma edge [Henderson:NF2008, Strauss:FED2013]. The schematic view of ITER UL mounted to the vacuum vessel is shown in Fig. 2.8.

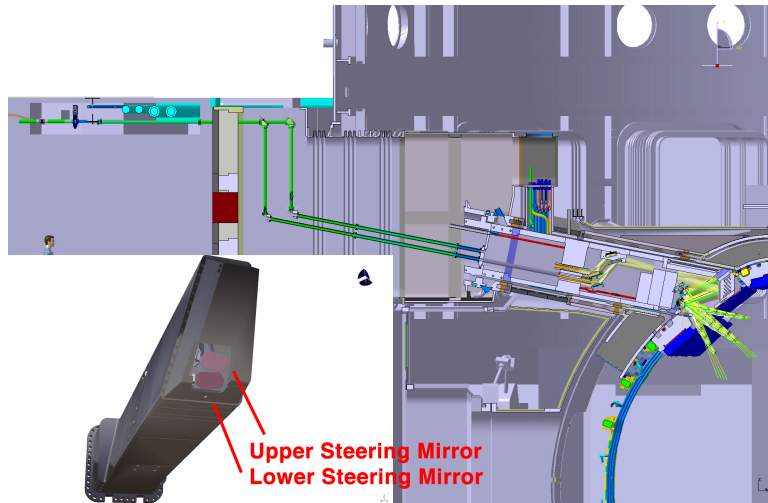


Figure 2.8: ULs comprise USM and LSM which can direct four beams to the plasma. The head of launcher with USM/LSM is indicated as trapezoidal shapes in Figs. 2.9 and 2.10. Acknowledgement for this figure: *J-D.Landis, CRPP/ECHUL/F4E*

In this work, we focus on the USM of each ULs as a sawtooth control tool (since it aims somewhat more centrally than the LSM). Each gyrotron generates 1.0MW of power, but there is a 14% of loss in power as it is transmitted to the plasma, so the effective power from each source is 0.86MW. The beam width is about 0.01 - 0.04 in ρ_{tor} from the individual sources from the USM, across the plasma minor radius. Note that the beam width is wide at the central region and becomes narrower as the beam moves to off-axis.

The deposition positions of the USM beams are determined by the actuator control parameter γ (steering mirror rotation angle). Each USM has its own γ value that determines the position of four beams from that USM (the beams do not strongly overlap on the USM and so they are launched from slightly different locations given the same γ). Though the optics of the ULs are optimised to provide a good overlap of the four beams coming from the USM when aiming at $q = 2$ surface for NTM control, they are less well aligned near $q = 1$ surface. The position of each individual beam from a USM is calculated as a function of γ in the GRAY code [Farina:FST2007], which computes the beam width, beam power density, driven current density and the total driven current at the position of each beam.

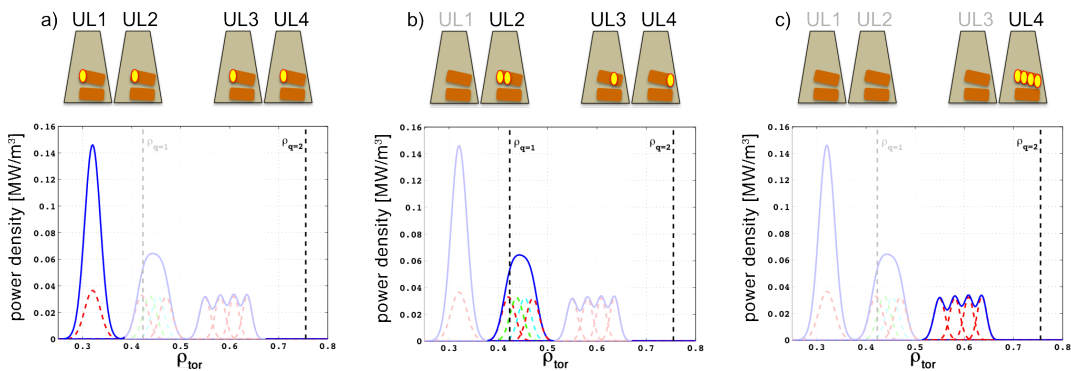


Figure 2.9: Examples of possible EC beams from four USMs of ITER ULs. Blue curves indicate the resulting beam shape and coloured dashed profiles represent a beam shape from each ULs. (a) One USM of each ULs with a single value of γ bring perfectly overlapped EC beam. (b) Two USMs from one UL and one USM from two ULs with three different γ and (c) four USMs from one UL. The black dashed lines show $q = 1$ and $q = 2$ surfaces. The beam shape can be different depending on the deposition position as the distance among the beams from USMs changes.

The combination of ULs and USM beams with the control parameter γ can provide a large variety of injected EC powers and deposition profiles in the plasma. As an example, beam profiles using four sources (3.44MW) are shown in Fig. 2.9. The chosen USMs from each UL are indicated as yellow circle above the EC beam profiles. The best beam overlap using four USM beams is obtained by using one input source line to each UL and a single value of γ as shown in Fig. 2.9 (a). The blue curve shows the sum of four overlapped beams and the individual beams are indicated as a red dashed curve. In this way, all the power from each USM can be deposited at the same location. Taking two USM beams from one UL and one beam from two of the other ULs results in another type of EC deposition profile as shown in Fig. 2.9 (b). Three different γ values are chosen; the two extras are used to fill the gap between the two beams from one UL with the single beams from the two other ULs, in order for the resultant beam shape to have a

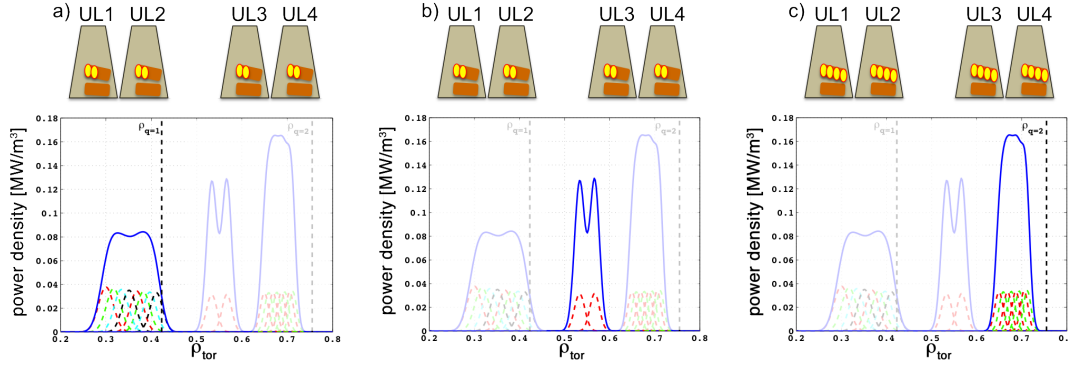


Figure 2.10: Examples of possible EC beams from 8 and 16 USMs of ITER ULs. Blue curves indicate the resulting beam shape and coloured dashed profiles represent a beam shape from each ULs. (a) Two USM of each ULs with four γ values, (b) two USMs from each ULs with a single value of γ and (c) four USMs from two ULs with one γ value and four USMs from two ULs with another value of γ . The black dashed lines show $q = 1$ and $q = 2$ surfaces. The beam shape can be different depending on the deposition position as the distance among the beams from USMs changes.

gaussian-like profile. The colour of the dashed curves corresponds to each γ value. In Fig. 2.9 (c) it is shown that using one control parameter and the four beams from only one launcher results in a wide non-gaussian beam shape with lower maximum power density due to the reduced overlapping of the beams. The other examples with more (8 and 16) beams are presented in Fig. 2.10. In (a) and (b), two USM beams from each UL result in different EC beam shapes depending on the γ values used. Using four different γ values, the individual pairs of beams are able to be positioned without big gaps between them; whereas there are two highly peaked values if the same single γ value is used for all 4 ULs. At the maximum EC power (13.76MW) from USM mirrors, all 16 USM beams are shown with one γ value for the first 8 beams and another value for the rest in Fig. 2.10 (c). Note that the intrinsic gap between the four USM beams of a single UL decreases as the beams are deposited in the outer region of plasma; thus, the resultant beam shapes at different deposition locations can be different than those shown in these figures.

Using a combination of ULs with different γ values, it is possible to control not only the beam shape and width but also the maximum beam power density. Since the current density and sawtooth period are affected by the beam width and power density, the feasibility of sawtooth period control by the combined beams is one of the very important inputs for the EC control system design.

Chapter 3

Predictive electron transport model for L-mode plasmas

3.1 Introduction

3.1.1 Overview

The main goal of tokamak plasma research is to sustain burning plasmas with sufficient performance. The performance is evaluated by the produced fusion power, which is determined by density and temperature profiles. Therefore, for a proper prediction of fusion power, it is necessary to know appropriate density and temperature profiles. In other words, assuming local transport processes, the particle and heat transport coefficients should be predicted to properly evaluate the density and temperature profiles' time evolution.

For the **density profile**, there have been a number of research progress aimed at predicting the density peaking factor, as discussed in Refs. [Weisen:NF2005, Angioni:PoP2005, Angioni:PoP2005b] and references therein. Due to the convective term driven of turbulent transport, a peaked density profile can result. Investigation of the dependence of the density peaking factor on various plasma parameters such as magnetic shear, collisionality and electron to ion temperature ratio leads to the idea of a simplified way in which to predict the density profile. Based on gyrokinetic simulation, the density peaking factor can be found in the different turbulence regimes (i.e. different types of modes) and be used for predicting the density profile [Fable:PPCF2010, WagnerD:PPCF2012]. Preliminary results to include these effects will be presented in this chapter.

The **temperature profile** is mainly evaluated using a heat diffusivity coefficient and relevant heating sources. The heat diffusivity can be simply determined by neoclassical transport theory [Hinton:RMP1976]. However, due to turbulence in plasmas, there is anomalous transport [Liewer:NF1985] that cannot be explained by neoclassical theory. The turbulence results in so-called “stiff” regions in the plasma cross-section where the temperature inverse scale-length does not increase much with an increase of heat flux ([Sauter:PoP2014] and references therein). In addition, one can define different regions in plasma regarding the stiffness [Kotschenreuther:PoP1995, Garbet:PPCF2004]. According to Ref. [Garbet:PPCF2004], the plasma can be separated by three regions, non-stiff central and edge regions and a stiff region in between. Numerous researches for the pre-

diction of the heat diffusivity profile, involving the different characteristics in each region, have been carried out with various models such as RLW [Rebut:IAEA1989], WEILAND [Nordman:NF1990], IFS-PPPL [Kotschenreuther:PoP1995], GLF23 [Waltz:PoP1997], OHE [Ottaviani:PPCF1997], MMM [Zhu:PoP2000], TGLF [Staebler:PoP2007] and TRINITY [Barnes:PoP2010]. Using one of these models, taking into account the plasma parameters, one can define a suitable heat diffusivity profile having the correct shape and amplitude (e.g. producing a match of the modelled and measured temperature profiles in Tokamaks). These models aim to find the exact transport coefficients based on gyrokinetic or gyrofluid theory evaluating the plasma turbulence, each requiring a relatively long time to perform the calculation. In this thesis work, the main goal of the simulation is not to find the precise density and temperature profiles but rather to investigate the control of sawteeth and NTMs. Thus, if reliable profiles can be provided, it is more efficient to use a simple and fast transport model to evaluate these profiles over long time scales in the presence of the instabilities we would like to control. In addition, with the simple model, it is easier to test the sensitivity of the control results to changes in plasma parameters such as plasma current and heating power, since the calculations take much less time: the final goal is to be able to apply this simple method to real-time simulations to provide credible predicted profiles in a very short calculation time. This is why we also need to develop and test simplified models capable of predicting density and temperature profiles. Ultimately, we would like to have faster-than-real-time transport calculations in order to predict whether or not an experimental discharge is evolving as expected, and to allow us to take actions to prevent disruptions. In this chapter, we will discuss this alternative model to evaluate the transport coefficients of density and temperature, in particular those of electrons.

For particle transport, a density peaking factor is employed to describe the density profile. This factor can be predicted as discussed in Refs. [Fable:PPCF2010, WagnerD:PPCF2012]. However, in this work, we have used an interpretative method to compute the density profile, choosing a fixed value of the density inverse scale-length to match the simulated density profile to the experimental one. Note that the density inverse scale-length is known not to change much within a range of similar scenarios (I_P scan, power scan etc.) [Sauter:PoP2014], that is why our simple model is quite useful. Note also that we *do* need to simulate the density profile *evolution* because each sawtooth crash changes the density profile, which in turns determines the post-crash temperature profile. Therefore, a self-consistent time-evolution simulation of a sawtooth plasma requires predictive modelling of both density and temperature profiles. This was not the case in previous works. Even if the averaged temperature profile is known, $T_e(\rho, t)$ needs to be solved with a proper electron heat diffusivity χ_e profile if the effects of localised ECCD, for example, on sawteeth are to be analysed.

For heat transport, an ad-hoc model, defined using the safety factor profile, will be presented that determines the *shape* of the electron heat diffusivity profile. The *amplitude* is automatically rescaled using a scaling law [Yushmanov:NF1990, ITER-PhysicsBasis:NF1999] so that the effect of heating power is correctly included in the model; in addition, a new scaling factor taking into account the effect of the heat deposition *location* will be introduced. This has not been included in present scaling laws but, as shown in Ref. [Kirneva:PPCF2012], off-axis heating degrades the expected plasma confinement; so, this additional effect is now included, here. It will be shown that without using one of the

more 1st-principles-based models mentioned above, this ad-hoc model nevertheless provides a simple and fast way to evaluate heat diffusivity, resulting in a reliable temperature profile in both L- and H-modes. The present ad-hoc models also aim at avoiding “free” parameters, as much as possible as discussed in the following sections.

3.1.2 Transport equations

All the simulations in this work have been carried out using the 1 $\frac{1}{2}$ D (1D transport + 2D equilibrium) transport code ASTRA (Automated System for TRansport Analysis) [Pereverzev:2002]. The basic set of transport equations implemented in the ASTRA code is shown below (original set is shown in Eq. (59) from Ref. [Pereverzev:2002]).

$$\begin{cases} \frac{1}{V'} \frac{\partial}{\partial t} (V' n_e) + \frac{1}{V'} \frac{\partial}{\partial \rho} \Gamma_e = S_e, \\ \frac{3}{2} (V')^{-5/3} \frac{\partial}{\partial t} [(V')^{5/3} n_e T_e] + \frac{1}{V'} \frac{\partial}{\partial \rho} \left(q_e + \frac{5}{2} T_e \Gamma_e \right) = P_e, \\ \frac{3}{2} (V')^{-5/3} \frac{\partial}{\partial t} [(V')^{5/3} n_i T_i] + \frac{1}{V'} \frac{\partial}{\partial \rho} \left(q_i + \frac{5}{2} T_i \Gamma_i \right) = P_i, \\ \sigma_{\parallel} \frac{\partial \psi}{\partial t} = \frac{V'}{2\pi\rho} (j_{\parallel} - j_{BS} - j_{CD}). \end{cases} \quad (3.1)$$

These are 1D diffusion equations for the electron density n_e (1st Eq.), the electron and ion temperatures T_e , T_i (2nd and 3rd Eqs.) and the poloidal magnetic flux ψ (4th Eq.). In the original equation set, there are additional terms for \dot{B}_0 (the time derivative of toroidal magnetic field), but these are neglected in this thesis work since B_0 and the plasma shape are constant in time. In Eq. 3.1, $V' = \partial V / \partial \rho$ is the volume derivative with respect to ρ , $\Gamma_{e,i}$ are the electron and ion particle fluxes, S_e is the electron particle source, $q_{e,i}$ are the electron and ion heat fluxes, $P_{e,i}$ are the power density sources distributed on electrons and ions, respectively, σ_{\parallel} is the neoclassical conductivity, $j_{\parallel,BS,CD}$ are the flux-surface-averaged parallel, bootstrap and externally driven (e.g. electron cyclotron) current densities, respectively. The radial coordinate ρ represents an effective minor radius which is defined by the square root of the toroidal magnetic flux, $\sqrt{\phi / \pi B_0}$. In this work, mostly the *normalised* effective minor radius $\rho_{tor} = \sqrt{\phi / \phi_{edge}}$ is employed. The conductivity σ_{\parallel} and j_{BS} in the 4th equation need to be defined. Since anomalous transport does not necessarily apply to these two terms, it is sufficient to predict them using neoclassical theory alone. Thus, they can be directly defined using the formulas in Refs. [Sauter:PoP1999, Sauter:PoP2002].

There is no equation for the ion density, n_i , since it can be derived using quasi-neutrality and the definition of the effective charge Z_{eff} :

$$\begin{aligned} n_e &= \sum n_{\sigma} Z_{\sigma}, \\ Z_{eff} &= \frac{\sum n_{\sigma} Z_{\sigma}^2}{n_e}, \end{aligned} \quad (3.2)$$

where σ indicates the various ion species such as the main ions, α -particles, fast particles

from NBI or ICRH, and the impurity species; Z is the charge of each species. However, since there can be more than two unknown values, more information is needed to find the ion density. We could solve for the impurities, adding equations in Eq. 3.1. However, again for simplicity, we have not chosen this method. As an example, in ITER plasmas there will be deuterium, n_d , and tritium, n_t , as the main ions, fast particle from NBI, n_{NBI} , or ICRH, n_{ICRH} , α -particles, n_α , from fusion reactions and impurities, n_{imp} . To evaluate the ion densities, at first, one can assume that the two main ions have a given relative density, in our case we chose $n_d = n_t$. For the n_{NBI} and n_{ICRH} , additional tools to calculate the populations of fast particles are necessary. For example, in ASTRA, there is a module for NBI and this routine provides the profiles of the density of fast particle as well as the NB driven current, the pressure due to fast particles, the beam power absorbed by background particles, and so on (More detail is in Ref. [Pereverzev:2002] Sec. 4.10.2). The n_α can be determined by an additional particle transport equation having the same form as the first equation of Eq. 3.1, but with the particle flux written explicitly in terms of diffusion and advection:

$$\frac{\partial}{\partial t}(V'n_\alpha) - \frac{\partial}{\partial \rho} \left(D_\alpha \frac{\partial n_\alpha}{\partial \rho} - v_\alpha n_\alpha \right) = V'S_\alpha. \quad (3.3)$$

The diffusion coefficient D_α can be assumed to be equal or linearly proportional to the electron diffusion coefficient, and the source term S_α is specified by the fusion reaction rate. The pinch velocity term v_α can be determined in the stationary state from D_α , S_α and the density scale-length which must be defined.

For the n_{imp} , it is necessary to know the impurity species; their distributions can be assumed to be fixed fractions of the total impurity density or electron density (e.g. $n_{imp,1} = 0.8n_{imp,tot}$, $n_{imp,2} = 0.2n_{imp,tot}$ or $n_{imp,1} = 0.02n_e$, $n_{imp,2} = 0.0012n_e$). If all this information is provided, one can find the ion density using Eq. 3.2. In this work, mainly TCV plasmas are studied and it is much easier to determine the ion density. In TCV, there are no α , nor fast particles and we can, and do, assume carbon as the only impurity; thus, the ion density is simply defined as $n_i = n_e(Z_c - Z_{eff})/(Z_c - 1)$.

In Eq. 3.1, the first three equations include the electron particle flux Γ_e , the electron heat flux q_e and the ion heat flux q_i ; these must be defined to solve the transport equations (Note that ion particle flux Γ_i can be obtained using Γ_e , similar to n_i). The three flux values can be described using n_e , T_e , T_i and their derivatives with respect to ρ , while introducing transport coefficients. Unlike $\sigma_{||}$ and j_{BS} , the transport coefficients for Γ_e , $q_{e,i}$ are determined by both the neoclassical and turbulence (anomalous transport) theories, so here we introduce and discuss the relation of fluxes using a vector matrix:

$$\begin{pmatrix} \frac{\Gamma_e}{n_e} \\ \frac{q_e}{n_e T_e} \\ \frac{q_i}{n_i T_i} \end{pmatrix} = -V' \langle |\nabla \rho|^2 \rangle \begin{pmatrix} D_n & 0 & 0 & D_E \\ 0 & \chi_e & 0 & 0 \\ 0 & 0 & \chi_i & 0 \end{pmatrix} \cdot \begin{pmatrix} \frac{1}{n_e} \frac{\partial n_e}{\partial \rho} \\ \frac{1}{T_e} \frac{\partial T_e}{\partial \rho} \\ \frac{1}{T_i} \frac{\partial T_i}{\partial \rho} \\ -1 \end{pmatrix}. \quad (3.4)$$

In this matrix, only dominant terms are retained and the other terms are set as zero for the transport coefficients. $D_{n,E}$, χ_e , χ_i indicate transport coefficients for n_e , T_e , and T_i , respectively. D_n is the diffusion coefficient which describes the particle transport due to the density gradient and D_E is the pinch velocity (e.g. see Eq. 3.3) (including the Ware pinch effect) which results in inward particle transport. $\chi_{e,i}$, the electron and ion heat diffusivities, describe the heat transport via each species resulting from the temperature gradients. Combining Eqs. 3.1 and 3.4 yields the following transport equations:

$$\left\{ \begin{array}{l} \frac{1}{V'} \frac{\partial}{\partial t} (V' n_e) - \frac{1}{V'} \frac{\partial}{\partial \rho} \left\{ V' \langle |\nabla \rho|^2 \rangle \left(D_n \frac{\partial n_e}{\partial \rho} - D_E n_e \right) \right\} = S_e, \\ \frac{3}{2} (V')^{-5/3} \frac{\partial}{\partial t} \left[(V')^{5/3} n_e T_e \right] \\ \quad - \frac{1}{V'} \frac{\partial}{\partial \rho} \left[V' \langle |\nabla \rho|^2 \rangle \left\{ \chi_e n_e \frac{\partial T_e}{\partial \rho} + \frac{5}{2} T_e \left(D_n \frac{\partial n_e}{\partial \rho} - D_E n_e \right) \right\} \right] = P_e, \\ \frac{3}{2} (V')^{-5/3} \frac{\partial}{\partial t} \left[(V')^{5/3} n_i T_i \right] \\ \quad - \frac{1}{V'} \frac{\partial}{\partial \rho} \left[V' \langle |\nabla \rho|^2 \rangle \left\{ \chi_i n_i \frac{\partial T_i}{\partial \rho} + \frac{5}{2} T_i \left(D_{n,i} \frac{\partial n_i}{\partial \rho} - D_{E,i} n_i \right) \right\} \right] = P_i, \\ \sigma_{\parallel} \frac{\partial \psi}{\partial t} = \frac{V'}{2\pi\rho} (j_{\parallel} - j_{BS} - j_{CD}). \end{array} \right. \quad (3.5)$$

ASTRA solves these equations to get self-consistent profiles of n_e , T_e , T_i and ψ . Γ_i can be replaced in the same way as Γ_e using ion particle transport coefficients $D_{n,i}$ and $D_{E,i}$. Note that these terms are not included in the matrix 3.4 since in this work n_i is not solved for, but is instead derived from n_e .

In the stationary state, these equations are basically the same as the matrix 3.4 and we can get three relations: for electron density, for electron temperature and for ion temperature. It is possible to get the fluxes if the source terms are given. The electron particle source S_e is specified by various processes such as recombination and ionisation. The electron power density source P_e is calculated as the sum of Ohmic power, the absorbed auxiliary heating power, the absorbed power from α -particle, the equipartition power loss and the radiation power loss. For the ion power density source P_i , there are contributions from the absorbed auxiliary heating power, the absorbed power from α -particle and the equipartition power coming from electrons. In the 4th equation, the externally driven current density is also one of the source terms and must be defined using additional codes or calculation packages such as the NBI module in ASTRA. In TCV, the S_e has been estimated to be very small in the core region [Zabolotsky:NF2006] and is only important in the very edge; thus, one can assume that $S_e \approx 0$ in the core region. Since ECH is the only auxiliary heating in TCV and the radiation power loss, measured by the bolometers, is negligibly small compared to other heat sources [Fable:Thesis], P_e can be calculated as $P_e = P_{ohm} + P_{ECH} - P_{eq}$; the equipartition power is the only ion power source $P_i = P_{eq}$. All the power sources can be calculated by straightforward equations except for the ECH power density P_{ECH} , which needs to be evaluated by an EC beam

tracing code like TORAY-GA [Matsuda:IEEE1989], TORBEAM [Poli:CPC2001] or GRAY [Farina:FST2007] as does the EC driven current density j_{ECCD} .

Using these source terms, the fluxes can be obtained and therefore, if the transport coefficients are given, electron density, ion and electron temperatures can be calculated. As discussed above, the transport coefficients can be taken from neoclassical and transport theory for predictive simulations. For interpretative simulations, it is possible to use experimental measurements for some, or all, of the kinetic profiles. In this case the relevant equation is not used and the transport coefficients can be inferred, if need be. Note that the fourth equation in Eq. 3.5 always needs to be evaluated to provide the total current density profile evolution ($j \sim \partial\psi/\partial\rho$), since it is hard to obtain from measurements.

It is thus imperative to determine the transport coefficients, and in order to perform long-time-scale simulations it is necessary to determine them rapidly while plasma parameters are evolving. In the following section, a simple ad-hoc description for the determination of the transport coefficients for T_e (i.e. χ_e) and n_e (i.e. D_n, D_E) will be discussed. Since we focus on the prediction of electron transport, the evaluation of T_i and n_i will not be examined.

3.2 Simplified transport model for a predictive simulation

3.2.1 Power balance heat transport coefficient

When steady-state experimental measurements are available, one can calculate the transport coefficient χ_e^{PB} (“power balance”). In order to simulate the T_e profile, one uses the equation for T_e from Eq. 3.1. In stationary state, the time derivative term vanishes; in addition, the energy convection term coming from a particle flux Γ_e can be neglected due to its small contribution. The resultant relation for T_e is then written as:

$$\int P_e dV = q_e = -V' \langle |\nabla\rho|^2 \rangle \chi_e n_e \frac{\partial T_e}{\partial\rho}. \quad (3.6)$$

All the terms in Eq. 3.6 can be determined from the experimental measurements of T_e and n_e , the magnetic equilibrium reconstruction and the absorbed power. With this data, one can calculate a ‘power balance’ heat transport coefficient rewriting Eq. 3.6 as:

$$\chi_e^{PB} = -\frac{\int P_e dV}{V' \langle |\nabla\rho|^2 \rangle n_e \partial T_e / \partial\rho}. \quad (3.7)$$

It is expected that a simulation performed using this χ_e^{PB} will reproduce the stationary experimental T_e profile, if the relevant electron heat sources are well reproduced as well; this has been tested with ASTRA for benchmarking purposes.

If $\chi_e^{PB}(\rho)$ is insensitive to the absorbed power, this same χ_e^{PB} can be used to calculate T_e at a different power level; that is, if the profile shape of χ_e remains the same and only the amplitude changes. In the plasma core region, due to the stiffness, the scale-length of T_e is constant with power therefore one can expect self-similar χ_e profiles. Thus the $\chi_e(\rho)$ used in the simulation is modified, taking into account the change of absorbed power, by using the energy confinement scaling law ($\tau_E \propto P^{-0.7}$)

3.2. Simplified transport model for a predictive simulation

[Yushmanov:NF1990, ITER-PhysicsBasis:NF1999]: χ_e at a new power level P is calculated from χ_e^{PB} (determined at the reference power P_{ref}) using:

$$\chi_e = \chi_e^{PB} \left(\frac{P}{P_{ref}} \right)^{0.7} \quad (3.8)$$

An example of a T_e profile from an ASTRA simulation using a known $\chi_e (= \chi_e^{PB})$ is shown in Fig. 3.1, using experimental measurements from an Ohmic plasma TCV #41388. In this simulation, sawtooth activity is not taken into account and n_e is fixed by data from the experiment, as is T_i . The resultant T_e profile is well aligned with the experimental result as displayed in Fig. 3.1(b). From the relation 3.7, it is obvious that if there are two known parameters (χ_e , P_e), one can find the other term (T_e). This result simply confirms that ASTRA can properly reproduce the measured T_e profile, verifying that there are no internal problems with, for example, the equilibrium calculation. Note that it also implies that the χ_e profile is consistently evaluated from the experimental measurements, and that the Ohmic power density matches as well (current density, Z_{eff} , V_{loop}).

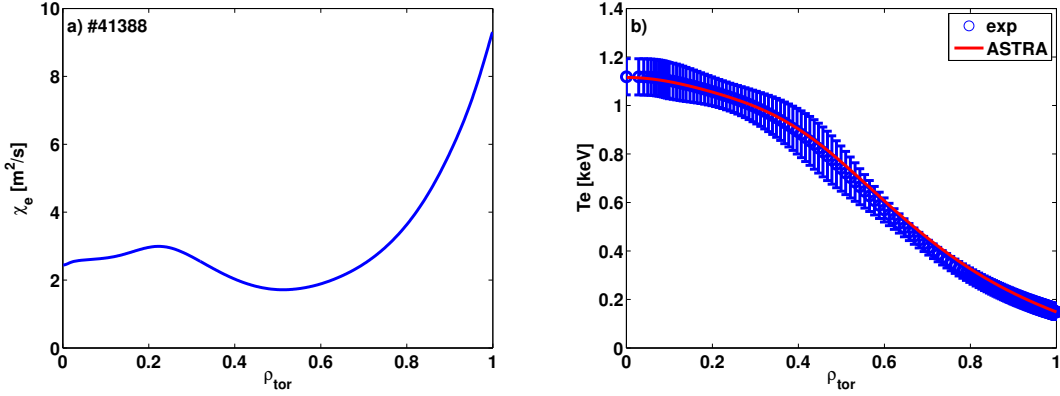


Figure 3.1: The χ_e profile (a) comes from experiment data and corresponding T_e profile (red) is displayed with experimental profile with error bar (blue) in (b). With correct χ_e , the T_e profile from ASTRA simulation is well matched to experimental result. The horizontal axis is the normalised effective minor radius ρ_{tor} which is defined as ρ/ρ_{edge} .

Scaling χ_e using Eq. 3.8 is a simple and rapid way to solve a transport equation for T_e . Though there might be some discrepancy between the simulated and experimental T_e profiles when the modified χ_e^{PB} is used, reasonable global values of τ_E can be obtained. Nevertheless, when χ_e^{PB} cannot be calculated, as for ITER plasma where experimental measurement do not yet exist, one needs to find another way to predict χ_e . We now discuss a different way to provide a simple predictive χ_e profile.

3.2.2 Ad-hoc model for electron heat diffusivity χ_e

χ_e is determined in two separate steps. First, the shape of χ_e is defined. From experiments, it is found that χ_e is related to the q profile in L-mode plasmas, so it is feasible to use the q profile to set the shape of the χ_e profile. Note that $q(\rho)$ is calculated through the self-consistent time evolution of $\psi(\rho, t)$. Next, the amplitude of the χ_e profile is rescaled

using an energy confinement scaling law and an H factor that quantifies how well the plasma follows the scaling law (e.g. some scenarios, such as those with internal transport barriers (ITBs), are expected to enhance confinement; $H > 1$). In this way, one can model a χ_e profile dealing with any power and plasma parameters. T_e can then be predicted if the H factor is given.

For the χ_e profile, we begin by dividing χ_e into three separate regions:

$$\begin{aligned}
 \textit{Central region} & : \rho \leq \rho_1 \\
 \textit{Core region} & : \rho_1 \leq \rho \leq \rho_{ped} \\
 \textit{Edge region} & : \rho_{ped} \leq \rho
 \end{aligned} \tag{3.9}$$

where ρ_1 is the position of $q = 1$ surface which is in general close to the sawtooth inversion radius, and ρ_{ped} is the position where the stiff core and non-stiff edge regions are separated [Sauter:PoP2014]. ρ_{ped} varies with plasma parameters such as plasma current and EC heating power but lies between 0.7 and 0.9 in ρ_{tor} in many cases for L-mode plasmas. The *central* region transport and profiles are governed by sawtooth activity, so a precise transport coefficient is not required. The *core* region is known to be stiff; that is, the normalised inverse scale-length of the T_e profile (R/L_{T_e}) does not change much beyond a critical value as heating power is increased. The stiffness can be quantified by the stiffness factor χ_s [Garbet:PPCF2004]. The *edge* region is a non-stiff region where R/L_{T_e} can exceed the core critical value [Sauter:PoP2014]. It should be mentioned that T_e and n_e profiles in the edge region are not evaluated but taken from experimental data since the way to predict these edge profiles is not yet clear. Note that the central region is defined in the same way as the core region in Ref. [Garbet:PPCF2004], but in this work we allow different definitions of the central and core regions, as above. Our model allows us to define the shape of χ_e profiles for each region and combine these into a full χ_e profile.

Rescaling the amplitude of the χ_e profile

Since we define χ_e without using a transport model, the shape of χ_e profile is only determined to within an arbitrary amplitude. Therefore we need a method by which to set the amplitude. This can be done by using energy confinement time scaling laws [Yushmanov:NF1990, ITER-PhysicsBasis:NF1999]. These laws predict the energy confinement time as a function of various plasma parameters. The scaling laws for L- and H-mode plasmas are defined below [Yushmanov:NF1990, ITER-PhysicsBasis:NF1999]:

$$\begin{aligned}
 \tau_{E,89P} &= 0.048 I_p^{0.85} B^{0.2} n_{20}^{0.1} M^{0.5} R^{1.2} a^{0.3} \kappa_a^{0.5} P_L^{-0.73} \\
 \tau_{E,98L} &= 0.023 I_p^{0.96} B^{0.03} n_{19}^{0.4} M^{0.2} R^{1.89} a^{-0.06} \kappa_a^{0.64} P_L^{-0.73} \\
 \tau_{E,H98(y,2)} &= 0.0562 I_p^{0.93} B^{0.15} n_{19}^{0.41} M^{0.19} R^{1.39} a^{0.58} \kappa_a^{0.78} P_L^{-0.69}
 \end{aligned} \tag{3.10}$$

where I_p [MA] is the plasma current, B [T] is the vacuum magnetic field at the major radius, $n_{19,20}$ [$10^{19,20} \text{ m}^{-3}$] is the line averaged electron plasma density, M [amu] is the effective mass of the gas, R [m] and a [m] are the plasma major and minor radii, κ_a is the elongation at the separatrix and P_L [MW] is the loss power.

The energy confinement time from simulations or experiments should ideally match these $\tau_{scaling}$ values, depending on the scenario. The energy confinement time is defined as

3.2. Simplified transport model for a predictive simulation

the ratio of the total plasma energy to the loss power (W_{tot}/P_L , $W_{tot} = W_e + W_i$) and the plasma energy is the volume integral of the product of n and T ($W = \sum_{\sigma} 3/2 \int n_{\sigma} T_{\sigma} dV$, σ being the plasma species). Consequently, the amplitude of χ_e can be adjusted in the simulation using the ratio of the simulated to scaling-law confinement times. The rescaled χ_e can be defined:

$$\chi_{e,rescaled} = \chi_e \cdot \left\langle \frac{\tau_E}{\tau_{scaling} \cdot H} \right\rangle_{time} \quad (3.11)$$

where τ_E and $\tau_{scaling}$ are the energy confinement times from simulations and the relevant scaling law, respectively, and H is the so called H factor which is the prescribed ratio of τ_E to $\tau_{scaling}$. When this factor is prescribed as unity the simulation result will match the expected value, but it can also be set to a different value if desired (e.g. depending on plasma parameters of different tokamaks and scenarios such as ITBs). $\langle \rangle_{time}$ is the average over a given simulation time scale to avoid specious oscillations.

In the following sections, since only T_e is evaluated by χ_e (and in some cases T_i measurements are not accurate) we have considered only electron energy confinement time for the rescaling; therefore we rewrite Eq. 3.11 as:

$$\chi_{e,rescaled} = \chi_e \cdot \left\langle \frac{\tau_{E,e}}{\tau_{scaling} \cdot H_e} \right\rangle_{time} \quad (3.12)$$

where $\tau_{E,e}$ is *electron* energy confinement time (defined as W_e/P_L) and H_e is *electron* H-factor which is typically supposed to be 0.5. More discussion for $\tau_{E,e}$ and H_e will follow in section 3.2.3.

Description of the χ_e profile in core region

In the theoretical work [Taroni:PPCF1994] describing the shape of χ_e for a Bohm type transport model, χ_e is defined as proportional to q^2 . Regardless of the type of transport, we find experimental evidence that roughly agrees with the theory. Figure 3.2 shows the ratio of χ_e^{PB} to q^2 from TCV L-mode plasmas: χ_e^{PB}/q^2 in the core region is found to be nearly constant for a given shot; though the ratio has a different value for different shots. Therefore, it is reasonable to take χ_e proportional to q^2 in the core region. Note that the experimental data is averaged in stationary state during several sawtooth cycles.

Then the amplitude is determined by rescaling. Thus the core χ_e is defined as

$$\chi_{e,core} = \chi_{e,0} \cdot q^2 \cdot \left\langle \frac{\tau_{E,e}}{\tau_{scaling} \cdot H_e} \right\rangle_{time} \quad (3.13)$$

Note that an additional term $\chi_{e,0} = 1\text{m}^2/\text{s}$ is added to have the correct unit of heat diffusivity. In this section, the *edge* T_e profile is determined from experimental measurements: the transport equation for T_e is solved only inside ρ_{ped} with $T_{e,ped}$ as a boundary condition. In addition, it is assumed that the sawtooth crash is taken into account so that central T_e profile is influenced mainly by regular reconnection events. An example of a T_e profile calculated with these conditions and Eq. 3.13 is presented in Fig. 3.3 for one of TCV Ohmic discharge #40119 in the stationary phase. In this simulation, H_e is set to

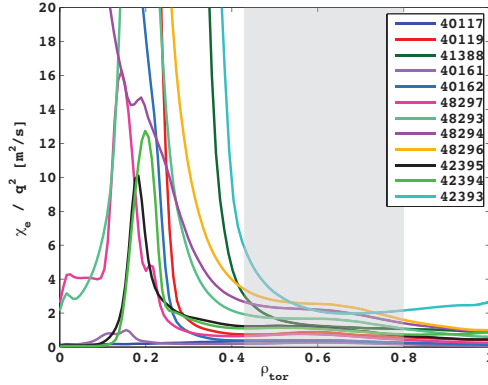


Figure 3.2: From the experimental data, we see that χ_e is almost proportional to q^2 in the core region (shaded region) of TCV L-mode plasmas.

the experimental value 0.52. In Fig. 3.3(a) the converged rescaled χ_e profile used in this simulation is shown along with the experimental profile. The χ_e used in the simulation inside ρ_1 is not so important due to the sawtooth crash; therefore it is initially set to unity (this is modified by the rescaling). Outside ρ_1 , χ_e increases monotonically and is similar to experimental profile. Outside ρ_{ped} ($\rho_{tor} = 0.8$ in this case), the edge χ_e has been defined using q^2 , as with the core profile. (Recall, this χ_e is not used to solve the transport equation for T_e since the edge T_e profile is fixed to the experimental (or predicted) value: the discrepancy between the χ_e profiles in the edge region does not affect the resultant T_e profile.) With this χ_e profile, T_e is calculated in Fig. 3.3(b) during a sawtooth cycle. With a boundary condition at ρ_{ped} and a rescaled χ_e profile that are constant in time, the resultant T_e profiles agrees well with experimental measurements in the core region; in addition, R/L_{T_e} matches well the experimental values, Fig. 3.3(c). Note that due to scatter in the experimental data points there is a large variation of R/L_{T_e} , but the trend of both experimental and simulation results are in good agreement. Like the core region, simulated T_e and R/L_{T_e} in the central region are also similar to the experimental data. For the central region, a more detailed discussion will follow in the next section.

χ_e profile in central region

Simulations can include, or not, the effects of the sawtooth instability: the sawtooth module can be turned on or off. In experiments, in standard scenarios, the central region profile is governed by the sawtooth instability; due to sawtooth crashes, the T_e and n_e profiles are flattened periodically inside ρ_1 . In other words, the gradient of T_e in this region is very small compared to the other regions. We see from Eq. 3.7, that to get a small value of T_e gradient, a large value of χ_e is required; therefore, in the central region, one expects χ_e to be larger than in the core region. Accordingly, in simulations, χ_e can be set to a large constant value in the central region to generate a flat T_e profile regardless of whether the sawtooth crash phenomena is simulated; in TCV, a χ_e as low as $2 \text{ m}^2/\text{s}$ can be sufficient to result in a flat T_e profile, but more often a value of $\sim 5 \rightarrow 10 \text{ m}^2/\text{s}$ is

3.2. Simplified transport model for a predictive simulation

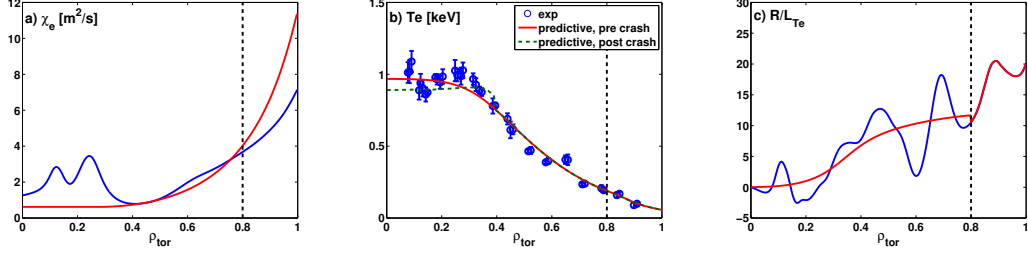


Figure 3.3: (a) core χ_e profile (red) is predicted by q^2 and rescaled. In the core region, χ_e profile is similar to experimental one (blue). (b) The resultant T_e profile is also well matched to experimental data (blue) with sawtooth crash. The profiles before (red) and after (green dashed) crash are similar to experimental profile in the core region. (c) there are some variations of experimental R/L_{T_e} (blue) in the core region due to one juttet point in the T_e profile but in average both R/L_{T_e} profiles from experiment and simulation (red) are comparable.

required.

On the other hand, if the sawtooth crash is taken into account during the T_e evaluation, a large central χ_e value is not necessarily required to result in a flat T_e profile. Due to the modification and recovery of the T_e profile during sawtooth cycles, the central T_e profile never peaks as much as without sawtooth crashes; that is, the sawtooth instability resets the T_e evolution in the core with each crash. As a consequence, χ_e can be defined to be the same as it is in the core region, or can be a small constant number. In this work, we have set the central χ_e to unity, in general. Note, however, that even when sawtooth activity is taken into account, if the sawtooth period is long (or with central ECH), the experimental T_e profile can become more peaked; in this case a larger central χ_e is required in the simulations even when the sawteeth *are* simulated.

Examples of these two approaches, with and without the sawtooth crash, are shown in Fig. 3.4. The same shot (#40119) as used in the core χ_e test case is employed. In Figs. 3.4(a) and (b), χ_e and T_e profiles from both the experiment and simulation are presented. The experimental χ_e^{PB} (blue) is larger in the central region where the T_e profile is flat. This is compared to two different simulation pairs each with (dashed) and without (solid) simulated sawteeth. The red colour curves are for the case of central $\chi_e = 1\text{m}^2/\text{s}$ whereas the green curves are for a large value of $10\text{m}^2/\text{s}$. These central χ_e values (1, 10) are those given initially; they are self-consistently rescaled during the simulations and so are not those seen in Fig. 3.4(a) (but are indicated in the legend). Note that the χ_e and T_e profiles shown with sawteeth turned on are the profiles at a moment just before a sawtooth crash.

For the small χ_e case, the rescaled χ_e values are almost the same. Due to this small value and lack of sawteeth, the T_e profile (red, solid) is peaked and higher than the experimental data in the centre. Alternately, the T_e profile that is periodically modified by sawtooth crashes (red, dashed) remains flat, similar to the experimental one. Because of the reconnection process caused by the sawtooth crash, the T_e profile is flattened and then recovers. If the sawtooth period is short, another crash occurs during the time that T_e is evolving (mostly in the central region) and the central T_e profile never reaches a higher value (i.e. the red, solid curve). In this simulation, the sawtooth period and the electron energy confinement time are about 2.8 and 13.5ms, respectively (experiment: 2.9 and 14.5ms).

For the large central χ_e case, the T_e profile is flat in the central region even without the sawtooth crash (green, solid). T_e values are slightly lower than experimental measurements but are still within the error bars. This is because the simulated ρ_1 expands further than in the experiment, to where $T_{e,q=1}$ is lower. The larger ρ_1 results in a wider range where χ_e is high; inside ρ_1 , T_e has a similar value to that at $T_{e,q=1}$.

On the other hand, with sawtooth crashes (green, dashed), as seen in the χ_e profile, ρ_1 does not evolve as much as in the case without sawteeth. Therefore the flat T_e region is narrower and the T_e value is slightly higher. Nevertheless, with a large central χ_e , the T_e profiles with and without sawtooth crashes show profiles that are both similar to the experimental measurements, within the error bars. This example shows that with the sawtooth crash switched on, the simulations of the T_e profiles can match the experimental measurements using a large range of χ_e values for the central region; said alternatively, the simulation results are insensitive to the exact value of central χ_e . Note that in all simulation cases, the *core* χ_e profiles are defined by q^2 and are rescaled (Eq. 3.13).

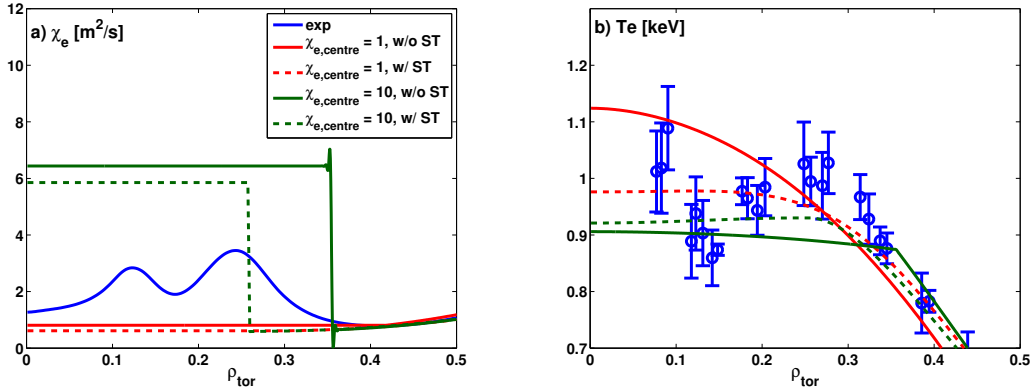


Figure 3.4: Two rescaled constant χ_e profiles are shown with experimental result in (a). With large value (green), T_e in (b) is flat without (solid) and with (dashed) sawtooth crash. On the contrary, with small value (red), T_e is peaked without sawtooth crash (solid) but is as flat as experimental profile with crash (dashed).

3.2.3 Constraints of the model

As seen in the previous section, the ad-hoc predictive χ_e model can properly evaluate the T_e profile in the *central* and *core* regions given $T_{e,\text{ped}}$ and the H_e factor. Conversely, if *these* two values are not correct, the model cannot be applied to the prediction of the T_e profile. Therefore, more investigation of how to choose these values is warranted. These are essentially sensitivity studies on these two parameters.

Sensitivity of simulations to the choice of $T_{e,\text{ped}}$

Recall that in this work the calculation range is between axis and ρ_{ped} , so T_e at ρ_{ped} , $T_{e,\text{ped}}$, represents a boundary condition. As discussed in Ref. [Sauter:PoP2014], the T_e profile is mainly determined by $T_{e,\text{ped}}$ due to the stiff and non-stiff characteristics of *core* and *edge* regions, respectively.

3.2. Simplified transport model for a predictive simulation

Though there have been theoretical works to predict the pedestal height and width in H-mode plasmas such as the EPED model [Snyder:NF2011], for L-mode plasmas there is no scaling law nor prediction for ρ_{ped} and $T_{e,ped}$. At this stage, one cannot obtain a predicted value of $T_{e,ped}$.

To overcome this limitation, we propose to use the robust experimental observation [Garbet:PPCF2004, Sauter:PoP2014] that the core region is stiff to help us choose an appropriate $T_{e,ped}$ value: measured core R/L_{T_e} values typically fall between 8 and 14 [Ryter:NF2001]; therefore, by modifying the $T_{e,ped}$ value, one can generate profiles for which the simulated R/L_{T_e} value falls in this range.

To test this proposition, we fix H_e at 0.52, define the core χ_e profile by q^2 and rescaled the χ_e as defined in Eq. 3.13. We then scan the $T_{e,ped}$ value around the value measured in an experiment (0.19 keV) and compare the resulting simulated T_e and R/L_{T_e} profiles. The simulation results of this scan are shown in Fig. 3.5. The reference boundary condition $T_{e,ped} = 0.19$ keV and six other values (0.05, 0.1, 0.15, 0.25, 0.3, 0.35) are used. Due to the rescaling, the core χ_e profiles are different for each $T_{e,ped}$ value, as are the corresponding T_e profiles. When $T_{e,ped}$ is smaller than the experimental value, the electron plasma energy is also smaller and the ratio between $\tau_{E,e}$ and $\tau_{scaling}$ is lower than the chosen fixed H_e . As a result, χ_e is rescaled (reduced) and the rescaled χ_e generates a higher T_e gradient in the core region to increase the stored energy and reach the chosen H_e value. At the opposite extreme, when $T_{e,ped}$ is too high, χ_e is rescaled upwards and the resulting T_e gradient is smaller.

As $T_{e,ped}$ is increased, the ρ_1 shrinks and the n_e profiles are affected, since the flattened area due to the sawtooth crash decreases. R/L_{n_e} was fixed to the experimental value of 5.8. This gradient is kept up to near the $q = 1$ radius, as seen in Fig. 3.5(d). Therefore smaller $q = 1$ radii lead to increased central density values. (Note that the detailed description of the n_e evaluation and role of R/L_{n_e} will be discussed in section 3.2.4.)

The R/L_{T_e} profiles vary with $T_{e,ped}$ as described above and shown in Fig. 3.5(c). The R/L_{T_e} values at $\rho_{tor} = 0.6$ are plotted in Fig. 3.6 as a function of $T_{e,ped}$; the typical experimental range of R/L_{T_e} is indicated by the shaded box and the red circle represents the measured reference value. R/L_{T_e} decreases monotonically (nearly linearly) as $T_{e,ped}$ increases. From these simulations, and using the “expected” core R/L_{T_e} to determine $T_{e,ped}$, we can state that $T_{e,ped}$ should lie in the range of 0.12 ~ 0.25 keV. Though the $T_{e,ped}$ estimation is not very precise, one can nevertheless choose a *reasonable* $T_{e,ped}$ value, and use it as the boundary condition for core T_e evaluation in simulations for which no direct experimental data is available, based on the requirement that R/L_{T_e} takes on a *reasonable* value (or range of values) in the core region.

Sensitivity of simulations to the choice of H_e

To rescale the χ_e profile using Eq. 3.12, we have used the *electron* energy confinement time $\tau_{E,e}$ instead of the *total* energy confinement time τ_E . From the definition of τ_E , one can simply define $\tau_{E,e}$ as (assuming no significant fast particles contribution here for simplicity):

$$\tau_E = \frac{W_{tot}}{P_L} = \frac{W_e}{P_L} + \frac{W_i}{P_L} = \tau_{E,e} + \tau_{E,i}, \quad (3.14)$$

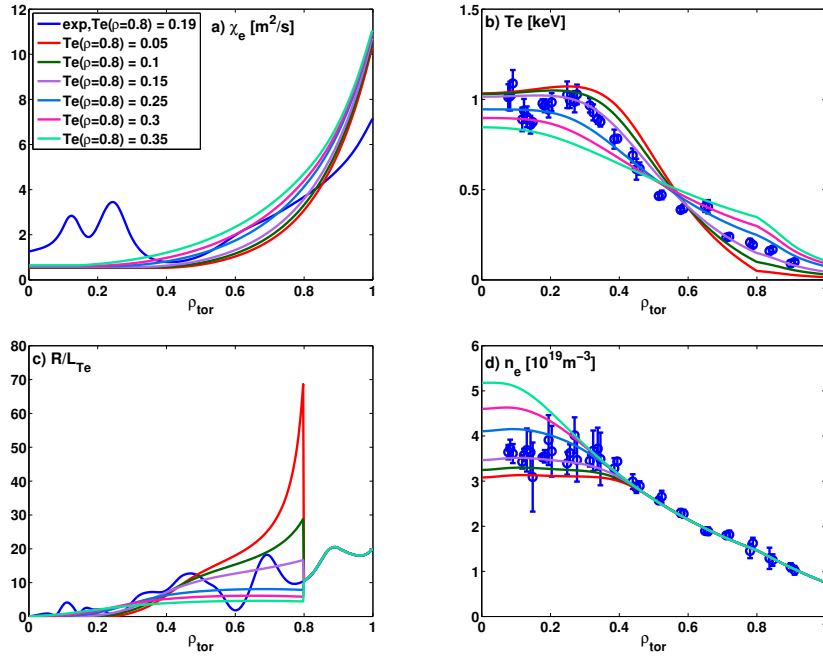


Figure 3.5: (a) χ_e profiles are defined by q^2 and rescaled to satisfy given H_e with various $T_{e,ped}$. (b) T_e profiles have various gradient due to χ_e in the core region. All these profiles produce $\tau_{E,e}$ value which is same as $H_e \cdot \tau_{scaling}$. (c) R/L_{T_e} in the core decreases with increment of $T_{e,ped}$. (d) n_e profiles with a fixed $R/L_{n_e} = 5.8$ outside the $q = 1$ radius.

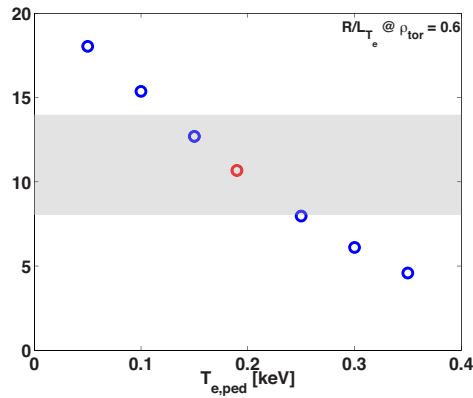


Figure 3.6: R/L_{T_e} value at $\rho_{tor} = 0.6$ decreases with the increase of $T_{e,ped}$. The shade box indicates the proper range of R/L_{T_e} value and the reference data is shown as red circle. To match the range, $T_{e,ped}$ should be between 0.12 and 0.25keV in this case.

3.2. Simplified transport model for a predictive simulation

where, $W_{tot,e,i}$ are the total, electron and ion thermal energy, respectively, and P_L is the loss power. In the same way, an H_e factor can be defined using:

$$H = \frac{\tau_E}{\tau_{E,scaling}} = \frac{\tau_{E,e}}{\tau_{E,scaling}} + \frac{\tau_{E,i}}{\tau_{E,scaling}} = H_e + H_i, \quad (3.15)$$

where $\tau_{E,scaling}$ is the scaling law for the total confinement time. From Eq. 3.15, one might reasonably assume that H_e is 0.5; but in fact the ratio of $\tau_{E,e}$ to $\tau_{E,i}$ is unknown and tends to increase with increased electron heating and/or at smaller density. One can also rewrite the definition of H_e using H , W_{tot} and W_i :

$$H_e = H \left(1 - \frac{W_i}{W_{tot}} \right). \quad (3.16)$$

Then, if a scaling law for the ratio of W_i to W_{tot} is available, an H_e factor could be determined. Otherwise, if an energy confinement time scaling law for electrons alone can be established, one uses $H_e = \tau_{E,e}/\tau_{E,e,scaling}$. Since these scaling laws are not available, we instead perform a sensitivity study similar to what we have performed for $T_{e,ped}$ using the same TCV shot.

For this study, T_e outside ρ_{ped} ($\rho_{tor} = 0.8$) is set to the experimentally measured value and six different H_e values (0.15, 0.25, 0.4, 0.7, 0.85, 1.0) spanning the reference value of 0.52 are used in the simulations. The resultant χ_e , T_e , R/L_{T_e} and n_e profiles are shown in Fig. 3.7. Using Eq. 3.13, χ_e is rescaled by H_e .

With a small H_e value, χ_e is increased and T_e decreases in the core region so as to obtain the needed $\tau_{E,e}$ value. As a result, the corresponding R/L_{T_e} is much smaller than the target range. In addition, due to the lower T_e , the entire q profile increases and ρ_1 shrinks to such an extent that there is no sawtooth crash, or it occurs only in the very centre. This results in an excessively peaked n_e profile.

With a high H_e value of 1.0, χ_e is small, T_e is high, and R/L_{T_e} is large. In this case, the sawtooth crash flattens the central region so that the simulated n_e is comparable to the reference profile. From R/L_{T_e} profiles and Fig. 3.8, R/L_{T_e} at $\rho_{tor} = 0.6$ is between 8 and 14 when the H_e is varied between 0.4 and 0.85. Unlike the relation between R/L_{T_e} and $T_{e,ped}$, R/L_{T_e} is not linearly proportional to the H_e factor. In this experiment the reference H_e value was 0.52, but if the H_e factor is not known *a priori* one can use any value between 0.4 and 0.85 and end up with a reasonable R/L_{T_e} at $\rho_{tor} = 0.6$. Using a range of ρ_{tor} between outside the inversion radius and 0.75, for example, can help constraining better the H_e factor.

These two sensitivity studies suggest that by choosing $T_{e,ped}$ and H_e to satisfy a reasonable R/L_{T_e} , one can provide the boundary conditions required to simulate the sawtooth instability. It also suggests how new analyses could be performed to better characterise these parameters. On the one hand, the database used to determine the scaling laws could be used to determine separately the electron and ion confinement times. On the other hand, studies similar to the one in Ref. [Sauter:PoP2014], performed across machines, can yield scalings of the edge value and gradient with plasma parameters in both L- and H-modes. The latter should also be compared to the EPED model predictions [Snyder:NF2011].

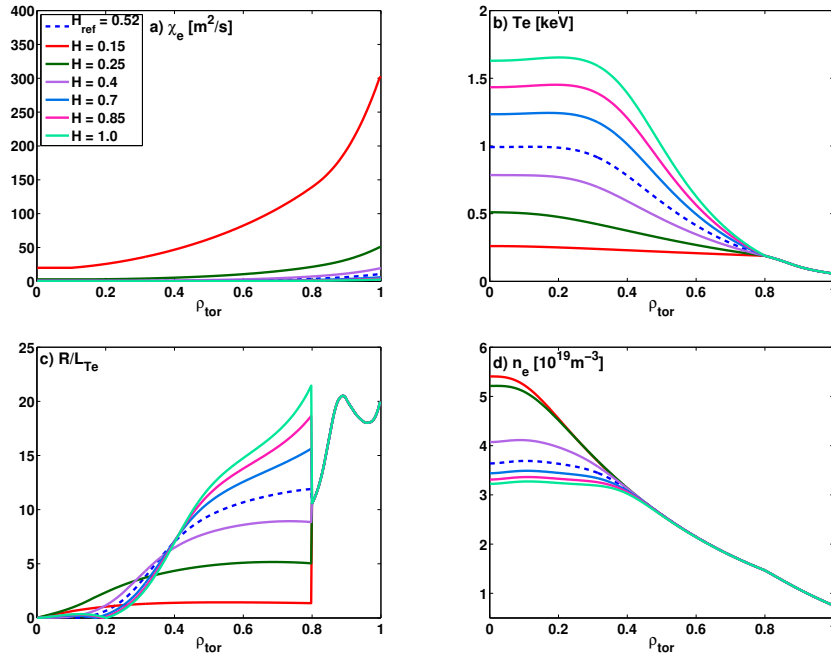


Figure 3.7: Depending on H_e values, (a) χ_e is differently rescaled and results in (b) T_e profiles. Employed H_e values for this investigation are listed in the legend. Smaller H_e brings larger rescaling factor and in consequence, larger χ_e and lower T_e profiles are obtained. As H_e values increase, χ_e decreases and T_e raises as shown in (a), (b). H_e of 0.4 and 0.7 which are about 30% different from reference H_e result in T_e profiles close to reference one. However, from R/L_{T_e} profile in (c), a reasonable range of H_e is found as [0.5 0.7] that agrees with target range of R/L_{T_e} . For small H_e cases, due to lower T_e , ρ_1 does not exist or is very small. As a result, n_e profiles for these cases in (d) are still peaked and other profiles are flattened by sawtooth crash in the central region.

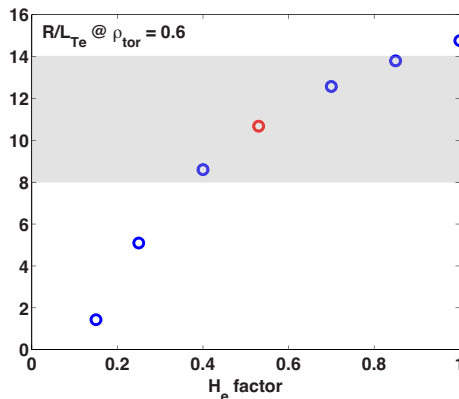


Figure 3.8: R/L_{T_e} value at $\rho_{tor} = 0.6$ increase with H_e factor. The reference data is shown as red circle. R/L_{T_e} rapidly increases with smaller H_e factor and gradually increases with larger H_e factor. Therefore, even for a large value of H_e factor, the resultant R/L_{T_e} stays within the proper range. To match the range, H_e can vary between 0.4 and 0.85.

3.2.4 Determination of transport coefficients for density profile

Similar to the electron heat diffusivity χ_e , the transport coefficients for the evaluation of electron density can be determined using simple models. From Eqs. 3.4 and 3.5, the definition of electron particle flux Γ_e and the equation for n_e are taken to evaluate the transport coefficients. In the stationary state, the time derivative term is zero so that the equation can be written as

$$\int S_e dV = \Gamma_e = -V' \langle |\nabla \rho|^2 \rangle \left(D_n \frac{\partial n_e}{\partial \rho} - D_E n_e \right). \quad (3.17)$$

The diffusion coefficient D_n is defined by the electron heat diffusivity χ_e : D_n can be assumed to be linearly proportional to χ_e [Baker:NF2000]. Usually, it can be assumed that particle transport is about five times slower than heat transport [Fable:Thesis]; thus $D_n = 0.2 \cdot \chi_e$. For D_E (often called V in other references), one can rewrite Eq. 3.17 as a definition of D_E :

$$D_E = -D_n \frac{R/L_{n_e}}{R} + \frac{\Gamma_e}{V' \langle |\nabla \rho|^2 \rangle n_e}, \quad (3.18)$$

where R/L_{n_e} is the normalised inverse scale-length of the n_e profile (defined as $-R \partial \log n_e / \partial \rho$) and R is the plasma major radius. In TCV, the electron particle flux Γ_e is negligible since the particle source in the core region is almost zero, as mentioned in Sec. 3.1.2. Consequently, D_E is determined by D_n and R/L_{n_e} , and we have:

$$\frac{R/L_{n_e}}{R} = -\frac{D_E}{D_n}. \quad (3.19)$$

Therefore, in stationary state, it is only the ratio of $-D_E/D_n$ that determines the density inverse scale-length. The value of D_n affects the characteristic time evolution of n_e in transient phases, and the ratio $D_n/\chi_e = 0.2$ reflects the fact that particle transport is typically five times slower than thermal energy transport. The calculation of R/L_{n_e} has been carried out for TCV [Fable:PCCF2010, WagnerD:PCCF2012], AUG [Angioni:PoP2005] and JET [Angioni:PoP2005b]; a prediction for ITER [Weisen:NF2005] has been made as well.

The prediction of R/L_{n_e} is out of the scope of this work so we have chosen a fixed constant value of R/L_{n_e} in the core region; justified according to Ref. [Sauter:PoP2014]. The constant value is chosen to provide a match of the simulation to the experimental (or predicted) “reference” n_e profile. In the centre, R/L_{n_e} is set to decrease to zero. The effective inversion radius of the n_e profiles is often larger than that of the T_e profile [Sauter:PoP2014] but it is not precisely known. Therefore, it is assumed that the $q = 1$ surface is smaller than the radius where the n_e profile is flat. In order to compensate for this difference, the R/L_{n_e} quickly decreases following a parabolic curve from $q = 1$ surface to the axis. The central n_e profile is in any case modified by sawtooth crashes. As a boundary condition, the edge profile is taken from experimental measurements or estimated predicted edge values, fixed at $\rho_{tor} = 0.8$ or the relevant top of pedestal radius.

(It is not necessary to define R/L_{n_e} in the edge region; the n_e profile is calculated only inside this boundary point, as in most simulations.)

Fig. 3.9 shows an example of the n_e profile from ASTRA simulations and the corresponding R/L_{n_e} profile. The experimental data comes from TCV shot #40119. Again we can turn the sawtooth cycle modelling on or off in the simulations. Without the sawtooth crash (cyan), n_e is peaked; whereas, with sawtooth crashes (red, green dashed) the central profiles are modified and agree well with the experimental measurements. For both cases, n_e profiles in the stiff region are well matched to the experimental profile. R/L_{n_e} equals 5.8 well into the central region without sawtooth crashes, but is constant only in the stiff region when sawteeth are simulated, as expected.

The R/L_{n_e} profile of both cases also well match the experimental profile in the stiff region. In the central region, R/L_{n_e} profiles with and without sawtooth crash are not perfectly matched to the experimental profile but close enough to bring the n_e profiles within error bars. This simple particle transport model has effectively only one free parameter, the value of R/L_{n_e} (via the advective velocity), given the boundary condition. When available, the experimental density profile can be used for the averaged R/L_{n_e} in the stiff region as shown in Fig. 3.9. For ITER simulations, we rely on cross-tokamak studies such as in Ref. [Weisen:NF2005] that provide a relatively well-defined value of the expected R/L_{n_e} .

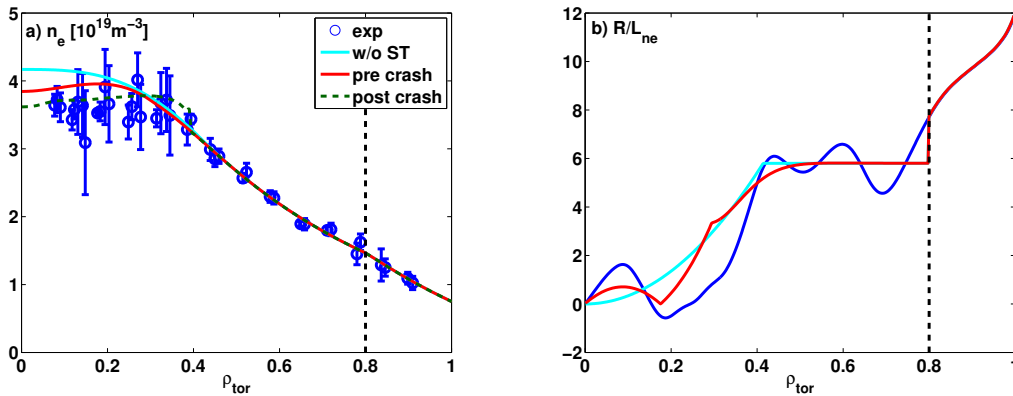


Figure 3.9: Example of (a) n_e and (b) R/L_{n_e} profiles. Regardless the effect of sawtooth crashes, the n_e profile in the stiff region agrees well with experimental result (blue). In the central region n_e is peaked without considering sawtooth crashes in the ASTRA simulation (cyan) while is well matched to the experimental result with crashes (red: pre crash, green: post crash). With fixed R/L_{n_e} , the particle transport coefficients are well defined and the resultant n_e is also well determined. Note that between $\rho_{tor} = 0.8$ and 1.0 (outside the black dashed line), n_e is fixed by the experimental profile (or by the predicted edge value) as a boundary condition.

3.2.5 Simulation results using simplified ad-hoc models for T_e and n_e

In this section, the ad-hoc transport models will be tested for different L-mode cases. For T_e evaluation, the H_e factor is taken from the experiment as well as the averaged R/L_{n_e} value in the core. With several examples, it is shown that this ad-hoc model, with essentially only two constants which can be easily predicted experimentally, can be

3.2. Simplified transport model for a predictive simulation

applied in the simulations to provide a simple and fast way to evaluate the whole T_e and n_e radial profiles.

The edge χ_e of the model is not used at this stage to simulate the T_e profile in the edge region; instead the edge T_e profile is set to the measured data from the experiment. The measurements define $T_{e,ped}$ and the simulated q^2 defines the shape of χ_e in the core. In addition, n_e is simulated with a constant R/L_{n_e} and fixed edge profile as mentioned in Sec. 3.2.4 to match the experimental data.

In this section the simulation results for the T_e and n_e profiles will be presented for Ohmic cases at different plasma currents and central EC heating at different EC powers to show the applicability of the discussed ad-hoc transport model.

Ohmic heating at different values of I_p

For the first test, three TCV Ohmic plasmas with different I_p are considered: shots #40117, #40119 and #41388 which have I_p of 127, 228 and 312 kA, respectively. The comparison of the simulated results to the experimental profiles T_e and n_e are presented in Fig. 3.10. For all cases, the edge region is defined as $0.8 \leq \rho_{tor} \leq 1.0$.

For shot #40117 ($I_p = 127$ kA), the T_e profile from the ASTRA simulation shows good agreement with the experimental profile using the experimental H_e factor of 0.62. Since I_p is small, the $q = 1$ surface is small and the effect of sawtooth crashes is small as well. Before (red) and after (green dashed) the sawtooth crash, the central T_e profiles are almost the same and are slightly lower than the experimental one. With higher I_p (228 kA), shot #40119, shows a similar result. In the centre, with sawtooth crashes, central T_e values match well the experimental profiles (within the error bars). In the core region, with the experimental H_e factor of 0.52, the simulated T_e profile is also in a good agreement with the experimental data. Note that H_e ensures only that the integral of p_e is the same as the experimental value. An error in either the T_e or the n_e radial variation would result in both profiles being mismatched. For shot #41388, the H_e factor is 0.44. Due to the high central density, the central T_e profile is slightly smaller than the experimental one; nevertheless it is still reasonable (within the error bars). The core T_e profile from the ASTRA simulation is higher than the experimental one; in this case the χ_e profile from the simulation is lower in the core region than the experimental value. Presumably, with high I_p , the relative decrease of the q profile results in a lower χ_e profile and the difference between the modelled and experimental χ_e becomes larger. In this case, the T_e profile resulting from the χ_e model is still reasonable, but more tests should be carried out for higher I_p cases to better understand this discrepancy. Note that the inversion radius is large in such cases, therefore time-resolved measurements during the whole sawtooth cycle should be considered.

In the second row in Fig. 3.10, n_e profiles from experiments (blue) and simulations with sawtooth crashes (red, green dashed) are presented for the three discharges. With R/L_{n_e} of 5.5, 5.8 and 6.5 respectively, the simulated n_e profiles are well matched to the experimental data (within the error bars). For the last case, discharge #41388, the calculated $q = 1$ surface is perhaps smaller than the experimental value (measured inversion radius cannot be specified due to a large variation) so that the effect of a sawtooth crash influences in a narrower region and the resultant n_e profile is higher.

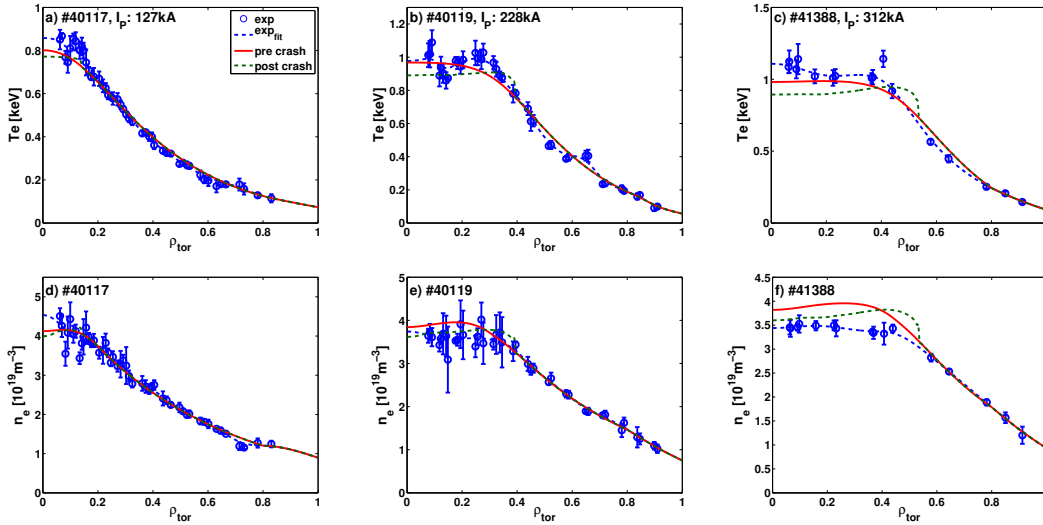


Figure 3.10: T_e and n_e profiles for the Ohmic test cases: TCV shot #40117, #40119 and #41388 with $I_p = 127\text{kA}$, 228kA and 312kA , respectively. (a)-(c) T_e profiles using H_e of 0.62, 0.52, 0.44 are well matched to the experimental results for each cases. (d)-(f) n_e profiles using constant R/L_{n_e} of 5.5, 5.8 and 6.5 are also in good agreement with the experimental profiles. Sawtooth crash modifies the central T_e and n_e and results in the flat profiles inside ρ_1 .

Central EC heating cases at different power levels

As a second test, cases using this simple transport model for TCV plasmas with different EC heating power levels are carried out. EC heating power is deposited in the central region: zero EC power (Ohmic, #48297), 0.41 MW (#48293) and 0.82 MW (#48294). I_p is the same for all three cases (200 kA). As displayed in Fig. 3.11, T_e and n_e profiles taking into account sawtooth crashes accord with the experimental profiles. For shots #48293 and #48294, EC power density profiles for each case are plotted multiplied by 0.1 to fit in the same frame, along with the T_e profiles. Due to central EC heating, the central T_e profiles are peaked despite the sawtooth crashes. That is, the temperature evolution is fast enough to overcome the flattening effects of sawteeth seen in Ohmically heated plasmas. For this reason, a constant central χ_e value of 2.0 is used instead of unity (for the Ohmic shot, the central value is unity). As in the previous test, the edge T_e profile is fixed to the experimental data in between $0.8 \leq \rho_{tor} \leq 1.0$.

Shot #48297, Ohmic, has $H_e = 0.52$ and $R/L_{n_e} = 5.8$ and both the T_e and n_e profiles show good alignment with the experimental result. For shot #48293, 0.41 MW EC power is centrally deposited. The experimental H_e factor is 0.59 and $R/L_{n_e} = 5.0$. In the core region, the n_e profile is similar to the experimental one. Due to the smaller $q = 1$ surface, however, the simulated n_e profile shows a slightly higher value in the central region. For shot #48294, the EC power is doubled (0.82 MW) and the T_e profile is more peaked than at lower EC power. With an H_e factor of 0.67 and a modified central χ_e as used in #48293, the simulated T_e profile fits well to the experimental data. A constant R/L_{n_e} value of 4.0 is used to simulate the n_e profile. The core n_e profile is consistent with the experiment, while the central n_e is again slightly higher as in the shot #48293 case.

3.3. Effect of heating deposition position on confinement time

Note that the decrease of R/L_{n_e} with increased power is expected from increased TEM activity, driven by increased electron heat flux, assuming that the discharge was already in the TEM dominated regime [Fable:PPCF2010, WagnerD:PPCF2012].

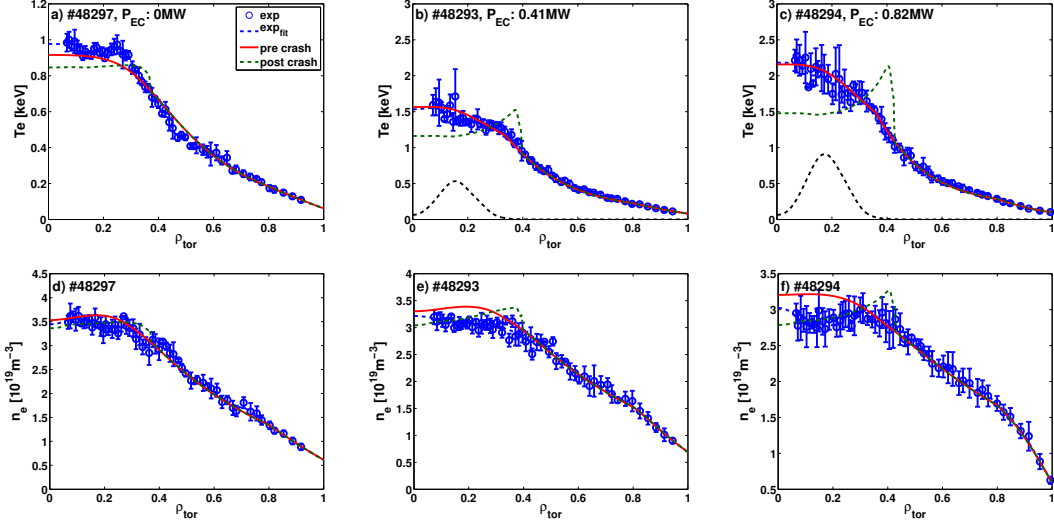


Figure 3.11: T_e and n_e profiles for EC heating test cases: TCV shot #48297, #48293 and #48294 with zero power, 0.41 MW and 0.82 MW, respectively. (a)-(c) T_e profiles using H_e of 0.52, 0.59, 0.67 are well matched to the experimental results for each cases. In (b) and (c), EC power density profiles are displayed with T_e profiles (black dashed). (d)-(f) n_e profiles using constant R/L_{n_e} of 5.8, 5.0 and 4.0 are also in good agreement with the experimental profiles.

3.3 Effect of heating deposition position on confinement time

Auxiliary heating in tokamak plasmas results in a deterioration of the energy confinement time as shown in the multi-machine scaling law (Eq. 3.10): τ_E is inversely proportional to the total heating power $\sim P_{\text{tot}}^{-0.7}$. This is a general effect of all auxiliary heating sources. As presented in Ref. [Kirneva:PPCF2012], it has been shown experimentally that τ_E degrades as the EC heating moves outside the $q = 1$ surface and that it is proportional to $P_{\text{tot}}^{-0.9}$. These experiments were consistent with earlier theoretical simulations [Sauter:PoP2001]. This additional effect of the heating deposition position on the confinement time is not included in the scaling law used to rescale χ_e , so this rescaling is not valid for off-axis heating simulations. In particular, simulations dealing with NTM control would not be correct if this rescaling were used. The off-axis EC heating effect has been taken into account as a 0-D model in Ref. [Sauter:PPCF2010], but not yet for 1-D transport models; therefore, we propose a new scaling factor describing the effect of the heating deposition position, which we can include in our simulations.

In this section, a tentative model of the deposition position scaling will be introduced. The new scaling factor is found to match the simulation result to the experimental data discussed in Ref. [Kirneva:PPCF2012]. To start, we repeat the same exercise as for

central heating, described previously. That is, we take the experimental T_e data and average between 1.4 and 1.95s when the EC beam is inside the $q = 1$ surface $\rho_{q=1}$; all the other parameters are taken at 1.4 s for the simulation. (When the EC heating is deposited inside $\rho_{q=1}$, the effect of the deposition position is negligible so that one can take any experimental data from inside $\rho_{q=1}$.) For the χ_e profile, the core part is taken from the q^2 profile and the edge T_e is fixed from the experimental data. In the central region a constant value of $5\text{m}^2/\text{s}$ is added inside $\rho_{q=1}$ to the initial χ_e profile to compensate the central EC heating. The integrated profile is rescaled using Eq. 3.12 with $H_e = 0.57$ which is the same as the experimental one (averaged between 1.4 and 1.95s). In Fig. 3.12, the χ_e , T_e and n_e profiles are presented. In Fig. 3.12(a) the blue line indicates the χ_e^{PB} profile while the red one represents the one used in the simulation. As shown in the previous section, the ad-hoc model (χ_e proportional to q^2) works well to produce a similar χ_e profile as the experimental one, so the resultant T_e profile, including sawtooth crashes, (red solid, green dashed) are well matched to the experimental profile (blue) as displayed in Fig. 3.12(b). The black dashed line indicates the central EC heating power density profile [MW/m^3], which is multiplied by 0.1 to fit in the same frame. In Fig. 3.12(c), the n_e profiles from the experiment (blue) and the simulation including the sawtooth crash (red solid, green dashed) are in good agreement using $R/L_{n_e} = 5.5$. From this simulation, all the necessary parameters are now obtained and will be used for further simulation of the effect of off-axis heating.

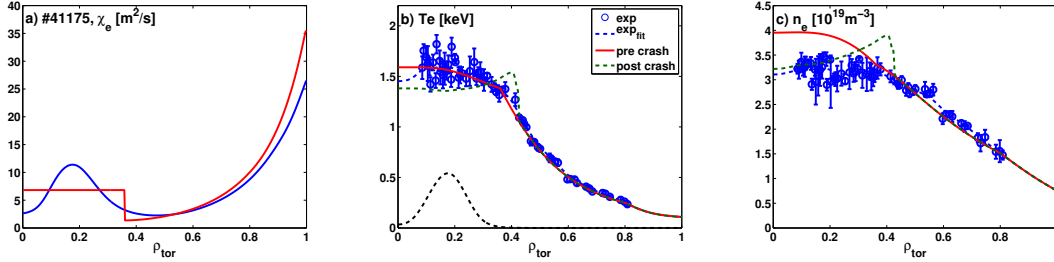


Figure 3.12: Experimental data (blue) taken from TCVC #41175 at 1.4 s and interpretative simulation results (red) are shown for (a) χ_e , (b) T_e and (c) n_e . With $H_e = 0.57$ and automatically rescaled χ_e , the resultant T_e shows good agreements with the experimental data. With a fixed R/L_{n_e} value of 5.5, the n_e profile with sawtooth crash is evaluated and is well matched the experimental one. From this simulation, all the necessary parameters are obtained for further simulation.

3.3.1 A new scaling factor for the heating deposition location

For the deposition scaling, a scaling factor is introduced in Eq. 3.20 to fit the simulation result to the experimental one:

$$s_{dep} = 1 - 0.28 \left[1 - \exp \left\{ -4 \left(\frac{\rho_{dep}^3 - \rho_{q=0.95}^3}{w} \right)^2 \right\} \right] \times H(\rho_{dep} - \rho_{q=0.95}), \quad (3.20)$$

where ρ_{dep} is the position of the maximum value of the EC power density and $\rho_{q=0.95}$ is

3.3. Effect of heating deposition position on confinement time

the location of the $q = 0.95$ surface. H indicates the Heaviside function. For simplicity, we started by setting the scaling factor as a gaussian shape, but later modified it. In order to adjust the shape of the scaling factor across the minor radius, the power of 3 has been applied to the ρ_{dep} and $\rho_{q=0.95}$ terms of the numerator inside the exponential while the denominator term is chosen from the typical EC beam width in TCV plasma ($0.05 \sim 0.2$). For this shot, 0.063 is used for w . With the Heaviside function, inside $\rho_{q=0.95}$ (i.e. $\rho_{dep} < \rho_{q=0.95}$), there is no dependence on the deposition position. Clearly outside $\rho_{q=0.95}$ there is no relative effect either, but a global reduction of about 30%. As mentioned in Ref. [Kirneva:PPCF2012], the effect of the deposition position is noticeable while the EC beam sweeps across the *vicinity* of the $q = 1$ surface but it is not necessarily exactly *at* the $q = 1$ surface. In addition to match with the simulated $q = 1$ radius and the deposition location, we needed to take $q = 0.95$ instead of the $q = 1$ surface. Note that the location, $\rho_{q=0.95}$, is chosen to reproduce the experimental data of TCV #41175 and will be compared with a negative triangularity case. However new experiments are required to better test this effect and the proposed s_{dep} form. This scaling factor s_{dep} results in the degradation of $\tau_{E,e}$ at larger ρ_{dep} ; one could consider a degradation of the H_e factor. Then it can be taken into account for the rescaling of χ_e by writing:

$$\chi_{e,rescaled} = \chi_e \cdot \left\langle \frac{\tau_{E,e}}{\tau_{scaling} \cdot H_e \cdot s_{dep}} \right\rangle_{time}. \quad (3.21)$$

When s_{dep} is smaller than unity, this scaling will cause $\tau_{E,e}$ to decrease in order to fit to the $\tau_{scaling} \cdot H_e \cdot s_{dep}$ value during the simulation; that is, χ_e will be increased with a concomitant decrease of the simulated T_e profile.

An example of s_{dep} is shown in Fig. 3.13. $\rho_{q=0.95}$ is about 0.09 in ρ_{tor} in this case. Far outside $\rho_{q=0.95}$, maximum degradation of the energy confinement time is expected and the effect is the same as in the far off-axis case. s_{dep} starts to increase as the deposition position is moved close to the $q = 0.95$ surface and is almost unity in the vicinity of the $q = 1$ surface. The minimum value 0.72 is taken from the ratio of the minimum to maximum value of the H_e factor in the experiment. Note again that s_{dep} in this section is only set to match to the experimental data of TCV #41175; it may not work for other discharges, so more detailed studies must be carried out to determine if this can be used as a general scaling factor. Nevertheless, the introduction of s_{dep} and these simulation results represent a first step towards studying an additional scaling factor in the scaling law which takes into account the effect of heating deposition position. Note that this effect is known and expected [Pochelon:RF1998, Henderson:FED2001, Sauter:PoP2001, Sauter:PPCF2010] but no systematic experimental studies have been performed. This is why our present model could not yet be validated. However it suggests an interesting result, namely that most of the difference comes from depositing heating inside or outside $q = 1$ and that this variation happens in a narrow region. This may be consistent with a decrease of confinement for $q > 1$ and $s > 0.5$ and effects near electron internal transport barriers [Zucca:PPCF2009], but requires specific analyses and experiments.

3.3.2 A test case using the new scaling factor

Using the parameters obtained from the previous simulation, the H_e factor and the new scaling factor s_{dep} separately, we have conducted time dependent EC beam sweeping

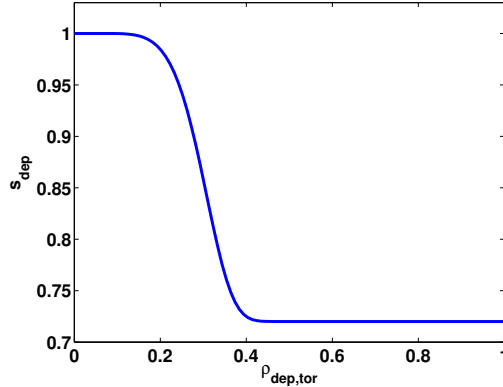


Figure 3.13: A scaling factor for heating deposition position from Eq. 3.20. Far outside the $q = 0.95$ surface (at $\rho_{tor} = 0.09$), maximum degradation of $\tau_{E,e}$ is anticipated and as the deposition position gets close to the $q = 0.95$ surface location, s_{dep} increases up to unity.

simulations. All the data are taken from the experimental result between 0.6 and 1.9s. The EC power density profiles are taken from the TORAY calculation result for each time point and the injected power P_{EC} is 0.5 MW. Note that the absorption rate of the EC power depends on the deposition position and is usually smaller for off-axis deposition. The absorbed power and deposition position used in the simulation are shown in Fig. 3.14. One EC beam sweeps from far off-axis to the centre. The H_e factor is fixed to 0.57 as obtained previously. For the n_e profile evaluation, a single value of R/L_{n_e} (5.5) is taken during the sweeping for simplicity.

As seen in Fig. 3.12(a), a constant value is added to χ_e when the EC beam is deposited inside the $q = 1$ surface. Sawteeth are included in the simulation, although the sawtooth periods do not perfectly match the experimental periods: sawtooth periods during the experiment are around 2.0 ~ 3.0 ms but in the simulation, they vary between 1.0 and 6.0 ms due to the fixed sawtooth trigger condition used for simplicity (see Sec. 4.2 on sawtooth modelling). The difference in the sawtooth period is not so large that it affects the global plasma energy thus the resultant $\tau_{E,e}$ is unaffected.

The simulation results are presented in Fig. 3.15 along with the experimental data. Figure 3.15(a) shows the temporal evolutions of the H_e factors from the experiment (blue circle) and the simulation (red cross). The experimental H_e factors are calculated from the L-mode scaling law ($H_{e,L98}$), as defined in Sec. 3.2.3. Using the new scaling factor s_{dep} , the degradation of $\tau_{E,e}$ (equivalently H_e) is well reproduced. At the beginning, the scaling factor is lowest since the EC beam stays far off-axis. From 1.0s, as the EC beam moves close to $\rho_{q=0.95}$, the effect of the deposition location increases and s_{dep} increases. At 1.2s, the EC beam almost reaches, or starts to cross, $\rho_{q=0.95}$ such that from this time onwards the H_e factor is approximately 0.57. There is a small discrepancy between 1.0 and 1.2s, but overall these two curves match very well. The same results are plotted versus ρ_{dep} in Fig. 3.15(b); where ρ_{dep} is given in ρ_ψ ($= \sqrt{\psi/\psi_{edge}}$) grid and the H_e factor is normalised to the value obtained with central deposition.

Another discharge (#41170) from the same experimental series has been employed to test the new scaling factor for different plasma conditions. As in the #41175 case, all

3.3. Effect of heating deposition position on confinement time

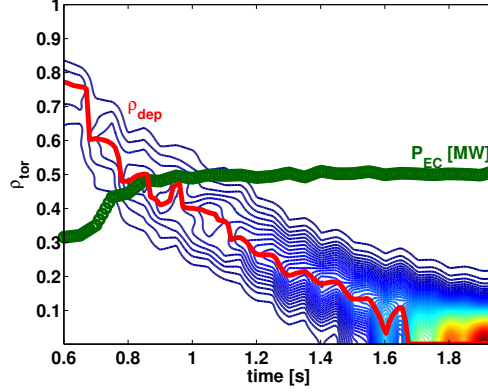


Figure 3.14: EC beam sweeps from far off-axis (0.8 in ρ_{tor}) to the centre (red line: ρ_{dep} , contour: power density profile). The absorbed power (green) increases to 0.5 MW while the beam moves to the central region.

the parameters are first defined from the simulation with the heating deposited inside $q = 1$, then a sweeping test is carried out including sawtooth activity. The #41170 and #41175 plasma parameters are similar except for a few values; triangularity δ , H_e factor and R/L_{n_e} . In particular, shot #41170 has a negative triangularity $\delta \approx -0.45$, whereas $\delta \approx +0.35$ for #41175. The maximum H_e factor is 0.84 in shot #41170 and the global degradation is also about 30% as in #41175. In #41170, the experimental n_e profile changes in time, hence the n_e profile is fixed to the experimental one for the first test and is simulated using two fixed R/L_{n_e} values (6.0 until 1.3s and 4.5 afterwards) during the EC beam sweeping. The scaling factor s_{dep} is first applied to #41170 with the same $w = 0.063$ value. However, as seen in the experimental result, the H_e factor of this discharge increases over a smaller range than #41175 case so that a smaller value of $w = 0.02$ in Eq. 3.20 is required. The H_e factors from the experiment (blue circle) and simulation are presented in Figs. 3.15(c) and 3.15(d) as a function of time and $\rho_{dep,\psi}$, respectively. The different simulation results are indicated by different colours and markers: fixed n_e and $w = 0.02$ (red cross), simulated n_e with two R/L_{n_e} values and $w = 0.02$ (green square) and fixed n_e and $w = 0.063$ (violet diamond). In Fig. 3.15(c), the experimental H_e factor gradually increases until 1.2s and then increases steeply. Using the same s_{dep} as in #41175 (violet, $w = 0.063$), the H_e factor starts increasing much earlier both in time and $\rho_{dep,\psi}$. Whereas with smaller w value (0.02), the H_e factor in the simulation is roughly constant until 1.1s and then starts increasing, up to the maximum value at 1.5s. Note that there are no differences between using the experimental or simulated n_e profiles. The simulation results in Fig. 3.15(c) exhibit sudden drops and recovery of the H_e factor, because of rapid modifications of the input ρ_{dep} values; when ASTRA takes the experimental EC beam profiles which are not gaussian, it fits the profiles to a gaussian shape and during this process the ρ_{dep} value can be calculated as moving in the opposite direction. Despite the differences in plasma equilibria between the two shots, the proposed method for modelling changes of the EC deposition allows us to successfully simulate changes in confinement during the beam sweeping.

The χ_e , T_e and n_e profiles (columns) of shot #41175 from experiment (blue) and

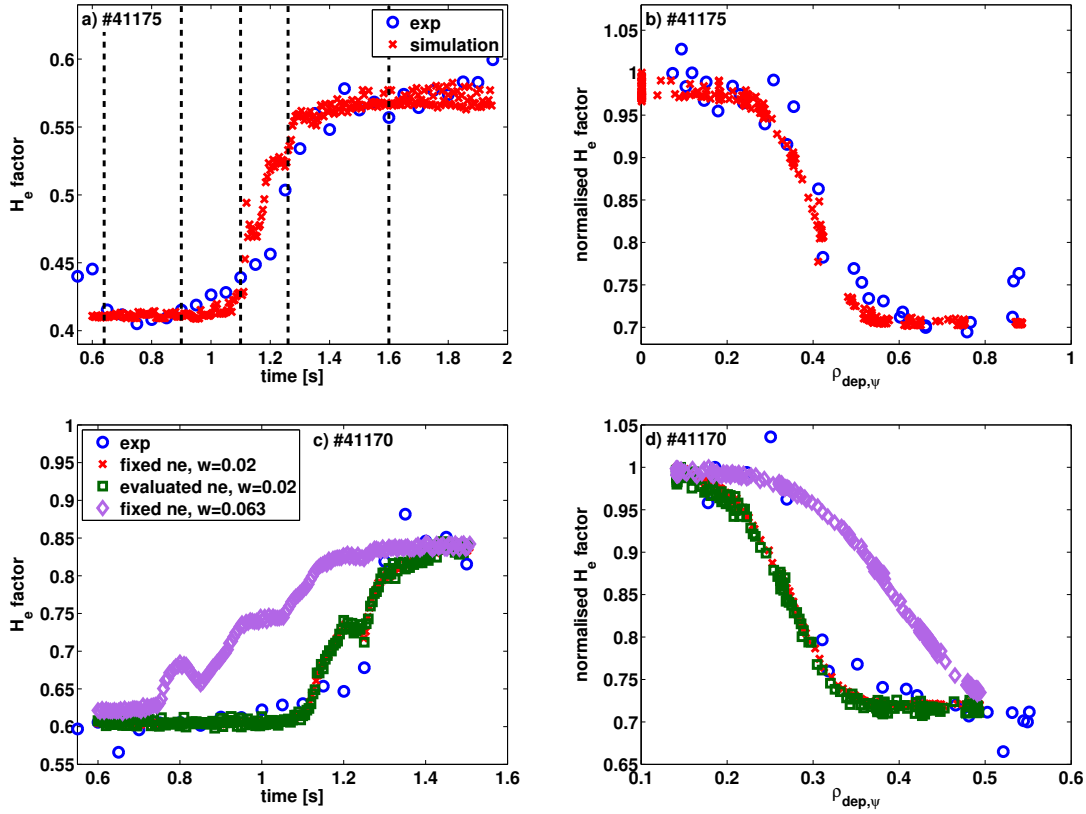


Figure 3.15: The experimental H_e factors are displayed with the simulated ones using the new scaling factor (Eq. 3.20) for the discharges #41175 ($\delta \approx 0.35$) and #41170 ($\delta \approx -0.45$) versus time (a), (c) and $\rho_{dep,\psi}$ (b), (d). For #41175 the simulation result is well matched to the experimental one while there is a big gap for #41170 with the same scaling factor (violet). With a modification of w in Eq. 3.20, experimental results can be reproduced by simulation regardless of the evaluation of n_e (red, green). In (a), black dashed lines indicate each time point in Fig. 3.16.

simulation (red) for several time points (rows, 0.64, 0.9, 1.1, 1.26 and 1.6s) are shown in Fig. 3.16 (the chosen time points are indicated by black dashed lines in Fig. 3.15(a)). The experimental profile is an averaged profile (around the specified time), but for the simulation, the edge profiles for both T_e and n_e use only data from the specified time point; consequently, in the edge region the experimental and simulated profiles do not perfectly coincide. EC heating power densities are presented as black dashed lines in the column for the T_e profile.

Until 1.1s, the EC beam is outside the $q = 1$ surface and the central χ_e is low; after that time, the central part of the χ_e profile is augmented by an additive factor. Since the H_e factor is almost the same as the experimental one, the T_e profiles from the simulation are quite similar to those of the experiment; the n_e profiles are also similar to the experimental profiles despite the fact that the n_e profiles are evaluated using a single value of R/L_{n_e} across the profile. Because of this, as discussed in Sec. 3.2.5, the central n_e profiles are centrally peaked before sawtooth crashes. The overall agreement between simulations and experiments is nevertheless reasonably good.

In this section, we have stressed the need for the new scaling factor, s_{dep} , accounting for the heating deposition position and have introduced a simple way to include s_{dep} in the scaling law. However, we note that s_{dep} has been used to fit only limited TCV experimental data. A more thorough study of deposition-location-dependant additional heating confinement scaling is nevertheless warranted. It might shed light on the relative narrow improved transport region near $q = 1$ which might be responsible for the sharp change of overall good confinement, similar to TCV electron internal transport barrier [Zucca:PPCF2009].

3.4 Application to H-mode

To this point, it has been demonstrated that the ad-hoc transport model can be successfully used to simulate TCV L-mode plasmas. Since one of the main goals of using this model is for predictive simulations of the ITER standard H-mode scenario, it is worthwhile to test this predictive model for TCV H-mode plasmas.

To that end, two H-mode discharges, one Ohmic plasma (#37395) and an EC heated plasma (#38012) are chosen for testing. Again, the edge T_e profile between 0.9 and 1.0 in ρ_{tor} is fixed to the experimental data and a χ_e model based on the q^2 profile is taken for the core T_e profile. The central region is dominated by sawteeth, so the initial χ_e value inside $\rho_{q=1}$ is set to unity as in the Ohmic case, but to a larger value for central EC heating (as in the L-mode simulations).

3.4.1 Comparison of the shape of the T_e profiles in L- and H-mode plasmas

Inspired by Ref. [Sauter:PoP2014], the T_e profiles are normalised by the value at ρ_{ped} , which is 0.8 for L-mode and 0.9 for H-mode. The normalised T_e profiles are shown in Figs. 3.17(a), (c) for TCV L-mode plasmas on linear and log scales, and Figs. 3.17(b), (d) for H-mode plasmas in TCV and AUG discharges (experimental measurements) and an ITER reference scenario (simulated, Ref. [Parail:NF2013]). For the AUG and ITER cases, more detail will follow in the next chapter.

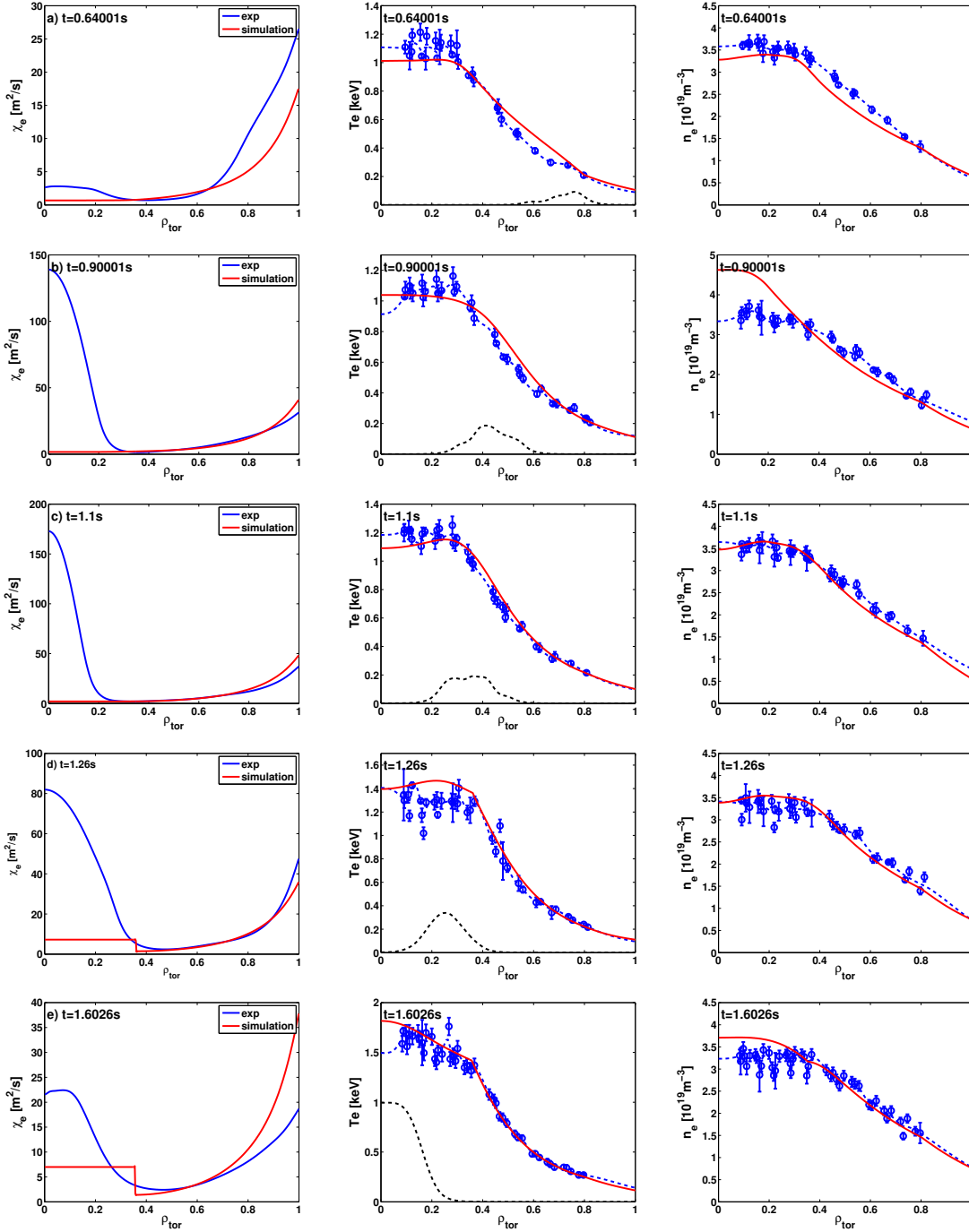


Figure 3.16: χ_e , T_e and n_e profiles from 0.64, 0.9, 1.1, 1.26 and 1.6 s. T_e and n_e profiles from EC beam sweeping agree well with the experimental data using the scaling factor.

The black lines are the fits (simple exponential functions) introduced in Eq. 3.22 as discussed in Ref. [Sauter:PoP2014]; they are normalised in the same way. The fitting functions remain peaked in the central region since sawtooth crashes are not taken into account and the fitting function aims to match the experimental data only in the core region. (Note that for the ITER case, no experimental data exists and sawtooth crashes are not included in the calculations, so the reference T_e profile and the fitting function coincide in the central region as well.) The fitting function is:

$$T_{e,core} = T_{e,0} \exp\{-\lambda_{T_e}(\rho_{tor} - \rho_1)\} \quad (3.22)$$

where $T_{e,0}$ is the T_e value at the $q = 1$ surface (ρ_1) and λ_{T_e} is an inverse scale-length of T_e , $1/L_{T_e}$.

For L-mode plasmas all the T_e profiles are well fitted in the core region by a single inverse scale-length $\lambda_{T_e} = 3.5$. It is similar for H-mode cases, but smaller λ_{T_e} values (2.3 for TCV and AUG and 1.6 for ITER) are required to fit the T_e profiles. For H-mode plasmas, due to a relatively large value at the pedestal, T_e profiles are less peaked compared to L-mode profiles and the λ_{T_e} values are smaller. Following our discussions above, the fact that λ_{T_e} in the ITER reference case is smaller than both AUG and TCV would indicate that the assumed top of pedestal T_e is too high. It is easier to see this difference when plotted on a log scale: comparing Figs. 3.17(c) and 3.17(d), we see that the slopes of H-mode profiles are less steep than those of L-mode profiles in the core region, in particular the ITER one.

3.4.2 H-mode T_e and n_e profile simulations using the same ad-hoc model as in L-mode

As seen in Fig. 3.17, H-mode plasmas have different T_e scale-lengths from those of L-mode plasmas. Despite the different slope, the χ_e profile proportional to q^2 can still be applied to evaluate the T_e profiles in TCV H-mode plasmas as shown in this section. In this case the H_e rescaling is used with the H-mode scaling law (Eq. 3.10) to adjust the amplitude of the χ_e profiles. Using this χ_e model, T_e profiles of two cases of TCV H-mode discharges (Ohmic: #37395, central EC heating: #38012) are evaluated.

The simulation results for an Ohmic H-mode case (#37395) is shown in Fig. 3.18. For this shot $H_e = 0.55$ and the T_e profiles in both central and core regions are well matched to the experimental profile using our ad-hoc model (before (red) and after (green) a sawtooth crash profiles are shown). Note that Ohmic TCV H-modes are obtained at very high plasma current (q_{95} below 3). As shown in Fig. 3.18(c), the resultant R/L_{T_e} (red) agrees well with the experimental data (blue). R/L_{T_e} decreases between $\rho_{tor} = 0.6$ and 0.8 but the value is still in the typical range for H-mode, between 5 and 8. For the n_e profile, with a fixed R/L_{n_e} value of 3.2, the simulation reproduces the whole experimental n_e profile within the error bars and the resultant R/L_{n_e} profile is also well matched to the experimental one as shown in Figs. 3.18(b) and 3.18(d), respectively. This is obtained thanks to the boundary condition at $\rho = \rho_{ped}$ and the sawtooth effects in the centre (or naturally flat profiles in the centre).

A centrally heated H-mode case, #38012, is shown in Fig. 3.19. In order to compensate the peaked T_e profile in the central region caused by central EC heating, a constant χ_e

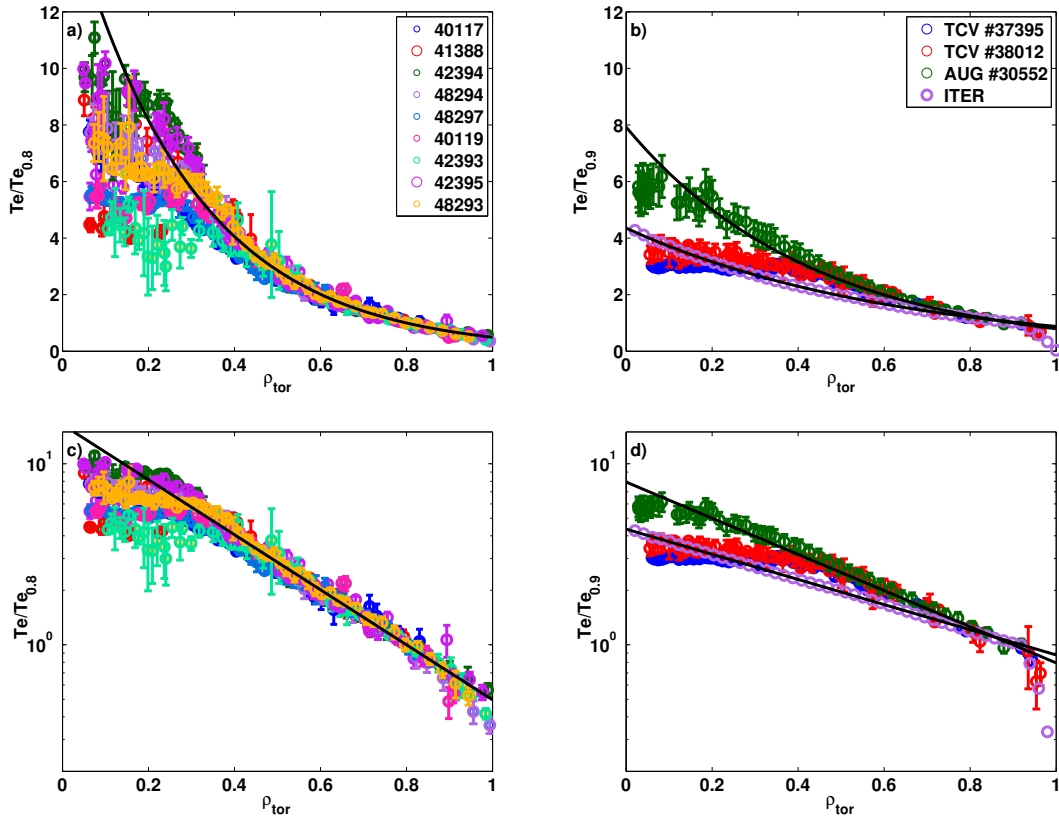


Figure 3.17: Comparison of T_e profiles of L- and H-modes in linear and log scales. (a) T_e profiles of TCV L-mode plasmas normalised to its value at $\rho_{tor} = 0.8$ are shown with fitting function. The inverse scale-length λ_{T_e} is 3.5. (b) T_e profiles of TCV, AUG and ITER H-mode plasmas normalised to its value at $\rho_{tor} = 0.9$ are less peaked compared to L-mode plasmas and have smaller inverse scale-lengths ($\lambda_{T_e} = 2.3$ for TCV and AUG and 1.6 for ITER). (c), (d) In log scale, it is easier to compare the difference of the slopes of T_e profiles in the core region.

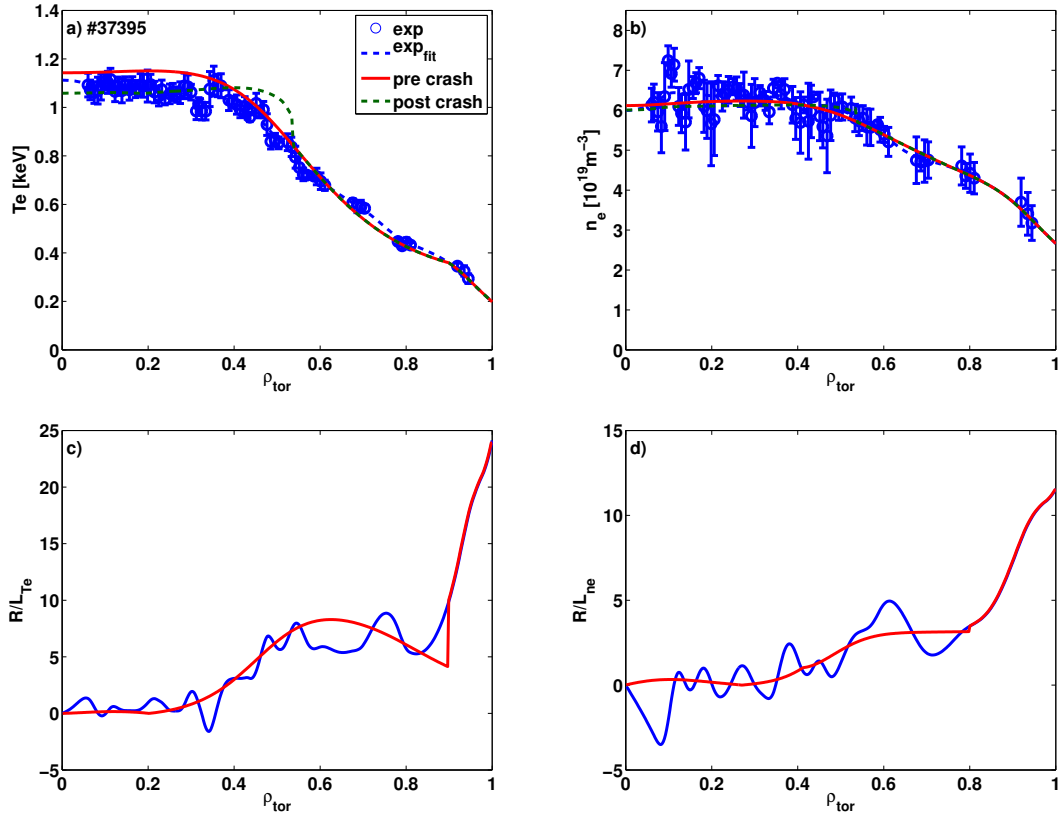


Figure 3.18: The simulation result of T_e and n_e profiles of TCV Ohmic H-mode discharge #37395 using $\chi_e \propto q^2$ and a fixed $R/L_{n_e} = 3.2$. (a) T_e profiles with a sawtooth crash (red, green dashed) are well matched to the experimental one (blue) as well as the corresponding R/L_{T_e} profile in (c) within error bar. (b) n_e and (d) resultant R/L_{n_e} profiles also match the experimental profiles in central and core regions.

of 2.0 is applied in the centre (inside $q = 1$ surface). The χ_e profile is rescaled using H_e factor of 0.8. In Fig. 3.19(a) T_e profiles are shown, the black dashed line indicates the central EC heating power density profile. In the core region, T_e profiles before and after a crash show a good agreement with the experiment within error bars. The R/L_{T_e} profile has similar shape as the Ohmic case. However, there is a jump due to the modification of the central χ_e and the resultant T_e gradient. The core R/L_{T_e} values are similar to the experimental profile and are varying within the same range between 5 and 8. With a constant R/L_{n_e} of 2.0 in the core region, proper n_e profiles are simulated with sawtooth activity, and the corresponding R/L_{n_e} profile agrees well with the experimental profile.

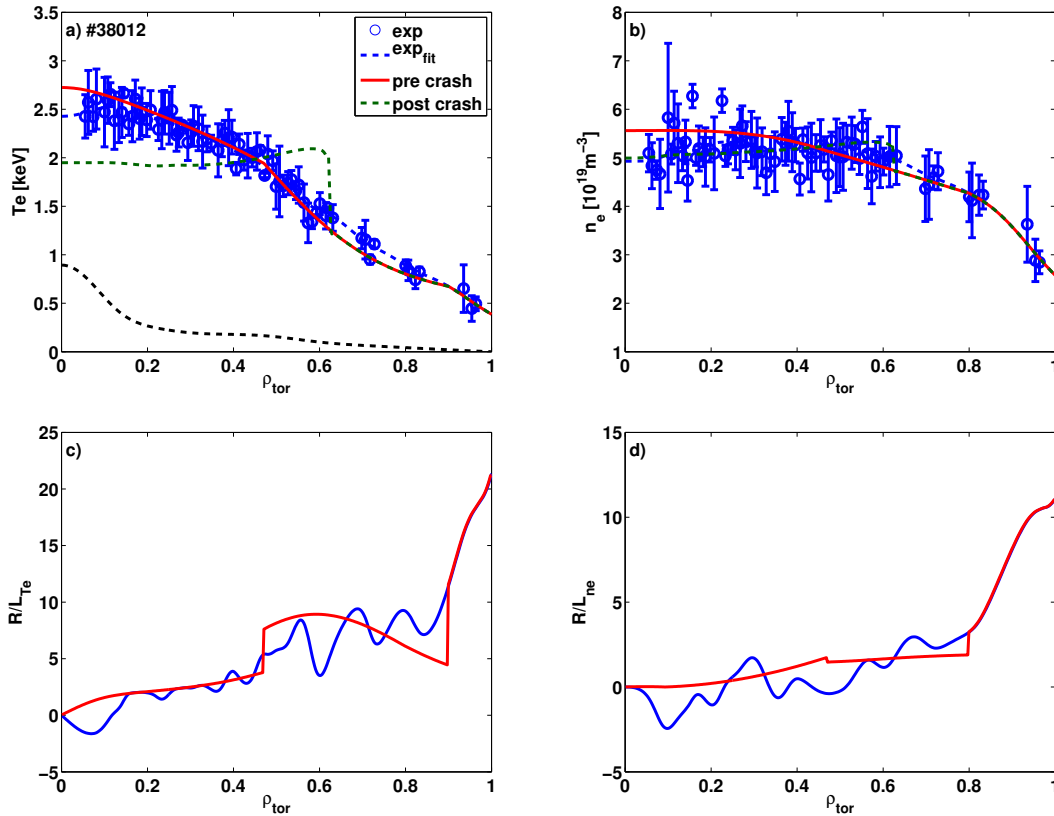


Figure 3.19: The simulation result of T_e and n_e profiles of a TCVC EC heated H-mode discharge #38012 using $\chi_e \propto q^2$ and a fixed core R/L_{n_e} value. Due to central EC heating, a constant value of 2.0 is added to central χ_e profile and χ_e profile is rescaled using H_e factor of 0.8. In (a), central EC heating profile is indicated by black dashed line. Same as previous case, (a) T_e with sawtooth crash (red, green dashed) and (c) R/L_{T_e} profiles have similar values as experimental one (blue). For the n_e profile, a fixed R/L_{n_e} of 2.0 is used and the evaluated n_e is well matched to the experimental data as well as the resultant R/L_{n_e} profile.

As mentioned above, H-mode plasmas have smaller scale-lengths (λ_{T_e}) than in L-mode. Nevertheless we show that our ad-hoc model based on $\chi_e \propto q^2$ and rescaling with the confinement scaling law, combined with a fixed R/L_{n_e} value works well with H-modes as well. It could be due in part because TCVC H-modes have large plasma current and therefore large $q = 1$ radius, yielding a small radial range for the core profiles. However

we have tested this model for AUG H-modes and it works as well. We can therefore use this model for sawtooth control simulations for ITER H-mode plasmas, as well as off-axis current drive for NTM simulations. If a closer match to the temperature gradients is required, another model could be used based on a fixed R/L_{T_e} as well [Sauter:PoP2014], this is proposed below for future studies.

Electron heat transport coefficient using the inverse scale-length λ_{T_e}

The χ_e profile can also be determined using the T_e fit in Eq. 3.22 and the definition of χ_e power balance in Eq. 3.7. With these equations, the χ_e for core region can be directly derived as

$$\chi_{e,core} = \frac{q_e \rho_{edge}}{V' \langle |\nabla \rho|^2 \rangle n_e \lambda_{T_e} T_{e,core}}. \quad (3.23)$$

The central χ_e profile is then set to a constant value matching $\chi_{e,core}(q = 1)$. χ_e defined in Eq. 3.23 allows us to simulate T_e of H-mode plasmas even more precisely, reproducing the experimental values for both Ohmic (#37395) and EC heated (#38012) plasmas. As in the previous case (core χ_e defined by q^2), the H_e values (0.55 and 0.8 for #37395 and #38012, respectively) are used for the rescaling of the amplitude of χ_e , and a λ_{T_e} value of 2.3 is taken from the fitting in Fig. 3.17 for the χ_e profile. In Fig. 3.20, the simulated T_e profiles for these two cases are shown with the corresponding R/L_{T_e} profiles. Note that since the n_e profile is mainly determined by R/L_{n_e} value, the n_e profile for this case is the same as the previous case so that it is not shown in this figure. Compared to the previous case, the T_e profile of the Ohmic plasma using the χ_e from T_e fitting equation shows good agreement with the experimental profile in the core region. The good agreement is also shown in the resultant R/L_{T_e} profile in Fig. 3.20(c). With the fixed λ_{T_e} value, R/L_{T_e} is almost constant, which is similar to the experimental value in the core region. With the sawtooth crash, T_e and R/L_{T_e} profiles in the centre are also well matched to the experimental data. As well as the Ohmic case, T_e and R/L_{T_e} profiles of the central EC heating case in Figs. 3.20(b) and 3.20(d) well reproduce the experimental data with the same λ_{T_e} . It confirms that little variation of λ_{T_e} is expected [Sauter:PoP2014] in H-mode, as is the case for L-mode.

As seen in Fig. 3.20 the χ_e profiles using λ_{T_e} can be applied to H-mode plasma simulation for T_e evaluation. It can be used for L-mode plasmas as well. This is a recent development which was not implemented yet in the ITER simulations shown in the next chapter. Note that there is still *one* free parameter λ_{T_e} , however it is expected that λ_{T_e} could be easily determined by a cross-machine study of the core region of H-mode plasmas. Then $T_{e,ped}$ can be given as discussed in Sec. 3.2.3 and Eq. 3.23 can be used to define the χ_e profile. In this case, either no rescaling to the predicted scaling law would be required, or the rescaling could be used to determine the pedestal values, reducing even further the free parameters.

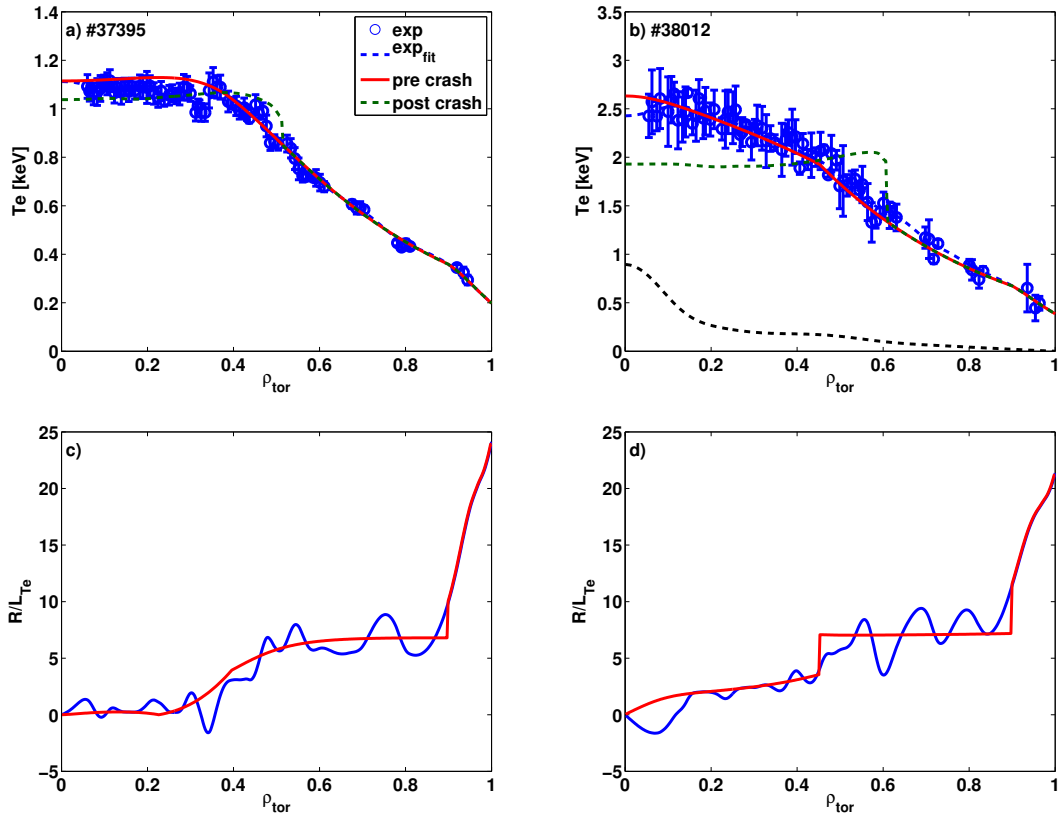


Figure 3.20: (a) T_e and (c) R/L_{T_e} profiles evaluated using χ_e in Eq. 3.23 are presented with experimental data (blue) for Ohmic H-mode plasma (#37395). In the core region, T_e shows precise agreement with experimental profile with constant R/L_{T_e} . With sawtooth crash (red, green dashed), not only T_e in the core region but also that in the central region are well matched to the experiment. EC heated H-mode plasma (#38012) case has also (b) T_e and (d) R/L_{T_e} profiles well matched the experimental results. In (b) the central heating profile is shown as the black dashed line.

3.5 Summary

In this chapter, a simple and fast way to evaluate T_e and n_e profiles has been introduced. To calculate $T_e(\rho, t)$, the electron heat transport coefficient χ_e is defined in central and core regions taking into account sawtooth crashes. From the experimental data, it has been shown that the χ_e profile in the core region is proportional to the square of the safety factor (q^2) in TCV L-mode plasmas. We have taken advantage of this property.

For the central χ_e profile, an operational-scenario-dependant constant value is used, but the central T_e profile is governed essentially by sawtooth crashes. Since there is no presently known way to predict χ_e in the edge region, T_e and n_e profiles in the edge region are taken from experimental or predicted data, providing boundary conditions to the simulations. Given the modelled *shape* of the χ_e profile, the *amplitude* is automatically adjusted in the simulations using an appropriate energy confinement scaling law. In this way, the change of power and plasma parameters are consistently included in the evaluation of χ_e . The only restriction would be in the case of improved confinement, however this can be included as a relative increase of the H factor.

In order to apply the predictive χ_e model, one has to know the H_e factor and the T_e value at the boundary between the core and edge. There is no full scaling or predictive model for the T_e value at the boundary, but this is a problem for most present models. We have shown that this value can be estimated using the experimental observation that stiffness of the T_e profile in the core region corresponds to a scale-length of T_e ; R/L_{T_e} lying in the range between 8 and 14. A sensitivity study of the boundary T_e value can thus be used to determine which boundary T_e values will satisfy this R/L_{T_e} range in the core region. Since there are two free parameters that can affect this inverse scale-length, a similar sensitivity study of the H_e values has been carried out. We have shown how these sensitivity studies can constrain the transport model used.

For the n_e profile, transport coefficients D_n and D_E are defined assuming $D_n = 0.2\chi_e$ and a constant R/L_{n_e} across radius. In this way $n_e(\rho, t)$ can be simulated. The central n_e profile is mainly determined by sawtooth activity (unlike T_e , n_e is less strongly affected by centrally deposited EC power). R/L_{n_e} can be predicted by kinetic theory or cross-tokamak study so that a scaling law could be obtained to allow a simple predictive simulation.

From experiments (TCV discharges #41175 and #41170), it has been shown that off-axis heating degrades the energy confinement more than on-axis heating does. However, this effect is not included in the energy confinement scaling laws. Therefore a new scaling factor which takes into account the effect of heating deposition position on the confinement has been introduced and tested. Using this new scaling factor, the degradation of confinement has been well reproduced while the EC beam sweeps from off-axis to the centre. The temporal and spatial variations of the H_e factor from experiment are well reproduced by the simulation as are the T_e and n_e profiles evaluated at several times during the sweep. Even though the new scaling factor is based solely on TCV discharge #41175 and tested with #41170, it provides an acceptable starting point for later simulations. To define a more general scaling factor, more detailed experimental studies must be carried out. Our results show that the change of confinement properties occurs across a narrow region near $q = 1$, but are essentially constant when far from this region. Specific studies should be performed to check if this is a general result, with other heating methods, in H-modes, and in other tokamaks.

The predictive χ_e model has been applied to H-mode plasmas as well. It is shown that it also works well with $\chi_e \propto q^2$, despite the fact that the observed R/L_{T_e} values tend to be smaller in H-modes than in L-modes. This can be understood from our sensitivity study on pedestal parameters. Since the global confinement is well predicted through the H_e rescaling, increasing the edge values leads to reduced core gradients. The H-modes do have higher pedestal values than L-mode and therefore are consistent with lower R/L_{T_e} values. The present model for ITER H-mode simulations, presented in the next chapter, predicting both T_e and n_e profiles time evolution, is therefore justified. Nevertheless, since recent experimental results have shown that both R/L_{T_e} and R/L_{n_e} values are relatively constant across the core region [Sauter:PoP2014], the next step will be to use this effect. We have shown preliminary results demonstrating that it can lead to better prediction of the T_e profile and to predict the pedestal T_e value through the H_e scaling law.

Chapter 4

Control of sawtooth instability

4.1 Introduction

In order to achieve a significant fusion gain in fusion-grade tokamak experiments, the use of heating power should be optimised to have appropriate temperatures and confinement regimes. Moreover, heating systems are demanded to be able to prevent instabilities that degrade the plasma performance, or at least to control them for retaining efficient fusion yield.

There are various auxiliary heating systems in present tokamak experiments such as neutral beam injection and ion or electron cyclotron resonance heating. Among those systems, in this work, we focus on the use of electron cyclotron heating (ECH) and current drive (ECCD). EC beams are ideally suited to control plasma instabilities since their power can be deposited in a flexible way: the beams can aim across (nearly) the entire plasma cross-section and quickly change the deposition position using mirror actuators. The interaction between EC beams and plasma electrons is very localised and the induced heating and current drive required to affect instabilities is therefore deposited at a relatively precise location, or position. Of particular interest in this chapter, we note that EC waves have been used to control the sawtooth instability (e.g. [Angioni:NF2003, Lennholm:PRL2009, Paley:PPCF2009, Goodman:PRL2011]).

The sawtooth instability in tokamak plasmas is characterised, on temperature and X-ray measurement time traces, by periodic fast relaxations, followed by a slower recovery of the signal amplitude in the central region where the safety factor q is lower than unity [Porcelli:PPCF1996]. A long sawtooth period can create a seed island, triggering neoclassical tearing modes (NTMs) that limit the safe operating regime of the tokamak [Canal:NF2013, Chapman:NF2013]. It is also able to change the β limit for NTM onset by more than a factor of two and trigger NTMs at low β_N [Sauter:PRL2002].

In TCV experiments, it has been shown that large $q = m/n = 3/2$ and $2/1$ seed islands for NTMs can be triggered directly at the sawtooth crash (i.e. within $10 - 20\mu\text{s}$) that follows a long sawtooth period [Canal:NF2013]. It has also been observed that the formation of the NTM can be prevented by EC preemption [Felici:NF2012]; that is, by adding ECH/CD near $q = 3/2$ or $2/1$ surface close to the time of the sawtooth crash. Therefore, it is particularly important to address the question of the feasibility of the ITER EC system to provide NTM preemption at the time of the sawtooth crash in ITER, since it is predicted that in ITER relatively long sawtooth periods will be produced by energetic

α -particle stabilisation [Porcelli:PPCF1996]. By transport modelling, a sawtooth period of 20-50s is anticipated for ITER [Onjun:NF2009, Budny:NF2008] and the scaling law in Fig. 4.1 [Chapman:NF2013] shows that for the standard ITER ELMy H-mode scenario, with a target $\beta_N = 1.8$, a sawtooth period of about 70s (with a large error bar) will probably be able to trigger NTMs. Therefore, it would be helpful to control the sawtooth period and to know when the next sawtooth crash is likely to occur in order to avoid NTMs triggering. Foreknowledge of the crash time would allow us to add EC power on the $q = 3/2$ and/or $2/1$ surface before the islands are triggered, potentially preempting the formation of large NTMs, as was demonstrated on TCV [Felici:NF2012, Canal:NF2013].

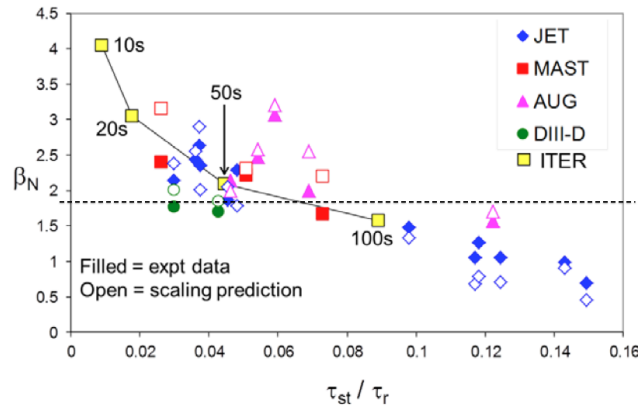


Figure 4.1: Figure from Ref. [Chapman:NF2013]. In ITER, due to α -particle stabilisation, a long sawtooth period is expected and it can lower the β limit for NTM onset. For the standard H-mode scenario with the target $\beta_N = 1.8$, NTMs can be triggered if a sawtooth period is longer than 70s.

ECH/CD can be used for sawtooth period control because it affects the evolution of the magnetic shear at the $q = 1$ surface, which determines the time of the sawtooth crash as defined in the standard sawtooth model (see Sec. 4.2.1). Absorbed EC power can lengthen (stabilise) or shorten (destabilise) sawtooth periods depending on the “deposition” (i.e. absorption) position, ρ_{dep} , relative to the $q = 1$ rational surface location, ρ_1 , as well as the direction of any driven EC current (ECCD) [Angioni:NF2003]. Recent experiments have shown that sawtooth pacing [Goodman:PRL2011] and locking [Witvoet:NF2011, Lauret:NF2012] are two efficient ways to control the sawtooth instability using EC *power pulses* rather than the slower *deposition location* control provided by adjusting the antenna mirror. Both power pulse methods can stabilise the sawtooth period by adding EC power during some pre-set time. For pacing, EC power is turned on by a real-time control system when a crash is detected; whereas the timing is determined *a priori* for locking, so that no real-time control is necessary. The on/off timing of EC power provides the sawtooth period control through a rapid change in the evolution of the magnetic shear. The sawtooth period can also be affected by the deposition width, w_{dep} . When the beam width decreases, EC beam becomes very localised and makes the sawtooth period even longer for a given power level when deposited in a stabilising location, within a beam width of ρ_1 .

On the other hand, heating near the centre is much more efficient with respect to plasma performance than off-axis EC deposition (near $q = 3/2$ or $2/1$, see Sec. 3.3). As

discussed in Ref. [Sauter:PPCF2010], the optimisation of the fusion performance Q with regards to NTM stabilisation needs to be taken into account along with the sawtooth control possibilities. The main sawtooth control strategy to destabilise the sawteeth (i.e. to shorten the period as much as possible) is to drive continuous wave ECCD in the direction of plasma current near the centre, so that the sawtooth period is short enough to avoid NTMs triggering [Hender:NF2007, Sauter:PPCF2010, Chapman:NF2010, Canal:NF2013]. However, if the resultant sawtooth period is still too long, i.e. sawtooth crashes do trigger NTMs, then sawtooth period control and NTM preemption and stabilisation will be needed. This is the subject of the experiments and simulations presented here [Kim:PoP2014].

In this chapter we show the experimental and simulation results of the main sawtooth control schemes foreseen with localised ECCD ($|\rho_{dep} - \rho_1| \lesssim w_{dep}$), namely pacing [Goodman:PRL2011] and locking [Witvoet:NF2011, Lauret:NF2012], in different tokamaks. Prior to the main discussion, the sawtooth simulation model, involving criteria for the sawtooth crash and the reconnection process caused by the crash, will be discussed in Sec. 4.2. In the following Section, Sec. 4.3, there will be a discussion of the control of sawtooth period using localised EC deposition, including the description of sawtooth pacing and locking. The simulation results of sawtooth pacing and locking on TCV tokamak will be presented in Sec. 4.4 together with the experimental results.

Using TCV as a starting point, the experimental and simulation results of sawtooth control on other tokamaks follows in Secs. 4.5 (KSTAR) and 4.6 (ASDEX Upgrade). Since the specific real-time control algorithms required for sawtooth pacing were not yet in operation for these tokamaks, only sawtooth locking was investigated experimentally. But, in Sec. 4.7, a predictive simulation result of both sawtooth pacing and locking on ITER will be shown [Kim:PoP2014]. Based on the present (2013) design of the ITER EC system, the applicability of these two methods and their differences are analysed, as well as their link with NTM preemption and performance optimisation. Finally, this chapter is summarised in Sec. 4.8.

4.2 Model for sawtooth simulation

A sawtooth model is implemented in the ASTRA code to describe the sawtooth crash and the subsequent modifications that result in the profiles. The overview of the sawtooth model based on Ref. [Porcelli:PPCF1996] will be presented in the following sections; for the sawtooth crash criteria, Sec. 4.2.1, and for the post-crash profiles, Sec. 4.2.2.

4.2.1 Criteria for sawtooth crash triggering

In the ideal MHD limit, the ideal internal kink is unstable when the ideal growth rate γ_{ideal} is positive and it can be written as

$$\gamma_{ideal} = -\frac{\delta\hat{W}_{MHD}}{\tau_A} > 0 \quad (4.1)$$

where $\delta\hat{W}_{MHD}$ is the internal kink mode potential energy for ideal MHD case and τ_A is the Alfvén time. The $\delta\hat{W}_{MHD}$ consists of the effects of toroidicity for a circular

plasma [Bussac:PRL1975] and the effects of the plasma shape [Lutjens:NF1992]. The analytic formulae of those two effects are presented in Refs. [Bussac:PRL1975] and [Porcelli:PPCF1996], respectively. In this work, however, $\delta\hat{W}_{MHD}$ is not evaluated by those two terms but taken from the formula in Ref. [Martynov:PPCF2005] as written below

$$\delta\hat{W}_{MHD} = -0.44 \frac{\epsilon_1 \kappa_1}{1 + 7\epsilon_1 s_1} (\beta_{p1} - \beta_{p1}^c). \quad (4.2)$$

ϵ_1 , κ_1 , s_1 are the inverse aspect ratio, the elongation and the magnetic shear, respectively and the subscript “1” indicates that these quantities are evaluated at the $q = 1$ surface. $\beta_{p1} = (2\mu_0/B_{p1}^2) (\langle p \rangle_1 - p_1)$, in which B_{p1} is the poloidal magnetic field, $\langle \cdot \rangle_1$ indicates the volume averaging within the $q = 1$ surface for the total plasma pressure p and the critical $\beta_{p1}^c = 0.9 - (0.6 + 0.1s_1) \kappa_1$. In Eq. 4.1, not all kinetic effects are taken into account. Therefore, the ideal kink mode would be unstable when $\delta\hat{W}_{MHD}$ is negative. However, since there is an additional stabilising effect provided by diamagnetic effects, the stability threshold increases and Eq. 4.1 has to be modified to the following form

$$- \frac{\delta\hat{W}_{MHD}}{\tau_A} > 0.5\omega_{*,i}, \quad (4.3)$$

where $\omega_{*,i}$ is the ion diamagnetic frequency.

In addition, there is another stabilising effect, arising from trapped thermal ions, in the internal kink potential energy for standard tokamak profiles [Kruskal:PoF1958]. Since the thermal electrons are collisional, the compressional electron contribution can be neglected and therefore, only the collisionless thermal trapped ions contribute. The expression for the ion contribution, which is called Kruskal-Oberman effect $\delta\hat{W}_{KO}$, is [Porcelli:PPCF1996]:

$$\delta\hat{W}_{KO} = \frac{3}{2} \epsilon_1^{1/2} \frac{\beta_{i0}}{s_1} \int_0^1 x^{3/2} \frac{p_i(x)}{p_{i0}} dx, \quad (4.4)$$

where β_{i0} is the ion toroidal beta computed at the centre, $x = r/r_1$ is the minor radius normalised by the radial position of the $q = 1$ surface and p_i and p_{i0} are the ion pressure and its central value, respectively. Taking into account the trapped ion effect, the internal kink potential energy and Eq. 4.3 can be rewritten as

$$- \delta\hat{W}_{core} = -\delta\hat{W}_{MHD} - \delta\hat{W}_{KO} > 0.5\omega_{*,i}\tau_A. \quad (4.5)$$

In tokamak plasmas, auxiliary heating such as ICRH and NBI can generate fast particles in the plasma. In addition, there will be fast energetic α -particles in ITER plasmas. The fast particles have a stabilising influence on the internal kink which results from the conservation of the third adiabatic invariant Φ , corresponding to the magnetic flux through the precessional drift orbits of the fast trapped ion [Porcelli:PPCF1991, VanDam:PoF1982, Porcelli:PPCF1996]. The constraint of conservation of Φ becomes relevant when the trapped orbit of the fast particles is completed many times within the internal kink mode growth timescale γ^{-1} [Angioni:Thesis]. In other words, the frequency

of the bounce motion of the fast trapped particles is much higher than the growth rate. The frequency is defined as the bounce-averaged toroidal precessional drift frequency of fast trapped particle, ω_{Dh} , which is usually larger than the ion diamagnetic frequency ω_{*i} [Porcelli:PPCF1996]. In this case, the threshold of internal kink mode stability is further modified taking into account the fast particle effect and can be rewritten as

$$-\delta\hat{W}_{core} > c_h\omega_{Dh}\tau_A, \quad (4.6)$$

where c_h is a correction factor of order unity. As well as the influence on the instability threshold, the fast trapped particle has a contribution to the internal kink potential energy itself. The fast particle term $\delta\hat{W}_{fast}$ is negative and negligibly small when the inequality Eq. 4.6 is satisfied while the term is positive and cannot be neglected when the internal kink is stable [Porcelli:PPCF1996]. The $\delta\hat{W}_{fast}$ term is defined in Ref. [Porcelli:PPCF1996] in the following form

$$\delta\hat{W}_{fast} = -c_f \frac{\epsilon_1^{3/2} 2\mu_0}{s_1 B_{p1}^2} \int_0^1 x^{3/2} \frac{dp_f}{dx} dx. \quad (4.7)$$

There is a numerical factor c_f which is of order unity and only the fast particle pressure p_f is considered. With the $\delta\hat{W}_{fast}$ term, the internal kink potential energy and the stability condition are modified as

$$-\delta\hat{W} = -\delta\hat{W}_{MHD} - \delta\hat{W}_{KO} - \delta\hat{W}_{fast} > 0.5\omega_{*i}\tau_A. \quad (4.8)$$

Therefore, the internal kink mode is ideally stable if both the inequality Eqs. 4.6 and 4.8 are not satisfied. However, when the potential energy $\delta\hat{W}$ is close to zero, the dynamics and the growth rate of the mode are determined by non-ideal effects in a narrow layer around $q = 1$ surface, where the reconnection of magnetic field lines can occur. In this layer, the plasma is no longer ideal, resistivity plays a role in the reconnection process. Thus, the nature of the internal kink mode changes from an ideal mode to a resistive mode. In particular, there is a stabilising effect of the reconnection layer when $\delta\hat{W} < \hat{\rho}$ by changing the structure of the mode to a drift-tearing mode localised near the $q = 1$ surface [Cowley:PoF1986, Migliuolo:PoFB1991]. The global resistive internal kink mode can then be destabilised under the following condition

$$-c_\rho\hat{\rho} < -\delta\hat{W} < 0.5\omega_{*i}\tau_A, \quad (4.9)$$

where $\hat{\rho} = \sqrt{\rho_i^2 + \rho_s^2}/r_1$, ρ_i is the thermal ion Larmor radius, ρ_s is the same quantity as ρ_i except calculated with the electron temperature instead of the ion temperature, and c_ρ is a numerical factor of order unity.

The growth rate of the resistive internal kink mode can be characterised by different reconnecting regimes determined by the relation between the thermal ion Larmor radius ρ_i and the resistive layer width δ_η . If δ_η is bigger than ρ_i , due to the finite resistivity, the resistive internal kink mode becomes unstable with a growth rate γ_η [Coppi:SovJPP1976];

Chapter 4. Control of sawtooth instability

whereas, when $\rho_i > \delta_\eta > d_e$ (the inertial skin depth), the growth rate of the ion-kinetic-regime γ_ρ is what is important [Pegoraro:PoFB1989]. The definition of those two growth rates are written in the following form [Porcelli:PPCF1996]

$$\gamma_\eta = s_1^{2/3} S^{-1/3} \tau_A^{-1}, \quad (4.10a)$$

$$\gamma_\rho = \left(\frac{2(1+\tau)}{\pi} \right)^{2/7} \hat{\rho}_i^{4/7} S^{-1/7} s_1^{6/7} \tau_A^{-1}, \quad (4.10b)$$

where $S = \tau_\eta/\tau_A$ is the magnetic Reynolds (Lundquist) number, with the resistive time τ_η , $\tau = T_{e1}/T_{i1}$ and $\hat{\rho}_i = \rho_i/r_1$. Furthermore, one can define the effective growth rate of resistive kink mode as $\gamma_{eff} = \max(\gamma_\eta, \gamma_\rho)$. Based on the relation of the resistive growth rate proposed in Ref. [Porcelli:PPCF1996] and its modification from Ref. [Sauter:Varenna1999], one condition for the growth of the unstable resistive internal kink mode can be defined as

$$\gamma_{eff} = \max(\gamma_\eta, \gamma_\rho) > c_r (\omega_{*,i} \omega_{*,e})^{1/2}. \quad (4.11)$$

c_r is a numerical factor and $\omega_{*,e}$ is the electron diamagnetic frequency. When both Eqs. 4.9 and 4.11 are satisfied, the resistive internal kink mode is unstable.

As seen in Eq. 4.10, growth rates of both regimes have a dependence on s_1 and hence Eq. 4.10 with Eq. 4.11 can be rewritten as equations for a critical value of s_1 in the following form:

$$s_{1,crit,\eta} = c_r^{3/2} (\omega_{*,i} \omega_{*,e})^{3/4} S_1^{1/2} \tau_A^{3/2}, \quad (4.12a)$$

$$s_{1,crit,\rho} = c_r^{7/6} (\omega_{*,i} \omega_{*,e})^{7/12} \left(\frac{2(1+\tau)}{\pi} \right)^{-1/3} \hat{\rho}_i^{-2/3} S_1^{1/6} \tau_A^{7/6}, \quad (4.12b)$$

and the growth rate condition can also be modified as

$$s_1 > \min(s_{1,crit,\eta}, s_{1,crit,\rho}). \quad (4.13)$$

All together, the criteria for the triggering of a sawtooth crash can be specified by Eqs. 4.6, 4.8, 4.9 and 4.13, summarised below:

$$\begin{aligned} -\delta \hat{W}_{core} &> c_h \omega_{Dh} \tau_A, \\ -\delta \hat{W} &> 0.5 \omega_{*,i} \tau_A, \\ -c_\rho \hat{\rho} &< -\delta \hat{W} < 0.5 \omega_{*,i} \tau_A \quad \text{and} \quad s_1 > s_{1,crit}. \end{aligned} \quad (4.14)$$

The values of the free parameters c_h , c_ρ , c_f (inside $\delta \hat{W}_{fast}$) and c_r (inside $s_{1,crit}$) will determine at which level the internal kink becomes unstable. If one of these condition is satisfied, a sawtooth crash occurs and in the following sawtooth modelling, the triggering of a sawtooth crash is determined by these criteria. Note that other effects like rotation

[Chapman:NF2010b] and passing fast particles [Graves:PRL2004] have not been taken into account in the above expressions. These effects are implicitly included in the free parameters.

4.2.2 Modification of profiles after sawtooth crash

The sawtooth crash is assumed as an instantaneous event which is much faster than the relevant transport time scale. Therefore, in the simulation, the reconnection process is not considered in detail; instead, it is assumed that all the relevant profiles are changed to the post-crash profiles in one time step. The relaxed profiles after the sawtooth crash can be evaluated based on the Kadomtsev complete reconnection model [Kadomtsev:SovJPP1975] that will be discussed in the following section. However, the *complete* reconnection model is not always consistent with the experimental results. Hence, a modified Kadomtsev model was introduced in Ref. [Porcelli:PPCF1996] that is called a *incomplete* reconnection model. A brief description of this model follows that of the Kadomtsev model.

Kadomtsev complete reconnection model

According to the Kadomtsev model, after the sawtooth crash the profiles over the entire plasma volume bounded by the mixing radius r_{mix} (the boundary of reconnection, see Fig. 4.2) are modified. The relaxed q profile equals unity at the centre and is larger than unity elsewhere. The Kadomtsev model is based on two assumptions. The first is that magnetic surfaces of equal helical flux ψ^* reconnect. The helical flux is defined for a circular plasma cross-section and a cylindrical approximation as,

$$\psi^*(r) = \int_0^r B_p (1 - q) dr. \quad (4.15)$$

Since the amplitude of ψ^* is not important, ψ^* can be replaced by a normalised value as

$$\psi^*(r^2) = \int_0^{r^2} (q^{-1} - 1) dr^2. \quad (4.16)$$

In addition, if the minor radius is defined as the effective minor radius ρ , using the definition of $q = d\phi/d\psi$ and the relation between the toroidal magnetic flux ϕ and the minor radius, $\phi \propto \rho^2$, Eq. 4.16 can be redefined as $\psi^*(\phi) = (\psi - \psi_0) - (\phi - \phi_0)$. Since the sign of I_P and the magnetic fluxes ϕ and ψ are dependant on the definition of the magnetic coordinates of each tokamak, one must ensure that the q profile has a positive value in the calculation of ψ^* . According to Ref. [Sauter:CPC2013], one can define the q profile taking into account the sign of I_P , B_0 and B_P as well as the definition of ψ (with or without 2π). The conventional q profile can be written as

$$q = \frac{\sigma_{I_P} \sigma_{B_0} \sigma_{B_P} d\phi}{2\pi(1 - \epsilon_{B_P}) d\psi} \quad (4.17)$$

where σ_{I_P} , σ_{B_0} , σ_{B_P} indicate the sign of I_P , B_0 and B_P , respectively, each taking on

the value of 1 or -1. e_{B_p} is a correcting factor for the definition of ψ , having the value of either zero or unity. In this way, one can be sure to have positive q and ψ^* profiles.

An example of the pre crash helical flux ψ^* profile evaluated from a monotonic q profile is shown in Fig. 4.2 (blue). The ψ^* has a positive radial gradient when q is lower than unity and has a maximum value at the $q = 1$ surface. In the region where the q value is greater than unity ψ^* has a negative gradient. Therefore there are two surfaces, at r_1 and r_2 , having equal ψ^* values. These lie between $r = 0$ and r_{mix} (where $\psi^*(r_{mix}) = \psi^*(0)$). The surfaces of equal ψ^* (black dashed line) reconnect.

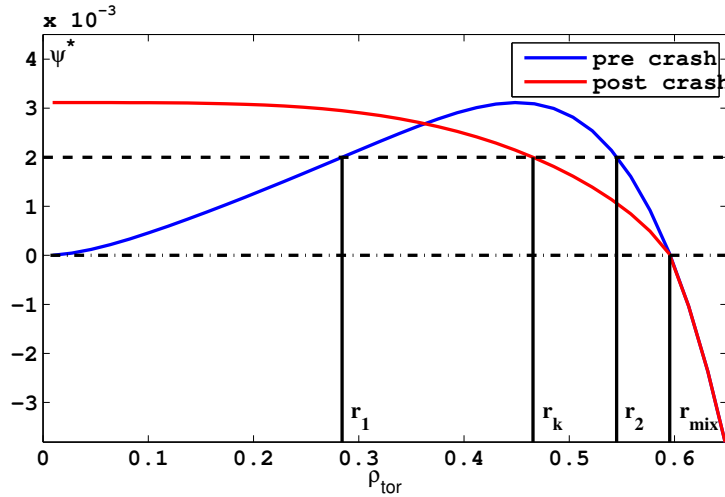


Figure 4.2: The helical magnetic flux ψ^* (blue) is obtained by monotonic q profile. Within r_{mix} , two magnetic surfaces, for instance r_1 and r_2 , which have same value of ψ^* , reconnect in a magnetic surface of radius r_k . Once r_k is identified, the reconnected ψ^* profile (red) after a sawtooth crash is determined.

The model also assumes that the toroidal flux ϕ is conserved during reconnection. The conservation of ϕ corresponds to the conservation of the area between the reconnected surfaces. From the first assumption, one can choose two reconnecting surfaces which are indicated as r_1 and r_2 in Fig. 4.2. After reconnecting, the reconnected magnetic surface has the same ψ^* as that of the two initial surfaces (r_1 and r_2) and has the radius of $r_k = \sqrt{r_2^2 - r_1^2}$ in the circular plasma approximation. In this way, the new radial grid r_k is identified and the resultant post-crash profile is determined, as shown by the red line in Fig. 4.2. Using this post-crash profile ψ^* and the grid r_k , the post-crash profiles of other quantities can be evaluated. The resultant post-crash profiles of q , j , T_e and n_e are plotted in Fig. 4.3. The profiles before a crash are indicated in blue while the post-crash profiles are in red. The q profile is directly evaluated using Eq. 4.16 or can be computed using the post-crash ψ profile:

$$q_{post} = \frac{1}{\left(1 + \frac{d\psi_{post}^*}{dr^2}\right)} = \frac{1}{\frac{d\psi_{post}^*}{d\phi}}. \quad (4.18)$$

The ϕ profile is assumed to remain constant during the reconnection process, thus the

post-crash ψ profile can be evaluated as $\psi_{post} = \psi_{post}^* + \phi$. Inside r_{mix} , the post-crash q profile is almost flat and the values are close to, or slightly larger than, unity. While outside r_{mix} , the profiles before and after a crash are the same. The current density profile is calculated in ASTRA using the new q profile and the equilibrium. Due to the jump in the q profile, there is a narrow current sheet in the post-crash j profile near r_{mix} . The modification of density and temperature profiles can be obtained from the conservation of particles and energy inside each reconnecting layer during the reconnection as described below:

$$\int_{r_1^2}^{r_2^2} n_{pre} dr^2 = \int_0^{r_k^2} n_{post} dr^2, \quad (4.19)$$

$$\int_{r_1^2}^{r_2^2} n_{pre} T_{pre} dr^2 = \int_0^{r_k^2} n_{post} T_{post} dr^2.$$

These can be used for both ions and electrons in the circular flux surface approximation. The total number of particles and the total energy between the reconnecting surfaces r_1 and r_2 are conserved after a crash and therefore equivalent to those inside of r_k . The shape of the modified profiles inside r_{mix} is almost flat but depends on the shape of the pre-crash profiles.

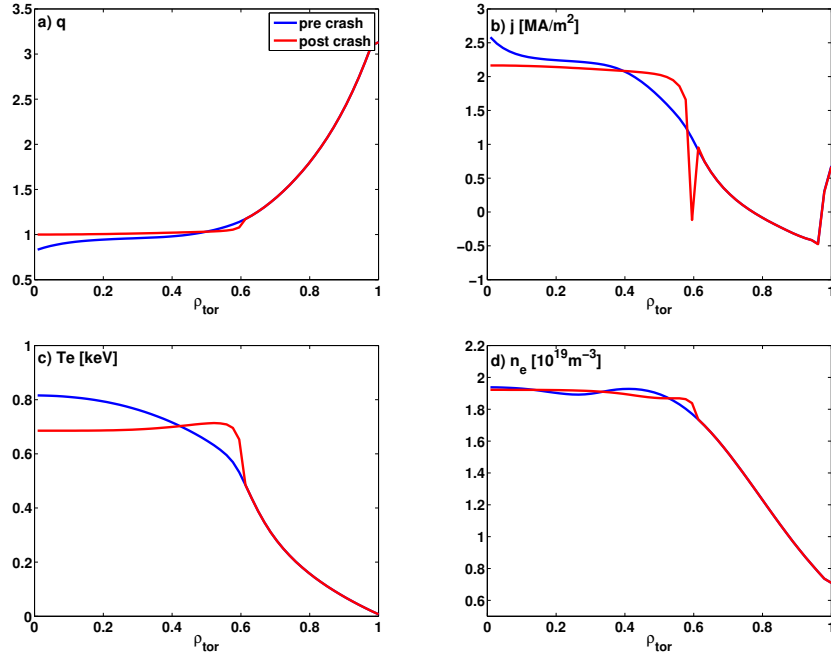


Figure 4.3: (a) q (b) j (c) T_e (d) n_e profiles before (blue) and after (red) a sawtooth crash are presented. Inside r_{mix} all the profiles are modified and have almost flat profiles. As assumed, the crash does not affect profiles outside r_{mix} thus there is no modification of the profile in that region.

Modification of the q profile

In order to describe the modification of profiles based on the Kadomtsev model, a monotonic q profile is required; with the monotonic q profile, the helical flux ψ^* is evaluated and the new radial grid r_k is identified. However, in many cases, the q profile can be non-monotonic and can have multiple $q = 1$ surfaces (in particular with slightly off-axis EC heating). In such cases, the reconnected radial grid cannot be evaluated in the same way as for Kadomtsev full reconnection. An alternative way, taking into account the multiple $q = 1$ surfaces to compute a new radial grid and a post-crash ψ^* profile, has been introduced in Ref. [Witvoet:NF2011b]. In our work, a simpler way is taken, as shown in Fig. 4.4. When there are multiple $q = 1$ surfaces, the outermost $q = 1$ surface is considered. If one of the sawtooth crash criteria is satisfied at this location and there are multiple $q = 1$ surfaces, the q profile is modified such that $q = \min(q, 0.998)$ inside this $q = 1$ outermost surface before evaluating ψ^* and the reconnection transformation. An example is shown in Fig. 4.4(b). In this way ψ^* is strictly increasing up to $q = 1$ and the standard procedure can be applied (if $q < 1$ inside $q = 1$). Note that the pre- and post-crash ψ^* profiles using the q modification are very similar to those presented in Ref. [Witvoet:NF2011b] Fig. 3(c).

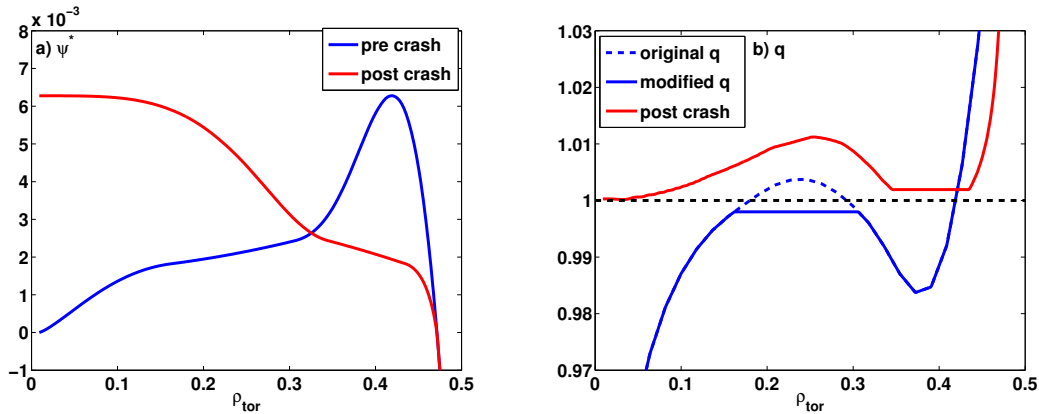


Figure 4.4: When one of sawtooth criteria is satisfied, if there are multiple $q = 1$ surfaces, q profile in (b) is modified from blue dashed one to solid one to ensure only one $q = 1$ surface. Using the modified q profile, (a) evaluated ψ^* has positive gradient inside $q = 1$ surface and therefore the new radial grid and ψ^* profile after reconnection are well defined.

Incomplete reconnection model

As mentioned, the Kadomtsev model is not always consistent with experimental observations. In particular, several experiments such as in Ref. [Chapman:PRL2010] have shown that the central q value is still below unity after a sawtooth crash. In order to model this type of experimental result, a heuristic model called the incomplete reconnection model has been introduced in Ref. [Porcelli:PPCF1996]. In this model, it is assumed that there is a reconnection only between two magnetic surfaces r_1 and r_2 where ψ^* values are equal ($\psi^*(r_1) = \psi^*(r_2)$). Those two surfaces can be defined as $(r_2 - r_1) / r_{\text{mix}} = w_{\text{norm}}$. w_{norm} is an island width normalised by r_{mix} and it can vary from zero (no island) to

4.3. Control of sawtooth period using localised EC injection

unity (full reconnection; $r_1 = 0$, $r_2 = r_{mix}$). w_{norm} is a free parameter so that w_{norm} value determines the position of reconnecting layers and the width of magnetic island. The relaxed profiles can be evaluated in two regions; the island region and the inner core region. Inside the island ($r_1 < r < r_2$), all the reconnected surfaces have the same ψ^* values, $\psi^*(r_1)$, which implies that $q = 1$ in this interval. On the other hand, the inner core region (inside r_1) is governed by a Taylor relaxation process [Gimblett:PPCF1994], which results in a parabolic post-crash ψ^* between $r = 0$ and r_1 . The corresponding q value $q_{0,post}$ is constant and less than unity for $0 \leq r \leq r_1$ and is defined in the following form

$$q_{0,post} = \frac{r_1^4}{4} \bigg/ \int_0^{r_1} \frac{r^3 dr}{q}. \quad (4.20)$$

Both profiles of ψ^* and q for pre- and post-crash cases are shown in Fig. 4.5. $w_{norm} = 0.5$ is applied for the island size. As discussed, ψ^* has parabolic shape inside r_1 while ψ^* is constant in the island region. The corresponding q value in the inner region ($\rho_{tor} < r_1$) is flat and below unity, while it is kept as unity between r_1 and r_2 . Due to the discontinuity in the q values, the shape of the post-crash current density has dips reflecting current sheets. Since the transport of density and temperature across the reconnected region is very fast, it is assumed that the post-crash profiles of density and temperature become flat inside r_2 resulting from the particle and energy conservation [Porcelli:PPCF1996].

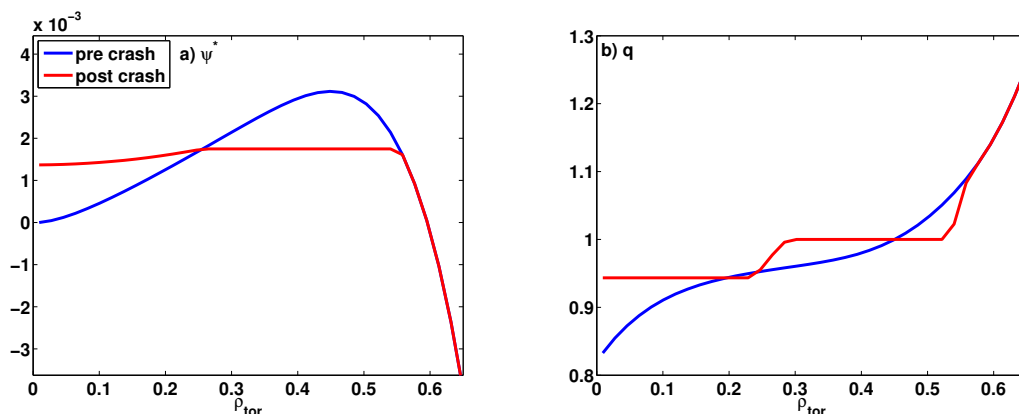


Figure 4.5: (a) Helical magnetic flux ψ^* and (b) q profiles before (blue) and after (red) a sawtooth crash based on the incomplete reconnection process. In inner core region, due to the shape of ψ^* , corresponding q becomes flat and the constant value is below unity after a crash while flat ψ^* results in $q = 1$ across the island region.

4.3 Control of sawtooth period using localised EC injection

4.3.1 Effect of EC beam on shear evolution

It has been long known that EC injection affects the behaviour of the sawtooth instability. The EC beam influences the evolution of shear at $q = 1$ surface s_1 and sawtooth period is determined in accordance with the third criterion of sawtooth triggering. The change

of s_1 evolution and resultant sawtooth period depend on the EC deposition position [Angioni:NF2003] relative to $\rho_{q=1}$. When EC beam is located inside $q = 1$ surface, the evolution of s_1 is fast and s_1 exceeds the critical value early. As a result, the sawtooth period becomes short compared to the ohmic case. On the other hand, when the EC beam aims near, or just outside, the $q = 1$ surface, a longer sawtooth period results from the slow evolution of s_1 . In addition, it has been demonstrated that a narrower beam width brings longer sawtooth period and the most stabilising position is closer to $q = 1$ surface compared to wider beam width [Angioni:NF2003]. The sawtooth period can also be altered depending on the amount and direction of current drive [Angioni:NF2003]. When the current is driven in the same direction as I_P (co-ECCD), the maximum sawtooth period is obtained with deposition just outside $q = 1$ surface while for the opposite case (counter-ECCD), the maximum stabilising position is inside the $q = 1$ surface.

The deposition position of the EC beam(s) is an important actuator to control the sawtooth period. In plasmas, the location of the $q = 1$ surface can change by a larger amount due to a change in plasma current, density or confinement. However, if we track the $q = 1$ surface to maintain a constant relative deposition location between the beam and the $q = 1$ surface, one can still obtain the desired sawtooth control. Thus, the deposition position is controlled in real-time as introduced in Ref. [Zucca:Thesis]:

$$\rho_{dep} = \rho_{q=1} + \eta w_{EC}, \quad (4.21)$$

where η is a free parameter which determines the relative position with the beam width w_{EC} . In ITER predictive simulation in Ref. [Zucca:Thesis], the maximum sawtooth period is obtained when η is close to zero, in other words, the EC beam is located very close to $q = 1$ surface with respect to w_{EC} . In addition, in Ref. [Kim:EPS2012], it is shown that under certain conditions, the sawtooth can be fully stabilised with real-time controlled EC deposition position; whereas, a sawtooth crash occurs for a fixed ρ_{dep} . This is consistent with the simulations showing that maximum stabilising effects are obtained with real-time control of the relative deposition location with a small η value [Zucca:Thesis, Kim:EPS2012].

4.3.2 Sawtooth period pacing and locking

The effect of the EC beam on the sawtooth period, discussed in the previous section, relies on changes in the deposition location relative to the $q = 1$ surface. In recent TCV experiments, a new and active way of sawtooth control using sawtooth pacing [Goodman:PRL2011] and locking [Lauret:NF2012, Witvoet:NF2011] has been demonstrated. These methods use EC power control instead of (or, eventually, in addition to) position control.

Sawtooth pacing [Goodman:PRL2011] can be used to set the sawtooth period and to know when the next sawtooth crash would occur. Sawtooth pacing is used to control the time evolution of the magnetic shear at the $q = 1$ surface, s_1 , for a preset time τ_{set} in either a stabilising or destabilising way. In Fig. 4.6(a) [Felici:Thesis], the basic idea of sawtooth pacing for sawtooth stabilisation is explained. The EC beam is deposited during τ_{set} to slow down the evolution of s_1 (red) compared to ohmic case (black). Then the EC power is turned off (or decrease power), s_1 increases faster (blue) and a sawtooth

4.3. Control of sawtooth period using localised EC injection

crash occurs soon after. When the crash is detected in real-time, the EC beam is again switched on and the cycle can be repeated. In addition, with various τ_{set} , the moment of the sawtooth crash can be controlled (Fig. 4.6(b)). The time interval between the EC-off time and the sawtooth crash event (τ_{st}) is called the time delay ($= \tau_{st} - \tau_{set}$). The pacing method is very robust, assuming a robust real-time sawtooth detector exists, since it has been shown experimentally that each sawtooth period can be independently controlled.

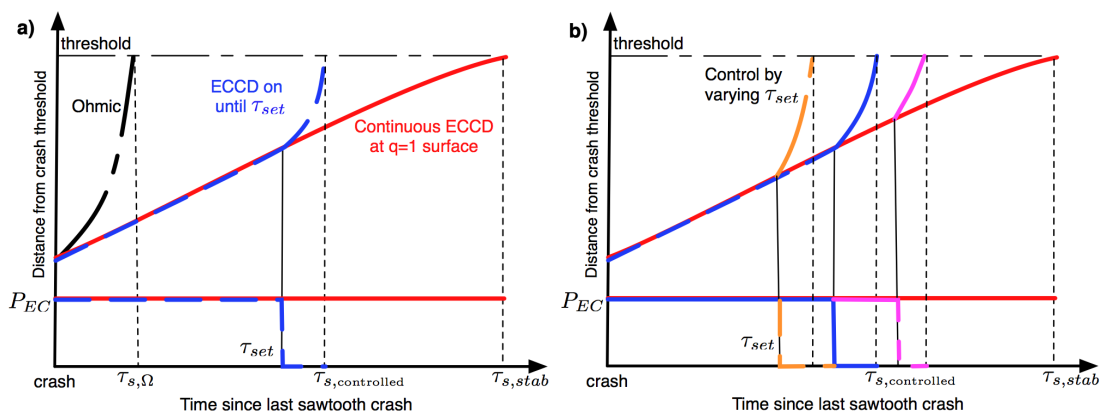


Figure 4.6: Figures from Ref. [Felici:Thesis]. Due to the stabilising EC beam, s_1 slowly evolves during EC power is on. Then after EC power is turned off, s_1 rapidly increases and reaches to the critical value to trigger a sawtooth crash. With various τ_{set} , a sawtooth period can be paced by the EC injection and the moment of a sawtooth crash can be predicted.

The locking method [Lauret:NF2012, Witvoet:NF2011] is similar to pacing but it does not require real-time feedback capabilities. The EC pulse is on during a fixed time interval and then is turned off, regardless of whether a sawtooth crash event has occurred. This sequence of EC on-off is repeated with a fixed period. The ratio of the on-time to the period is called the duty cycle (τ_{on}/τ_{set}). Note that the pre-set period τ_{set} of pacing is EC-on time but for locking it indicates the total time of EC-on plus off times. (The naming comes from the parameter that is set in the control algorithm, and for successful control is generally close to the sawtooth period.) If the period and the duty cycle are appropriate, the sawteeth lock with the pulsed EC and lead to regular sawtooth periods [Lauret:NF2012, Witvoet:NF2011]. The phase between the EC pulse and the sawtooth crash can vary with the EC power, period and duty cycle, leading to a variable delay between the EC-turn-off time and the next sawtooth crash.

For both pacing and locking, there are delays between turning the EC power off and a sawtooth crash. These delays are important since the EC beams will be used for many purposes on ITER; for example, to reach H-mode, profile peaking control, impurity control, sawtooth control, NTM control and disruption control. Therefore the topic of actuator sharing is crucial for ITER and it is important to analyse which tasks can be performed by the same actuators. In this case, if the time delay mentioned above is sufficient, the same beam can be used to control the sawtooth and then to aim at $q = 3/2$ or 2 to preempt or stabilise an NTM that would be triggered by the sawtooth crash. On ITER, a few seconds of time delay is anticipated (as shown in Sec. 4.7.3) and can be sufficient for both sawtooth and NTM controls.

4.4 Control of sawtooth period on TCV

Sawtooth period control experiments using sawtooth pacing and locking have been carried out on TCV. Based on those experiments, modelling of sawtooth pacing and locking has been tested and reproduces the experimental results. Furthermore, the modelling has provided insight into the details of sawtooth pacing and locking experiments, providing better understanding.

4.4.1 Experimental demonstration

For demonstrating the capability of sawtooth pacing and locking for sawtooth period control, a series of experiments were performed on TCV. Among these experiments, one case of sawtooth pacing and another case of locking have been chosen for simulation; the results will be discussed in this section. Further detailed discussion about sawtooth pacing and locking experiments can be found in Refs. [Felici:Thesis, Goodman:PRL2011, Laurent:NF2012].

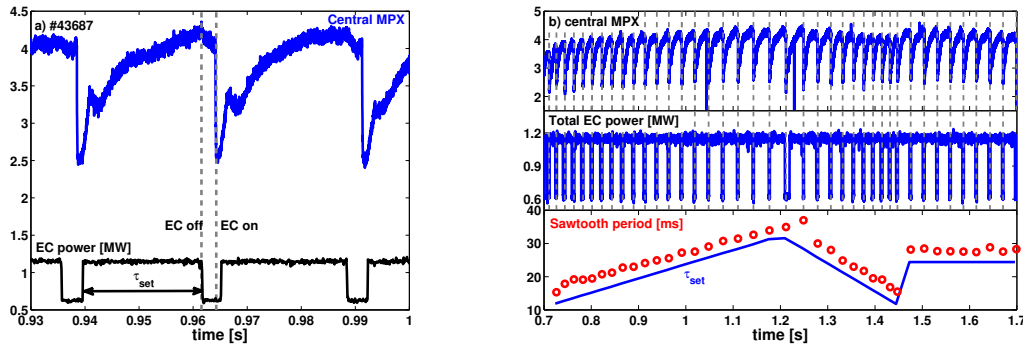


Figure 4.7: (a) During τ_{set} , EC beam (black) has the maximum power and then the power decreases. Once a crash occurs EC power recovers its maximum level. (b) This process is repeated for each crash with the given τ_{set} and the sawtooth period is well paced by EC modulation.

For sawtooth pacing, TCV discharge #43687 is chosen and the experimental result is shown in Fig. 4.7. In this experiment, the maximum sawtooth period is about 40ms with total absorbed EC power of 1.0MW from 3 gyrotrons at a fixed stabilising position. During pacing, one gyrotron is modulated by real-time command thus the minimum power becomes about 0.5MW during pacing and the decrease of EC power results in a sawtooth period of about 10ms. In Fig. 4.7(a), a detailed view of the central MPX data and EC pulse are plotted. During the pre-set time τ_{set} , all EC beams are on and sawtooth is stabilised. Then one gyrotron is turned off. After the EC power decreases, a sawtooth crash is detected and the modulated EC beam is switched on. (Note that there can be a small delay between the moment of crash and the EC power is increased, due mostly to the rise time of the gyrotron current.) Pacing pulses are repeated during the entire discharge and in Fig. 4.7(b) the central MPX (top panel), modulated EC power (middle) and resultant sawtooth period (bottom, red circles) with τ_{set} (bottom, blue line) are shown. The grey dashed lines indicate the moments of sawtooth crashes. The crash timing and the EC power increase are well aligned. With almost constant delay, the

resultant sawtooth periods (red circle) are well paced by EC modulation while varying τ_{set} .

Similarly, the experimental result of TCV discharge #43686 for sawtooth locking is shown in Fig. 4.8. The experimental set-up is the same as in the pacing case; except, for locking, the modulation period τ_{set} and duty cycle are defined prior to the discharge. Both τ_{set} and duty cycle vary during the discharge to maintain the appropriate conditions for successful sawtooth locking found from previous locking experiments. In Fig. 4.8(a), a detailed view of the central MPX data and EC pulse are plotted. With varying τ_{set} and duty cycle, the time spent at maximum EC power is altered. The sawtooth crash occurs while EC power is off and the period is regulated following EC modulation. The locking result is shown in Fig. 4.8(b). Even without real-time control of the EC power with respect to the sawtooth crash, the moment of crash and EC power modulation are well aligned. All sawtooth periods show a good agreement with the given τ_{set} (i.e. period). The duty cycle is shown in the bottom panel. Note that for locking, τ_{set} is different from that of pacing and indicates the whole period; sum of both EC on and off time which are determined by the duty cycle.

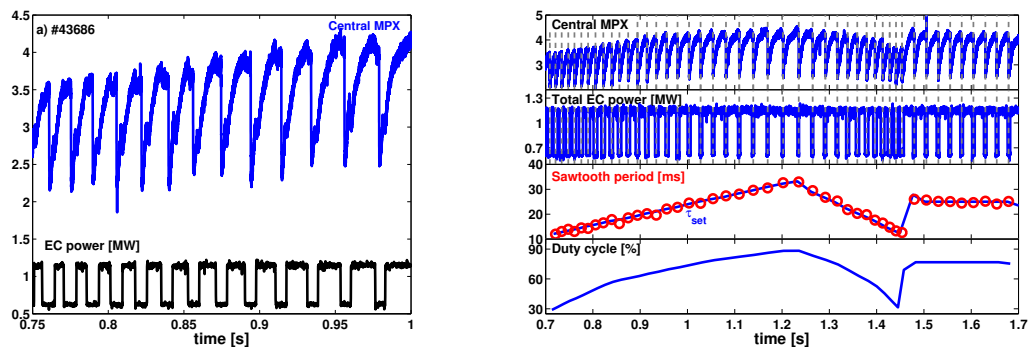


Figure 4.8: (a) EC power is modulated depending on given τ_{set} and duty cycle. (b) τ_{set} and duty cycle vary to provide an appropriate set for successful locking and resultant sawtooth periods lock to EC modulation.

4.4.2 Simulation of sawtooth pacing and locking

For sawtooth pacing and locking simulations, we have taken the experimental data from the discharge #43687 (pacing case). Since discharges #43687 and #43686 are equivalent, with the exception of the way in which sawtooth control is managed, only one discharge data set for the plasma parameters has been used for the simulation. Modelling of the sawtooth instability requires calculation of the time-evolution of the pressure and current profiles and permits the sawtooth period to be determined. We use the ASTRA code [Pereverzev:2002] for the transport evolution using the χ_e model introduced in the previous chapter. In addition, a standard sawtooth model for sawtooth crash triggering and complete reconnection described in Sec. 4.2 is taken for simulating the sawtooth events. The maximum and the minimum sawtooth periods of about 46 and 10ms are obtained adjusting the free parameters in the sawtooth trigger criteria. Note that sawtooth crashes are mostly triggered by the third criterion, in particular the shear condition, in TCV so

that the only free parameter which determines the sawtooth period is c_r . Note also that this value is determined by matching the ohmic sawtooth period; after that (keeping the ohmic c_r) both the maximum and the minimum periods of 46 and 10ms are obtained for the maximum and minimum power levels 1.0 and 0.5MW, respectively, used in the experiment.

Sawtooth pacing simulation

As seen in Fig. 4.7, during the discharge #43687, τ_{set} continuously varies between 10 to 30ms. In the simulation, τ_{set} values between 10 to 40ms in steps of 5ms are chosen for sawtooth period pacing. Figure. 4.9(a) shows the simulation result of sawtooth period (blue) and τ_{set} (red). Sawtooth periods for each τ_{set} are almost constant which means that sawtooth period is well paced by EC modulation with constant delay. The delay from simulation is compared to experimental measurements in Fig. 4.9(b). For the $\tau_{set} = 10$ ms case simulations result in longer delays, but overall simulations and experiments yield similar values.

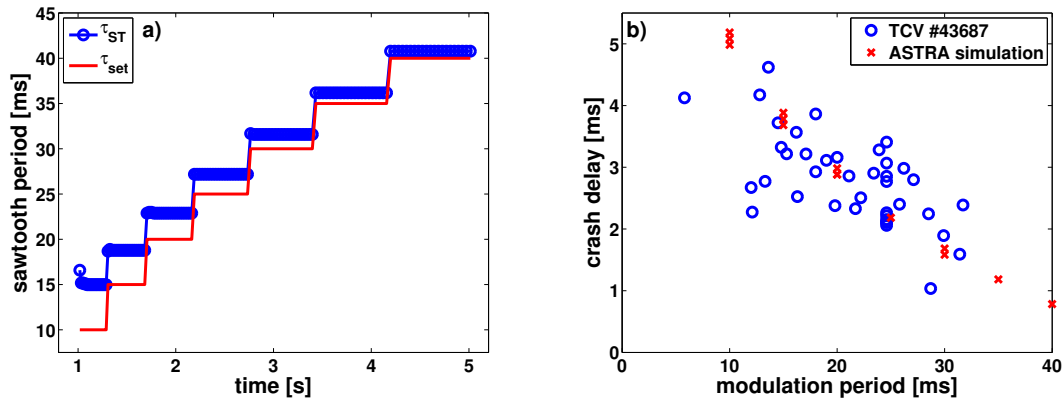


Figure 4.9: (a) Sawtooth period (blue) and τ_{set} (red) from sawtooth pacing simulation. With almost constant delay, sawteeth are well paced by EC modulation. (b) The delay is compared to experimental one. Those two results are consistent in the value and both delay decrease while τ_{set} increases.

As seen in Fig. 4.9, the delay decreases with the increase of τ_{set} . This tendency can be explained by investigating the evolution of shear at $q = 1$ surface s_1 . Figure 4.10 represents the evolution of s_1 (solid line with circle) and $s_{1,crit}$ (dashed dotted line) for each τ_{set} (including continuous heating case) during a sawtooth cycle. For Fig. 4.10(a), the abscissa is time measured from the moment of the preceding sawtooth crash. A pair of coloured, vertical, solid lines indicate the time when EC power decreases and when the sawtooth crash occurs. As expected, s_1 rapidly increases when the EC power decreases; $s_{1,crit}$ has a jump at the same time.

As seen in Fig. 4.6, generally $s = 1$ increases with time and, depending on the τ_{set} , the difference between s_1 and $s_{1,crit}$ values at the EC off time is determined; larger for shorter τ_{set} and vice versa. However, in each case, due to the current drive, the shape of shear evolution is different; thus, the main effect on the delay is not the difference between s_1

and $s_{1,crit}$ values. The evolution itself is faster, once the EC turns off, for the long τ_{set} case and the detailed view of the increasing part is shown in Fig. 4.10(b). In this figure, only the increasing part after the EC power is off is taken to compare each case and s_1 is normalised as $s_{1,normalised} = (s_1 - s_{1,min}) / (s_{1,crash} - s_{1,min})$ (here, the $s_{1,min}$ refers to the dip seen later in the evolution - not the value at $(t - t_{crash}) = 0$). For the shorter τ_{set} case, the normalised slope of s_1 evolution is smaller, whereas it is larger for the longer τ_{set} case. The difference of the growth rate after EC power down is the main reason for the difference in the delay. The detailed discussion will follow.

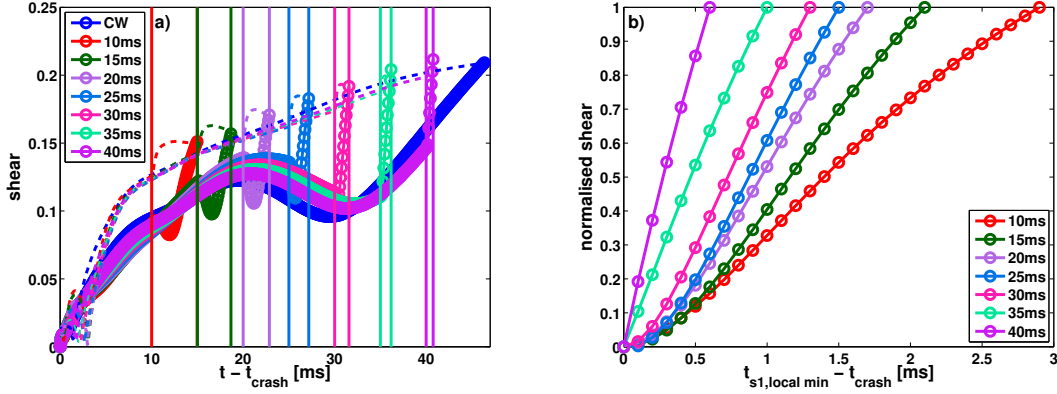


Figure 4.10: (a) s_1 slowly evolves with EC injection and the evolution of s_1 becomes rapid when EC power level decreases. (b) Depending on the different shear evolution rate after EC power is turned down, the time delay is determined.

For short τ_{set} cases, s_1 first decreases when EC power is turned down; but, s_1 increases immediately for τ_{set} longer than 30ms. This difference results from the shape of shear profile. In Fig. 4.11, the evolution of s_1 and $s_{1,crit}$ for the $\tau_{set} = 15$ ms case is shown. The q , shear and current density profiles are shown for chosen time points, indicated by the vertical lines. Due to the off-axis ECCD, j has a local maximum that induces a minimum value in the shear profile; thus, as the position of $q = 1$ surface increases, s_1 crosses its minimum value. For the τ_{set} of 10 to 25ms cases, at the time when the EC power is turned down, the $q = 1$ surface is still evolving and located inside the minimum shear position so that s_1 first decreases then increases. While for longer τ_{set} case, the $q = 1$ surface has already passed this minimum position thus s_1 can directly increase when the EC power is decreased. In addition, as seen in profiles, when the EC power level decreases, the localised j is reduced and as a result, the local minimum of the shear profile disappears. This change in the shear profile causes s_1 to quickly stop decreasing and begin to increase. Therefore, the combined effects (the position of $q = 1$ surface and shear profile evolution) result in the different evolution after EC power down and the delay until the crash; longer for shorter τ_{set} and shorter for longer τ_{set} .

The simulation using an ad-hoc transport model and a standard sawtooth model reproduces sawtooth pacing experimental results well. In simulations, details of the shear evolution can be investigated and the effect of EC beam on the evolution of s_1 is clearly observed. Using the same conditions, a sawtooth locking simulation is now described.

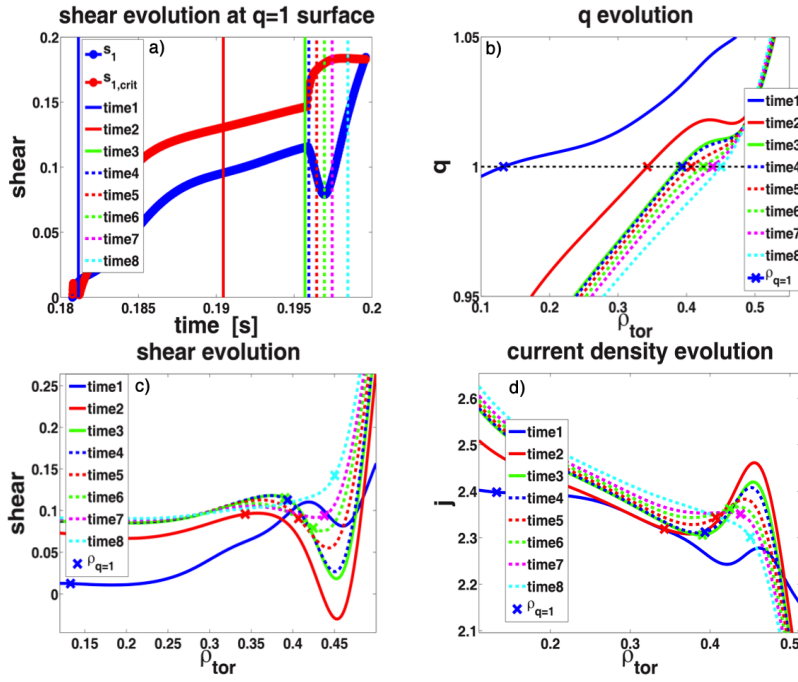


Figure 4.11: (a) The evolution of s_1 and $s_{1,crit}$ for $\tau_{set} = 15\text{ms}$ case. Solid lines are the time points before EC power down while dashed lines indicate the time points after EC power decreases. (b) q , (c) shear, (d) j profiles for each time points are shown. Due to j profile, there is a local minimum in shear profile and it causes the initial drop of s_1 after EC power decreases. The localised current is reduced when EC power down and as a result the minimum value of shear increases. Due to this change in the profile, s_1 does not decrease until its initial minimum level (red solid) and increase again until it reaches the critical value.

Sawtooth locking simulation

For the sawtooth locking simulation, the EC modulation period τ_{set} is changed from 10 to 35ms with 5ms step-increases. For each τ_{set} , duty cycles of 10 to 100% are considered. Recall that for sawtooth locking τ_{set} is the period, so 100% duty-cycle means continuous wave (CW) EC injection. Figure 4.12 gives an example of locking simulation results. In Fig. 4.12(a), the sawtooth period (blue circle) with τ_{set} (red solid line) is plotted in the top panel and the duty cycle is shown in the bottom panel. Sawteeth lock to the EC modulation and the resultant period is equal to τ_{set} of 10ms for duty cycles between 30 to 70%. With duty cycles of 80 and 90%, the sawtooth periods are 20 and 30ms (the 2nd and 3rd harmonics of the EC modulation period). The evolution of s_1 for the 80% duty cycle case is shown in Fig. 4.12(b). At 8ms, due to the change in EC power, the evolutions of s_1 and $s_{1,crit}$ are modified; however, before s_1 reaches to $s_{1,crit}$, the EC power is again increased so s_1 evolves with a low growth rate. At the second EC power decrease phase starting at 18ms, since s_1 value is already large and close to $s_{1,crit}$, the concomitant rapid growth of s_1 brings about a sawtooth crash just as the power is increased again, with period of 20ms. The same phenomenon also occurs for 90% duty cycle and a sawtooth period of 30ms is obtained.

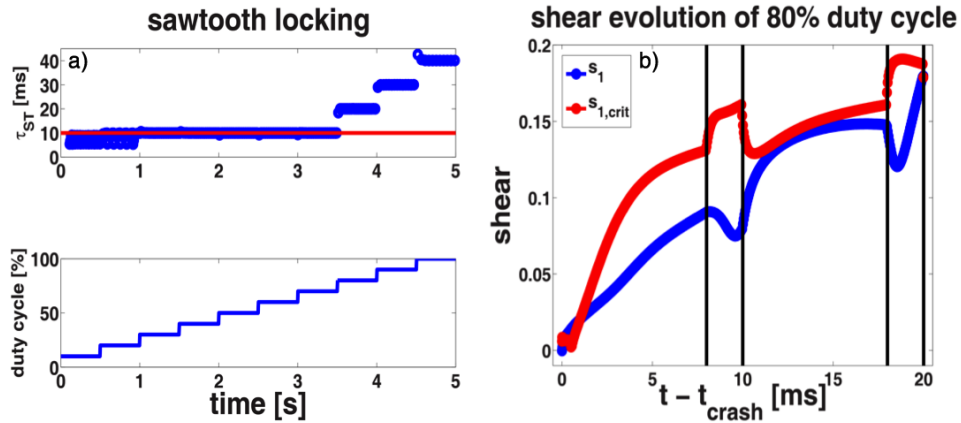


Figure 4.12: (a) Sawtooth periods lock to EC modulation period of 10ms with duty cycle of 30~70%. For 80 and 90% duty cycle case, the harmonics of EC modulation period are observed. (b) s_1 does not evolve close enough to $s_{1,crit}$ during the first 10ms for duty cycle of 80%. s_1 continues evolving and is close to $s_{1,crit}$ when EC power is down in second time. During EC power down phase, s_1 rapidly increases and reaches to $s_{1,crit}$ to trigger a sawtooth crash with period of 20ms.

The simulation is repeated in the same way for different τ_{set} values. From the scan of τ_{set} and duty cycle, one can characterise the locking range as shown in Fig. 4.13(a). Successful locking cases are indicated as blue circles, while red crosses represent cases for which sawteeth do not lock to the desired EC modulation period. Blue crosses denote cases where locking to harmonics of τ_{set} are found. The pacing results are also included and indicated by black circles. The locking range and pacing results from the experiment is also shown in Fig. 4.13(b). The two locking ranges, from simulation and experiment, show similar area of successful locking range. The range in the experiment is slightly wider and covers the mid-range of both τ_{set} and duty cycle. Nevertheless, both pacing and locking can be simulated and used for the prediction of the sawtooth responses to localised power

deposition for different plasmas and different tokamaks, since these simulations have been performed with our predictive χ_e model. Based solely on TCV experimental results, we may suppose that the simulation results provide a conservative prediction of the locking range.

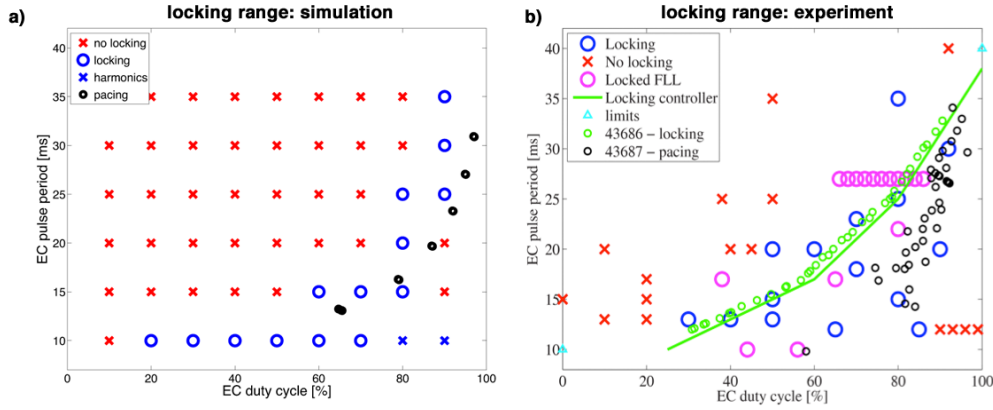


Figure 4.13: (a) From the scan of τ_{set} with various duty cycle, a locking range can be obtained for locking (blue circle), non-locking (red cross), harmonics (blue cross) and pacing (black circle) cases. The locking range from simulation is similar to experimental result in (b).

4.5 Sawtooth period control experiment on KSTAR

During the 2011-2012 KSTAR experiment campaign, it has been observed that the different sawtooth period behaviours result from various ECH injection conditions [Bae:FST2014]. As witnessed in TCV experiment, depending on the deposition position of the EC beam, the sawtooth period is shortened (on-axis) or lengthened (off-axis) in NBI-heated plasmas (e.g. KSTAR discharges #7070, #7072). In addition, as expected, the sawtooth period depends on the direction of the driven current (co-ECCD, counter-ECCD, ECH only).

Based on these experiments and successful TCV results, sawtooth control experiments have been extended on KSTAR during the 2013 campaign to include active sawtooth period control by means of sawtooth locking [JeongJH:EC2014]. Periodic pulses of EC power were deposited near the $q = 1$ surface. In the following sections the experimental results of sawtooth locking experiments will be described. Note that since KSTAR real-time control system was not available for sawtooth pacing in the 2013 campaign, only sawtooth locking has been attempted.

4.5.1 Experimental set up

In the KSTAR experimental series, the value I_P at the flat top is fixed to 0.7MA and the line averaged electron density is kept between 2.0 and $3.0 \times 10^{19} \text{m}^{-3}$. The toroidal magnetic field B_ϕ is 2.9T and q_{95} is about 5.5. The plasmas are heated by 0.9MW of NBH from 0.5 to 8s. The 170GHz second harmonic EC wave with nominal power of 0.8MW is used as the main actuator. The actual absorbed power depends on the absorption rate. The launcher is installed at the equatorial plane and using a steering mirror the

EC beam can sweep across the plasma minor radius. For the locking experiment, the gyrotron power is modulated (on and off) relatively quickly with a period in the same order of magnitude as the sawtooth period τ_{ST} .

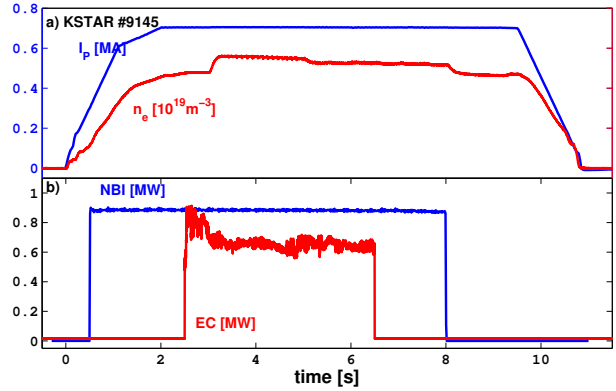


Figure 4.14: I_p ramps up to 0.7MA and line averaged electron density is about $2.0\sim 3.0\times 10^{19}\text{m}^{-3}$. NBI power of 0.9MW heats the plasma from 0.5s and EC powers is added from 2.5~3.0s. The EC power is between 0.6 and 0.8MW depending on the absorption rate.

4.5.2 Results of sawtooth locking experiments

Sweeping of EC beam to find the maximum sawtooth period

Prior to the locking experiment, a scan of the EC beam across the plasma minor radius is performed to find the optimal location of EC deposition position for maximising the τ_{ST} (discharge #9145). The EC beam is turned on at 2.5s and starts sweeping from the plasma core outward across the $q = 1$ surface. The results of this sweeping experiment are shown in Fig. 4.15. In Fig. 4.15(a), the ECE signals of electron temperature in the core and the absorbed EC power are presented. The EC-deposition position, changing in poloidal plane at the same resonance layer position with $B_\phi = 2.9$ T and $I_p = 0.7$ MA, and the τ_{ST} which results from the sweeping are shown in Fig. 4.15(b) and (c), respectively.

Before EC power is turned on, τ_{ST} is constant at about 20ms. At 2.5s, the EC beam is switched on and the poloidal scan begins from $z = 10\text{cm}$: τ_{ST} is shortened to 10ms due to the central co-ECCD injection. Until 4.5s, the EC beam stays inside the $q = 1$ surface, resulting in short sawtooth periods. There is no clear minimum in τ_{ST} , as might be expected from simulations [Angioni:NF2003]; nevertheless, the significant decrease of the period with EC injection inside $q = 1$ surface is consistent with these simulations and the experimental result from other tokamaks. From 4.5s onwards, the sawtooth period begins to grow while the EC deposition sweeps to near $q = 1$ surface; the maximum period about 100ms is obtained at 5.7s (marked by the light blue coloured region). The sawtooth crashes are clearly seen in the ECE signal and the corresponding deposition position is about $z = 26\text{cm}$ from the mid-plane. As the EC beam crosses the $q = 1$ surface, τ_{ST} quickly decreases and after EC power is turned off at 6.5s, returns to its initial ‘‘EC-free’’ value.

From this discharge, the maximum τ_{ST} is found when the EC beam is deposited at $z = 26\text{cm}$ and this position can be chosen for the fixed deposition position for maximum τ_{ST} . However, this is the beam position at the time of the crash and the beam is still sweeping during the sawtooth period, so the maximum stabilising effect without sweeping might be obtained at a slightly lower position than 26cm . Therefore, for sawtooth locking experiment, we have chosen $z = 25\text{cm}$ as the fixed deposition position.

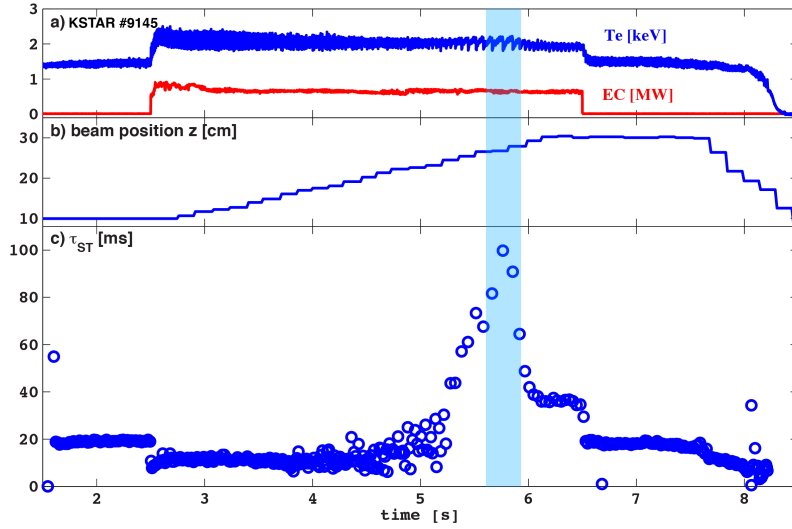


Figure 4.15: The sawtooth period according to EC deposition position across $q = 1$ surface with T_e , P_{EC} and the beam position in z . The sawtooth period decreases (destabilised) by the EC beam injection at the beginning of the sweeping from $\tau_{ST} = 20\text{ms}$ to 10ms . Then, as the EC deposition position is increased in poloidal direction, τ_{ST} increases up to maximum 100ms at the EC deposition of $z = 26\text{cm}$ from the mid-plane.

Sawtooth period control by injection locking

Subsequently, the sawtooth locking experiment is carried out by injecting modulated EC power. Due to the engineering constraints, all the settings such as modulation period, power level and duty cycle, are fixed during a discharge. In all experiments, the absorbed EC power is about $0.6\sim 0.7\text{MW}$ at the optimum position ($z = 25\text{cm}$) in the direction of I_P (co-ECCD) and the NBI power of 0.9MW is switched on at 0.5s . The reference τ_{ST} (without EC injection) is 18ms .

The first attempt at sawtooth locking (KSTAR discharge #9215) is presented in Fig. 4.16. In the top panel (a), the central electron temperature (blue) from the ECE signal and the modulated EC power (red) are shown. EC power is turned on at 3.0s and starts modulating from 5.0s . During the first 2.0s , the EC beam is continuously injected to check the τ_{ST} from the fixed deposition location. The ECE signal and EC power trace of this part are presented in detail in Fig. 4.16(b) with the corresponding τ_{ST} in the bottom panel. The τ_{ST} varies a lot during the transient phase and then saturates around 100ms , as expected for the maximum from the sweeping discharge.

4.5. Sawtooth period control experiment on KSTAR

From 5.0s, the modulation of EC beam begins. A modulation period of 43ms and duty cycle of 70% are used for sawtooth period locking. The ECE signal and the modulated EC power are shown in Fig. 4.16(c) and the resultant τ_{ST} (blue) and the modulation period (red) are presented in the bottom panel. The temperature is lower than continuous wave (CW) injection case and the crashes occur more frequently. The τ_{ST} varies between 40 and 65ms. In some cases, for instance between 7.1 and 7.4s (red coloured region), it is close to the pre-set modulation period. On the other hands, there are also several cases that τ_{ST} does not follow the modulation period, e.g. between 6.3 and 6.6s in blue coloured region. Therefore, in this case, sawteeth do not really lock to the modulation EC pulse.

One possible explanation why the behaviour of sawteeth is different is that the injected EC power is not constant at each pulse during the modulation. When the gyrotron is switched on, the EC power is low and then grows, which results in “non-square” EC pulse shape, and the power level is also different for each pulse. As a result, the integrated power per each pulse varies during the modulation and it affects the evolution of sawtooth cycle. Figure 4.16(d) allows us to see more detail of two cases, the blue and red coloured regions in Fig. 4.16(c). The first two panels show the central electron temperature between 6.3 and 6.6s and between 7.1 and 7.4s, respectively. In the bottom panel, EC power traces for both cases are presented (the colour represents each case). In this figure, the time is shifted for the second case to match the EC pulse for better comparison and the coloured dashed lines indicate the moment of sawtooth crashes for each case. For the first and second EC pulses, two cases have similar EC pulse shape (or integrated power) and the resultant τ_{ST} are also similar. Nevertheless, the phases between sawteeth and EC pulse are different. However, from the third pulse, the blue case brings larger power while the red case has similar level as previous pulse. Due to the higher power, the evolution of sawtooth is retarded and the next EC pulse also affects on the same sawtooth cycle. The effective EC power per each sawtooth crash becomes larger and a longer τ_{ST} occurs while the same period is obtained for the red case.

Therefore, the variation of τ_{ST} can be explained by the different input power during each sawtooth crash. It can be confirmed by the integrated power per each crash and the τ_{ST} exhibited in Fig. 4.17. In Fig. 4.17(a) the τ_{ST} for CW (blue) and locking (green) phases are shown with the integrated power per crash (red). As discussed above, τ_{ST} varies with the integrated power thus when the integrated power is higher, τ_{ST} is longer and vice versa as shown in Fig. 4.17(b). Therefore, in this discharge, the variation of τ_{ST} mainly resulted from the EC power variation instead of sawtooth locking control.

In this discharge, although sawteeth do not perfectly lock to the EC modulation, it is demonstrated that τ_{ST} can be regulated by the EC power. In addition, it is shown that sawtooth period control using the locking method in KSTAR plasmas can be possible if the integrated EC power level is better controlled, otherwise sawtooth pacing can be used when real-time control is available.

Two other experiments have been carried out with different modulation period and duty cycle. For the discharge #9146, the modulation period is 62.5ms and the duty cycle is 50% while for the discharge #9147, a duty cycle of 70% with the same modulation period is used. For these two shots, EC beam injection starts at 2.5s and power modulation starts at 3.5s. The EC beam is located at $z = 20\text{cm}$ at 2.5s and sweeps to the optimum position ($z = 25\text{cm}$) at 3.5s.

The resultant τ_{ST} of the discharge #9146 is presented in Fig. 4.18(a) with the modu-

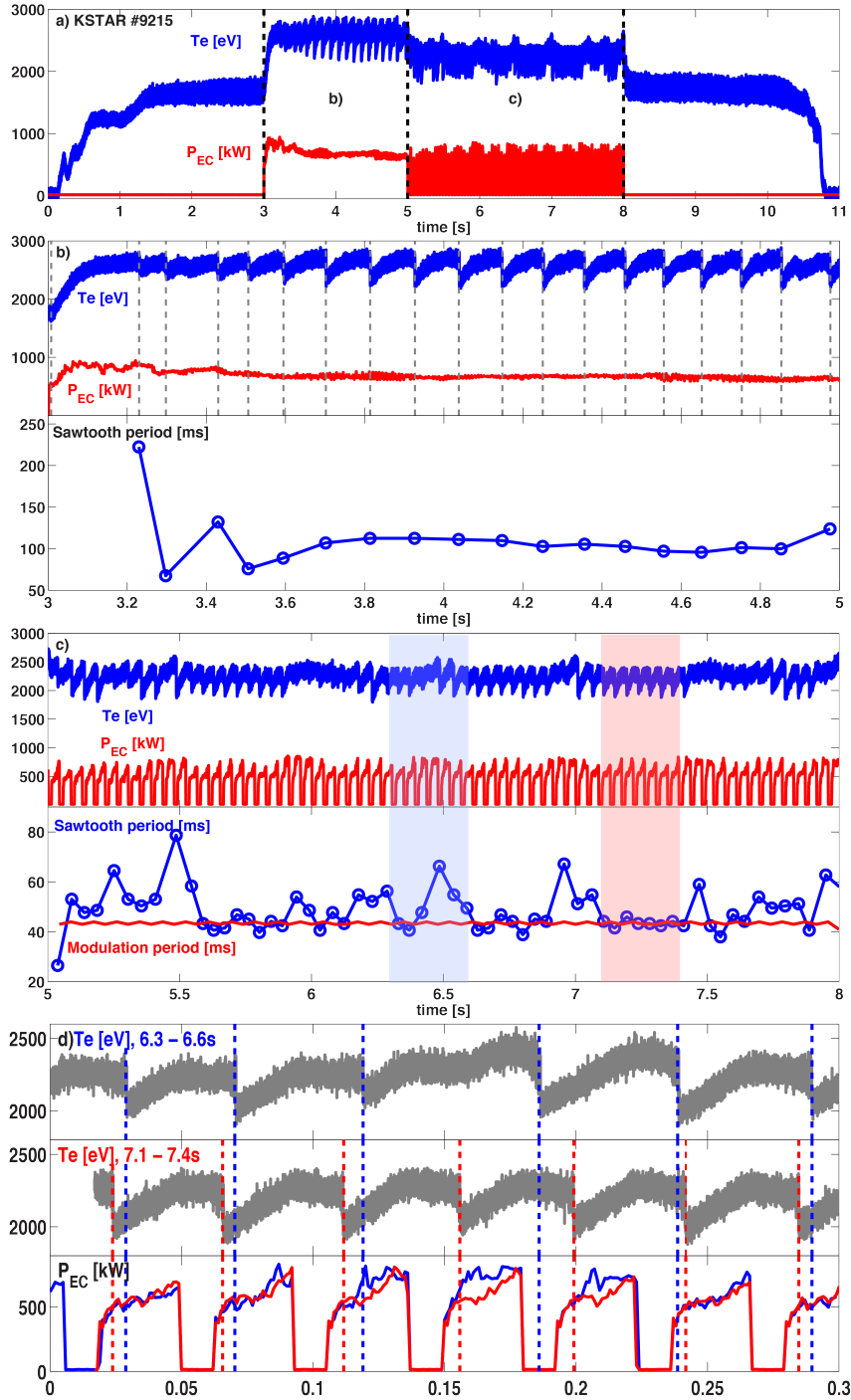


Figure 4.16: (a) Central T_e and EC power trace for KSTAR discharge #9215 are shown. (b) The detailed view of CW phase shows the sawtooth crashes (grey dashed lines) and the resultant τ_{ST} . τ_{ST} is fully extended with the period of around 100ms. (c) During the modulation phase, EC power level is not constant. The resultant τ_{ST} varies with the power and in some case, it is different from the modulation period (blue region) while sawteeth almost lock to the EC pulse (red region). (d) The EC pulse shapes are different between blue and red regions. For the blue case, the integrated EC power of each pulse is larger and therefore more EC power is injected during a sawtooth cycle and longer τ_{ST} is resulted. While with same power level, τ_{ST} which are similar to the modulation period are obtained.

4.5. Sawtooth period control experiment on KSTAR

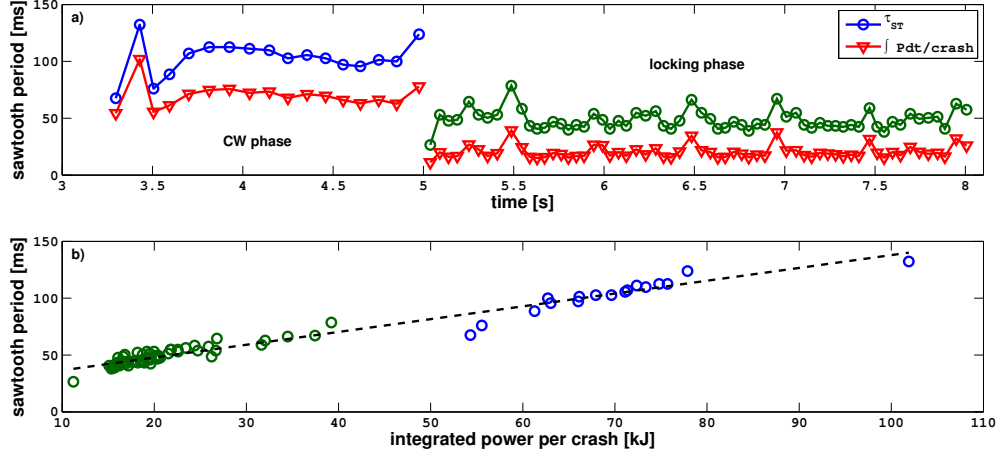


Figure 4.17: (a) The variation of τ_{ST} for CW (blue) and modulation (green) phases well synchronise with the integrated EC power per each crash (red). (b) τ_{ST} increases with higher input power and vice versa.

lation (red, solid) and reference (red, dashed) periods indicated. Due to the EC deposition sweeping, the τ_{ST} is shorter than the reference (i.e. without EC) period when the EC beam is turned on. After the modulation begins at 3.5s, the sawteeth are measured to have two separate periods, one is same as the reference period and another is regulated at about 45ms between the reference and τ_{set} values. These two sets of τ_{ST} are marked as different colours (red for the shorter one and green for the longer one). This phenomenon results from the long EC-off time. In this case, EC power is switched on during 31.25ms and off during the same duration. Since the EC-off duration is longer than the reference period, there are sawtooth crashes between the time that EC turns off and when EC turns on again, yielding short τ_{ST} . Nevertheless, during the EC-on duration, the evolution of sawteeth is regulated, resulting in an almost constant period of 45ms. The details of the ECE signal and the EC power modulation are shown in Fig. 4.18(b). As discussed, the shorter crash always occurs during the EC-off duration and the longer one occurs shortly after the EC power is switched off, similar to sawtooth pacing on TCV. This is also consistent with some successful locking cases of TCV experiments. Nevertheless there are two different τ_{ST} , which was not the goal of the experiment; but the behaviour of the sawteeth is regular, that is “locked in phase” to the modulation. In particular, note that the sum of the two sawtooth period values (violet) is equal to the modulation period of the injected EC beam. This result shows that one condition for single-period successful locking is that the EC-off duration be shorter than the reference period; this should be the case nominally for the 70% duty cycle discharge.

Results of the discharge #9147 are shown in Fig. 4.19. In this case, a duty cycle of 70% with same modulation period (62.5ms) is used. As seen in Fig. 4.19(a), the τ_{ST} does not follow the EC modulation period at all. The τ_{ST} has large variations between the reference (red, dashed) and the modulation (red, solid) periods. As seen in Fig. 4.19(b), sawtooth crashes occur randomly during both EC-on and off times. Therefore, τ_{ST} cannot

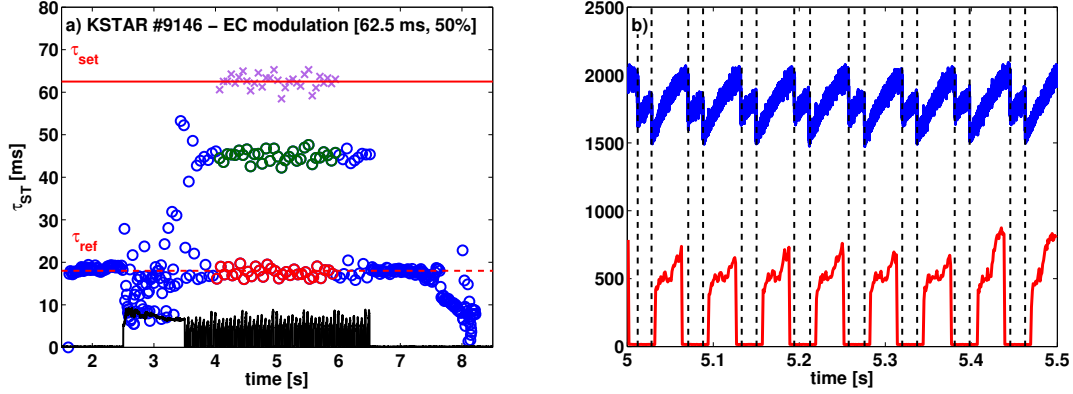


Figure 4.18: The resultant τ_{ST} from a sawtooth locking experiment, KSTAR discharge #9146, is shown in (a). EC beam started at 2.5s from $z = 20$ cm and the EC beam modulation begins from 3.5s at the stabilising position ($z = 25$ cm) with the modulation period of 62.5ms and the duty cycle of 50%. During the modulation phase, two separated periods are observed and the sum of these periods is matched the modulation period. (b) The detail of central temperature behaviour and EC power modulation show that the short crash occurs during EC-off time and the long one occurs after EC beam is switched off.

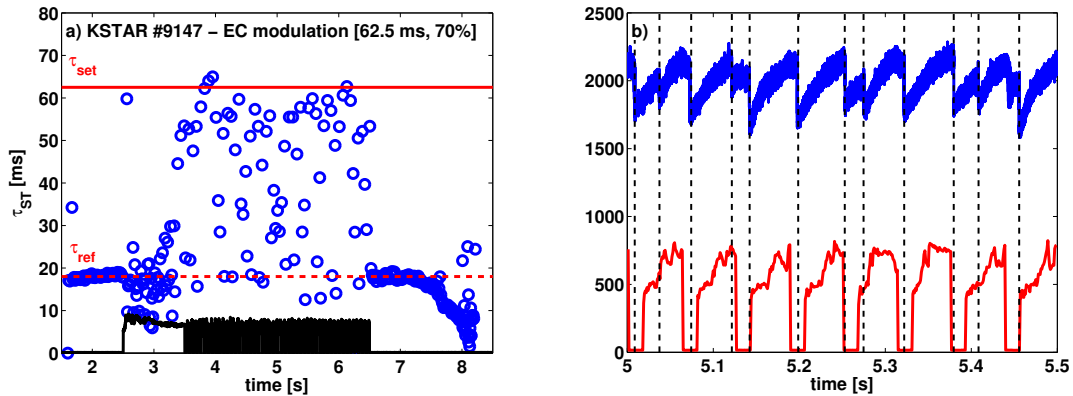


Figure 4.19: The resultant τ_{ST} from a sawtooth locking experiment, KSTAR discharge #9147, is shown in (a). The modulation period is 62.5ms and the duty cycle is 70%. The τ_{ST} does not lock to the modulation period (red, solid) but varies between the reference (red, dashed) and the modulation periods. (b) Unlike the previous case, sawtooth crash does not occur only during the EC-off time. The crash happens randomly during EC-on and off times and is not regulated.

be regulated with this duty cycle and modulation period.

In this experimental series, it has been shown that sawtooth locking can be applied to control the τ_{ST} in KSTAR plasma. During the KSTAR 2013 campaign, there were few chances to demonstrate the applicability of sawtooth locking so exploration of the locking region was not completed. In addition, due to the lack of necessary experimental data such as T_e and n_e profiles, detailed investigation using simulation was not available; further sawtooth locking experiments and simulations with different injection conditions would be needed.

4.6 Experiment and simulation of sawtooth locking on AUG

In the AUG 2014 campaign, as part of the medium size tokamak (MST) program¹, the capability of sawtooth control has been investigated using sawtooth destabilisation and active control sawtooth locking. In this section, we focus on the experimental results of sawtooth locking experiments; preliminary sawtooth locking simulation results will also be presented.

4.6.1 Preparation of sawtooth locking experiment

Experimental set up

For the sawtooth locking experiment series, a fixed value of $I_P = 1.0\text{MA}$ is taken and n_e is around $7.0 \times 10^{19}\text{m}^{-3}$. For the auxiliary heating, 7.0MW NBI, 1.7MW IC and 1.8MW EC powers are delivered to the plasma. The IC power is deposited at the plasma centre and three EC beams are used. Each EC beam has a power of 0.6MW. One beam deposits power on axis to expel the impurities in the central region (tungsten accumulation avoidance) and the other two beams aim near the $q = 1$ surface to stabilise sawteeth. In Fig. 4.20 the scenario time traces and ECH and ECCD profiles are shown. The flattop of I_P and n_e occurs from 1.0 to 8.0s. During the flattop phase, NBI power is injected from three ports in steps and afterwards IC and EC power injection follow. For sawtooth locking, EC power is modulated with pre-set modulation period and duty cycle. In contrast to KSTAR experiments, and similar to TCV experiments, several combinations of period and/or duty-cycle have been used in each discharge. A continuous wave is injected from the central EC beam for pure heating while the two beams with current drive near $q = 1$ surface are modulated. With this set up, sawtooth locking experiments are conducted.

EC beam scan across plasma radius

Similar to KSTAR experiments and as commonly performed on TCV, first an experiment with EC power sweeping has been carried out and then sawtooth locking experiments follow using various power waveforms. In order to find the optimum EC deposition position for the maximum sawtooth period τ_{ST} , poloidal scan of EC power has been performed

¹This work has been carried out within the framework of the EUROfusion Consortium and has received funding from the European Union's Horizon 2020 research and innovation programme under grant agreement number 633053. The views and opinions expressed herein do not necessarily reflect those of the European Commission.

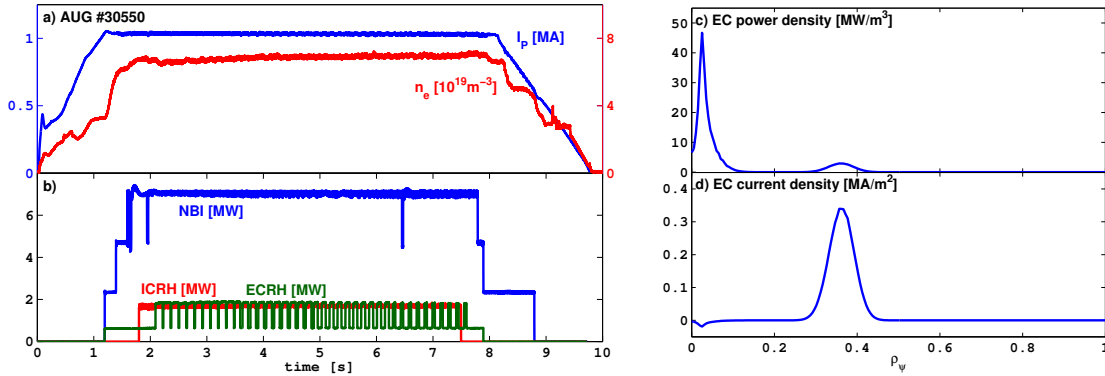


Figure 4.20: (a) I_P and n_e are kept constant to 1.0MA and $7.0 \times 10^{19} \text{m}^{-3}$ during flattop phase. (b) NBI, IC and EC power heat the plasma with 7.0, 1.7 and 1.8MW, respectively. NBI and IC powers are continuously injected while EC beams are modulated for sawtooth period control. (c, d) One EC beam is located in the plasma axis for heating and two other beams are deposited on nearby $q = 1$ surface for current drive.

in the AUG discharge #30543. The central EC beam is turned on at 1.1s and the two sweeping beams are switched on at 2.1s. During the first 1.0s of the current flattop, NBI power is increased in steps and IC deposition begins. As a result the reference sawtooth period τ_{ref} without sawtooth-control EC beams cannot be determined from this phase of the discharge; instead, it is estimated from the phase when EC beams are far outside the $q = 1$ surface. Two beams sweep from $\rho_\psi \approx 0.2$ to 0.6 between 2.1 and 4.6s. The central temperature measured by ECE and the EC power are plotted in Fig. 4.21(a) and the deposition position of EC beams and the resultant τ_{ST} are shown in Fig. 4.21(b) and (c), respectively. When EC power is deposited in the central region, τ_{ST} becomes short, around 10ms. τ_{ST} increases as EC beams approach the $q = 1$ surface and around 3.7s, the maximum τ_{ST} of 165ms is obtained when EC beams are located at $\rho_\psi = 0.45$ (light blue box). Once the EC beams cross the $q = 1$ surface, τ_{ST} rapidly decreases and stays around 60 ~ 70ms until the end of the sweeping. This period can be referred to as τ_{ref} since EC beams deposited far outside the $q = 1$ surface have a small effect on τ_{ST} . As discussed in the KSTAR case and observed on TCV, the τ_{ST} associated with a crash time is actually an average value obtained while the EC beams scan over the positions immediately preceding the crash. For this reason, the fixed deposition position of $\rho_\psi = 0.42$ was chosen, assuming it would correspond to a maximum $\tau_{ST} \approx 150\text{ms}$ and this position is used for locking experiments described here. Note that in this experiment, the EC sweeping across the plasma minor radius is relatively fast compared to the energy confinement time $\tau_E \sim 70\text{ms}$ without control EC beams. Therefore a slower reduced range sweeping should be conducted for a more precise determination of the optimal position. As seen in Fig. 4.21, the sawtooth period decreases rapidly once the EC beams pass the maximum position, this is why it is safer to choose a timing a bit earlier when sweeping from inside to outside the $q = 1$ radius.

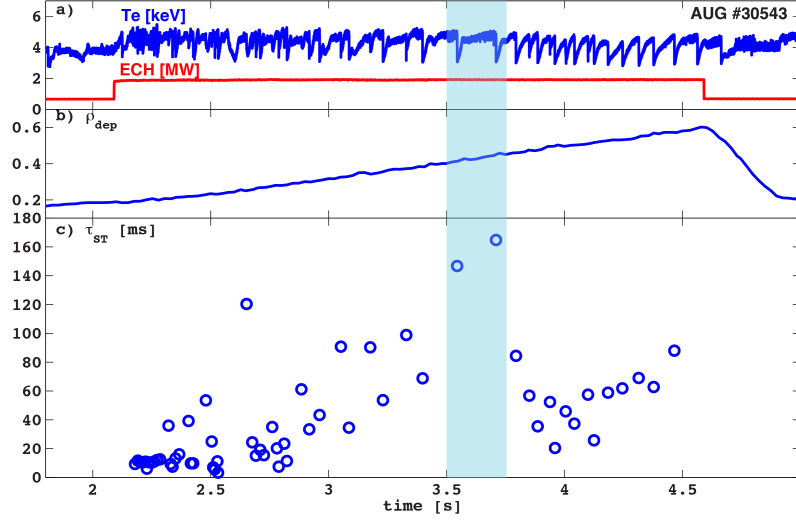


Figure 4.21: From 2.1s EC power is switched on and starts sweeping from 0.2 to 0.6 in ρ_{ψ} . τ_{ST} increases as EC beams approach close to $q = 1$ surface and have the maximum value of 165ms at $\rho_{\psi} = 0.45$. For the further sawtooth locking experiment, the fixed EC deposition position is set to $\rho_{\psi} = 0.42$ which is expected to bring τ_{ST} of 150ms.

Prediction of locking range

Prior to the experiment, we have done ASTRA simulations to predict a possible locking range for the reference discharge AUG #30233. As a reference, experimental data at 4.0s was taken and the ASTRA simulation using the transport model described in Chap. 3 reproduced the reference data. In Fig. 4.22, the T_e , T_i , n_e , n_i , power and current densities and q profiles (red: before a crash, green: after a crash) evaluated by the simulation are presented with the reference data (blue). As discussed in Sec. 3.4, $\chi_e \propto q^2$ can be used for the T_e evaluation in H-mode plasmas. However, in this case, in order to have a better fit to the experimental profile, χ_e is assumed to be proportional to q instead of q^2 and is rescaled using the energy confinement time scaling law and H factor (Eq. 3.11). Since the reference T_i profile is available, T_i is also evaluated using formulae from neoclassical theory [Angioni:PoP2000] and is modified by the sawtooth crash. A fixed R/L_{n_e} of 1.5 and H factor (not H_e factor) of 0.85 are taken to evaluate n_e and T_e profiles. Auxiliary heating powers of NBI (7MW) and central ECH (1.2MW) are applied.

After that an EC beam sweeping simulation has been performed to find the optimum position for sawtooth locking. In this simulation, it is assumed that two EC beams (1.2MW) are applied at the same position so that central EC deposition is not kept but EC beams sweep across the minor radius from the centre. The estimated sawtooth periods from the simulation are 140ms without EC beam and 65ms with central EC deposition. From the sweeping, the maximum period of 600ms is found without central EC heating and current drive. We have chosen the EC deposition position of $\rho_{\psi} \sim 0.41$ to have a sawtooth period of about 500ms and performed several tests for sawtooth locking.

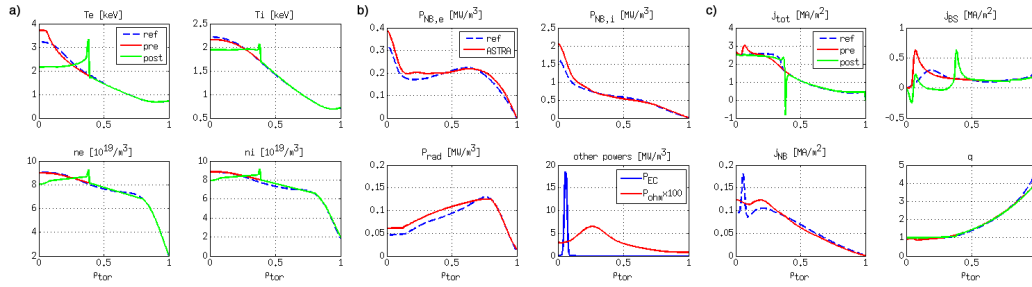


Figure 4.22: Profiles calculated from ASTRA (solid red/green: before/after a crash) and reference data from AUG #30233 4.0s (dashed, blue). (a) Kinetic profiles (T_e, T_i, n_e, n_i) evaluated using the developed transport model (T_e, n_e) and neoclassical theory (T_i) show good agreement with the reference ones with and without sawtooth crash. (b) NBI power contributions to electron and ion, radiated power, EC and ohmic powers (c) current density (j_{tot}, j_{BS}, j_{NB}) and q profiles from ASTRA are also well matched to reference data.

Three modulation periods of 200, 250 and 450ms are taken for the locking simulation. Note that due to the lack of preparation time, we could not fill the whole locking range. For 200ms case, sawteeth lock to the modulation period with duty cycles from 20 to 80% while from 40 to 80% for 250ms case. For long modulation period (450ms), sawteeth lock to EC modulation only for larger duty cycle cases (80 and 90%). Since the maximum and reference sawtooth periods from the simulation are different from those of sweeping experiment result, the periods are normalised as $\tau_{normalised} = (\tau_{set} - \tau_{ref}) / (\tau_{Max} - \tau_{ref})$. The tested periods correspond to about 0.18 (200ms), 0.3 (250ms) and 0.86 (450ms) in normalised period. From these simulation results, one can get an intuition for choosing modulation periods and duty cycles for the locking experiments, even though the locking range is not fully predicted and the maximum and reference periods are different from the experimental result. Note that ASTRA simulations have been performed using the experimental data from AUG #30543 2.0s after the experiment and the full normalised locking range will be shown in Fig. 4.26.

4.6.2 Experimental results of sawtooth locking

Sawtooth locking with various modulation periods and duty cycles

Based on the results from the sweeping experiment and simulations, sawtooth locking experiments by injecting modulated EC power are carried out. For the first test, we have fixed a modulation period τ_{set} with various duty cycles in the AUG discharge #30550. With fixed deposition position at $\rho_\psi = 0.42$, a period of 150ms is anticipated. Based on the simulation results, the normalised modulation period of about 0.4 which corresponds to 100ms is used for the EC modulation period (it is expected that sawteeth lock to EC modulation from 40 or 50 to 80%). The actual deposition time (EC on-time duration) is determined by the duty cycles of 90, 70, 50 and 30%. However, a wrong EC control command caused a modulation period of 140ms in the real experiment and the result is much different from the expected one. In Fig. 4.23, the experimental results are shown. In the top panel the central electron temperature and injected EC power time-traces are plotted. τ_{ST} and τ_{set} are presented in the mid-panel (Fig. 4.23(b)) as blue circle and red

4.6. Experiment and simulation of sawtooth locking on AUG

line, respectively, and the bottom panel shows the duty cycle.

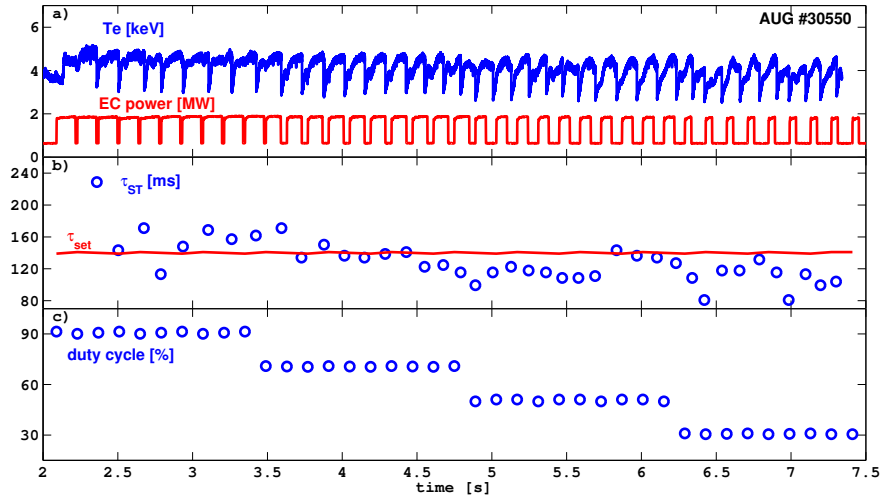


Figure 4.23: A sawtooth locking experiment with τ_{set} of 140ms and various duty cycles. When EC power is switched on and starts modulation, plasma changes much and needs time to settle down. In this transient phase, a long sawtooth crash occurs and then τ_{ST} becomes about 160ms for 90% duty cycle case. With 70% duty cycle, there are a few sawteeth which have similar periods as τ_{set} . In 50 and 30% phases, τ_{ST} varies much compared to previous two duty cycle cases. There are no clear sawtooth locking, except a few near 6s and the average τ_{ST} in each duty cycle phases decrease with reduction of averaged power for each phase.

At 2.1s, control EC beams are switched on and bring changes in the plasma state. During a transient phase, a very long sawtooth with period of 230ms occurs and then τ_{ST} decreases. During this phase, the modulation does not have much effect; since the duty cycle is 90%, EC beams are almost continuous. After the first several sawtooth crashes, τ_{ST} becomes close to 160ms, which is longer than τ_{set} and shows the expected maximum period is about 165ms. In this discharge, the plasma state appears to be different from that during the sweeping discharge so that the EC deposition position relative to $q = 1$ surface may differ from the expected one; as a result, τ_{ST} is longer than 150ms. (Note that in the sweeping discharge the maximum period was about 165ms for continuous injection.)

The duty cycle decreases to 70% at 3.5s. At the beginning of this phase, τ_{ST} is still long but soon τ_{ST} is reduced to a similar level as τ_{set} which means close to locking. Regular sawteeth do not last long and τ_{ST} slightly decreases under the same modulation condition, indicating that locking has not occurred: for true locking the phasing of the pulses to the sawteeth should stabilise at a near constant value. For 50% duty cycle case, τ_{ST} varies between 100 and 120ms. At the end of the phase, τ_{ST} suddenly increases and stays around 140ms. In this case, the EC off time is similar to τ_{ref} . Since sawtooth crashes occur with delay after EC power is turned off, the off time is not long enough to have a crash during that time. Therefore, before the next crash EC power is back on and causes a τ_{ST} longer than τ_{ref} . With 30% duty cycle, τ_{ST} has a wider variation, between 80 and 130ms. At first, τ_{ST} decreases from the period it had at 50% duty cycle and then, at a certain moment, a complete sawtooth cycle occurs during the EC-off duration, since

that duration is longer than τ_{ref} ; as we saw in the KSTAR experiment. Note that on AUG, however, the τ_{ST} during the off duration is 80ms, which is longer than the expected reference period. The delay between a crash and EC turn-off time is not regular. As a result, sawteeth are not regulated by the EC modulation and there are only a couple of complete sawtooth cycles that occur during EC-off duration.

In this experiment, there is no clear sign that sawteeth lock to the EC modulation. Only a few crashes have similar τ_{ST} as τ_{set} for the 50 and 70% duty cycle cases. Furthermore, the overall sawtooth behaviour depends on the averaged injected power same as seen in KSTAR case. Since τ_{set} is fixed and the duty cycle decreases, the averaged powers for each duty cycle phase decrease. As the averaged power is reduced, the resultant τ_{ST} decreases as well. The averaged τ_{ST} are about 152, 137, 120, 110ms for 90, 70, 50, 30% duty cycles, respectively. Therefore, for 70% duty cycle case, sawteeth have periods similar to τ_{set} because of either partial locking or a coincidental match while decreasing the averaged power. On the other hand, for 50% case, even with smaller averaged power, τ_{ST} becomes about 140ms; this might be considered as sawtooth locking though phase stability over a longer period should be demonstrated. Detailed experiment for each cases will be demanded for further understanding.

In a second experiment, three different modulation periods τ_{set} with a fixed duty cycle are used. In the AUG discharge #30552, τ_{set} values are 70, 100 and 140ms (about 0.05, 0.4 and 0.88 in normalised period, respectively) and the duty cycle is constant as 80%. In Fig. 4.24(a), the experimental traces of the central electron temperature from ECE measurements and the injected EC power are shown. τ_{ST} and τ_{set} are presented in Fig. 4.24(b) as blue circles and a red line, respectively, and the duty cycle is plotted in the bottom panel. In this experiment, EC beams are placed at $\rho_{\psi} = 0.2$ to test destabilisation during the first part (between 2.0 and 3.0s) of the discharge; then, the EC power is turned off while the EC deposition is moved to a new target position. At 3.3s, EC power is switched on to stabilise sawteeth.

From 3.3 to 4.1s, continuous EC beams are applied at the fixed position to determine the maximum τ_{ST} . As in the previous case, when EC beams are switched on, long τ_{ST} occur during the transient phase and afterwards τ_{ST} decreases to around 125ms. This τ_{ST} is shorter than that of the previous discharge. From the post-shot analysis, it is shown that the EC deposition position was different from the command. The actual deposition centroid for each launcher is presented in Fig. 4.24(d). They are at slightly different deposition positions and are at $\rho_{\psi} \sim 0.38$ on average. From Fig. 4.21, at this position, τ_{ST} can be between 100 and 140ms depending on the relative position to the $q = 1$ surface, so τ_{ST} of 125ms is not surprising. (Note that for the discharge #30550, the beam deposition position was the same as that of the shot #30552. So a difference in distances between the deposition position and the $q = 1$ surface may be the reason for the unexpectedly long τ_{ST} in discharge #30550.)

From 4.1s the EC beam modulation begins with $\tau_{set} = 70$ ms and 80% duty cycle. Due to a problem of timing, the 70ms phase is much shorter than the other phases; consequently, there is only one sawtooth crash ($\tau_{ST} = 130$ ms) and this phase cannot be examined. During the $\tau_{set} = 100$ ms phase, there are a few crashes which have τ_{ST} similar to 100ms but overall the sawtooth periods are around 120ms. This suggests that for this plasma, EC heating during 80ms is sufficient to have essentially the maximum τ_{ST} : 80% duty cycle for a 100ms period is too high to cause the sawtooth cycle to lock

4.6. Experiment and simulation of sawtooth locking on AUG

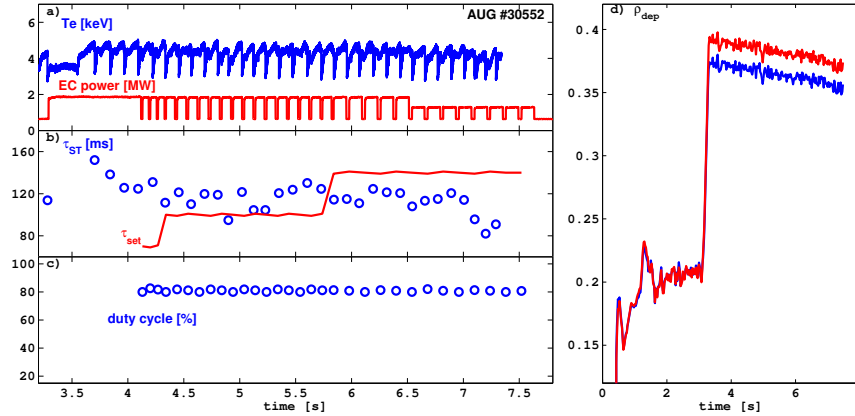


Figure 4.24: τ_{ST} is about 125ms with the continuous EC injection at the deposition position $\rho_{\psi} \sim 0.38$. EC beams are modulated with τ_{set} of 70, 100 and 140ms and fixed duty cycle of 80%. For the all cases, sawteeth do not lock to the EC modulation.

to the EC modulation. Indeed from the predictive simulation, it is anticipated that this combination of values is at the edge of the locking region and will be sensitive to changes in the plasma and launching parameters. For $\tau_{set} = 140\text{ms}$, the target period is longer than the maximum period possible with continuous injection; therefore, the sawteeth cannot lock to the EC modulation. Near 6.5s, one of EC beams is turned off early and with lower EC power the τ_{ST} decreases.

From Figs. 4.23 and 4.24, we try to show whether sawteeth lock to the EC pulse or not, based largely on the similarity between τ_{ST} and τ_{set} . To be more clear, the phase of the sawtooth crash relative to the EC modulation period has also been investigated, as shown in Fig. 4.25. The colours of the vertical bars indicate electron temperature and the length of the bar (y direction) represents τ_{set} : each bar corresponds to one EC modulation cycle. The blue line and black circle denote the EC-on duration and τ_{ST} , respectively. After a crash, the temperature drops (blue colour) and recovers (red). The alignment of the sudden change to lower temperature suggests that the timing of sawtooth crash is similar to the EC modulation period; one can see if sawteeth are more-or-less regulated. For the discharge #30550 (Fig. 4.25(a)), we see that with 90% duty cycle τ_{ST} do not match to τ_{set} and the moments of each crash are not regular: the blue colours form diagonal lines. On the other hand, for the 70% case, sawtooth crashes occur almost right after EC powers are switched off and the blue colours are well aligned horizontally; similar alignment is shown at the end of 50% phase. At the beginning of 50% phase and the whole phase with 30% duty cycle, sawtooth crashes are never aligned. A similar graphic is presented in Fig. 4.25(b) for the discharge #30552. The moment of the crash drifts continually and there is no indication of synchronised sawtoothing. As an example of a successful locking case, the experimental result of TCV discharge #43642 is shown in Fig. 4.25(c). Here, τ_{set} varies between 15 and 35ms in steps of 10ms with 80% duty cycle. τ_{ST} is well matched to τ_{set} for the 15 and 25ms EC modulation period cases and the drops of temperature are also well aligned and do not drift in time (compare to 4.25(a) near 4 and 6s where, though roughly horizontal, the blue regions still slowly drift downwards and in the long-run locking is lost). For the 15ms case, crashes always occur just after EC power is switched on again,

while the crashes always happen just after the EC-off time for 25ms case. For the 35ms, at the later phase some regulated crashes are shown. In this discharge, regardless of the timing of the sawtooth crash with respect to the EC-off time, the sawtooth instability is well regulated for 10 or more cycles by the EC pulse only when the sawteeth phase locks to the EC modulation. Note that after an initial transition phase (a few cycles), the jitter in crash timing becomes small and apparently random.

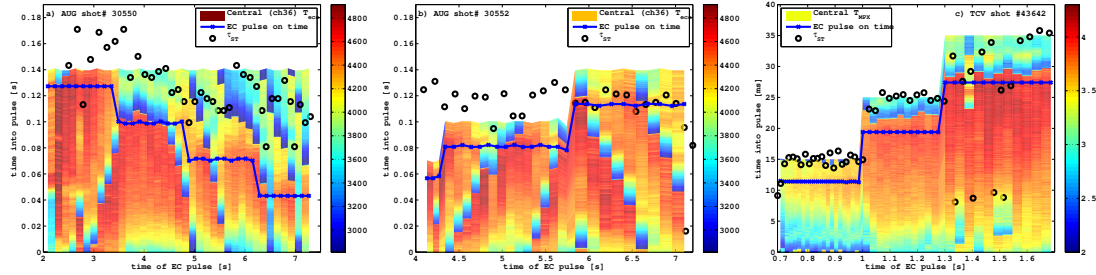


Figure 4.25: The change of temperature during modulation periods are shown with τ_{ST} and EC pulse on time for (a) AUG #30550, (b) AUG #30552 and (c) TCV #43642. When sawteeth lock to EC modulation, the change of temperature well aligns while the timing is random or drifts for non-locking case.

From two discharges, the maximum τ_{ST} for a fixed aiming turned out to be different from the one expected, so one cannot compare them in detail to the simulation result. For this reason, we have put the three cases on the same locking range with normalised modulation period in Fig. 4.26. Based on the simulation result from AUG #30543, the experimental results from two locking discharges are presented. The simulation results aiming for the maximum sawtooth period of 145ms are represented by blue circles (locking), red crosses (non-locking) and blue crosses (harmonics). The green squares show the predicted simulation results using AUG #30233 data which are quite similar. The AUG #30550 discharge cases are indicated by stars. Since the exact value of the maximum and reference periods for the discharge #30550 are unknown, the upper and lower boundary of the *expected* normalised periods for this case are marked as black dashed lines. The 30% duty cycle case is located outside the successful locking range, locking is expected for the 50 and 70% cases, and the 90% case may lie just outside the locking range. These are somewhat similar to, but not precisely the same as, the experimental result; in particular, the 50 and 70% cases do not really lock. The triangles in Fig. 4.26 denote the AUG #30552 data. For the 70ms modulation period, the 80% duty cycle case is far from the successful locking range ($\tau_{normalised} \approx 0.1$) and for the 100ms period, it is close to the edge of the locking region (as in the #30550 90% case). Since the deposition positions relative to the $q = 1$ surface were different for each discharge, the expected locking range may differ accordingly as discussed in Refs. [Witvoet:NF2011, Kim:PoP2014]. In particular, for the discharge #30552, because the heating position is further towards the axis, a narrower successful locking range is anticipated. This may be a possible explanation for unsuccessful locking. Therefore, additional simulations and experiments should be performed to explore the possible locking ranges in different positions and to better understand the present results. Compared to TCV and KSTAR plasmas, AUG plasmas appear to require more time to adjust to the EC modulation; the transition period is

longer. Hence, for a clear demonstration, experiments using a more simple set-up may need to be performed with one τ_{set} and one duty cycle during a whole discharge, near 60% duty cycle and $\tau_{normalised} \approx 0.5$ as seen in Fig. 4.26. This may allow an investigation of the transition dynamics to locking itself and allow better prediction capability for further experiments. Furthermore, it would be helpful to map the full locking range, to be compared to the simulation results.

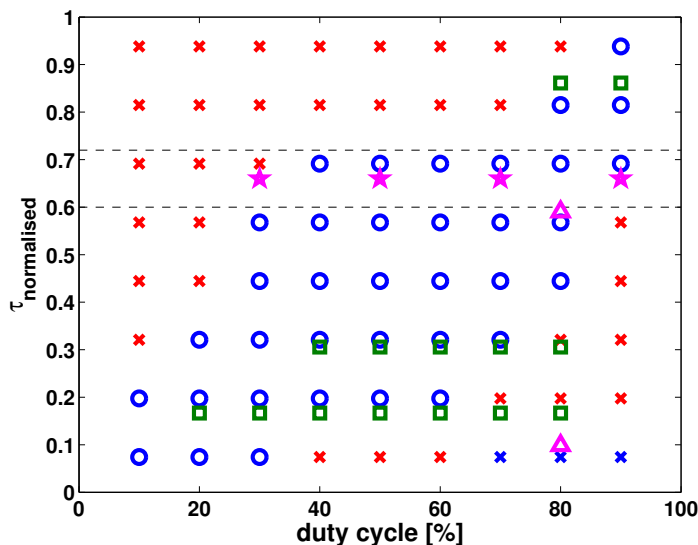


Figure 4.26: Normalised locking range for the maximum τ_{ST} of 145ms with the predictive simulation results (green square) and experiment cases. Both results from #30550 (star) and #30552 (diamond) cases are similar to the simulation result.

4.7 Predictive sawtooth control simulation for ITER

In order to investigate the feasibility of sawtooth and NTM control in ITER plasmas, using the present EC launcher design, numerical simulations have been carried out². In this work, we concentrate on sawtooth locking and pacing as tools of sawtooth period control. We also restrict ourselves to using the effective launcher geometries provided by the mirrors. The main results and figures presented in this section have been published in Ref. [Kim:PoP2014].

²This work was supported by Fusion for Energy under Grant No. F4E-GRT-161 and within the European Electron Cyclotron Heating Upper Launcher Consortium (ECHUL). The authors would like to thank Daniela Farina for providing the results of extensive ray-tracing calculations. The views and opinions expressed herein do not necessarily reflect those of the European Commission. ECHUL is a collaboration among CRPP- EPFL, Switzerland; KIT, Germany; IPP, Germany; IFP- CNR, Italy; DIFFER, The Netherlands.

4.7.1 Preparation of ITER simulation

Physics model

As a reference, the standard ITER inductive H-mode scenario [Kessel:NF2009, Parail:NF2013] ($I_P = 15\text{MA}$) has been taken. The main ions are deuterium and tritium. α -particles (H_e) from the D-T fusion reaction are included and as impurity particles, carbon is assumed to be the only impurity species. The ohmic current constitutes about 70% of the total current. Auxiliary powers of 33MW neutral beam (NBI) and 7.5MW ion cyclotron heating (ICH) are used; 420MW α -heating power is assumed resulting in a fusion gain factor $Q = 10$.

For reproducing the main parameters of this scenario, the ASTRA code [Pereverzev:2002] has been employed with the transport model presented in chapter 3 for electron temperature T_e and density n_e , using $\chi_e \propto q^2$ and fixed R/L_{n_e} , respectively. For T_e profile evaluation, the H-mode scaling factor ITER-H98(y,2) $H_{H98} = 0.92$ (reference data value: 0.94) is taken to rescale the amplitude of χ_e and obtain $Q = 10$. Note that in this simulation, the effect of EC deposition position (τ_{Ee} reduction effect) has not been taken into account since the target deposition position is very close to $q = 1$ surface. The value of R/L_{n_e} is set to 0.25 to reproduce the relatively flat density profile. In addition, the second term of Eq. 3.18, electron particle flux Γ_e , is not neglected since there is particle source from NBI. For ion temperature T_i , the transport coefficient χ_i is assumed to be proportional to χ_e ($\chi_i = 1.2\chi_e$). Ion density n_i is determined as explained in Sec. 3.1.2 assuming quasi-neutrality and $Z_{eff} = 1.76$. Moreover, the densities of the two main ions are assumed to be the same $n_D = n_T$ and the α -particle density n_α can be determined using Eq. 3.3. The fast particle density from neutral beam, n_{NB} , is calculated by the ASTRA NBI module, and as mentioned above, only one impurity carbon, n_C , is assumed. Note that in this simulation the H -factor is used instead of H_e since both T_e and T_i are evaluated and can be compared to reference profiles [Parail:NF2013]. The boundary for temperature and density calculations is fixed at $\rho_{tor} = 0.8$, where ρ_{tor} is the square-root of the normalised toroidal flux ϕ , and the boundary values are taken from the reference profiles; all calculations are done inside of this boundary.

Figure 4.27(a) shows the electron and ion temperatures, electron density, and q profiles calculated by the ASTRA simulation (blue, solid) together with the reference data (red dashed). Sawtooth activity is included in the simulation; all the profiles are taken just before the sawtooth crash. Temperature profiles from the ASTRA simulation slightly differ from the reference data because of the different heat diffusivity model. Nevertheless, temperature profiles from the ASTRA and reference are in reasonably good agreement. Furthermore the χ_e model can be clearly applied to provide reasonable ion temperature, as seen in this figure. Electron density and q profiles also have small differences in the central region, with respect to the reference profiles, but are otherwise in good agreement.

Power densities calculated from ASTRA are also compared to the reference profiles. The radiative power is calculated as the sum of Bremsstrahlung and synchrotron powers. Those two are calculated based on the one impurity assumption (carbon), the power from line radiation is neglected. The power densities from NBI and α -particle are self-consistently evaluated in the ASTRA simulation. The NBI module in ASTRA provides the power densities distributed to electrons and ions, fast particle density, driven current density and perpendicular and parallel pressures. The fusion power densities to the

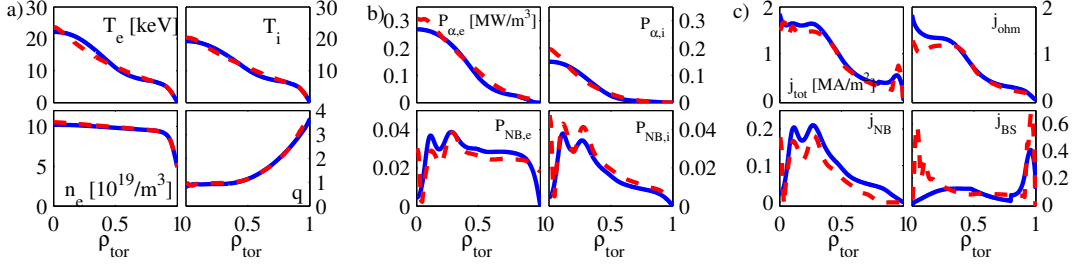


Figure 4.27: Profiles calculated from ASTRA (solid, blue) and reference data (dashed, red). (a) Kinetic profiles (T_e, T_i, n_e) and q profile: Temperature profiles are slightly different due to heat diffusivity and replacement of ICH power but still in a good agreement. (b) α and NBI power contributions to electron and ion, (c) current density profiles ($j_{tot}, j_{ohm}, j_{NB}, j_{bs}$) from ASTRA are also well matched to reference data.

electrons and ions are calculated using the reaction rate $n_D n_T \langle \sigma v \rangle$. As mentioned, the α -particle density is calculated in the same way as the electron density using Eq. 3.3; that is, defining $D_\alpha, v_\alpha,$ and R/L_{n_α} so that the α -particle density matches the reference profile. Furthermore, as for the electron density, the source of the α -particle, i.e. fusion reaction rate, cannot be ignored. In this case, D_α is assumed to be proportional to $D_n,$ and R/L_{n_α} is fixed to 13.5. With these two values and the source term, v_α is defined similarly to D_E in Eq. 3.18.

In Fig. 4.27(b) the α and NBI power densities resulting from ASTRA simulation are shown. The α power distributions to electron and ion are slightly different from the reference data. This results from the difference between ASTRA and reference temperature profiles because the α power density depends on the ion temperature. Similarly, the NBI powers show differences due to the temperature dependence. In order to test the effect of the different power density, two separate simulations have been done. One is using the reference data as fixed power profiles, while another takes the self-consistent power density profiles generated by ASTRA. From the test, no significant difference has been found in the kinetic profiles, current densities, sawtooth periods and all the other factors for the two cases. Therefore, for evaluating the effect of the sawtooth crash on the power density profiles, self-consistently evaluated powers are used in what follows.

In the ITER standard operation scenario, ICH will play a role to heat both ions and electrons; therefore, in the reference data, 7.5MW of ICH is used. It is known that fast ions generated by ICH can modify the sawtooth period depending on the deposition position and the trajectory of fast particles (passing or trapped) ([Chapman:PPCF2011, Graves:Nature2012] and references there in). However, at this stage, there is no tool for rapidly evaluating the fast ion distribution from ICH and its effects on sawteeth in the ASTRA simulations. Therefore, we take an alternative approach; we replaced ICH by ECH for compensating the ICH heating effect and the effect of ICH fast particles on the sawtooth period is imitated by modifying the free parameter in the fast particle term (Eq. 4.7) in the sawtooth criteria (Eq. 4.14). Since the ICH power profile is roughly a centrally-peaked gaussian profile, EC beams from the equatorial launcher (EL) are chosen to match the ICH profile because the EL can deposit power centrally. Eight equatorial EC beams are deposited at $\rho_{tor} = 0.2$. Since no current drive from ICH is assumed four

EC beams have the same direction as plasma current while the other four beams are in the opposite direction to result in pure central heating. Even though the resultant EC heating power density does not precisely match the initial ICH profile, the effect is similar since the resulting power is clearly deposited well inside the $q = 1$ surface ($\rho_1 \sim 0.4$), which does not affect the location of the $q = 1$ surface and leads to similar temperature profiles.

The difference of ECH beam position, width and total power (6.88MW) relative to ICH results in slightly lower electron and ion temperature ($\leq 1\text{keV}$) and thus the corresponding α and NBI power densities. However, the fusion gain factor still remains around 10 and in addition, using the calculated profiles the resultant energy confinement time τ_E (2.67s) is slightly longer than the reference value (2.54s) due to the difference of temperatures and smaller total power. Note that replacing ICH by ECH is a realistic option that will be tested in ITER. This has been discussed in more details in Ref. [WagnerF:PPCF2010].

Now we have an ASTRA simulation that matches the reference data quite well despite the change from ICH to EC central heating. Therefore we can proceed to investigate the sawtooth control possibilities on ITER using the EC upper launchers (UL) using the remaining 13.76MW.

Sawtooth model

In the ITER plasma, the presence of energetic α -particles is expected to have a strong stabilisation effect reducing the $-\delta\hat{W}$, in particular $-\delta\hat{W}_{fast}$ term in the sawtooth crash criteria. Therefore, the third criterion and its modification will play the most important role in determining the moment of the sawtooth crash. From Eqs. 4.14 and 4.13, the sawtooth crash criteria for ITER simulation are as below (both need to be satisfied to trigger a crash):

$$-c_\rho\hat{\rho} < -\delta\hat{W} < 0.5\omega_{*,i}\tau_A \quad (4.22a)$$

$$s_1 > \min(s_{1,crit,\eta}, s_{1,crit,\rho}) \quad (4.22b)$$

As well as the ITER case, in TCV plasmas the same criteria are dominant in determining the crash timing. In TCV plasmas, the first expression 4.22a is always fulfilled and therefore the moment of the sawtooth crash is determined by the shear condition 4.22b. While, in the ITER plasma, because of the fast particle stabilisation effect, the first condition is satisfied later than the shear condition. Therefore the sawtooth crash occurs when $-\delta\hat{W}$ exceeds $-c_\rho\hat{\rho}$ and the sawtooth period stabilised by fast particle can be adjusted by the free parameters c_ρ and c_f in $-\delta\hat{W}_{fast}$ term. In this work, using c_ρ and c_f of 0.12 and 2 and the reference data [Parail:Nf2013], a sawtooth period of $\tau_{ST} = 40\text{s}$ is found. This value is within the expected sawtooth period range in ITER as discussed in Refs. [Zucca:Thesis, Onjun:Nf2009, Budny:Nf2008]. This period of 40s is estimated using all the power from reference data, i.e. NBI, ICH. Due to the replacement of ICH by central ECH, the sawtooth period is modified: the period decreases to about 36s and is used as the reference period (τ_{ST}^{ref}) in our work. Since the exact reference period is not well known, we test the sensitivity of our simulation results to the value of τ_{ST}^{ref} . As will

be discussed in Sec. 4.7.3, it is shown that the value of τ_{ST}^{ref} does not affect much the simulation results; neither do the values of c_ρ and c_f .

4.7.2 Description of the EC beams

Defining the shapes of the EC power deposition profiles from ITER upper launchers

In these simulations, 8 beams from the equatorial launcher (EL) deposit 6.88MW in the central region ($\rho_{tor} = 0.2$) to replace ICH. The remaining EC power of 13.76MW can be delivered from 16 sources from the 4 upper steering mirrors (USMs) of 4 upper launchers (ULs) at the stabilising or destabilising position for the sawtooth period.

As discussed in 2.4.2, there are various possibilities to define the combination of EC beams using up to 16 USM sources with different steering mirror rotation angle γ values. In this work, we have chosen 3 different combinations and the resultant $P_{EC}(\rho)$ shapes are shown in Fig. 4.28.

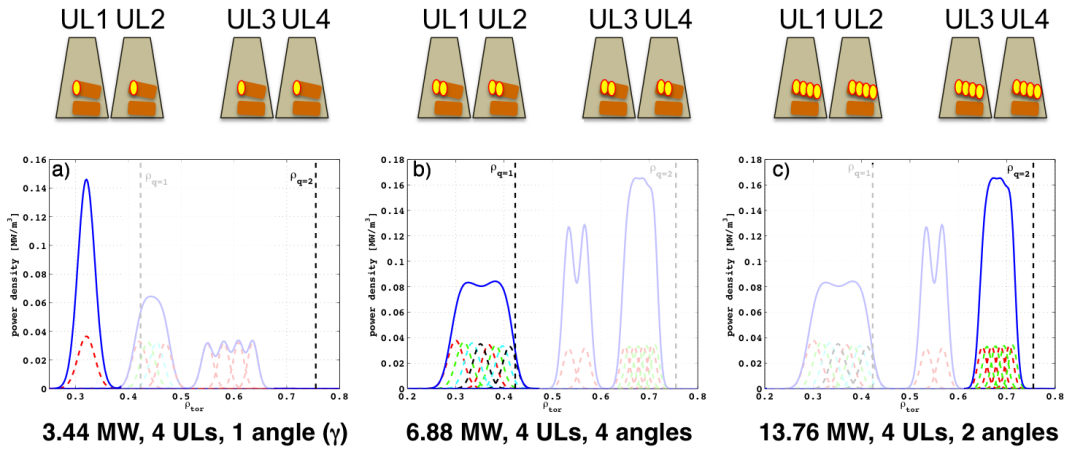


Figure 4.28: Different $P_{EC}(\rho)$ shapes from (a) four, (b) eight and (c) sixteen beams. For each case, the chosen beams from each launcher are shown in upper part. Solid curves (blue) are resultant beam shape and the other dashed curves represent each beam from the various launchers. With different control factor γ and the number of beams, it is possible to have various types of power density shapes.

In the upper part of the figure the trapezoids indicate the approximate cross-section of the ULs as seen from the plasma. The two orange ovals schematically represent the two steering mirrors of each launcher on which four separate gyrotron beams are actuated together (i.e. as a group). The USM beams that are used to define the beam shape in the lower panels are indicated by the yellow circles. The solid curves (blue) are the resultant EC power density profile shapes, which are the sum of the individual beams marked as dashed curves with various colours. Each colour indicates a different γ (actuator) value. For the first case, 4 beams are taken to deliver the total absorbed power of 3.44MW. As shown in Fig. 4.28(a), 4 USM beams, one from each launcher, are perfectly aligned with the same γ and the resultant power density profile has a gaussian shape and high peak power density. The second option using 8 beams is shown in Fig. 4.28(b). 2 USM beams

are chosen from each UL to deposit a total absorbed power of 6.88MW; 4 different γ values are used, one for each launcher. The minimum misalignment of 2 beams from the same launcher is fixed and occurs when using two adjacent beams in the present design; therefore, the two additional beams coming from each of the other launchers are used to “fill in” the space between the 2 beams of the first launcher. This results in the tightest possible packing of 8 sources. Finally, in Fig. 4.28(c), 16 beams (13.76MW) are combined using two different γ values, two launchers have the same γ value and the other two have a different γ that places their beams between those of the first pair of ULs. For the following sawtooth simulations, these three types of beams are used. This allows us to perform a realistic (i.e. technically realisable) power scan. Note that for any given combination of the launchers, the beam shapes will change with the deposition position since the widths of individual beams and the relative alignment between the USMs depends on the aiming location.

Determination of EC beam deposition position, beam width and driven current

The position of each individual beam from a USM is calculated as a function of γ in the GRAY code [Farina:FST2007], which computes the beam width, beam power density, driven current density and the total driven current at each beam’s position; in this work, the GRAY code is not directly run, instead tabulated GRAY data provided by D. Farina [Farina:private] is used. Due to the launcher optical configuration, the four beams from the same USM do not perfectly overlap, in particular near the plasma centre. Therefore, with one γ value, one finds a different position ($\rho_{tor,1-4}$) for each of the four beams launched from any single USM. The control parameter γ maps to a pair of poloidal and toroidal angles α , β . The relations between the control parameter γ and the deposition location ρ_{tor} for each beams are defined as 3rd order polynomial fitting equations below:

$$\begin{aligned}
 \rho_{tor,1} &= -0.00020\gamma^3 - 0.00621\gamma^2 - 0.08455\gamma + 0.41174 \\
 \rho_{tor,2} &= -0.00015\gamma^3 - 0.00492\gamma^2 - 0.07182\gamma + 0.46252 \\
 \rho_{tor,3} &= -0.00013\gamma^3 - 0.00416\gamma^2 - 0.06283\gamma + 0.50488 \\
 \rho_{tor,4} &= -0.00011\gamma^3 - 0.00352\gamma^2 - 0.05512\gamma + 0.54413.
 \end{aligned}
 \tag{4.23}$$

The polynomial equations are plotted in Fig. 4.29(a).

Since there is no target ρ_{dep} , an arbitrary position can be chosen in the range that is shown in Fig. 4.29(a). Once a ρ_{dep} of EC beam is defined, corresponding γ value is obtained using the relation between ρ_{tor} and γ . Subsequently, the three other ρ_{dep} s are determined by the γ value. This approach is used for each of the 4 ULs. Thus, one can have four γ values determining the positions of sixteen beams from the USMs.

From the GRAY calculation for a USM beam, an estimate for the beam width and driven current can be found as a function of ρ_{tor} . Note that in the GRAY calculation the toroidal angle β is fixed at 20°, but all possible poloidal angles α are considered. In order to avoid an interpolation during the ASTRA simulations, a polynomial fit is used to define the relations between ρ_{tor} and w_{EC}/I_{EC} . The equations are written as:

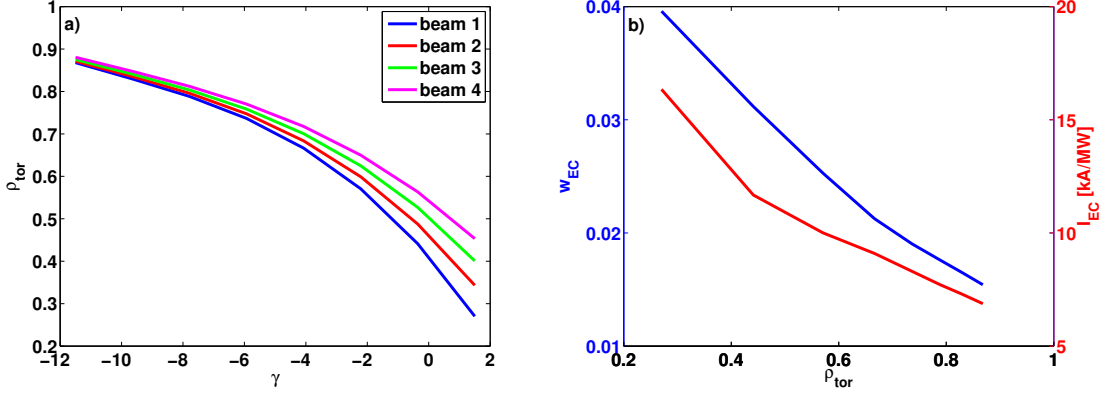


Figure 4.29: (a) The polynomial fits between γ and ρ_{tor} provide the deposition position of each beam with one control parameter γ . The deviation among beams is larger in the central region while smaller in the edge region. (b) Using the GRAY calculation results and estimated ρ_{tor} from γ , the relations between ρ_{tor} and w_{EC}/I_{EC} are found.

$$\begin{aligned}
 w_{EC} &= -83.45\rho_{tor}^8 + 424.17\rho_{tor}^7 - 926.19\rho_{tor}^6 + 1132.33\rho_{tor}^5 - 846.00\rho_{tor}^4 \\
 &\quad + 394.76\rho_{tor}^3 - 112.12\rho_{tor}^2 + 17.64\rho_{tor} - 1.13 \\
 I_{EC} &= -6274.91\rho_{tor}^8 + 22697.54\rho_{tor}^7 - 33071.16\rho_{tor}^6 + 24634.14\rho_{tor}^5 - 9691.49\rho_{tor}^4 \\
 &\quad + 1693.38\rho_{tor}^3 + 97.57\rho_{tor}^2 - 122.42\rho_{tor} + 35.73.
 \end{aligned} \tag{4.24}$$

Using ρ_{dep} determined by the γ value for each UL, the width and driven current can be determined for each individual beam. In this simulation, w_{ECH} and w_{ECCD} are taken to be identical and are both referred to as w_{EC} , which is assumed as full width half maximum (FWHM) value. ρ_{dep} is taken to be the same for both ECH and ECCD. The width and driven current as functions of ρ_{tor} are displayed in Fig. 4.29(b).

After all the simulations were complete, it was discovered that the definition of w_{EC} used in the GRAY calculation is not w_{FWHM} , but rather the full profile width at $1/e$ of the peak value. This misinterpretation resulted in the use of a beam width in the simulations that is $\sim 20\%$ larger than those predicted by GRAY. However, since both beam widths are quite small, smaller than the intrinsic misalignment, the beam profiles with the two types of beam width (w_{FWHM} , $w_{1/e}$) are not significantly different as shown in Fig. 4.30. The results are therefore not significantly affected, in particular since the total power is enforced for each beam and does not depend on the effective beam width.

4.7.3 Simulation results

Beam sweeping

Based on the models described above, predictive simulations of sawtooth activity are carried out with EC beams from the UL USMs. For the remainder of this work, the EC beam, or profile, refers only to the USM beams since the EC aiming from the EL is at a fixed location and power level, making no contribution to the sawtooth control.

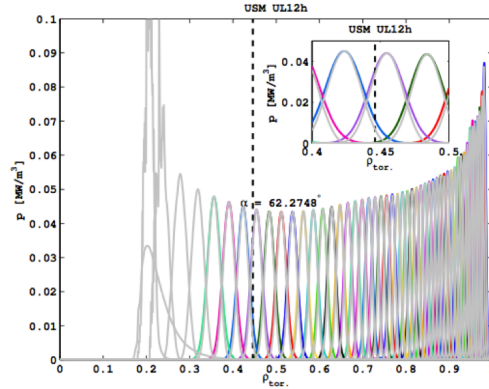


Figure 4.30: GRAY profiles (light grey) and profiles used in the sawtooth simulations (colour). With two different types of beam width, the resultant beam profiles are similar.

As mentioned in Sec. 4.7.2, three different EC deposition profiles are evaluated for their sawtooth control capabilities. Initially, as done in the TCV experiments, the EC profile is swept across ρ_{tor} to determine the most effective deposition position for sawtooth stabilisation. For each case, the range of the control parameter γ is defined by the innermost beam of the group of beams that make up the profile and causes that beam to move from $\rho_{tor} = 0.2$ to $\rho_{tor} = 0.8$; the other beams follow as a function of γ .

In Fig. 4.31, curves of the sawtooth period are shown as a function of the relative position of the leftmost beam position (i.e. the one at smallest ρ_{dep}) to the $q = 1$ surface position. Figure 4.31(a) is the sweeping result with four perfectly aligned beams (3.44MW) – the narrowest beam width. The sawtooth period is shortened (i.e. sawteeth are destabilised) when ρ_{dep} is far inside $\rho_{q=1}$ and increases strongly (stabilising) close to $\rho_{q=1}$. The maximum period is obtained when the EC beam is located at $\rho_{q=1}$. The effect of the EC beam is negligible when the beam is deposited far outside $\rho_{q=1}$ (i.e. the sawtooth period is essentially the same as without the control beams on). The shape of the sawtooth period curve closely matches that of the beam profile (red dashed line, maximum and minimum values are normalised). A similar curve is found in Fig. 4.31(b) using eight beams: the sawtooth period decreases when all beams are deposited inside $q = 1$ and increases when they start to pass $q = 1$ surface. Since the beam at the smallest ρ_{dep} is used as the reference beam of each group, the period starts to increase at negative values of $\rho_{dep} - \rho_{q=1}$ because the profile is wider (see Fig. 4.28(b)). Furthermore, the destabilising effect on the sawtooth period is clearer than in the first case since a larger amount of EC power (6.88MW) (and driven current) is deposited inside $q = 1$ surface. The shape of the sawtooth period curve is still similar to the beam shape. Note that the location of the red dashed curve is chosen to match the overall profile but does not correspond to the ρ_{dep} value at maximum sawtooth period.

By contrast, with sixteen beams (13.76MW, Fig. 4.31(c)) there is a disagreement between the shape of the sawtooth period curve and the beam shape, at least near the edges of the profile. In this case the outermost beam of the group is already near the $q = 1$ surface when the innermost beam of the group is at a destabilising position, therefore the mixture of stabilising and destabilising effects of the beams leads to a mismatch between

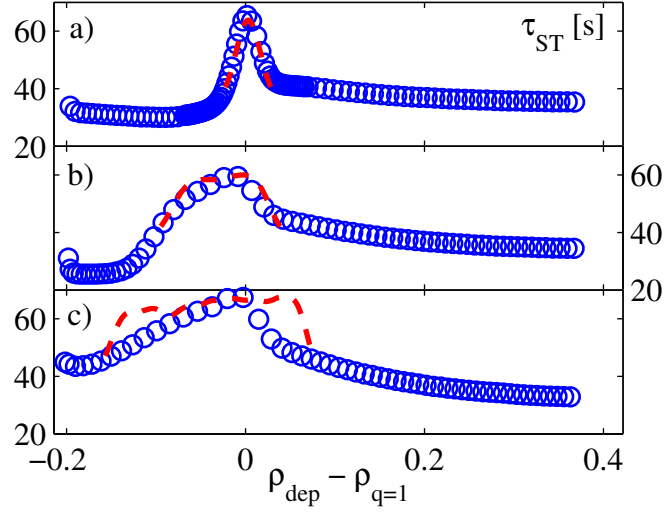


Figure 4.31: Sawtooth periods result (blue, circle) from EC beam sweeping with different EC profiles (red, dashed) as a function of distance to the $q = 1$ location: $(\rho_{dep} - \rho_{q=1})$. (a) With 4 beams, 3.44MW gives maximum 65s sawtooth period near by $q = 1$ surface and minimum period 30s inside $q = 1$ surface. (b) same curve with 8 beams, 6.88MW and (c) 16 beams, 13.76MW, respectively. The maximum sawtooth period (59s, 67s, respectively) appears around $q = 1$ surface for both, while the minimum (25s) appears only for (b).

the sawtooth period curve and the beam shape. In addition, the destabilising effect has disappeared since it is not possible to have all the power deposited inside of $q = 1$ given the beam width at the most central aiming position. Note that the beam shape displayed in this figure is wider than the one from Fig. 4.28(c), since in that figure $\rho_{dep} \sim 0.68$, whereas $\rho_{q=1} \sim 0.44$; the distance between the 4 beams of one USM increases at smaller radius and the widths increase as well. The γ values of the 4 USM used for this profile are chosen to provide the tightest packing.

The maximum sawtooth periods are approximately 65s, 59s and 67s with the injected powers 3.44MW, 6.88MW and 13.76MW, respectively. Despite the power differences, the maximum sawtooth periods are similar because of the profile widths: although adding more beams increases the power, only the power that is localised very near the $q = 1$ surface helps increasing the sawtooth period. This non-intuitive result demonstrates why it is important to perform these simulations using the expected real mirror geometry.

Sawtooth pacing

Sawtooth pacing [Goodman:PRL2011] is one promising method to control the sawtooth period to avoid triggering NTMs. Sawtooth pacing can be used for either stabilising or destabilising sawteeth. For stabilising, pacing results in long sawteeth that may trigger NTMs; therefore, each crash should be followed by pre-emptive NTM control at the mode resonant surfaces. Alternatively, one can destabilise sawteeth with pacing to avoid the creation of large NTM seed islands. It should be noted that the shortest sawtooth periods are expected with high continuous wave (CW) power inside of $q = 1$ and no pacing. However NTMs might still be triggered, in which case a better strategy is to control the

sawtooth in order to control the timing of the sawtooth crashes and apply preemption. It might also turn out that long sawtooth periods with targeted preemption leads to better performance. The EC beam sweeping result shows the most effective deposition locations for stabilising and destabilising. For the 3.44MW case, the largest (smallest) τ_{ST} can be achieved at $\rho_{dep} \sim 0.43$ (~ 0.34).

Sawtooth pacing simulation results for the 3.44MW case are shown in Fig. 4.32 for both stabilisation (Figs. 4.32(a), (b)) and destabilisation (Figs. 4.32(c), (d)). In the simulation, the EC power is on for the selected pulse width τ_{set} and then is turned off until the subsequent sawtooth crash. When the sawtooth crash is detected, the EC power turns back on and the cycle repeats. For stabilisation, τ_{set} is changed from 40s \rightarrow 60s in steps of 5s (the choices bounded by $\tau_{ST}^{Max} = 65$ s, CW and $\tau_{ST}^{ref} = 36$ s, with no EC control power). In Fig. 4.32(a), the blue curve shows the resulting sawtooth period and the red curve, the control pulse-width value τ_{set} . As expected, the sawtooth periods are not the same as the pulse widths; there is some delay between the end of the EC power pulse and the time of the crash. This delay time ($\tau_{ST} - \tau_{set}$) is, however, nearly constant for a given τ_{set} : in other words, τ_{ST} is well paced by the applied EC power, so the sawtooth crash time becomes predictable. The curves are continuous in Fig. 4.32 because each sawtooth is controlled. (In the locking examples of Fig. 4.39 in later section, the individual crash periods are shown since, at each change of τ_{set} , at least one crash is not locked).

Properly placed EC power retards the evolution of s_1 and $\delta\hat{W}$, and results in the long sawtooth period. As soon as EC power is removed, the evolution quickly returns to its natural rate. If the EC power is turned off when s_1 and $\delta\hat{W}$ are close to their respective thresholds, the subsequent faster evolution results in a sawtooth crash with a short delay, as in the case of $\tau_{set} = 60$ s in Fig. 4.32(b). However, if $\tau_{set} = 40$ s, even though s_1 and $\delta\hat{W}$ increase quickly after EC is off, it takes more time to reach the threshold resulting in a longer delay. In general on ITER the delays are on the order of seconds; the longest delay shown here being about 4.4los. During this delay time, it is anticipated that the same USMs that aims at the $q = 1$ surface to pace sawteeth can move to pre-empt NTMs as far away as the $q = 2$ surface.

From the ASTRA simulation, the $q = 1$ and the $q = 2$ surface are located at about $\rho_{tor} = 0.42$ and 0.75, which are converted to the poloidal angle (α) 63° and 47° , respectively. The present launcher design will allow movement from the $q = 1$ to the $q = 2$ surface within ~ 1.0 s (maximum rate: 20° /s) or within ~ 2.5 s (slowest rate: 8° /s) [Collazos:FST2009]. Note that these rates correspond to a given step-up or down, and they are not symmetric due to the technical constraints in the mirror actuator design. Barring other plasma operation constraints, the paced sawtooth period can be chosen for convenience to permit the same ULs to be used for both pacing and preemption. However, the USMs are required to return to their $q = 1$ aiming position after preemption, so the pacing scenarios investigated to date on TCV (in which the power is turned on at the $q = 1$ immediately at the time of the crash) are not directly applicable. Therefore a modified pacing scenario, in which the power is turned on a short time after the crash would be applicable as shown in Fig. 4.33. EC power is applied 10s after a sawtooth crash and turned off at 40s as in the case when EC power is turned on directly after the crash. The sawtooth period is again well paced. The behaviour of s_1 (Fig. 4.33(a)) is also similar, as are the delays (Fig. 4.33(b), maximum 4.1s). This simulation result demonstrates that the same USMs can move the deposition repeatedly, back and forth, between $q = 1$ and

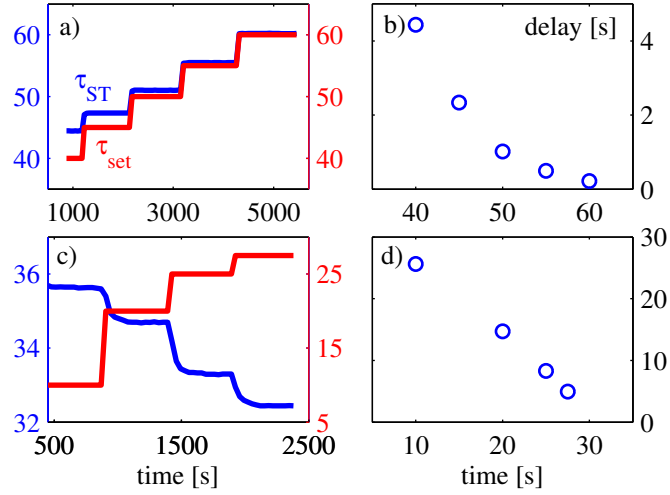


Figure 4.32: Sawtooth pacing on stabilisation and destabilisation position show that sawtooth period control is feasible to avoid NTM. (a) and (c) show the sawtooth period (blue) and EC modulation period (red). In (b) and (d), the delay between the end of the EC power pulse and the time of the sawtooth crash are shown. For both cases, sawtooth period is well paced or regulated with some delays.

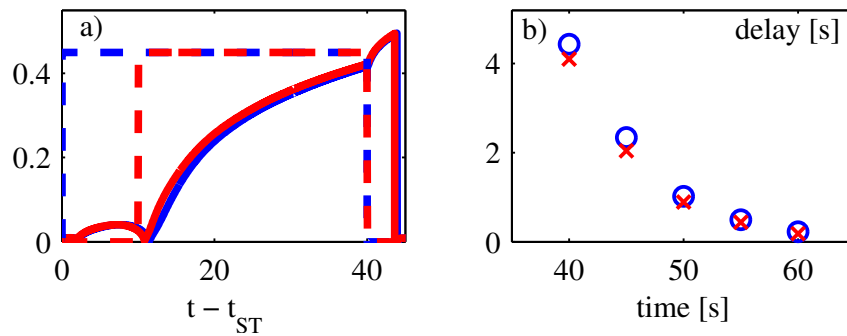


Figure 4.33: Magnetic shear (s_1) evolutions (solid) and EC power traces (dashed) are shown in (a) for both EC on right after crash (blue) and after 10s (red) cases for 40s τ_{set} . (b) With 10s late start, sawtooth period is still well paced and the delays are similar.

$q = 3/2$ or 2 surfaces in the required time range to accomplish both sawtooth pacing and NTMs preemption/stabilisation.

Figures 4.32(c) and (d) show the pacing simulation results for destabilisation: the sawtooth period and EC pulse length in Fig. 4.32(c) and the delay in Fig. 4.32(d). Contrary to the stabilisation case, s_1 and $\delta\hat{W}$ evolve more quickly when the EC power is on so the EC deposition causes the sawtooth period to shorten as τ_{set} increases. When τ_{set} is small, EC injection does not have much effect on the sawtooth period: τ_{ST} is similar to the case without the controlling EC beams. When τ_{set} is large, the evolution of the two parameters is more rapid; but, for 3.44MW the difference between the natural sawtooth (without EC) and paced τ_{ST} is not significant ($< 10\%$ change). More EC power and current drive are needed to significantly shorten τ_{ST} as shown in Fig. 4.31(b). Nevertheless, the simulation shows that the sawtooth period can be shortened and paced so that the moment of the crash becomes predictable, permitting preemption of NTMs by appropriate application of EC power at the NTM resonant surface – as in the case of stabilisation. Again, it should be remembered that the smallest seed island is expected for the shortest sawtooth period and therefore with the injection of CW EC power.

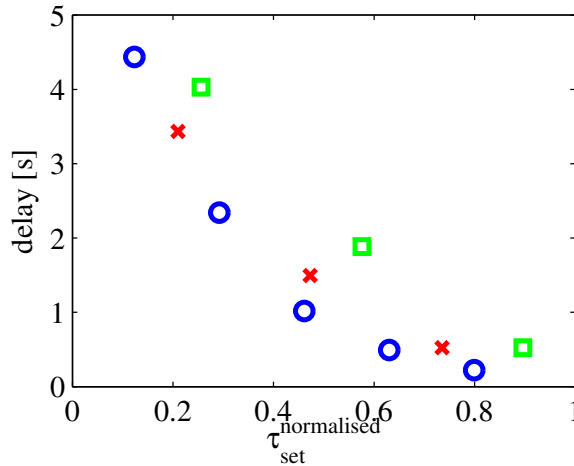


Figure 4.34: Delays for fixed power 3.44MW and different deposition position, $\rho_{dep} = 0.432$ (blue circle), $\rho_{dep} = 0.42$ (red cross), $\rho_{dep} = 0.442$ (green square) with normalised τ_{set} .

In this simulation work, it is easy to find the maximum sawtooth period and the corresponding EC beam position. However, in the real experiment, it is quite difficult to find the exact maximum position. It is more likely that the EC deposition position will be either inside or outside of the maximum position. (It is known, both experimentally and in simulations, that changing the power causes the $q = 1$ surface to shift slightly, so in practice, if more power is suddenly required to control τ_{ST} , one must expect the position of the control profile to change relative to the actual $q = 1$ location.) Therefore it is necessary to test the sensitivity of sawtooth control on either side of the position of maximum effect. To that end, the same pacing simulation is carried out with 3.44MW at two other deposition positions: $\rho_{dep} = 0.42$ and $\rho_{dep} = 0.442$. In Fig. 4.31(a), these positions correspond to -0.0106 and 0.0164 on the abscissa and the sawtooth periods are 55s and 51s, respectively.

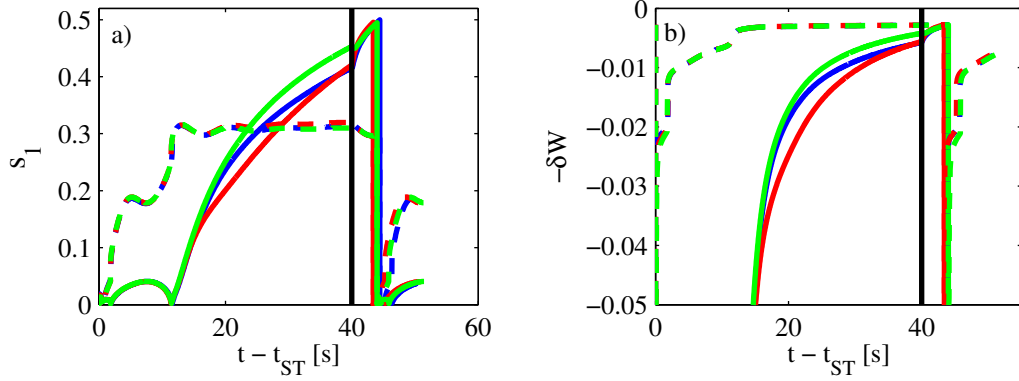


Figure 4.35: The evolution of (a) s_1 (solid) and $s_{1,crit}$ (dashed), (b) $-\delta\hat{W}$ (solid) and $-c_\rho\hat{\rho}$ (dashed) for different deposition position, $\rho_{dep} = 0.432$ (blue), 0.42 (red), 0.442 (green) with fixed power 3.44MW . EC power is turned off at 40s (black line). s_1 and $-\delta\hat{W}$ values at 40s and the growth rates determine delay and sawtooth period.

Given these maximum sawtooth periods, τ_{set} is chosen between 40s and 50s in both simulations. The resultant delays are shown in Fig. 4.34 with the $\rho_{dep} = 0.432$ case ($\tau_{ST}^{Max} = 65\text{s}$, blue circle) as a reference. Since these three cases have different maximum sawtooth periods, the τ_{set} data is normalised using $\left(\tau_{set}^{normalised} = (\tau_{set} - \tau_{ST}^{ref}) / (\tau_{ST}^{Max} - \tau_{ST}^{ref})\right)$, where $\tau_{ST}^{Max,ref}$ are the maximum sawtooth period with CW heating and the reference sawtooth period without EC control power ($\tau_{set} = 0$). Compared to the reference case, both of these latter cases have longer delays for the same $\tau_{set}^{normalised}$ ($\rho_{dep} = 0.42$ case (red cross) has shorter delays than $\rho_{dep} = 0.442$ (green square)). The full-width half-maximum beam sizes are $w_{FWHM} \sim 0.032$ in these three simulations and the delays increase with the absolute value of the distance of the deposition from the optimum position normalised to the beam width (i.e. $\delta = 0, |-0.33|, 0.53$ for $\rho_{dep} = 0.432, 0.420, 0.442$, respectively).

Further analysis of the sawtooth crash criteria, for $\tau_{set} = 40\text{s}$ and each case of ρ_{dep} , is carried out with the help of Fig. 4.35. The abscissa is the time relative to the preceding crash: the black vertical line at $t - t_{ST} = 40\text{s}$ indicates the moment at which the EC beam is turned off. Shear is shown on the vertical axis of Fig. 4.35(a); s_1 (solid) and $s_{1,crit}$ (dashed) curves are presented for the three cases. Before the crash, s_1 is already greater than $s_{1,crit}$ and after the EC power is turned off s_1 increases quickly, as described above. At 40s, the $\rho_{dep} = 0.42$ case (red) has a similar but slightly larger s_1 value than the $\rho_{dep} = 0.432$ case (blue). After the removal of the power, all cases have similar increasing rates of change (though the $\rho_{dep} = 0.442$ case (green) is slightly slower).

Figure 4.35(b) shows the two important terms of the first expression of Eq. 4.22: $-\delta\hat{W}$ (solid) and $-c_\rho\hat{\rho}$ (dashed). Since all the three component of $-\delta\hat{W}$ depend on s_1 , the solid curves are qualitatively similar to those of s_1 in Fig. 4.35(a). Starting from 40s, $\rho_{dep} = 0.432$ (blue) and 0.42 (red) have similar $-\delta\hat{W}$ values and rates of increase; the $\rho_{dep} = 0.442$ case (green) has larger $-\delta\hat{W}$ and a slower rate of increase. For all three cases, the $-c_\rho\hat{\rho}$ curves are very similar; therefore, if $-\delta\hat{W}$ of the $\rho_{dep} = 0.442$ case were to start from the same value as the other two cases, the delay would be even longer than that shown in Fig. 4.34. As mentioned above, the $\rho_{dep} = 0.442$ case has little effect on

Chapter 4. Control of sawtooth instability

Table 4.1: 8 or 16 different beams position used for pacing simulation. In ρ_{ij} : i represents the launcher index and j indicates the beam index.

	ρ_{11}	ρ_{12}	ρ_{13}	ρ_{14}
8 beams	0.413	0.4636	N/A	N/A
16 beams	0.42	0.4695	0.5110	0.5495

	ρ_{21}	ρ_{22}	ρ_{23}	ρ_{24}
8 beams	0.4256	0.4743	N/A	N/A
16 beams	0.42	0.4695	0.5110	0.5495

	ρ_{31}	ρ_{32}	ρ_{33}	ρ_{34}
8 beams	0.4383	0.4851	N/A	N/A
16 beams	0.4448	0.4906	0.5295	0.5657

	ρ_{41}	ρ_{42}	ρ_{43}	ρ_{44}
8 beams	0.4509	0.4959	N/A	N/A
16 beams	0.4448	0.4906	0.5295	0.5657

τ_{ST} . In the case of longer τ_{set} , the $\rho_{dep} = 0.42$ case will show a larger percentage change from the $\rho_{dep} = 0.432$ case because the average power per cycle is higher and the effect on $q = 1$ surface will be larger. For example, though the delay is $\sim 10\%$ longer than for the optimised case at $\tau_{set}^{normalised} \sim 0.2$, it is $\sim 50\%$ longer at $\tau_{set}^{normalised} \sim 0.75$ (see Fig. 4.34).

Coming back to deposition at the optimum stabilisation location, ρ_{dep}^{opt} , the influence of higher powers is studied. Figures 4.36 and 4.37 compare three power cases: $\rho_{dep}^{opt} = 0.432$ with 3.44MW (4 beams profile, blue), $\rho_{dep}^{opt} = 0.413$ with 6.88MW (8 beams profile, red), and $\rho_{dep}^{opt} = 0.42$ with 13.76MW (16 beams profile, green). Unlike the 3.44MW case in which the beams from four USMs can be exactly overlapped, for the other two cases, the sources cannot be perfectly aligned so the achievable profile parameters for the ITER ULs are different, as shown in the Table 4.1. There, ρ_{ij} indicates the beam deposition position from different {launcher (i), beam(j)}. For instance, ρ_{23} represents the deposition position of the third beam from the second launcher. For the 8 beams case, only the first two beams from each launcher are used; for the 16 beams case, launchers (1, 2) and (3, 4) have the same γ .

For each case, τ_{set} is changed in 5s steps from 40s to 55s (6.88MW case), or from 40s to 65s (13.76MW case) – to roughly match the maximum possible sawtooth period at the given power. Figure 4.36 replicates Fig. 4.34 for these cases, showing the different delays. This figure shows that the wider beam with higher power results in longer delays, relative to the reference case (3.44MW).

Figure 4.37 gives more detail of the simulations to explain the different delays, in a way similar to Fig. 4.35. Again, $\tau_{set} = 40s$ for all cases. Figure 4.37(a) shows s_1 (solid) and $s_{1,crit}$ (dashed) for each case and Fig. 4.37(b) shows $-\delta\hat{W}$ (solid) and $-c_\rho\hat{\rho}$ (dashed).

All three cases have different s_1 evolution at the beginning as in the previous case in

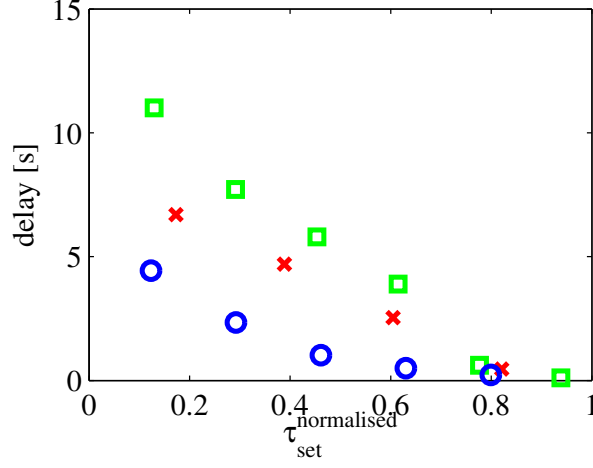


Figure 4.36: Delays for different EC power at the maximum sawtooth period position, 3.44MW at $\rho_{dep} = 0.432$ (blue circle), 6.88MW at $\rho_{dep} = 0.413$ (red cross), 13.76MW at $\rho_{dep} = 0.42$ (green square) with normalised EC modulation period.

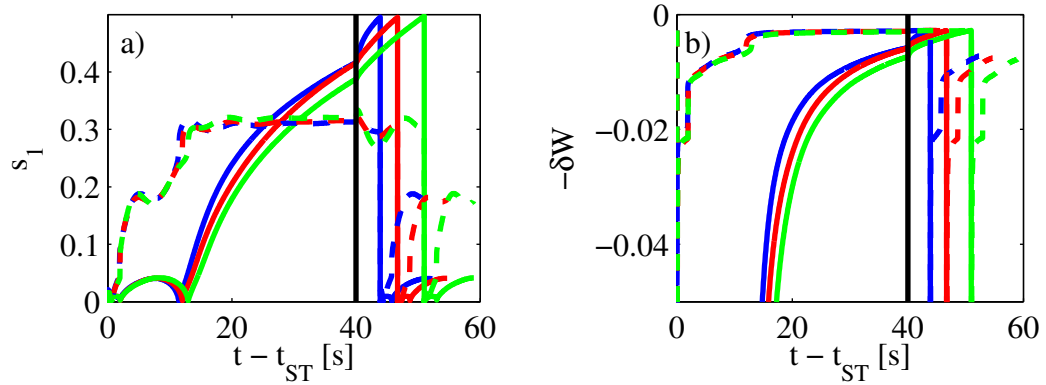


Figure 4.37: The evolutions of (a) s_1 (solid) and $s_{1,crit}$ (dashed), (b) $-\delta\hat{W}$ (solid) and $-c_\rho\hat{\rho}$ (dashed) are shown for different EC powers; 3.44MW at $\rho_{dep} = 0.432$ (blue), 6.88MW at $\rho_{dep} = 0.413$ (red), 13.76MW at $\rho_{dep} = 0.42$ (green) and EC power is turned off at 40s (black). s_1 and $-\delta\hat{W}$ values at 40s and the growth rates determine the delay to the crash and thus the sawtooth period.

Fig. 4.35(a). At higher power, the EC beam slows the evolution of s_1 . After ~ 12 s, the 3.44MW case has a faster increase of s_1 than the other two cases, which have almost the same rates (up to ~ 20 s). As long as the EC beam is deposited far outside of the $q = 1$ surface, there is no effect on the shear evolution. Due to the narrower beam width, for 3.44MW case, the $q = 1$ surface gets closer to the EC deposition position later than in the other cases and the effective current density is lower. Therefore the EC beam affects less the shear evolution and the shear evolves with almost the natural rate. Beyond ~ 20 s, as the $q = 1$ surface and EC deposition position become closer, the strong EC beam effect retards the shear evolution, depending on the effective current density and the distance between the $q = 1$ surface and the beam position. In both the 6.88MW and the 13.76MW cases, the $q = 1$ surface is located within a beam width of ρ_{dep} ($\rho_{q=1} = 0.4291, 0.4292$, for 6.88MW and 13.76MW, respectively). However for the 6.88MW case, the source at smallest radius ($\rho_{dep} = 0.413$) is further away from $\rho_{q=1}$ than in the 13.76MW case ($\rho_{dep} = 0.42$), and is thus less stabilising, explaining the faster average s_1 time evolution. After EC beam turns off, s_1 evolves very rapidly for the low power and narrow beam, because s_1 is modified only very locally by the EC injection. The curves in Fig. 4.37(b) evolve like the shear evolution; $-\delta\hat{W}$ of the 3.44MW case has a larger slope and increases rapidly after the EC power is turned off, while the other two cases have the same slope until the sawtooth crash, albeit with different initial values coming from the differences in power. Comparing the 3.44MW to the 6.88MW, or 13.76MW cases we see a different behaviour of s_1 and $-\delta\hat{W}$ during and after the EC phase; but, comparing the 6.88MW to the 13.76MW cases shows that they do not differ significantly in their behaviour – except for the initial evolution which results in the different delay. Therefore, both the beam width and the power affect the delay in the cases studied to date.

Sensitivity study on the effects of the free parameters and the predicted sawtooth period

In this work, two free parameters c_ρ and c_f are employed to set the reference sawtooth period. These parameters are required since the threshold value and the exact fast particle stabilising contribution of burning plasmas is difficult to predict, without the ITER results. Different sets of c_ρ and c_f may affect the results; therefore, it is necessary to test the dependence on these parameters. In an ITER plasma, due to the strong effect of α -particles (in the $Q \geq 10$ scenario), it is anticipated that $\delta\hat{W}_{fast}$ is larger than $\delta\hat{W}_{KO}$ (hence, our use of $c_f = 2$; so that $\delta\hat{W}_{fast}$ is about $1.5\delta\hat{W}_{KO}$). We determined c_ρ to reach our reference sawtooth period of 36s in the reference case. Then, to test the sensitivity of our results to these “educated guesses”, we increased c_f up to 8 (requiring $c_\rho = 7.72$ to get the same reference sawtooth period) and also changed the “target” sawtooth period to 100s. We performed simulation with these new parameters with the 3.44MW power case. Note that these lead to a variation of s_1 at the time of the crash from 0.5 (40s sawtooth period) to 0.75 (200s sawtooth period).

Testing first the cases with 36s as the reference sawtooth period, and performing an EC beam sweeping simulation, we find that the sawtooth period curves are almost the same. Furthermore the most stabilising position with ($c_\rho = 7.72$, $c_f = 8$) is $\rho_{dep} = 0.432$, as in the reference case ($c_\rho = 0.12$, $c_f = 2$). The maximum period is slightly different (i.e. within a few percent). Based on this, pacing simulations have been performed with

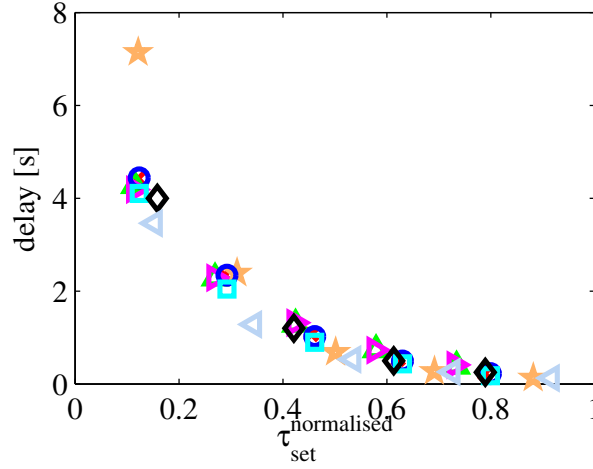


Figure 4.38: Delay for fixed power 3.44MW with different set of (c_ρ, c_f) . Blue circle: (0.12, 2), red cross: (0.55, 2.34), green upper triangle: (6.45, 7), magenta right triangle: (7.72, 8), cyan square: (0.12, 2) with 10s late EC beam, light blue left triangle: partial reconnection case with $w_{norm} = 0.5$ (0.12, 2.725), black diamond: locking case (0.12, 2), yellow star: long reference period 97s case (0.12, 2.9). All the data are laid on the same curve.

the same modulation period range (40 ~ 60s) and the results are shown in Fig. 4.38. In this figure the pacing delay of all cases are plotted versus the normalised set time. We also show the case with $(c_\rho = 0.12, c_f = 2.9)$, in which the reference sawtooth period is 97s and, from the sweeping, the maximum period is 202s at $\rho_{dep} = 0.45$. In this case, pacing simulations have been performed with τ_{set} from 110s to 190s in steps of 20s. The results are also presented in Fig. 4.38 with yellow stars. For the shortest modulation period, the delay is longer but otherwise all the results follow the same curve. Therefore we are confident that the basic dependencies presented here do not depend on the chosen “boundary conditions”. This is due to the fact that the effects mainly depend on the characteristic time evolution of s_1 , on the relative position of the beams with respect to $q = 1$ near the time of the sawtooth crash, on the power, and on the deposition profile.

Sawtooth locking

Sawtooth locking [Lauret:NF2012, Witvoet:NF2011] is very similar to sawtooth pacing, except it is based on feed-forward instead of feedback control. For pacing it is essential to detect the sawtooth crash to trigger the EC power modulation (using a given τ_{set} or τ_{set} waveform, which can, itself, be feedback controlled [Felici:Thesis]). For locking, the modulation period and duty cycle, are pre-determined and the sawtooth period locks to the feed-forward period if the duty cycle lies within a certain range of values. Figure 4.39 shows one example of sawtooth locking. The reference beam aiming is the same as for the pacing case; perfectly aligned beams from 4 USMs (3.44MW) are aiming at $\rho_{dep} = 0.432$ to maximise the sawtooth period. The upper panel of the figure is the sawtooth period (blue circle) and EC modulation period setting (red, solid line) and the bottom panel is the duty cycle feedforward setting. The EC modulation period is 50s and duty cycle

is increased from 10 to 90% in steps of 10%. These two control parameters determine the EC power on-off time. With the proper duty cycle, the sawtooth period locks to the modulation period; in this case, from 30% upward. This demonstrates that the same sawtooth period can be obtained with different duty cycles, meaning that it is possible to control the sawtooth period with low, as well as high, average power. During pacing, the duty cycle is not a control parameter, but the resulting pacing power waveforms can be converted to period and duty cycle. During TCV-like pacing, the duty cycle is typically large (e.g. 80~95%) at the same sawtooth period as during locking. Thus, once the locking range is determined, one can control τ_{ST} with less average power using locking than with pacing (at least as pacing is presently implemented – with the turn-on of power immediately after the crash). In the locking simulations, the abrupt change in duty cycle leads to a temporary loss of locking; however, control is regained after a few sawtooth periods.

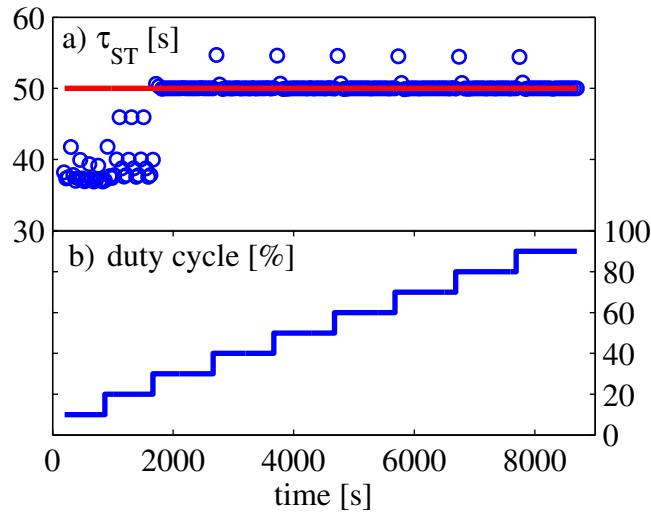


Figure 4.39: (a) Sawtooth period (blue circle) and EC modulation period (50s, red) and (b) duty cycle are presented. Sawtooth period locks to the modulation period from 30% to 90% duty cycle.

Basic locking simulation have been carried out with 3.44MW EC power and the same four different deposition positions as in the pacing case; one position for destabilisation ($\rho_{dep} = 0.34$) and three stabilisation positions ($\rho_{dep} = 0.42, 0.432, 0.442$). Appropriate ranges of modulation periods are chosen (as in the pacing cases) and for each ρ_{dep} the duty cycle is stepped from 10 to 90 %. In these locking cases the sawtooth period is the same as the modulation period, therefore we use τ_{ST} as the characteristic time. A locking map of the normalised sawtooth period versus the duty-cycle can be obtained from the locking simulation as shown in Fig. 4.40. (The normalised sawtooth period is defined as $(\tau_{ST} - \tau_{ST}^{ref}) / (\tau_{ST}^{Max} - \tau_{ST}^{ref})$ – similar to the pacing case with τ_{set} replaced by the sawtooth period – and plotted on the vertical axis. Note that for the destabilisation case, τ_{ST}^{min} is used instead τ_{ST}^{Max} .) The successful locking cases are indicated by blue circles. Red crosses indicate where the sawteeth failed to lock. The results from pacing simulation (green triangle) are added on each locking map. (The actual paced sawtooth

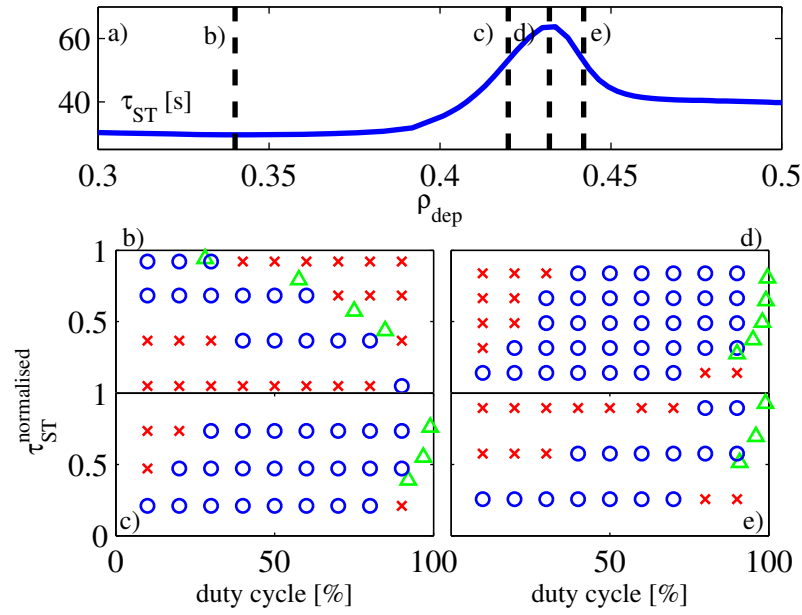


Figure 4.40: Sawtooth locking range at different positions: $\rho_{dep} = (b) 0.34, (c) 0.42, (d) 0.432, (e) 0.442$ with fixed power 3.44MW are shown with sawtooth period curve. Each coloured marker indicates locking (blue circle), non-locking (red cross) and pacing (green triangle) cases, respectively. Depending on the beam deposition position, the s_1 and $-\delta\dot{W}$ evolutions are different and it brings various locking ranges.

period $\tau_{ST} = \tau_{set} + delay$ is used and the duty cycle is defined by τ_{set}/τ_{ST} .) There are four different locking ranges. At $\rho_{dep} = 0.432$ (Fig. 4.40(d)), the locking range is largest. When inside of $\rho_{q=1}$, $\rho_{dep} = 0.42$ (Fig. 4.40(c)), the range is somewhat reduced, but is still larger than when outside of $\rho_{q=1}$, $\rho_{dep} = 0.442$ (Fig. 4.40(e)), where the range is narrower despite the fact that the maximum τ_{ST} is the same as at $\rho_{dep} = 0.42$.

Looking at the evolutions of s_1 and $-\delta\hat{W}$ can help us to understand these differences. Unlike pacing, the EC power turn-on and turn-off times, relative to the moment of the crash, depend on the modulation period and duty cycle. Therefore, it is necessary to investigate the change in the evolution when EC power is turned on as well as turned off (our only time of interest in the pacing case).

Figure 4.41 shows successful locking with 45s (34s) modulation period and 50% (60%) duty cycle for the three stabilisation (destabilisation) deposition locations. The black dashed lines indicate the EC power trace that causes the change of the s_1 (blue) and the $-\delta\hat{W}$ (red) evolutions when EC power turns on and off. In the $\rho_{dep} = 0.42$ case (Fig. 4.41(b)) after EC beams turn on, s_1 and $-\delta\hat{W}$ decrease initially but then increase with a slower rate than during the non-EC phase, prior to that moment. In the other stabilising deposition location cases, these parameters increase rapidly and then continue at the slower rate. In addition, as seen in Fig. 4.35, the evolutions when at $\rho_{dep} = 0.42$ are faster than at $\rho_{dep} = 0.432$, though after the EC power turns off the evolution rate is the same. The combination of these effects results in the same sawtooth period for each case, but these fine details lead to slightly different locking ranges. For the $\rho_{dep} = 0.442$ case, the first increase at power turn-on is larger than for $\rho_{dep} = 0.432$; and while the EC power is on, s_1 and $-\delta\hat{W}$ grow faster. Therefore when at $\rho_{dep} = 0.442$, it is necessary to have EC power earlier in the sawtooth cycle for locking to occur (that is, only the higher duty cycle cases lock), resulting in a narrower locking range.

Figure 4.40(b) is for $\rho_{dep} = 0.34$ - far inside of $\rho_{q=1}$. For this destabilisation case, the locking range is qualitatively different from the stabilisation cases - i.e. it is centred around the diagonal from (1,0%) to (0,100%), instead of (0,0%) to (1, 100%). Again, the pacing points (green triangles) are at the edge of the successful locking zone. No particular effect is evident on the s_1 and $-\delta\hat{W}$ curves in Fig. 4.41(a) (34s modulation period, 60% duty cycle) except at the very beginning. With a large duty cycle, the EC beam turns on very early and shortens the beginning of the evolution causing a shorter sawtooth period. Therefore, for destabilisation locking, the range is determined by how the initial evolution is affected. These four different locking ranges are qualitatively consistent with the detailed locking simulation results for a TEXTOR size tokamak in Ref. [Witvoet:NF2011] (Fig. 7).

In Fig. 4.42, the effect on the locking range of increasing the power (with the concomitant change in beam profile, as described above) is shown: the power levels are 3.44MW ($\rho_{dep} = 0.432$), 6.88MW ($\rho_{dep} = 0.413$), and 13.76MW ($\rho_{dep} = 0.42$). In Fig. 4.42(a) the modified pacing case - with a 10s delay in the start of the power - (green, down pointing triangle) is also overlaid with other cases. As previously, changes in the s_1 and $-\delta\hat{W}$ evolutions result in these differences. Now, however, the phase of the modulation with respect to the sawtooth period plays a stronger role. Since higher EC power injection affects the s_1 and $-\delta\hat{W}$ evolutions more strongly, it is necessary to put EC power earlier in the sawtooth cycle than in the lower power case to have the same locked period. Similarly, with higher duty cycle, the EC power should be injected earlier to have less

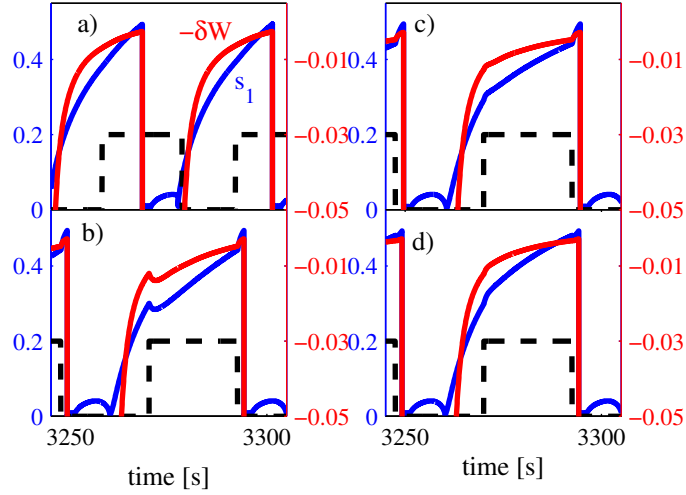


Figure 4.41: The evolution of s_1 (blue) and $-\delta\hat{W}$ (red) for $\rho_{dep} = (a) 0.34, (b) 0.42, (c) 0.432, (d) 0.442$. These figures show the different behaviour when EC power is on with respect to when it is off (black dashed), for stabilisation cases. For the destabilisation case ($\rho_{dep} = 0.34$), the EC beam affects the beginning of the evolution.

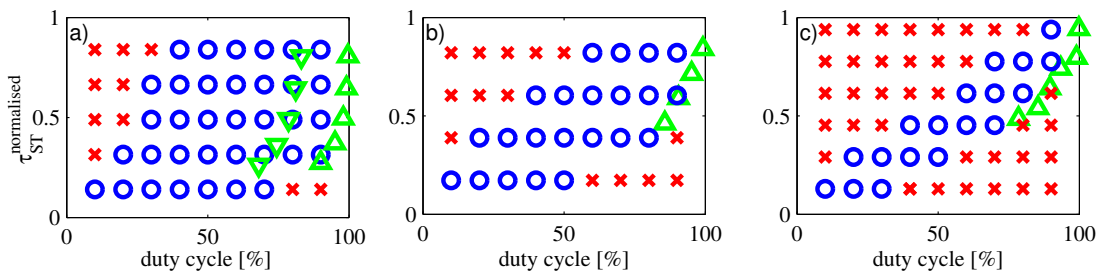


Figure 4.42: Locking range for three different power case, (a) 3.44MW ($\rho_{dep} = 0.432$), (b) 6.88MW ($\rho_{dep} = 0.413$), (c) 13.76MW ($\rho_{dep} = 0.42$). As well as the different s_1 and $-\delta\hat{W}$ evolution, locking range is dependant on the EC modulation phase and delay. Different delay set the boundary of maximum duty cycle for locking on each modulation period and therefore high power case has narrower locking range.

effect on the changes of the s_1 and $-\delta\hat{W}$ evolutions. As an example, the evolutions of the $q = 1$ radius, and the s_1 (solid) and EC power traces (dashed) for 3.44MW (blue), 6.88MW (red), 13.76MW (green) are shown in Figs. 4.43(a) and (b). The locking period is 40s and the duty cycle is 30%. The outermost $q = 1$ radius is taken if multiple $q = 1$ surfaces exist, which leads the rapid change of the $q = 1$ radius at 2 and 11s. The $q = 1$ radius fully evolves within 20s and its final value does not seem to be altered much by the level of EC power. Similarly, the central temperature increases rapidly after a crash, within 5s, consistent with the confinement time of about 2.7s. The effect of the EC power on the s_1 evolution is larger when the power is injected later, with respect to the sawtooth crash, than earlier. Accordingly, sawtooth stabilisation (lengthening the period) is stronger. Therefore with higher power, the phase of the EC power with respect to the sawtooth crash slips so that the EC power is effectively turned on earlier in the sawtooth cycle and eventually settles where the resultant s_1 values at 40s are similar. This explains why the high power case actually has a smaller locking range (Fig. 4.42(c)), as detailed below. Fig. 4.43(c) shows an example in which we use the same power (3.44MW) in each simulation, but different duty cycle (30% (blue), 50% (red), 70% (green)). With higher duty cycle a larger averaged power (per sawtooth cycle) is deposited and the effects are similar to higher power injection.

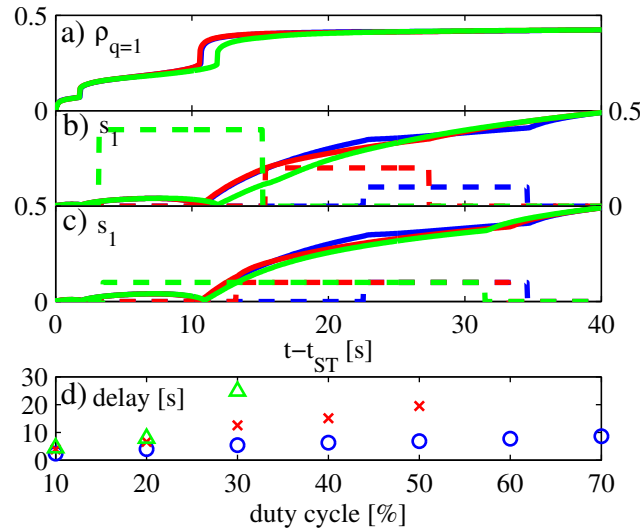


Figure 4.43: Evolution of (a) $\rho_{q=1}$, (b) s_1 (solid) and EC power on-off trace (dashed) for 40s locking period with fixed duty cycle 30% and different powers 3.44MW (blue), 6.88MW (red), 13.76MW (green) and (c) fixed power 3.44MW and different duty cycle 30% (blue), 50% (red), 70% (green). As EC power and duty cycle increase, EC power is turned on in earlier phase of sawtooth cycle and cause (d) longer delay.

These simulations show that higher power and/or duty cycle cause a longer delay between the sawtooth crash and the time when the EC power is turned off (Fig. 4.43(d), 40s locking period, 3.44MW (blue, circle), 6.88MW (red, cross), 13.76MW (green, triangle)). Sawteeth lock to the modulation period only when the crash occurs during the phase that the EC power is off. In other words, the delay has to be shorter or equal to the time interval for which the EC power is off, for successful locking. However, as power and/or

duty cycle increase, the delay gets closer to this time interval and at some point is longer than the EC off-time interval, so no locking occurs. As shown in Fig. 4.43(d) the delays of the higher duty cycle case are already similar to, or longer than, the EC off time of the next preplanned step in duty cycle. For instance, in the 13.76MW case, the delay when at 30% duty cycle is about 25s whereas when using 40% duty cycle the EC off-time interval is 24s. Therefore for 40% duty cycle, the sawtooth period cannot be regularly locked. These EC modulation phase and delay differences determine the shape of the locking ranges.

These results show the feasibility of controlling τ_{ST} on ITER by either locking or pacing, using the present design of the four USMs of the four ULs. After sweeping the beams to find the ρ_{dep}^{opt} for τ_{ST}^{Max} , a careful choice of control parameters can ensure that 1) locking or pacing will occur even if the position of $q = 1$ shifts with respect to the aiming location, and 2) the delay between the turn off of the power and the moment of the crash is long enough for the EC beams to reach the NTM resonant surfaces.

4.8 Summary

Central (sawtooth) and edge (ELM) instabilities are two of the common cyclic events that lead to meta-stable core modes (NTM) being triggered. Though sawteeth can have beneficial effects in burning plasmas, such as expelling helium ash and tungsten from the centre, long-lived NTMs are detrimental to fusion gain. Controlling the moment of the sawtooth crashes allows preemptive actions to be taken to mitigate NTMs.

As promising sawtooth control methods, sawtooth pacing [Goodman:PRL2011] and locking [Witvoet:NF2011, Lauret:NF2012] have been introduced. Sawtooth pacing and locking are techniques that control the stabilising influence of EC power on sawteeth. For pacing, EC power is removed or reduced after a given duration following a preceding sawtooth crash and is brought back to its initial level soon after the following crash is detected: a real-time control system is necessary for crash detection. For locking, the removal and reintroduction of EC power are determined by a pre-determined modulation period and duty cycle: real-time sawtooth crash detection is not required. Both methods have been experimentally demonstrated on the TCV tokamak [Goodman:PRL2011, Lauret:NF2012, Felici:Thesis]. Using pacing, the period of individual sawteeth is precisely controlled; alternately, the sawtooth period locks to the EC power modulation for a range of combinations of duty cycle and period.

The experimental results have been reproduced by ASTRA simulations. For sawtooth pacing, the time delay between the removal of the EC power and the appearance of the next sawtooth crash for each modulation period has been shown to match those from TCV discharge #43687. The delay decreases with increasing modulation period. From the detailed evolution of the magnetic shear at the $q = 1$ surface, it has been shown that the shear evolves to near the critical value with long modulation periods such that the shear crosses the critical one soon after EC power is reduced. For sawtooth locking, simulations have been carried out to find the locking conditions (τ_{set} and duty cycle pairs) and, similar to pacing, the details of the shear evolution for each case have been investigated. The resultant locking range is in good agreement with the experimentally determined range. TCV discharges show successful sawtooth control using sawtooth pacing and locking and these techniques have begun to be tested in other tokamaks under various operation

conditions.

KSTAR has demonstrated that sawteeth are affected by EC injection depending on the deposition position and the direction of driven current. In order to extend the control capability, in the 2013 KSTAR experimental campaign, we have tested the feasibility of sawtooth locking using modulated EC power for sawtooth period control in the presence of fast particle from NBI. Since the real-time control system was not ready for sawtooth pacing, only locking was attempted.

The optimum deposition position was determined by the sweep of EC power across the plasma minor radius. The deposition position of the EC launcher has been set to 25cm above the mid-plane to produce a maximum sawtooth period of 100ms. With this constant EC deposition location, sawtooth locking experiments were performed. In a first test, a constant modulation period of 43ms and duty cycle of 70% were used. Sawteeth were somewhat regulated by the EC pulses, i.e. the sawtooth periods were similar to the modulation period; however, due to the varying integrated EC power per pulse, the sawtooth period varied some. In a second test with a constant modulation period of 62.5ms and duty cycle of 50%, the sawtooth period was regular. In this case, the EC-off duration was longer than the reference sawtooth period so that two different types of regulated sawtooth crashes were observed. The sum of these two periods matched the modulation period. The last test was carried out with a constant modulation period of 62.5ms and a duty cycle of 70%. The sawtooth crashes were random in this case and the sawteeth did not lock to the modulation period.

These experiments demonstrated that on the KSTAR tokamak sawteeth can be controlled by injection locking. Although the experimental results were not as clear as those on TCV, they represent a good start and should be followed by more experiments to complete the investigation of the capability of predictable sawtooth locking on KSTAR. They also showed that for locking experiments, the off-duration, increasing with decreasing duty cycles, needs to be larger than the reference sawtooth period (i.e. the period found at 0% duty-cycle).

Sawtooth locking experiments have also begun in AUG plasmas. As in KSTAR, the real-time sawtooth detection required for sawtooth pacing was not available in the control system, thus only sawtooth locking has been tested. NBI and IC auxiliary heating powers were injected, as well as EC power. As usual, by sweeping EC beams across the poloidal cross-section of the plasma, a maximum sawtooth period (here about 165ms at $\rho_\psi = 0.45$) was obtained, along with a corresponding EC deposition position chosen for locking experiments (here $\rho_\psi = 0.4$). Using the result from sweeping experiment, sawtooth locking simulations were performed to find the possible locking range in the range of modulation periods between 70 and 140ms and 10 to 90% duty cycles. Based on the sweeping experiment and simulations, sawtooth locking experiments were carried out. In the first case, the modulation period was fixed to 140ms and the duty cycle was varied from 90 to 30% in steps of 20%. The deposition position relative to the $q = 1$ surface turned out to be different than in the sweeping case and therefore the maximum sawtooth period was longer than the expected one. In some parameter combinations, sawtooth periods followed the modulation period even though the match (locking) between the two did not last long (i.e. no robust locking occurred). In a second test, the modulation periods of 70, 100 and 140ms were used at a constant duty cycle of 80%. The maximum sawtooth period was about 125ms in this case. Post-shot analysis has shown that the deposition position

was slightly inside the requested target position, and this different deposition position resulted in shorter sawtooth periods. Consequently, the 100ms modulation at 80% duty cycle resulted in longer sawtooth periods which did not lock; the modulation period of 140ms was unattainable, even if CW power had been applied. Though the two discharges had different maximum sawtooth periods, after normalisation of the modulation periods, the two cases could be compared to the simulation results. The experiment results did not fully match the simulation result, though there are similarities which help understanding the experimental results. The experimental time was limited and in order to understand better the behaviour of sawteeth and to determine the full sawtooth locking range, more experiments will be required. This experience suggests that when time is limited, it may be prudent to attempt the scenario that is most robust to variations in the experimental parameters to provide a clear demonstration. Thanks to our results with TCV, KSTAR, AUG and simulations, we can better determine this scenario.

Simulations of the ITER baseline scenario show that the EC control system can be used to control the sawtooth period with either locking or pacing methods [Kim:PoP2014]. The simplest sawtooth control method is to destabilise the sawteeth (shortening the sawtooth period) with continuous central co-current drive. However, only a 20 – 30% reduction of the sawtooth period is predicted [Zucca:Thesis, Chapman:NF2013, Kim:PoP2014] and NTMs might still be triggered. In addition, continuous power is not necessarily optimum for fusion performance or actuator sharing. This is why we have analysed the role of sawtooth control that is compatible with NTM preemption. Preemption is the most efficient NTM control method while pacing and locking are the most efficient sawtooth control methods. The effect of increasing the EC power dedicated to pacing/locking and the resulting additional control margin has been investigated. The power from up to 8 beams appears to be the optimum; since, because of the launcher geometry, the power deposition profile depends strongly on the total power (number of beams) injected. Furthermore the time between the removal of the sawtooth control power and the moment of the crash is simulated to be of the order of seconds on ITER. This will allow enough time for the upper launchers to move the deposition position from near the $q = 1$ surface to the 2/1 or 3/2 NTM mode resonant surfaces and thus to apply preemptive ECCD at the time of the crash. Similarly, simulations show that a pacing method that uses a delay between the crash detection and the turn-on of the EC power will allow sufficient time for the same beams to be repositioned near the $q = 1$ surface to pace the next sawtooth. We plan to test this pacing method on TCV in the future.

From the experiments on TCV, KSTAR and AUG, we have tested the applicability of sawtooth pacing and locking. The three tokamaks have different sizes, machine characteristics (e.g. superconducting coils for KSTAR), energy confinement time scales and sawtooth periods. In addition, the auxiliary heating systems are different. In order to fully analyse a technique developed on one machine for use on a different machine, one needs significant time resources to understand and take into account all the various details. Additionally, for the KSTAR and AUG experiments, attempts were made to garner a maximum of information from each discharge; reducing the surety of success. Since this was not fully successful, we suggest that future experiments be as simple as possible. Nevertheless, the experimental results from KSTAR and AUG hint at the capability of sawtooth period control using EC power in the presence of fast particles from NBI and IC powers and of impurity accumulation control as in AUG.

This can be extended to ITER for sawtooth period control with all the possible heating systems. As seen in the AUG experiment, the distance between the EC deposition and the $q = 1$ surface is an important parameter. Recently, real-time equilibrium reconstruction codes such as the real-time version of LIUQE: RT-LIUQE [Moret:FED2015] can estimate the q profile in real-time. Initial experiments indicate that due to various data errors and offsets, the exact position of the $q = 1$ surface cannot be accurately determined. Thus, at present, the EC deposition cannot track the $q = 1$ surface as introduced in Eq. 4.21 and as a result the effect of EC injection varies depending on the plasma equilibrium. Real-time transport codes such as RAPTOR [Felici:NF2011] may be a tool to estimate the correct position. This kind of code can evaluate transport equations combining the experimental data and the equilibrium calculation. Therefore it is expected that sawtooth control will be continually improved in future experiments.

The simulation of ITER sawtooth control has been carried out assuming a steady-state condition; the purpose of the simulation was to estimate the possible level of control of the sawtooth period and the feasibility of sawtooth pacing and locking (and NTM preemption not modelled) using the present EC launcher design. However, as seen in AUG experiment, in a complex system experiments may turn out to be much more complicated. Therefore, in order to prepare the real ITER experiment, more detailed simulation work such as taking into account IC stabilisation effects needs to be carried out.

Chapter 5

Real-time control of neoclassical tearing mode

5.1 Introduction

Neoclassical tearing modes (NTMs), destabilised mainly by a helically perturbed bootstrap current, can degrade plasma energy and limit the achievable β value below the ideal limit [Sauter:PoP1997, LaHaye:PoP2006]. NTMs are resistive tearing mode islands localised at a resonant rational surface, $q = m/n$, with m, n the poloidal and toroidal mode numbers respectively. The island formation causes an enhanced radial heat transport which results in a flattening of the temperature and pressure profiles inside the island [Chang:NF1990]. The modification of the pressure profile inside the island induces a helical perturbation of the bootstrap current which destabilises the mode and reinforces its amplitude [Callen:IAEA1987, Carrera:PoF1986, Sauter:PoP1997, Hegna:PoP1998]. Due to the flat kinetic profiles, the energy confinement time τ_E is degraded by as much as 35% for the 3/2 mode and up to 50% for the 2/1 mode as predicted for ITER [Sauter:PPCF2010]. In addition NTMs, which rotate in the laboratory frame, can interact with a resistive vacuum vessel wall, causing the plasma rotation to slow down and mode locking can eventually occur [Nave:NF1990]. The mode locking can bring further growth of the mode and lead to disruptions [Ramponi:PoP1999, Luce:PoP2004, Westerhof:NF2007]. In ITER, islands as small as 5cm might lock [LaHaye:NF2006]. Therefore, for burning plasma devices such as ITER which aim at high β operation, control and stabilisation of NTMs are needed in order to obtain optimum performance.

The most promising way to control and stabilise NTMs is electron cyclotron resonance heating (ECRH) and current drive (ECCD) deposited near the flux surface where the mode is located. The feasibility of stabilising the mode has been shown theoretically ([Hegna:PoP1998] and references therein) and experimentally [Gantenbein:PRL2000, LaHaye:PoP2002, Isayama:NF2009, Felici:NF2012] in several tokamaks.

In TCV, there have also been several experiments to control NTMs using the EC system [Felici:NF2012, Felici:Thesis]. In these works, the stabilisations of NTMs are successfully demonstrated using real-time control of the launcher angle using pre-determined references for the mode location. Based on these previous experiments, we have enhanced the capability of NTM control using a real-time equilibrium reconstruction code

(RT-LIUQE) which has recently been implemented in the TCV real-time control system [Moret:FED2015]. Using RT-LIUQE, the locations of the relevant rational q -surfaces can be estimated in real-time and ECRH/ECCD can track these locations for stabilising or preempting the mode.

In this chapter, the results of recent NTM control experiments using real-time equilibrium reconstruction in TCV will be shown. The physics of NTMs is briefly recalled in Sec. 5.2. Prior to the main experiment, the capability of RT-LIUQE to produce a reliable q profile has been examined. We found several problems which were subsequently resolved for the most part. They are reported in Sec. 5.3.1 with a brief description of RT-LIUQE since they influenced the scenario used in these experiments and they are generic to all real-time equilibrium reconstructions, although at smaller amplitudes. The experimental demonstration of mode stabilisation will be discussed in Sec. 5.3.3 as well as the sensitivity of choosing the target q value. The experimental results for destabilising and preempting the modes follow in Secs. 5.3.4 and 5.3.5. In addition, results using a new simple and robust way of NTM control, which compensates for the uncertainty of equilibrium data, are shown in Sec. 5.4. Finally, the chapter is summarised in Sec. 5.5.

5.2 Physics of neoclassical tearing modes

5.2.1 The formation of magnetic islands

The equilibrium magnetic field \mathbf{B} near the rational surface, where $q = q_s = m/n$, can be approximated as a sum of the magnetic field at the rational surface \mathbf{B}_s and the magnetic field component \mathbf{B}^* in the helical direction ($\zeta = \theta - n\phi/m$, $\zeta \perp \mathbf{B}_s$) [Bateman:MHD, Sauter:PoP1997]. The helical component \mathbf{B}^* is written as

$$B^* = B_\theta \left(1 - \frac{q}{q_s}\right) \simeq -\frac{q'_s}{q_s}(\rho - \rho_s) B_\theta, \quad (5.1)$$

where B_θ is the poloidal magnetic field and ρ is the effective minor radius. The subscript s indicates a value at the rational surface and $'$ means the radial derivative with respect to ρ . As indicated in the equation above, the amplitude of B^* is zero at the rational surface and the directions (signs) of B^* inside and outside the rational surface are different. If a radial perturbation $\delta\mathbf{B}_\rho$ is added to \mathbf{B}^* , the magnetic field lines are perturbed and a string of magnetic islands can appear. Due to the magnetic island formation, the magnetic topology is also modified as shown in the Fig. 5.1(a) (figure from Ref. [Sauter:PoP1997]). Inside the island, heat rapidly moves across the island in the radial direction, through parallel transport, and a flat pressure profile results. This happens if the island is large enough with respect to the ratio of parallel to perpendicular transport [Fitzpatrick:PoP1995]. In Fig. 5.1(b) (figure from Ref. [Chang:NF1990]), a simple illustration shows the flattening of the temperature profile due to the enhanced radial transport inside the island. The modified temperature profile results in the decrease of plasma energy, the degradation of the plasma energy confinement.

The flattening of the pressure profile inside the island results in a reduction of the bootstrap current density, itself proportional to the radial pressure gradient, so a helically perturbed bootstrap current δj_{bs} arises in the direction opposite to the equilibrium current

density [Sauter:PoP1997]. As shown in Fig. 5.1(a), δj_{bs} induces magnetic fields in the same direction as the perturbed magnetic field around the island (assuming q' positive in Eq. 5.1). Therefore in the sense of stabilising NTMs, δj_{bs} should be reduced by adding external current inside the island to compensate the loss of equilibrium bootstrap current. More detail about the stabilisation or control of NTMs will be given in Sec. 5.2.3.

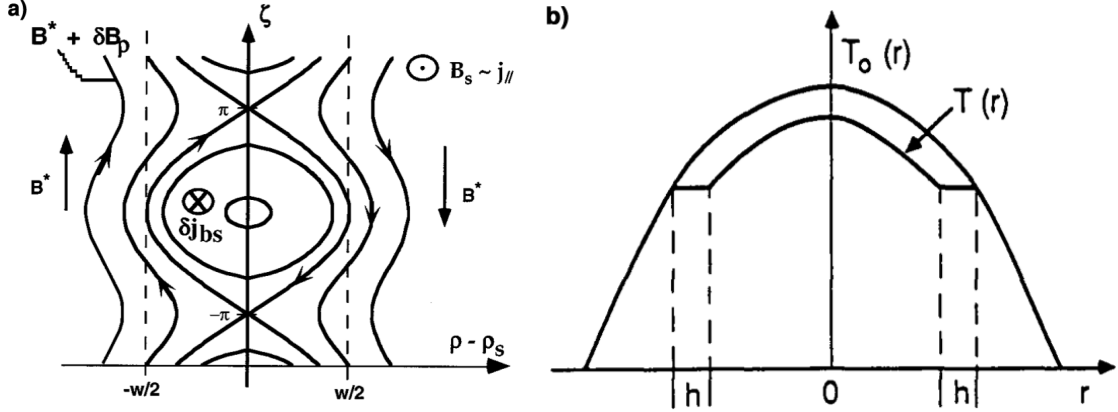


Figure 5.1: (a) Figure from Ref. [Sauter:PoP1997]. A radial perturbation (δB_ρ) results in a new topology of magnetic field in the vicinity of the island ($B^* + \delta B_\rho$) (with positive q'). (b) Figure from Ref. [Chang:NF1990]. The enhanced radial transport inside the island brings the flat temperature and pressure profiles. Due to the flat pressure profile inside the island, a negative perturbed bootstrap current arises in the direction of the helical magnetic field and destabilises NTMs.

5.2.2 Modified Rutherford equation

The time evolution of a magnetic island can be described by a nonlinear differential equation, called the modified Rutherford equation (MRE) [Rutherford:PoF1973]. The MRE can be combined with transport and/or an equilibrium solver for a self-consistent simulation in the presence of a tearing mode island. In this work, we have not conducted specific simulations, but looking at the main terms of the MRE can help us understand qualitatively the evolution of the mode in an experiment. The MRE can be written as

$$\frac{\tau_R dw}{\rho_s dt} = \sum_i \rho_s \Delta'_i(w) \quad (5.2)$$

where $\tau_R = \mu_0 \rho_s^2 / 1.22 \eta_{neo}$ is the resistive time, η_{neo} is the neoclassical resistivity, ρ_s is the radial coordinate of the mode location, and w is the full island width. The Δ'_i terms on the right-hand side of the equation describe different physical effects on the mode. The detail of some of the main Δ'_i terms will now be discussed.

Classical tearing mode stability index

From the linear theory [Furth:PoF1963, Furth:PoF1973], the stability of tearing mode can be evaluated by the classical stability index Δ'_0 . This parameter is defined through the jump of the logarithmic derivative of the radial magnetic field perturbation across

the rational surface. The mode is driven when the plasma current density is unstable. In accord with the definition and the detailed calculation in Refs. [Fitzpatrick:PoP1995, Hegna:PoP1998], assuming large aspect ratio tokamak and a constant perturbed magnetic flux inside the island ($\psi(\rho) = \Psi$), Δ'_0 can be written as

$$\begin{aligned}\Delta'_0 &= \lim_{\epsilon \rightarrow 0} \frac{d\psi}{d\rho} \bigg|_{\rho_s - \epsilon}^{\rho_s + \epsilon} / \Psi \\ &= -\frac{2\mu_0}{\Psi} \oint \frac{d\zeta}{2\pi} \int_{\rho_s - \epsilon}^{\rho_s + \epsilon} \delta j_z \cos\zeta \, d\rho,\end{aligned}\tag{5.3}$$

where δj_z is the perturbed current density in the axial direction, along B, ζ and Ω are the helical angle and the perturbed flux surface label, respectively. When Δ'_0 is positive, the plasma is unstable and there is free energy available to tear the magnetic equilibrium followed by the formation of magnetic islands. While a negative value of Δ'_0 indicates the stable status. In typical tokamak plasmas with $q_{95} \gtrsim 3$ and $q_0 \simeq 1$, $\Delta'_0 < 0$ and the plasmas are linearly stable [LaHaye:PoP2006, Sauter:PPCF2002].

Δ'_0 can be computed using noncircular toroidal codes such as PEST-III [Pletzer:JCP1994]. However, the calculation is very sensitive to the equilibrium q profile, so that $\rho_s \Delta'_0 \approx -m$ is used, which is a typical value obtained from the cylindrical and PEST-III calculations [Sauter:PoP1997, Brennan:PoP2002].

As seen in Eq. 5.3, Δ'_0 is independent of the island width. However, when the island grows and the size is large enough, the equilibrium current density profile is modified such that a decrease of Δ'_0 follows [Monticello:PoF1980, Reimerdes:PRL2002]. In order to take into account this change, an effective Δ' is defined as below:

$$\Delta'(w) = \Delta'_0 - \alpha w.\tag{5.4}$$

α is the reduction factor of the classical parameter. Due to the effect of the island, the classical tearing parameter is also dependent on the island size.

Neoclassical effects from helically perturbed bootstrap current

As mentioned in the Sec. 5.2.1, once the island is formed, the pressure profile becomes flat due to the fast parallel transport and the magnetic structure. The local flattening of the pressure results in a local reduction of the bootstrap current j_{bs} which is proportional to the perturbed pressure gradient. Due to its helical structure, which is the same as the island, the perturbed j_{bs} reinforces the destabilisation if q' is positive. Since j_{bs} arises from neoclassical effects, due to trapped particles [Hinton:RMP1976], an island that is dominated by this bootstrap effect is called a *neoclassical* tearing mode.

Following Refs. [Sauter:PoP1997, Sauter:PPCF2002, Fitzpatrick:PoP1995], one can define the bootstrap contribution as

$$\Delta'_{bs} = a_2 \beta_p (-L_{bs}) \frac{L_q}{-L_p w^2 + w_d^2} w.\tag{5.5}$$

The coefficient a_2 is a free parameter of order unity (~ 2.6). $L_p = p/p'$ and $L_q = q/q'$ are the scale lengths of pressure and q profiles, respectively, and L_{bs} is the bootstrap

coefficient associated with the contribution of these profiles to the j_{bs} [Sauter:PoP1997, Sauter:PPCF2002]. Since the Δ'_{bs} term is positive for $q' > 0$, the neoclassical contribution is destabilising.

When the island is small, perpendicular transport can compete with parallel transport and the pressure profile does not flatten completely. The neoclassical contribution from Δ'_{bs} decreases with w and this is assured by the additional term w_d which is defined below [Fitzpatrick:PoP1995, Sauter:PPCF2002]:

$$w_d = \left(5.1 \rho_s \left(\frac{1}{\epsilon s n} \right)^{1/2} \right)^{4/3} \left(\frac{\chi_{\perp}}{\chi_{\parallel}} \right)^{1/3}, \quad (5.6)$$

where $\epsilon = \rho_s/R_0$, s are the inverse aspect ratio and the magnetic shear estimated at the rational surface, n is the toroidal mode number, $\chi_{\perp, \parallel}$ are the perpendicular and parallel thermal conductivities, respectively.

Polarisation current effects

As proposed in Refs. [Waelbroeck:PRL2001, WilsonH:PoP1996], as the island propagates at frequency ω with respect to the plasma, a time varying electric field results. This is due to the different response of electrons and ions to the rotating island and a ‘‘polarisation’’ current arises. The effect of the polarisation current can be either stabilising or destabilising depending on the value of ω . For the case that $0 > \omega > \omega_i^*$, where ω_i^* is the ion diamagnetic drift frequency, the polarisation term has stabilising effect [Waelbroeck:PRL2001]. According to Refs. [Sauter:PoP1997, Sauter:PPCF2002, Poli:PRL2005], the contribution of the polarisation current on the MRE can be written as

$$\Delta'_{pol} = a_3 \beta_p \left(\frac{L_q}{L_p} \right)^2 \rho_p^2 g(\epsilon, \nu_{ii}^*) \frac{w}{w^4 + w_p^4}, \quad (5.7)$$

$$g(\epsilon, \nu_{ii}^*) = \begin{cases} \epsilon^{3/2} & \text{if } \nu_{ii}^* \leq 0.3, \\ 1 & \text{otherwise,} \end{cases}$$

where a_3 is a free parameter of order unity, ρ_p is the poloidal ion gyroradius. $w_p = \rho_b = \sqrt{\epsilon} \rho_p$ is present since when the island is small, the ions do not ‘‘see’’ it due to their banana orbits [Poli:PRL2005]. This results in a polarisation current proportional to w at small w .

Curvature effects

Due to the magnetic field curvature, a stabilising effect arises for tearing modes. The island modifies the field lines in a way that increases the magnetic energy, so the island becomes more stable. This is first pointed out by Glasser, Greene and Johnson in Ref. [Glasser:PoF1975] so it is called GGJ effect. The contribution is defined below based on the large aspect ratio approximation as discussed in Refs. [Sauter:PoP1997, Sauter:PPCF2002, Lutjens:PoP2001].

$$\Delta'_{GGJ} \simeq 6.35\beta_p \frac{\epsilon^2}{s} \left(\frac{L_q}{-L_p} \right) \left(1 - \frac{1}{q^2} \right) \frac{1}{\sqrt{w^2 + 0.2w_d^2}}. \quad (5.8)$$

The Δ'_{GGJ} term depends on the square of inverse aspect ratio, i.e. ϵ^2 . Thus the effect of GGJ term is not significant for conventional aspect ratio tokamaks ($\epsilon \sim 0.3$) and is often neglected in the modelling; while this effect can be comparable to the destabilising effect of Δ'_{bs} for the low aspect ratio or spherical tokamaks ($\epsilon \sim 1$) as shown in MAST [Buttery:PRL2002] and discussed in Refs. [Hegna:PoP1999, Rosenberg:PoP2002]. It has been shown that this term is stabilising even at $w = 0$ [Lutjens:PoP2001].

EC heating and current drive effects

Due to the neoclassical effect arising from bootstrap current, the destabilisation of the mode is reinforced by a “negative” current inside the island. Radio frequency (RF) waves, in particular electron cyclotron (EC) waves, can be used to replace the missing bootstrap current inside the island by driving current from external sources. This has been shown to be effective [Gantenbein:PRL2000, LaHaye:NF2005, Isayama:NF2009, Felici:NF2012]. Additional “current” can be driven by EC heating (ECH), which modifies the local conductivity and thus increases the inductive current locally. These terms have a stabilising effect and appear as additional terms (Δ'_H , Δ'_{CD}) in the MRE. Furthermore, due to the change of equilibrium current density, there is a supplementary modification on the classical tearing index Δ' [Westerhof:NF1987]. The detailed expression of the Δ'_H and Δ'_{CD} terms are introduced in Refs. [DeLazzari:NF2009, DeLazzari:NF2010]. Examples of the right-hand side of the MRE and the effects of ECCD stabilisation can be found e.g. for ITER cases in Ref. [Sauter:PPCF2010].

5.2.3 Trigger and control of NTMs

When the classical tearing parameter $\Delta'(w = 0)$ has a positive value, larger than $-\Delta'_{GGJ}(w = 0)$, due to an unstable current density profile, the island grows with positive dw/dt until its size reaches to the saturated level (w_{sat} , $dw/dt = 0$). In this case, the growth of the island is “spontaneous” and begins without triggering, nor seed island. Thus it is called “triggerless” or *classical* tearing mode. The cause of the triggerless mode is not always clear, in particular because the evaluation of Δ'_0 is difficult [Felici:EPS2009]. In TCV, NTMs are observed without triggering, with central ECCD [Reimerdes:PRL2002, Felici:Thesis, Nowak:IAEA2014]. There have also been attempts to find the reason for triggerless NTMs by studying the relation between the plasma rotation and the NTMs [Nowak:JPHYS2012, Sauter:IAEA2010], to see if the polarisation current might be the main cause for destabilisation.

In contrast to triggerless tearing modes, a mode can be triggered when $\Delta'(w = 0)$ is negative. In this case, due to a negative Δ' and small contribution of Δ'_{bs} at small w , the growth rate $dw/dt(w = 0)$ is negative so that the island cannot grow spontaneously. Instead, it self-stabilises whenever the island is smaller than a critical island width w_{crit} . When $w > w_{crit}$, any “seed” island evolves with positive growth rate to the saturated size w_{sat} . Therefore, in order to start growing, a seed island w_{seed} is necessary: NTMs are metastable. It has been shown that such a seed island can be provided by other

5.3. NTM control experiment using real-time equilibrium reconstruction

instabilities such as sawteeth [Sauter:PRL2002, Canal:NF2013], fishbones [Gude:NF1999] or ELMs [Rice:NF1999]. The details of the triggering mechanism are still debated but the correlation between the instabilities and the appearance of NTMs have been experimentally demonstrated. For instance, when sawtooth periods are long, the beta limit for the mode onset decreases and NTMs appear at lower β_N [Chapman:NF2010]; whereas, higher β_N can be obtained without NTMs when sawtooth periods are shorter [Sauter:PRL2002, Chapman:NF2013].

In order to effectively stabilise the mode and make predictions for ITER, it is important to determine operational parameters such as the width of EC beam, the amount of current drive, the alignment with the island and whether modulation of EC beam is required. A sufficient amount of driven current in the island O-point is essential for mode stabilisation. From the experiments in ASDEX Upgrade, DIII-D and JT-60U [Gantenbein:PRL2000, LaHaye:PoP2002, Isayama:PPCF2000, Isayama:NF2003], for the ECCD stabilisation of NTM, the current drive from ECCD, I_{eccd} , is about 1% – 2% of the plasma current I_P and the current densities from ECCD, j_{eccd} , and bootstrap current j_{bs} are similar. For complete stabilisation, the criterion on the required amount of ECCD current density is $j_{eccd}/j_{bs} \geq 1.2$ [Saibene:IAEA2006], based on Refs. [Zohm:EC2006, LaHaye:NF2006]. A modified criterion for ITER is introduced in Ref. [Sauter:PPCF2010]: $w_{cd}j_{eccd}/j_{bs} \geq 5\text{cm}$ with the beam width smaller than 5cm. As well as the amount of current drive, the alignment between EC beam and island is also important since a misalignment of more than 70% of the beam width (full width half maximum) results in a drop of the stabilising effect [Westerhof:NF1990, LaHaye:NF2006, Felici:NF2012]. It has been shown that when the power is modulated synchronously with the mode, the deposition of the EC beam at the island centre (O-point) is most effective to stabilise the mode while deposition at the separatrix (X-point) results in a destabilising effect. In-phase EC power modulation [Maraschek:PRL2007] is efficient, but only when the island width is smaller than the deposition width; otherwise the reduction in average power is detrimental.

5.3 NTM control experiment using real-time equilibrium reconstruction

Previous NTM control experiments in TCV have successfully demonstrated the capability of NTM stabilisation of EC beams using real-time launcher angle control [Felici:NF2012, Felici:Thesis]. The experimental results are shown in Fig. 5.2 (these figures are originally presented in Ref. [Felici:Thesis]). These NTM control experiments have been carried out using EC beam sweeping to find the mode location, both from inside to outside the mode location (radially) and from the opposite direction. In the first experiment, after the mode is detected, an EC beam sweeps from the central region to just inside the target position as quickly as the mechanical antenna allows. After that, the EC beam continues sweeping, but at a much slower rate, in the same direction, until the mode disappears. Once the mode is stabilised, the EC beam stays at its last position. This method is applied in the opposite direction in the second experiment. As in the first experiment, an EC beam starts fast sweeping from the centre but the EC power is turned off until the EC beam is aiming outside the target position. In this way, the EC beam does not aim *at* the mode location and stabilise the mode while crossing the island location. Once

the EC beam is located outside the target position, EC power is again turned on and the EC beam starts slowly sweeping towards the plasma centre until the mode disappears; at which time it keeps its last position. From either direction the mode is stabilised at a similar launcher angle around 20° and this angle agrees well with the estimation of the $q = 2$ surface using equilibrium reconstruction and a ray tracing code. Coming from inside, the mode is stabilised at 20.4° and from outside at 17.5° , i.e. within a $\Delta\rho$ of about 0.05 ($\sim 1.5 \rightarrow 2$ cm). The deposition width is about $\delta\rho = 0.2$ (~ 5 cm).

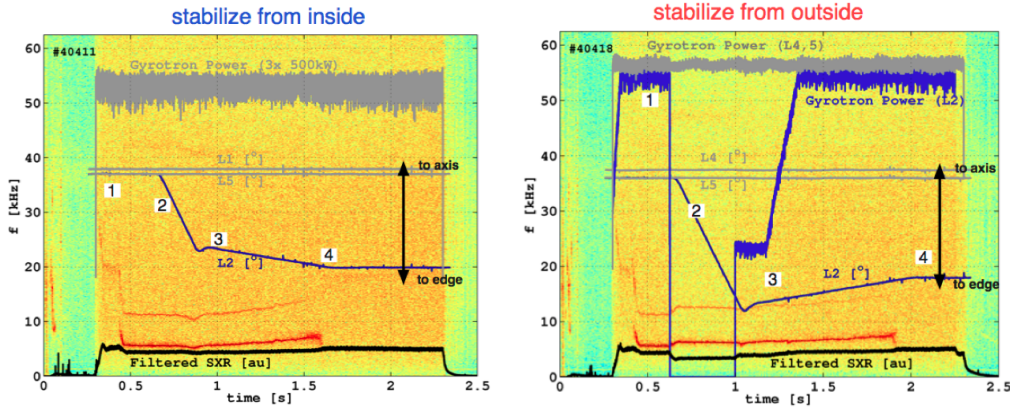


Figure 5.2: MHD spectrogram, with SXR emission, angle and power of launchers are shown (figures from Ref. [Felici:Thesis]). Left: (1) after the mode is detected, (2) an EC beam sweeps with the maximum rate from the central region to just inside the target position. (3) The EC beam slowly continues sweeping until the mode disappears. (4) The EC beam stays at the same position after the mode stabilisation. Right: repeated in the opposite direction with small modification. (1,2) a quick sweeping of an EC beam from the centre to off-axis is done while the EC power is turned off. (3) EC power is switched on when the position of EC beam is outside the target, and the EC beam slowly sweeps to the centre until the mode disappears. (4) It keeps its last position when the mode disappears.

In these experiments, the target launcher angle was pre-calculated using the offline equilibrium reconstruction LIUQE [Hofmann:NF1988] and the ray tracing code TORAYGA [Matsuda:IEEE1989]. In this section, we will refer to the “target launcher angle” defined as the angle required to heat at the mode resonant surface of interest (e.g. $\rho(q = 3/2), \rho(q = 2)$). Using this pre-estimated value, it was possible to define the fast and slow sweeping region, inside or outside the mode location. In other words, since the target position is already known, the mode can be stabilised with small variations of the launcher angle. However, if there are some changes in the plasma state, a variation of the q profile ensues and the mode radius moves. In that case, the pre-calculated target angle is not valid any more and consequently mode stabilisation cannot be achieved.

Therefore, we need to know the mode location in real-time to be sure of successful NTM control. Using real-time equilibrium reconstruction, the q profile evolution is evaluated as the plasma state changes. NTM control is enhanced by tracking the mode location in real-time without relying on a pre-estimated target position. However, as will be shown, some assumptions about beam refraction must be made and must remain valid if NTMs are to be successfully stabilised (in the present absence of real-time ray-tracing calculations in TCV). In the following sections, the real-time equilibrium reconstruction code and the

5.3. NTM control experiment using real-time equilibrium reconstruction

experimental results obtained while using it for mode tracking will be discussed. Though real-time equilibrium reconstruction enables us to follow relative changes of the q profile, due to a change in β or density, for example, NTM stabilisation requires a very accurate aiming at an absolute radial position. The q profile itself is influenced by the ECCD deposition, but is not directly taken into account by the code. The difficulties associated with this situation are also described and analysed in the following sections.

5.3.1 Real-time Liuqe

The real-time application of the equilibrium reconstruction code Liuqe

The real-time (RT) version of the equilibrium reconstruction code LIUQE (RT-LIUQE) [Moret:FED2015] included in SIMULINK has been implemented by TCV control experts in the TCV real-time control system. The algorithm of LIUQE is based on Picard iterations and for the real-time equilibrium reconstruction to be useful, the computation time for one iteration is required to be shorter than the evolution time of the equilibrium, typically 1ms for TCV. RT-LIUQE employs a sufficiently short sampling time ($\sim 200\mu\text{s}$), which results in a small change between two consecutive evaluated equilibria. Thus one iteration is performed to attain an acceptable convergence level and a new measurement set is taken by source term fitting at each cycle. RT-LIUQE employs the full 28 by 65 spatial grid (r, z) used by off-line LIUQE, the 133 measured data values and a grid of 17 radial by 32 angular points (ρ, θ) for the post processing. RT-LIUQE can be used for various purposes in TCV such as the shape control of the plasma boundary, provision of the equilibrium data to the real-time transport code RAPTOR [Felici:NF2011], as well as the calculation of the safety factor (q) profile for the real-time control of MHD instabilities, which is the main purpose of using RT-LIUQE in this work.

EC launcher angle control using RT-Liuqe

At TCV, a real-time version of a ray tracing code is not yet available. Thus a 2-D look-up table data for interpolation is pre-calculated with TORAY-GA [Matsuda:IEEE1989] using the experimental data from previous similar plasmas. A simple diagram of RT-LIUQE as a SIMULINK module with data transfer in node 3, shown in Fig. 5.3, illustrates how data are calculated and delivered to node 1. In addition, the 2-D look-up table data is presented in Figs. 5.3 (“transfer function 2”) and 5.4. Note that the non-uniformly spaced and multi-valued raw data coming from the different plasma targets and experimental uncertainties are “smoothed” by a polynomial fitting procedure. In the TCV RT-node 3, RT-LIUQE provides equilibrium data such as I_P and the q profile, in real-time. These data are transferred to RT-node 1 via the reflective memory [Le:FED2014]. One of the functions of the RT-node 1 is to run the EC system control (EC powers and launchers angles). In the RT-node 1, there are two transfer functions for the EC launcher mirror angle control. In the first transfer function, the q profile with ρ_ψ as the radial grid from RT-LIUQE and a pre-set target q_{target} value are used as input values and by simple linear interpolation, a target ρ_{target} value is given as an output. This ρ_{target} and the I_p from RT-LIUQE are inputs to the second transfer function. In this transfer function, a target launcher angle (θ_L) corresponding to the ρ_{target} is calculated by 2-D linear interpolation and fed to the launching antenna controller - the movement of the real launcher angle follows. For this

evaluation, third order polynomial fitting functions between ρ_ψ and θ_L for several I_P cases are implemented in a SIMULINK module. We have also checked that the 2-D mapping is not too sensitive to the plasma scenario being used, as long as z -axis is known in real-time and the density is not too high.

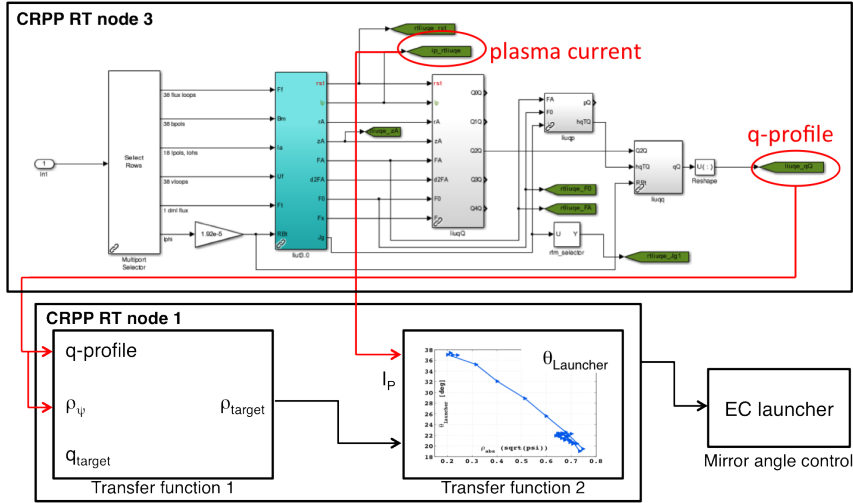


Figure 5.3: RT-LIUQE implemented in TCV RT-node 3 as a SIMULINK module (upper panel) calculates several equilibrium parameters including q profile and this is delivered to TCV RT-node 1 (lower panel) with I_P . In the RT-node 1, through two transfer functions, input values (q profile, ρ_ψ and target q value) return target launcher angle.

Problems of RT-Liuqe

Since it was the first time that RT-LIUQE was implemented in the TCV control system and tested, there were some significant problems at the beginning of the experimental series. The main problem was a noise on the q values produced by RT-LIUQE. In advance of applying RT-LIUQE to NTM control experiment, we have tested the accuracy of the q values for several shots with different conditions, mainly with different plasma current I_P . At first we have tested with low current (120kA, #47870), but a large level of noise on q_0 led to a large noise on the target ρ value. In this case, an NTM is triggered but it is not possible to use the RT-LIUQE q value to find a position of magnetic island. We then tried with a higher $I_p = 180$ kA. In this case the noise level was acceptable but we could not trigger an NTM with the available co-ECCD in the centre (see Sec. 5.3.4). We performed an I_p scan and found that $I_p \geq 160$ kA was required to reduce the noise to an acceptable level, however this is usually too high to allow triggering the mode with central co-ECCD. Therefore we developed a scenario with a first part at $I_p = 120$ kA, to trigger the mode, and then we changed to 160kA to perform the NTM stabilisation experiments with the RT-LIUQE information. This is the reason that some experiments reported here have two levels of I_p .

RT-LIUQE was then updated and it largely removed this noise problem at low I_p . We show in Fig. 5.5 the I_p trace and q_0 from RT-LIUQE. We see that the q_0 oscillations are still slightly larger at small I_p , but stay within a reasonable range. After 2s, X3 heating is

5.3. NTM control experiment using real-time equilibrium reconstruction

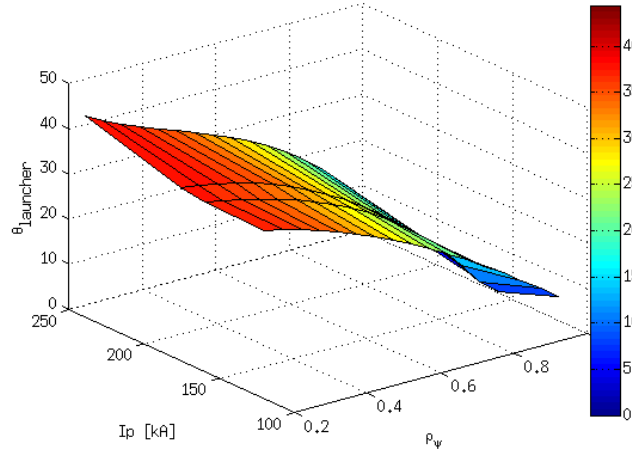


Figure 5.4: Pre-estimated 2-D look-up table data is implemented in the second transfer function in the SIMULINK module in Fig 5.3. With different set of target ρ_ψ value and I_P , target θ_L is calculated by linear interpolation.

added and an oscillation of I_p and density occurs (too high gain on the feedback control) which leads to a real oscillation of the q profile as well.

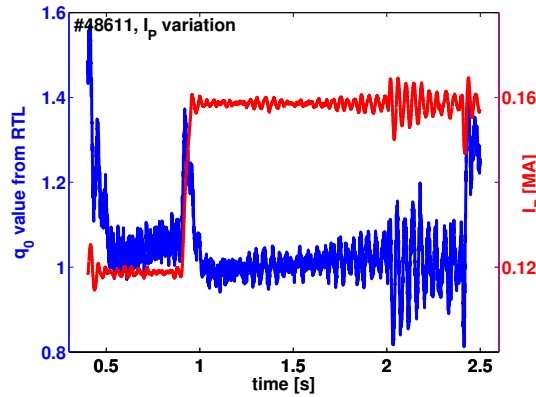


Figure 5.5: I_p and q_0 values from RT-LIUQE for a discharge with two levels of I_p . The noise on q_0 is slightly larger at smaller I_p . (The oscillation after 2s is due to the addition of X3 heating resulting in a feedback control problem on I_p and density).

In Fig. 5.6 we show the resulting oscillation on parameters needed for NTM stabilisation experiments. On the top left panel the target q value is shown versus time. It oscillates within a $\Delta q = 0.5$ and the average evolves between 2.1 and 2.5 during the discharge evolution. In the top right panel we present the q profile from LIUQE (that is LIUQE run offline, used throughout this thesis), RT-LIUQE and the RT-LIUQE profile (circles) shifted by an offset such that the $q = 2$ position coincides with the LIUQE profile. It shows that the offset is non-negligible and will need to be taken into account, as will

be discussed below. The profiles of RT-LIUQE and LIUQE are relatively self-similar, at least outside q of about 1.2. In the bottom panel, we compare the $\rho(q = 2)$ obtained from LIUQE and RT-LIUQE. Depending on the shot, the oscillations on $\rho_{RT}(q = 2)$ are larger than the case shown here and smoothing is required. Note that some “mechanical” smoothing occurs in any case since the mirrors cannot move so fast. However it is not good for the mechanical system to give an angle command with a high frequency noise. In other tokamaks, the real-time equilibrium is not calculated on such a short timescale; hence the smoothing occurs naturally. The bottom panel of Fig. 5.6 shows that the offset changes with time. This is inherent in the fact that real-time equilibria need to run fast and the inaccuracies are not systematic, but, rather, depend on plasma parameters. Note that LIUQE itself does not necessarily provide the actual $\rho(q = 2)$, however it has been shown to have less error. Figure 5.6 shows that RT-LIUQE can now provide sufficient information on the q profile for EC launchers to aim at the mode location, but that an offset may be required, for example setting $q_{target} = 2.2$, to aim at the actual $q = 2$ surface. This offset changes with plasma parameters and therefore some discharges might need to be repeated with a different offset, if executed in this way. This will be discussed in Sec. 5.3.3 and a new strategy to solve this problem is proposed in Sec. 5.4.

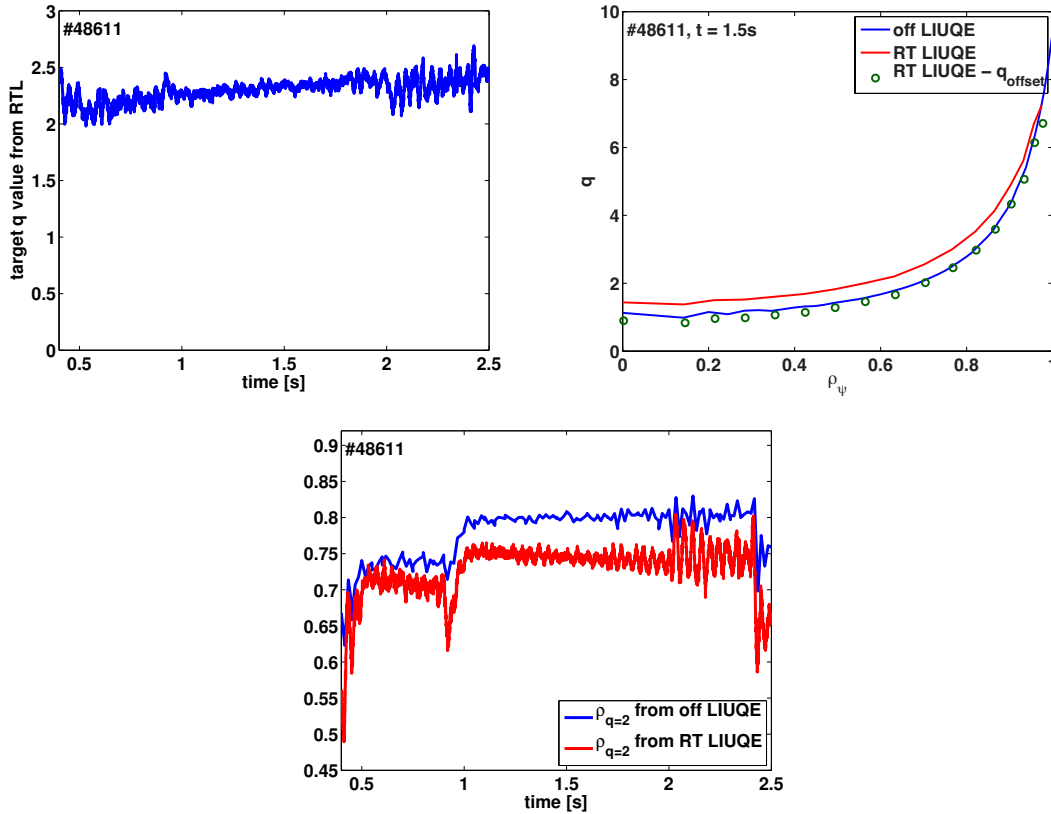


Figure 5.6: (top-left) The RT-LIUQE q target position defined as $q_{target} = q_{RT-LIUQE}(\rho_{LIUQE}(q_{LIUQE} = 2))$. (top-right) q profiles from LIUQE, RT-LIUQE and the latter shifted by $q_{offset} = q_{target} - 2$. (bottom) $\rho_{LIUQE}(q = 2)$ and $\rho_{RT-LIUQE}(q = 2)$ versus time.

5.3.2 Operation scenarios for NTM control experiment

For the NTM control experiments, we have used several operation scenarios. Basic plasma parameters are $I_p = 120\text{kA}$ and 160kA , $B_T = 1.44\text{T}$, $n_{e,l} = 1.4 \sim 2.2 \times 10^{19}\text{m}^{-3}$, $V_{loop} \simeq 0.2\text{V}$, $\kappa = 1.35 \sim 1.55$, $\delta = 0.15 \sim 0.3$ and $z_0 = 0.21\text{m}$. Two to four second harmonic (X2) and two additional third harmonic (X3) EC beams are used for electron resonance heating and current drive. The nominal EC power of each gyrotron is 0.5MW , thus total injected EC power is between 1.0MW and 3.0MW . Note that an EC beam from gyrotron No.2 has lower power ($\sim 0.4\text{MW}$) due to a technical problem and the absorbed power from X3 EC beams varies with the launcher angle and is known to be lower than 0.4MW as well.

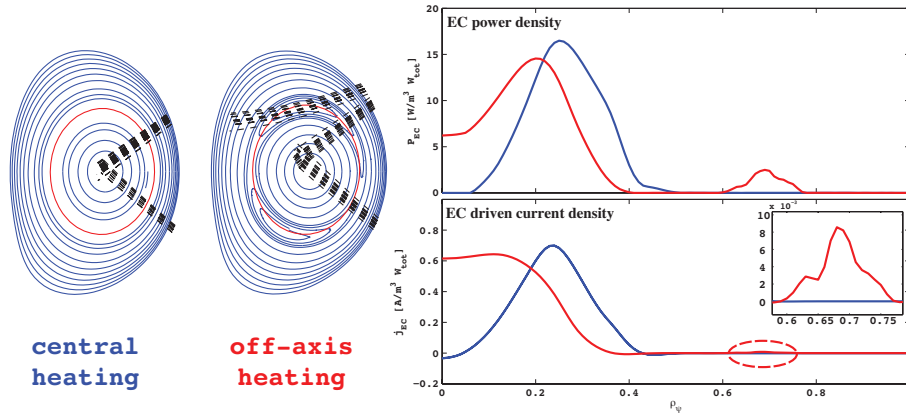


Figure 5.7: Flux surfaces at the beginning of discharge (central heating) and for mode stabilisation (off-axis heating) are shown on the left side. The red lines indicate the $q = 2/1$ position for each case. EC beams are deposited at the centre to trigger the mode and after the island is formed one beam sweeps to stabilise the mode. The power and current density profiles are plotted for central heating (blue) and off-axis heating (red) on the right side. Off-axis current density is zoomed in a box due to its lower value.

The basic scheme of EC beam deposition for NTM control is shown in Fig. 5.7. On the left side, the flux surfaces are shown with the trajectory of EC beams. The left-hand image indicates the centrally deposited EC beams during the first part of the discharge. Three X2 EC beams are deposited at the plasma centre at 0.4s to destabilise NTMs. As seen in the right-hand figure, after the mode is triggered, an island is formed typically at $q = 2/1$ surface (red line) and one or more EC beam moves to the location of the island to stabilise the mode. The EC power density (upper right panel) and driven current density (lower right panel) are exhibited for central (blue) and off-axis cases (red). For the current density profile, the insert shows a zoom of the off-axis current density due to its lower value compared to the central ones. Note that in this series of experiments, we have considered the current drive injection in the direction of plasma current (co-ECCD); the opposite direction (counter-ECCD) has not been investigated. Note also that we have not examined the effect of modulation of the EC beam power with respect to the mode frequency; continuous beam powers have been applied for all the experiments.

We have varied the number of EC heating and current drive beams. Two or three X2 beams are placed at the centre to trigger the mode and one or two X2 beams are

deposited at the mode location for stabilisation. In addition, two X3 beams are added to the central region in some cases to increase the plasma β . The combination of EC beams controlled in real-time using RT-LIUQE data are used to stabilise, destabilise or preempt the mode and the experimental results will be shown in the following sections. These experiments have taken place just before a long shutdown of TCV and once the RT-LIUQE was providing sufficient results. Therefore we have decided to test several aspects of NTM control, namely stabilisation, destabilisation and preemption without being able to perform detailed studies. Nevertheless, the interesting results, presented in the next sections, will help guide future more focussed studies and have already influenced the 2014 AUG programme.

5.3.3 Mode stabilisation using RT-Liuqe with a fixed q_{target}

First, we have experimentally demonstrated the feasibility of the 2/1 mode stabilisation using RT-LIUQE information and moving a launcher on the $q = 2$ surface accordingly in real-time. In this section, three discharges will be presented for describing mode stabilisation in different conditions.

The reference discharge (#49358) has $I_P = 120\text{kA}$ and three X2 EC beams (launchers 4 in ECH and 5, 6 in co-CD) deliver an EC power of 1.5MW (1.3MW absorbed in the plasma). Selected experimental data are shown in Fig. 5.8. In the first panel on the left side, I_P and line-averaged electron density $n_{e,l}$ are displayed. The second panel shows the total EC power (black) and the power from each individual beam (L4: red, L5: blue, L6: green). All three beams are deposited at the plasma centre to trigger the mode and only launcher 5 (L5) is later moved to suppress the island. The radial deposition position of launcher 5 - calculated by TORAY (blue) - and the calculated location of the $q = 2$ surface - from LIUQE (black) - are exhibited in the third panel, and the corresponding launcher angles are shown in the fourth panel - also showing the angle required to hit the $q = 2$ surface according to RT-LIUQE (black). One sees that L5 quickly reaches the required angle once the NTM stabilisation control begins (at 0.9s). The radial positions are evaluated in normalised effective minor radius ρ_ψ ($= \sqrt{\psi/\psi_{edge}}$). The island size (blue) and the poloidal beta (red) are presented in the fifth panel and the MHD spectrogram, which indicates the mode frequency, is shown in the last panel.

All three beams are deposited at the plasma centre from 0.4s and the mode appears at 0.53s. In this discharge, other instabilities (e.g. sawteeth) that produce the seed island are not detected and the mode is initially destabilised by central ECCD as discussed in Refs. [Reimerdes:PRL2002, Nowak:IAEA2014] and in Sec. 5.3.4. The island is most probably destabilised by an unstable Δ' and then, due to Δ_{bs} effect once the pressure profile flattens, the island size quickly increases up to the saturated size of about 5.5cm at around 0.6s. One can also see the appearance of the island from the spectrogram. The mode is a 2/1 mode and has a strong intensity with the frequency around 3.5kHz. The poloidal beta β_p slightly decreases with the increase of island size by about 10-15%, as expected since $\rho_V \sim 0.55$ [Chang:NF1990, Sauter:PoP1997]. For the stabilisation of the mode, at 0.9s feedback control starts and L5 moves to the mode location estimated by RT-LIUQE with the target q value of 2.0 while the others stay in the centre. As L5 moves to outside $\rho_{q=1}$ the destabilising effect of central EC decreases and as the launcher gets close to the target position, the stabilising effect increases. As a result, the island size begins to shrink. Note

5.3. NTM control experiment using real-time equilibrium reconstruction

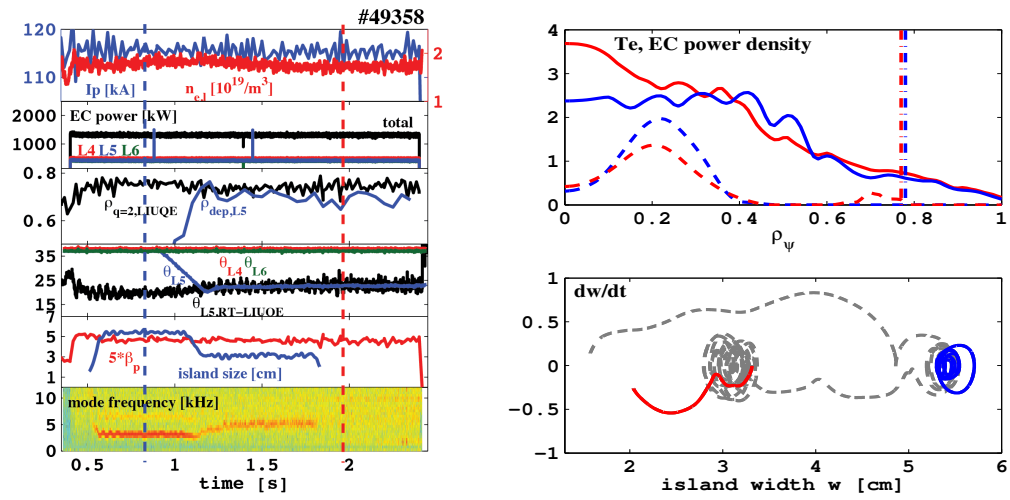


Figure 5.8: (Left): experimental result for the stabilisation of NTMs using RT-LIUQE. Launcher 5 (L5) follows the feedback control command which is based on the estimation from RT-LIUQE with the target q value of 2.0. The mode appears with centrally deposited EC powers and decreases its intensity when L5 moves to the mode location. L5 stays nearby the mode location and around 1.8s the mode disappears. (Right top): T_e profiles with (blue) and without (red) the mode show the different shape nearby $\rho_{q=2}$ (dash-dot lines). With the mode, T_e profile is flattened and the central value is dropped while after the mode stabilisation, T_e profile is not flat around $\rho_{q=2}$ and the central part also increases. (Right bottom): The growth rate of island size dw/dt is positive and the island quickly grows and is saturated ($dw/dt \simeq 0$ (blue)). With the deposition of EC beam nearby the mode location, dw/dt becomes negative and eventually the island disappears (red).

that as tested earlier and shown in Fig. 5.2, simply removing a central co-CD beam is not sufficient to stabilise the mode. This is due to the large hysteresis characteristic of NTMs related to the large Δ_{bs} contribution once an island is formed. The island size decreases until L5 reaches the target position at 1.2s. However, the island does not disappear but saturates at a smaller size of about 3.0cm. The mode disappears around 1.8s after a long stay of L5 near the mode location. This can be understood from several effects. The plasma evolves in time resulting in a change of the actual deposition position with respect to the $q = 2$ surface even though q_{target} remains the same. As shown in the third panel for $\rho_{dep,L5}$, the estimated deposition position slightly moves toward the centre and stays. Thus, L5 stays around the mode location and at some point, L5 is close enough to be able to stabilise the mode. In addition, it seems for this discharge the power from one EC beam is marginal to suppress the mode; therefore, as discussed in Ref. [Kolemen:NF2014] it is even more important to put the EC beam as close as possible to the mode location. (Alternative cases, with EC power clearly larger than the marginal power, will be shown later in other section and are easier to diagnose.) In this discharge, the density slightly evolves. At 1.1s, the launcher crosses a ρ position that is very nearly the same as its value at 1.8s; however, at 1.1s the density is slightly larger and temperature at $q = 2$ smaller. Following the value at $q = 2$ of T_e/n_e , proportional to j_{cd} , one finds that it increases after 1.5s, by about 30%, resulting in a larger peaked j_{cd} at 1.8s than at 1.1s as predicted by TORAY-GA. Therefore, if the power is marginal, this can also explain why the mode is only stabilised at 1.8s.

On the right side of Fig. 5.8, in the top panel, T_e (solid) and EC power density (dashed) profiles are shown. The blue lines indicate the case with the larger saturated mode around 0.8s while the red ones are after mode stabilisation (~ 2.0 s). These two cases are marked as blue and red dashed line in the left figure. One can see a flat T_e profile slightly inside the LIUQE $q = 2$ surface (blue dash-dot line), although the island width is only 10% of the minor radius. After the mode is stabilised, L5 still stays nearby, slightly inside the $q = 2$ surface (red dash-dot line). The central T_e is higher than the case with the mode even with less central EC power, due to a lower density as mentioned above. In the bottom panel, one can see how the island evolves plotting the growth rate, dw/dt (grey dashed) as a function of its size. The island is first measured with a width of 1.0cm and grows quickly with a positive dw/dt . The island width saturates at 5.5cm and remains at that size (blue). With the change of EC beam deposition position, the island width decreases (negative dw/dt) to first saturate near 3.0cm. After a while, dw/dt becomes negative again and the island disappears (red).

This discharge demonstrates that the radial position of the mode obtained from RT-LIUQE can be used in feedback control to fully stabilise a 2/1 mode, with only 0.4MW absorbed near the $q = 2$ surface. It also shows that it can take time until the mode is fully stabilised. This can be due to beam-mode misalignment, as we see that even the offline LIUQE gives a $q = 2$ position slightly outside the T_e flattening region and outside where the beam deposits its power at full stabilisation. But it can also be due to the fact that the power is marginal, and only with smaller local density and increased temperature (having the same affect as increasing the power somewhat), one can fully stabilise the mode. Let us first discuss the uncertainty related to the mode position.

Uncertainty for the mode stabilisation

To test the question of target position we have repeated similar discharges (up to 2s) decreasing only the target q value. In Fig. 5.9, two cases are shown. One case with $q_{target} = 2.38$ in which the mode is not stabilised (#48483) and another with $q_{target} = 2.34$ in which the mode is successfully stabilised (#48485).

In #48483, X3 heating is added at 2.0s as part of another study discussed later. L5 moves to the mode location estimated by RT-LIUQE from 0.65s. For discharge #48483, the island size saturates at about 3.0cm when the beam is near the mode but never disappears, during the whole discharge. At about 0.9s, as L5 approaches the mode location, the mode becomes weaker (mode frequency increases). As the plasma evolves, the deposition position of the EC beam gets closer to the mode location and the mode frequency keeps increasing, consistent with a smaller island and weaker drag from the wall, until X3 heating is added. During this time, the launcher angle increases slowly from 19.8° at 1.1s to 21° at 2s, following the RT-command signal.

For discharge #48485, the mode arises slightly earlier at 0.5s and the width grows to about 6.0cm until L5 is near the mode location. The island then shrinks to again about 3.0cm until the mode is stabilised at 1.27s. In this case, the angle crosses 21° at 1.22s and we see that the beam clearly crosses the estimated $q = 2$ position. In this series of discharges the successful stabilisation occurs when the beam clearly crosses the position just inside the $q = 2$ position given by LIUQE. This is consistent with the mode being usually slightly inside $\rho_{LIUQE}(q = 2)$ as mentioned above. This is also consistent with the fact that actually crossing the mode location, i.e. being sure to be aligned during at least a short time, is very important. Note that in #48485, following the RT-LIUQE $q = 2.34$ position resulted in moving the L5 angle slowly from 20.5° to 22.2° between 1.1s and 2s, respectively.

The various tests of q_{target} are summarised in Fig. 5.10. The values of $\rho_{dep,L5} - \rho_{q=2,LIUQE}$ being very negative indicate when the launcher moves rapidly to or from the centre. Figure 5.10(b) shows that the calculated deposition location depends on the launcher angle as expected (black dashed line), but that it can vary within 0.05 due to the actual equilibrium. This range is similar to the one due to the uncertainties in LIUQE and is similar to the range of uncertainty between shots with and without stabilisation as shown in Fig. 5.10(a).

5.3.4 Destabilisation/triggering condition

In TCV, with only X2 heating and L-modes, we cannot reach very high β_N values. Therefore NTMs are not triggered in general, except with significantly stabilised sawteeth and low q_{95} values as discussed in Ref. [Canal:NF2013]. In the latter conditions, NTMs can be destabilised due to long-period sawtooth crashes. At low current, sawteeth cannot trigger large enough seed islands. However it has been found that with co-ECCD in the centre the global q profile can be modified, making the modes unstable. There is concomitantly a change in rotation with increased EC power and the exact role of rotation is still under discussion ([Nowak:IAEA2014] and references therein). In this part we analyse the role of co-ECCD to destabilise NTMs in TCV at low plasma current. The next step would be to calculate the relative change in Δ' and perform a proper sensitivity study, but this is out of the scope of this work. Note that Δ' depends on q'' in the cylindrical approximation

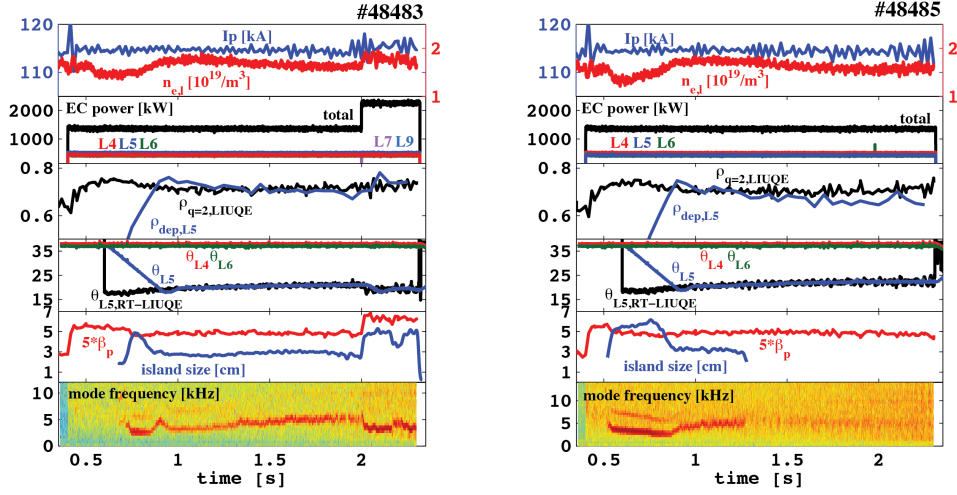


Figure 5.9: Experimental results of discharges #48483, #48485. Basic settings are same as shot #49358 except feedback control for L5 begins at 0.65s. For #48483, target q value is 2.38 and EC beam sweeps close to the mode location but does not stabilise the mode, while the mode is stabilised with q_{target} of 2.34 for #48485.

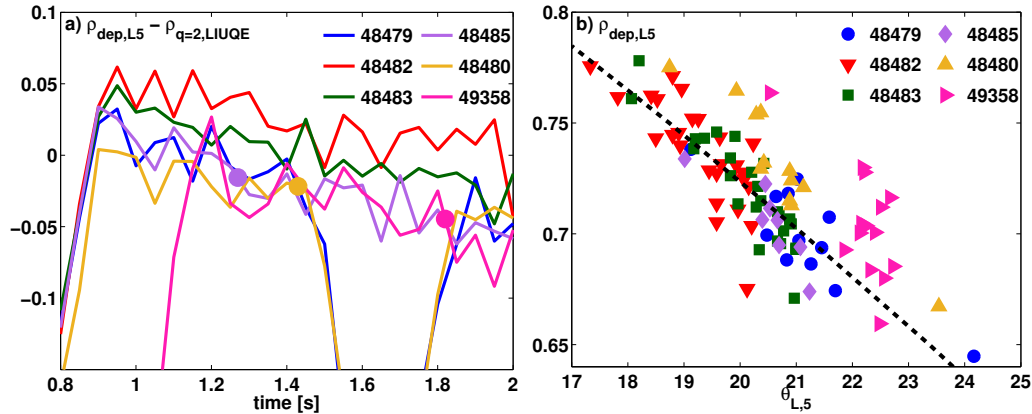


Figure 5.10: (a) Deposition position of L5 relative to LIUQE $q = 2$ surface and (b) deposition position calculated by TORAY-GA versus launcher angle. When the mode is stabilised, it is marked with a dot. Even with a fixed angle, there is a relatively large variation of the calculated ρ_{dep} of the same amplitude as the uncertainty in the effective position. ($q_{target, \#48479} = 2.3$, $q_{target, \#48480} = 2.38$, $q_{target, \#48482} = 2.45$, $q_{target, \#48483} = 2.38$, $q_{target, \#48485} = 2.34$, $q_{target, \#49358} = 2.0$. κ is slightly different for cases #48480 and #49358).

5.3. NTM control experiment using real-time equilibrium reconstruction

for example.

The discharge #48467 is first presented in Fig. 5.11 to study the relative roles of ECCD and plasma current. As in the discharges discussed above, 3 beams (one in ECH and two in co-CD) aim at the plasma centre with $I_p = 120\text{kA}$; they destabilise the mode. One launcher is then moved to stabilise the mode, while I_p is stepped up to 160kA ($0.9\text{s} - 0.95\text{s}$). The mode quickly stabilises when L5 approaches the rational surface ($\theta_{L5} = 20^\circ$, $\rho_\psi = 0.7$). L5 is moved back to the centre ($1.25\text{s} - 1.52\text{s}$), after I_p is changed back to 120kA ($1.25\text{s} - 1.3\text{s}$). The mode is destabilised again only once L5 is back to the very centre at 1.51s (36° , ρ_ψ inside 0.35). If the plasma current is kept at 160kA , then the mode is not destabilised. This indicates, first of all, that the mode is more stable at higher current: two co-CD and one ECH beam in the centre are not sufficient to destabilise the mode at high current, but clearly is at 120kA as shown in Fig. 5.11. It also shows that the mode is more stable when L5 is in between $q = 2$ and the centre; demonstrating that the local effect of ECCD on Δ' is not as large as predicted earlier [Westerhof:NF1987, Pletzer:PoP1999]. Furthermore, it is consistent with the results presented in the previous section, showing that when ECCD is slightly misaligned, either outside or inside the rational surface, the island width does not change much. In TCV, if the mode comes only from an unstable Δ' , it is because of a global effect on the q profile since it appears only with co-ECCD in the very centre where current drive is maximised (and confinement as well as discussed in Sec. 3.3). In these discharges, 0.45MW in the centre gives about $30\text{-}40\text{kA}$ ($\times 2$) compared to about $30\text{-}40\text{kA}$ of ohmic current and 25kA of bootstrap current for a total of 120kA . We know that central co-CD is destabilising for sawteeth [Angioni:NF2003] because it increases the shear outside the deposition location, which is also known to be destabilising for tearing modes.

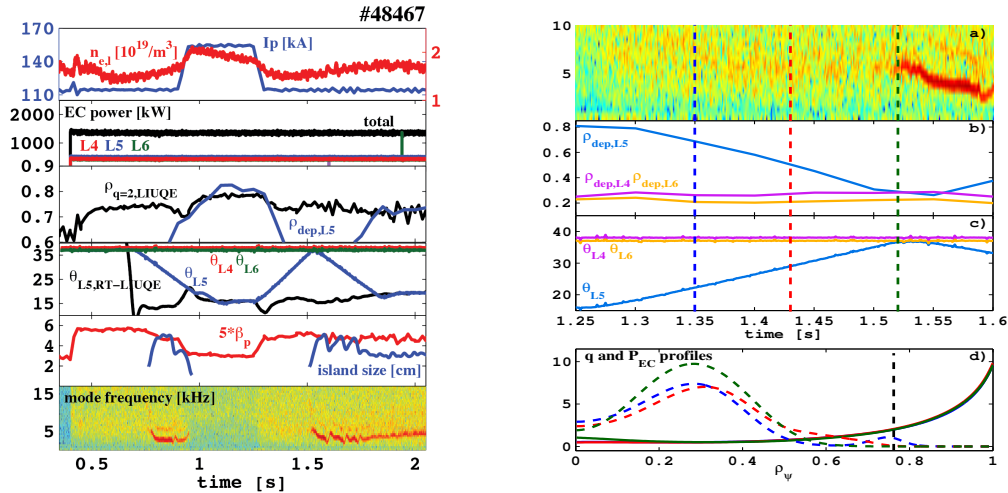


Figure 5.11: After the mode appears, L5 moves to the mode location to stabilise. With higher I_p , the mode becomes more stable and is easily stabilised by one EC beam. I_p decreases again and L5 comes back to the centre. While L5 is sweeping, there is no sign of mode appearance and when L5 recovers its initial position, the mode is finally triggered. From the ASTRA simulation, it is confirmed that EC beam is clearly away from $q = 2$ surface when the mode reappeared. This result supports that in order to destabilise the mode, sufficient central EC driven current is required.

We have seen in Fig. 5.9(a) that adding X3 heating in the centre can further destabilise an existing mode. We have tested whether X3 heating can be used to destabilise a mode if it does not initially exist. This is shown in Fig. 5.12, where the mode is first destabilised with only 2 co-CD in the centre. After I_p is increased to 155kA and the mode is stabilised by a third beam aiming at $q = 2$, X3 heating is added while keeping the beam near $q = 2$. Despite the presence of the preemptive beam and the higher current, a mode reappears after 0.2s of X3 heating, clearly demonstrating the significant destabilising role of X3 heating. As mentioned above, a quantification of the various effects requires a large simulation effort and a detailed sensitivity study. Indeed the various current contributions are not accurate and depend mainly on the effective charge Z_{eff} , which is not well measured in TCV. We note that this discharge provides additional useful information. We have seen above that 2 co-CD and 1 ECH beams in the centre with $I_p = 115 - 120$ kA is sufficient, while 1 co-CD and 1 ECH is not. Therefore we used 2 co-CD at the beginning of #48604; the modes' appearance shows that this is sufficient. Thus the simulation should find that about 30-40kA of driven current is not sufficient to destabilise the mode, while 50-60kA is. Of course variations in density need to be taken into account as well.

This discharge was also used to demonstrate that increasing I_p , even with only 2 co-CD beams in the centre, is not sufficient to stabilise the mode. This is why I_p is first increased to 155kA between 0.9-0.95s. Consequently the island width decreases, consistent with a more negative Δ' since Δ'_{bs} should slightly increase with I_p . Then L2 is turned on at 1.2s and the mode is stabilised at 1.28s.

Finally we present a set of experiments aimed at further analysing the effective level of driven current required to destabilise the mode. Similar power ramps as shown in Fig. 5.13 are performed using three gyrotrons aiming at the centre (inside $\rho_\psi = 0.45$) in co-CD (#48836); 2 co- and 1 cnt- (#48837); 1 co-, 1 cnt- and 1 ECH (#48841); 1 co- and 2 cnt- (#48839). In the first case, with 3 co-CD, a 3/2 mode is destabilised at 0.8s (700kW) and a 2/1 at 1.05s (820kW). In the 2nd case (#48837), the 2/1 mode is destabilised at 1.26-1.27s (950kW) with a short-lived small 3/2 mode at 1.25s. Finally with little CD (#48841) or slightly more cnt-CD (#48839), no mode are triggered even up to 1.2MW. This is consistent with central co-CD being destabilising and provides very useful data for a comparison with theoretical calculations. Note that rotation seems to be mainly influenced by the total injected power, therefore is not assumed to play a major role for the destabilisation of these modes. However detailed simulations should be used to confirm this as discussed in Ref. [Nowak:IAEA2014].

5.3.5 Preemption of the mode

Mode preemption is basically identical to mode stabilisation but EC beams are located at the mode location from the beginning to impede the mode triggering. For the first tests, we have taken the experimental set-up from the discharge #48604, but the timing of turning on the beams aiming at the rational surface has been shifted earlier. Note that preemption requires the results of the real-time equilibrium, since there is no mode present from which to diagnose the aiming position (e.g. from ECE, as used in other machines and proposed for ITER). Previous results (e.g. [Kolemen:NF2014]) seem to indicate that preemption requires much less power than stabilisation, which is what we

5.3. NTM control experiment using real-time equilibrium reconstruction

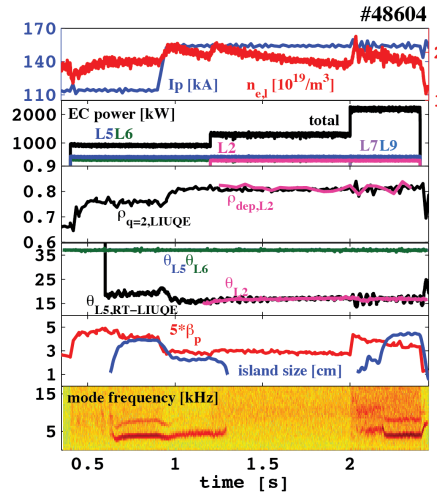


Figure 5.12: The mode can be triggered with two co-CD EC beams if there is sufficient current drive at the centre. After stabilising the mode, launcher 2 stays at the mode location and X3 power is turned on at 2.0s. Even with I_P of 160kA and preempting EC beam at the mode location, the mode reappears with X3 heating meaning that EC heating and current drive at the centre is sufficient to trigger the mode.

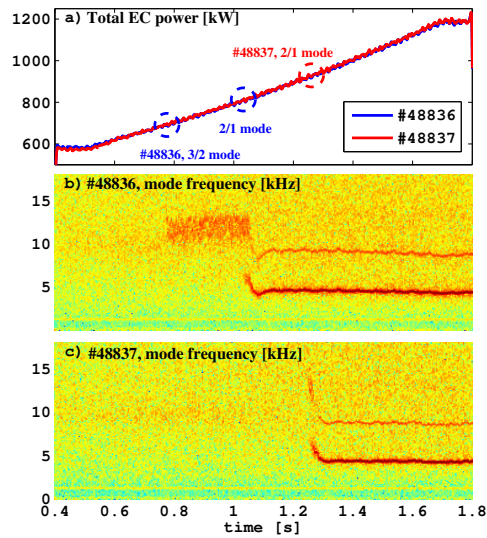


Figure 5.13: The power of three central beams is ramped-up slowly between 0.6 and 1.2MW. In #48836 the 3 beams are in co-CD and a 3/2 mode is triggered at 0.8s (700kW) and a 2/1 at 1.05s (820kW). In #48837, 2 beams are in co-CD and 1 in cnt-CD: a 2/1 mode is triggered at 1.27s (950kW). In other discharges less co-CD is provided and no mode appears even at full power. The reference ohmic discharge (#48838) has no mode as well.

want to investigate.

An example is shown in Fig. 5.14 for the discharge #48611. At 0.4s launchers 4 and 6 are located at the centre for mode destabilisation and L5 is deposited on the mode location. At 0.5s launcher 2 is added to L5. With two ECCD beams at the mode location, it is feasible to preempt the mode at 120kA. There is no indication of mode appearance in the MHD spectrogram in the first phase. At 0.9s, I_p is increased, the location of $q = 2$ changes and RT-LIUQE provides the relevant information such as to continue to preempt the mode. Note that at increased I_p it is easier to preempt, since the mode is more stable, but still we see that the aiming is relatively correct. In the third panel at the left, at the beginning the deposition position of launchers 2 and 5 provided by RT-LIUQE with q_{target} set to 2.34 is a little bit outside LIUQE $q = 2$ surface (0.04 in ρ_{ψ} for a full deposition width of about 0.15). It is not clear that the target position is correct and two launchers aim at the proper mode location. However, given that the mode is preempted, it is consistent with less power being required for the mode preemption [Kolemen:NF2014]. After I_p increases to 155kA, the target q value is modified to 2.25 and the EC beams follow LIUQE $q = 2$ surface well. At 2s, two X3 heating beams are added and a 2/1 mode is triggered at 2.08s, similar to the shot #48604. Note that we have attempted to preempt the mode with only L2, in the previous discharge, but without success. Thus the preemption power does not seem to be *much* lower than stabilisation requirements.

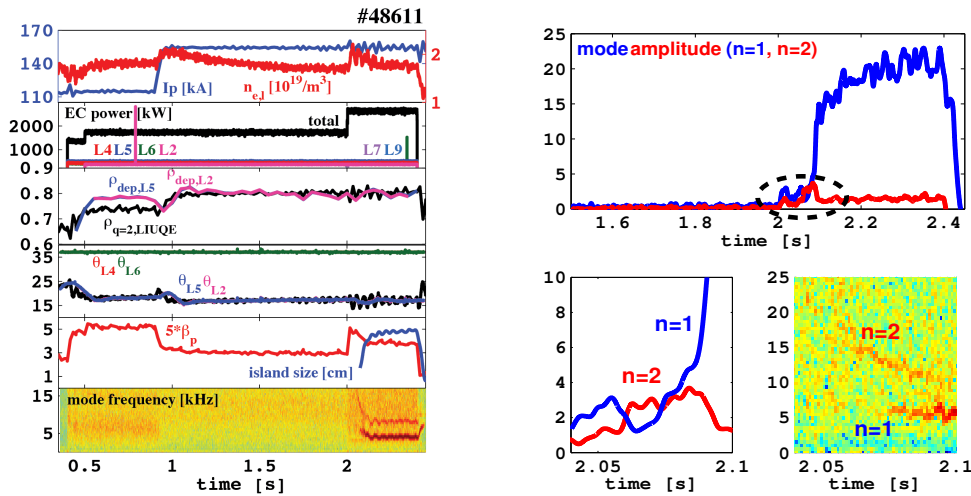


Figure 5.14: Launchers 4 and 6 are employed for driving current at the centre and launchers 2 and 5 are used for preemption at the mode location. With I_p of 120kA, two EC beams around the mode location are able to prevent the mode triggering. However, the preempting power is not sufficient when X3 heating is added on the central EC beams and the mode appears. From the investigation of the mode amplitude for $n = 1$ and $n = 2$ modes, $n = 2$ mode grows earlier than $n = 1$ mode and is stabilised once $n = 1$ mode begins rapid increase.

We have checked the onset of the mode in detail and the mode amplitude is presented on the right-hand side of Fig. 5.14. Due to X3 heating, the amplitudes of both the $n = 1$ and $n = 2$ modes increase slightly at 2.0s, but remain below the seed island threshold. The amplitude of the 2/1 mode first decreases when a 3/2 mode grows at 2.06s and then starts

5.3. NTM control experiment using real-time equilibrium reconstruction

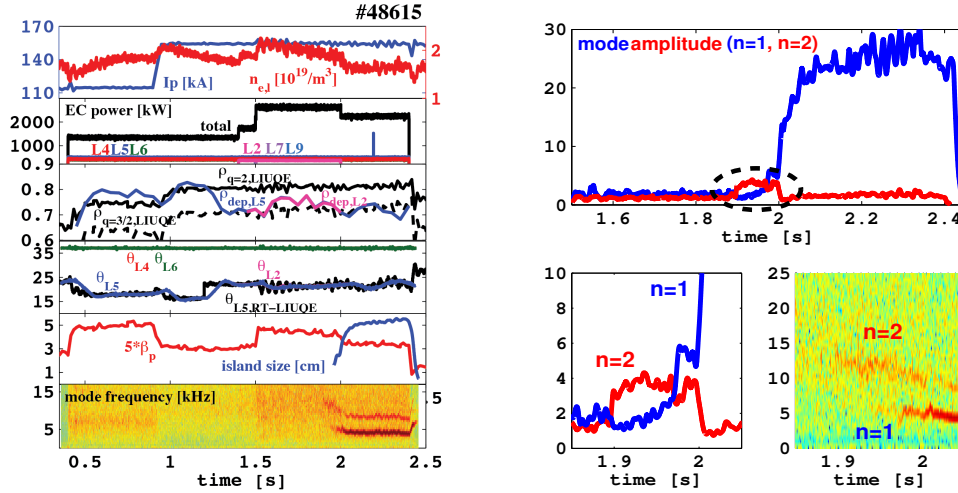


Figure 5.15: In the discharge #48615, it is proved that 3/2 mode preemption can prevent the onset of 2/1 mode. L5 preempts 2/1 mode and moves to 3/2 mode location together with launcher 2. After the X3 injection, neither 3/2 nor 2/1 mode appears with 3/2 mode preemption. At 1.9s, while two beams are on 3/2 mode location, $n = 2$ mode grows and stays longer than the previous discharge (#48611). $n = 1$ mode begins increasing at 1.95s and rapidly grows right after launcher 2 is turned off.

growing at 2.08s. Note that the same behaviour is observed for the discharge #48615, which will also be discussed. It is not clear if there is mode coupling helping to destabilise the 2/1 mode (like in Ref. [Raju:PPCF2003]), however the sequence is similar in shots #48604 and #48836, for example, which have a longer phase with the 3/2 mode. To test the relation between 3/2 and 2/1 modes, an additional experiment was carried out. In the discharge #48615, first only L5 is deposited on the mode location for preemption at low current, which is sufficient; thus, between 300 and 450kW is required for preemption. Next L2 is added at 1.4s and both L2 and L5 are aiming at $q = 3/2$ surface before the addition of X3 at 1.5s. The time traces and the mode amplitudes ($n = 1$, $n = 2$) are shown in the right-hand side of Fig. 5.15. As seen in the MHD spectrogram, there is no indication of mode appearance for both $n = 1$ and $n = 2$ modes with 3/2 mode preemption, until 1.9s. L2 is turned off at 2s and the mode further increases. The preemption was successful for 0.4s which is about 3 current redistribution time. We do not know if the mode appears at 1.9s because of eventual misalignment or because the power is too marginal. In addition, we do not know if preempting the 3/2 mode was the key to avoiding a 2/1 mode. Indeed the deposition width is about 0.15 and the $q = 3/2$ and 2/1 are at ρ_ψ of about 0.73 and 0.82, respectively. As indicated in Fig. 5.15 it might be that the preemption beams are in between, and covering both surfaces. We also see in the earlier part of the discharge that L5 successfully preempts the 2/1 while being somewhat misaligned. Therefore it could be that the alignment requirements to avoid the island from forming are less stringent at this power level; suggesting that less power would be required if the alignment were perfect. This requires further detailed experiments. It is important to characterise the preemption mechanism, but also the role of the 3/2 mode with respect to destabilising

2/1 modes (i.e. mode coupling).

5.4 Robust NTM control

Prior to beginning this new section, it may help to understand the following discussion if we first provide summary remarks concerning the consequences of the experiments in the previous sections:

- RT-LIUQE has been implemented in the TCV control system and has been used to provide the q profile in real-time. The mode location can be evaluated using RT-LIUQE and it is possible to track and suppress the mode in real-time.
- There are uncertainties in the determination of the mode location. Due to the intrinsic inaccuracies of a real-time equilibrium reconstruction, an offset needs to be used to set the correct q_{target} value to yield the correct ρ position.
- The offset value is changing in time with plasma parameters and cannot be evaluated in real-time. Therefore the choice of the q_{offset} value affects the ability to stabilise the mode. (Part of the offset is also due to the lack of real-time ray-tracing calculations, but this is a generic problem in any case.)
- To destabilise the mode, a sufficient amount of current drive is required at the centre or more precisely a sufficiently peaked current density profile. We have shown that off-axis current drive is not enough to destabilise the mode, be it on or nearby the rational surface. With increased central heating, less central current drive is required to destabilise the mode. We have also shown that increased plasma current is stabilising, most probably because it broadens the current density profile (the central CD is relatively smaller).
- It is possible to preempt the mode using the RT-LIUQE estimated mode location. It is observed that 3/2 modes usually arise before the growth of the 2/1 modes. Furthermore, preliminary results indicate that while preempting the 3/2 mode we have successfully preempted the 2/1 mode onset as well.

As summarised, the NTM control experiments using RT-LIUQE have been successful. However, in many unsuccessful cases it is not clear if it is due to a lack of stabilising power or due to misalignment with the mode rational surface. In addition, trial and error experimentation is used in order to find a good q_{target} (or equivalently q_{offset}) value. As a consequence, a new approach was developed to enhance NTM control experiments and was applied to new scenarios, without having problems due to these uncertainties. In the following, a simple and more “robust” way to effectuate NTM control is presented.

The main problem being the alignment, as shown in the previous sections, a systematic sweeping of the deposition location around the target position is introduced. We have seen that a clear crossing of the mode location from a $\Delta\rho$ of +0.05 to -0.05 (or vice versa) is necessary to ensure aiming at the rational surface. The sweeping also increases the chances that the EC deposition position reaches the mode location (and, if the power is insufficient to fully stabilise the mode, should show a dip in mode amplitude at the mode location - permitting an even more sophisticated control system to either lock in on that location

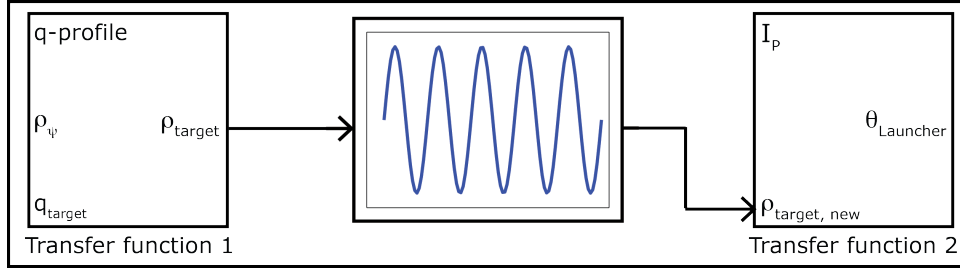


Figure 5.16: Once ρ_{target} is determined by RT-LIUQE, a sinusoidal wave form is added and this oscillating target position is converted to the launcher angle.

and/or subsequently increase the power to completely stabilise the mode.) To accomplish this sweep, a sinusoidal variation with two parameters (amplitude and frequency) is added to the estimated ρ_{target} position. It is simply explained by the conceptual diagram in Fig. 5.16, which is modified from Fig. 5.3. In this way, if the rational surface is nearby the target q value, the mode will be reached; this is not the case otherwise. Note that one still relies on an accurate RT-LIUQE, however the level of accuracy is relaxed, leading to a more robust control. The effectiveness of this method also relies on the observation that aiming away from the mode location (e.g. when slowly sweeping towards the mode position) does not show any significant destabilisation. That is, being off target appears to be ineffective, but not necessarily detrimental.

5.4.1 Application of robust control: Mode stabilisation

First we have examined different amplitudes and frequencies of the oscillation added on the estimated target position. The reference discharge #49358 is shown in Fig. 5.17 (left-panel). For all the experiments, the mode is triggered by three central EC beams (launcher 4 for ECH and launchers 5, 6 for co-ECCD). Real-time control of launcher angle starts to direct L5 to aim at the target location at 0.9s. The target location is calculated with $q_{target} = 2.0$ and for the case of discharges #49355 and #49357, additional oscillations for the robust control are added when the launcher reaches around the mode location (Fig. 5.17). For the shot #49355, a small amplitude (0.04 in ρ_ψ) and high frequency (10Hz) is added while for #49357 a larger amplitude (0.08 in ρ_ψ) and a lower frequency (3Hz) is chosen. We see from the middle panels (black curve) that the $\theta_{L,5}$ follows well the command for a small frequency, large amplitude or a larger frequency with a smaller amplitude. We have also tested a large amplitude and high frequency case (0.08 in ρ_ψ and 10Hz) but the mirror could not follow the given frequency so that the result was the same as #49355 case.

In Fig. 5.17, we show in the first panel the deposition range of L5 calculated by TORAY and the position of $q = 2$ surface given by LIUQE (black); in the second panel, the mirror angle of L5 (black) and the island size (blue); in the last panel, the MHD spectrogram indicates the mode intensity and frequency. For the reference discharge #49358, as discussed in Sec. 5.3.3, the mode is stabilised at 1.8s. The stabilising power seems to be marginal which also explains the un-steady island width and frequency. Note that even with a fixed launcher angle, the $q = 2$ surface evolves with the island width.

Additionally, the equilibrium evolves causing the requested angle to slowly increase with time (middle panel) from 22 to 23° . And finally, the error between RT-LIUQE and the actual $q = 2$ position may be changing in time. Any combination of these effects could explain why the mode is stabilised only at 1.8 s. Note that at this time the deposition is slightly inside the predicted LIUQE value, as expected from previous sections.

For the low amplitude case #49355, the deposition position of L5 and estimated $q = 2$ surface position look similar to the reference case (middle plot, top panel). This emphasises the fact that the combination of equilibrium & ray-tracing uncertainties are larger than the precision of the actuators: the mirror angle of L5 is definitely different from the reference case (middle panel). As expected, this amplitude is too small to really cross the island position by a $\Delta\rho$ of 0.05 , as found necessary for a clear experimental result in the previous sections. Nevertheless the mode is stabilised sooner, at 1.55 s. More importantly though, its width does not increase when the deposition is slightly misaligned. Here, the mode is almost stabilised near 1.35 s when the requested angle reaches 23° and then it is stabilised at 1.55 s when it reaches 23° again.

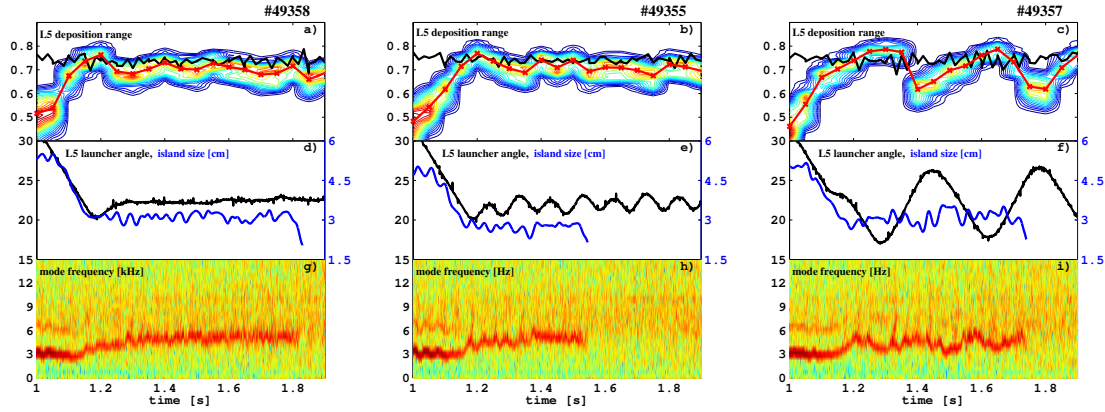


Figure 5.17: (Left): reference shot without applying robust control. With fixed target position the mode is stabilised at 1.8 s. (Middle): robust control is applied with an amplitude of 0.04 in ρ_ψ and frequency of 10 Hz. EC beam oscillates around the mode location so that the island size and mode frequency also oscillate. After 1.4 s, regardless the variation of deposition position, the island size and mode frequency keep a constant level and then the mode is stabilised at 1.55 s. (Right): robust control is applied with an amplitude of 0.08 in ρ_ψ and frequency of 3 Hz. Due to the slow sweeping, $q = 2$ surface moves and as a result the island size and the mode frequency vary with similar deposition position. With continuous variation of the island size and mode frequency, the mode is stabilised at 1.75 s.

In #49357, the excursions outside the mode location are clearer and visible in the TORAY results as well (right plot, top panel). Again, there is no clear increase of the mode amplitude, confirming that the destabilisation through Δ' modifications is not significant. (Note that changes do occur in the mode frequency, however.) The mode is stabilised at 1.75 s, again when the requested angle is near 23° . However, in this case, the beam clearly crossed this value earlier without stabilising the mode. In all these shots, the line averaged density decreases from about 1.85 to $1.7 \times 10^{-19} m^{-3}$ between 1.2 s and 2 s, so the power might be marginal indeed. It should be noted that in the discharges with sweeping, the mode is stabilised no later than with a fixed q_{target} ; and in that sense demonstrate a

more effective NTM control method.

In order to check if the power is marginal, we added launcher 2 (in addition to 5) on the mode location in the next two discharges. We have also chosen a significant “offset” for the q_{target} so that the launcher would definitely aim either too far outside (#49602, $q_{target} = 2.5$), or inside (#49603, $q_{target} = 1.6$), if the additional sweeping was not added. As shown in Fig. 5.18, with the addition of a sweeping of amplitude 0.1 and frequency 3Hz we could successfully stabilise the 2/1 mode. L2 is added at 1s and the target position is kept fixed until 1.2s as a reference part where the mode is not much affected because the target position is too far from the mode resonant surface. Once the sweeping starts, when it brings the beams towards the $q = 2$ surface (3rd panel), the mode is stabilised in both discharges (5th panel). Note that with the increased power of L2 (which is only about 300kW), the mode is stabilised quickly; in contrast to Fig. 5.17 using L5 alone (450kW). These results also show that once stabilised, despite the sweeping inside and outside the rational surface, the mode does not come back.

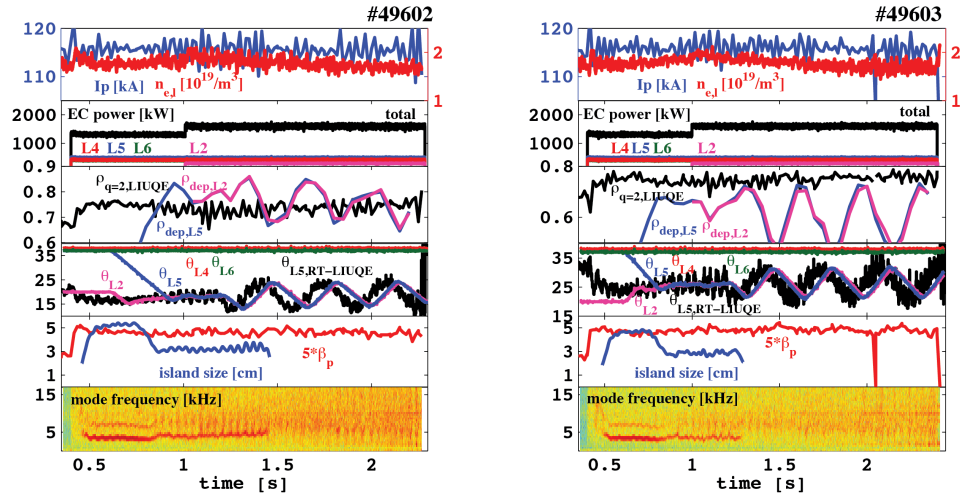


Figure 5.18: With large and slow oscillation (amplitude: 0.1 in ρ_ψ , frequency: 3Hz), robust control for wrong target position is demonstrated. Launchers 2 and 5 are deposited on the target position ($q = 2.5$ for #49602 and $q = 1.6$ for #49603) without robust control until 1.2s and then, robust control begins. Since the EC power is sufficient to suppress the mode, right after EC beams reach the mode location, the mode is stabilised in both cases. After stabilisation, EC beams keep sweeping but the mode is not destabilised.

These discharges clearly show that this new control method is more *robust*. Thanks to the relatively large oscillations and sufficient stabilising EC power, the EC beams have a chance to be placed at the optimum position and at once stabilise the mode even if the given average target position is incorrect: uncertainties in determining the target position are less detrimental. Several questions remain to be investigated; for example, how fast can the beam cross the island position and still stabilise the mode, or what is the required precision on the relative alignment between beams when using several beams for mode stabilisation as in Fig. 5.18. Another important question is whether it is possible to use this additional sweeping for mode preemption. We present the first results related to this

question in the next section.

5.4.2 Application of robust control: Mode preemption

We start from the previous experiment #48611 for mode preemption (Sec. 5.3.5), keeping $I_p = 115\text{kA}$ and without the additional X3 heating. Thus, there are two co-CD beams in the centre for destabilisation (L4+L6 at 0.4s) and L2+L5 in co-CD around $q_{target} = 2$ with a sweeping of $\Delta\rho = 0.08$ at 3Hz. We first failed to preempt the mode and it was triggered at 0.65s (shot #49618, not shown). However the density was higher than in the reference shot #48611 by about 25% (Fig. 5.19). Therefore we repeated with better control of the density (shot #49632). Figure 5.20 (left plot) shows that preemption with the robust control is successful in this case. At 1.35s, L2 is turned off and the mode appears immediately. At 1.75s, L2 is turned back on to stabilise the mode, but the power is not sufficient, though there is an obvious effect on the island width. This shows also that the power requirements for mode preemption are lower than for stabilisation of an existing mode. Thanks to the sweeping, we can actually test this fully, since we are sure to cross the island. Note that the preemption power is marginal, since with a slightly increased density the mode was not avoided and removing L2 the mode is not preempted anymore. Note also that with a similar set-up, the mode was stabilised as shown in Fig. 5.18; that is, the stabilising power is also marginal.

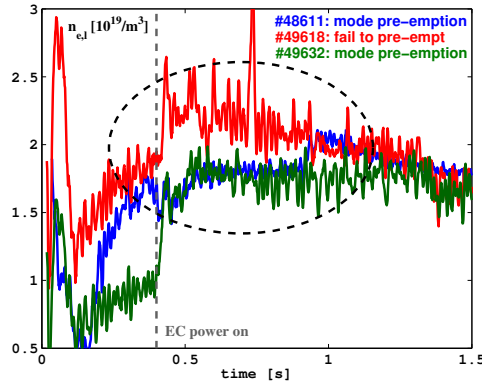


Figure 5.19: With higher density, the mode preemption fails for the shot #49618 (red). The density is modified and for #49632 (green), so that the density level is similar to the reference case (blue) when EC power is turned on.

In order to test better this last point, we have repeated this last case without L2 at the beginning, to see if L5 alone indeed cannot preempt the mode; then, we added a power ramp-down in the latter phase to test whether L5+L2 can stabilise the mode with a reduced central co-CD power. This is shown in Fig. 5.20 (right plot, #49639). The mode is destabilised at 0.71s, with only L5, confirming that the required power for preemption is between 450 and 780kW. After the addition of L2, the mode is stabilised during the ramp-down, at 1.75s, after a decrease of about 20% of the power in L4, L5 and L6 (same power supply). Thus the power is indeed marginal to stabilise the existing mode. We can estimate that a power between 780 and 940kW is required. However, further experiments

are required to better quantify this effect, and to quantify the effect of misalignment between launchers, since we have used two launchers for preemption/stabilisation.

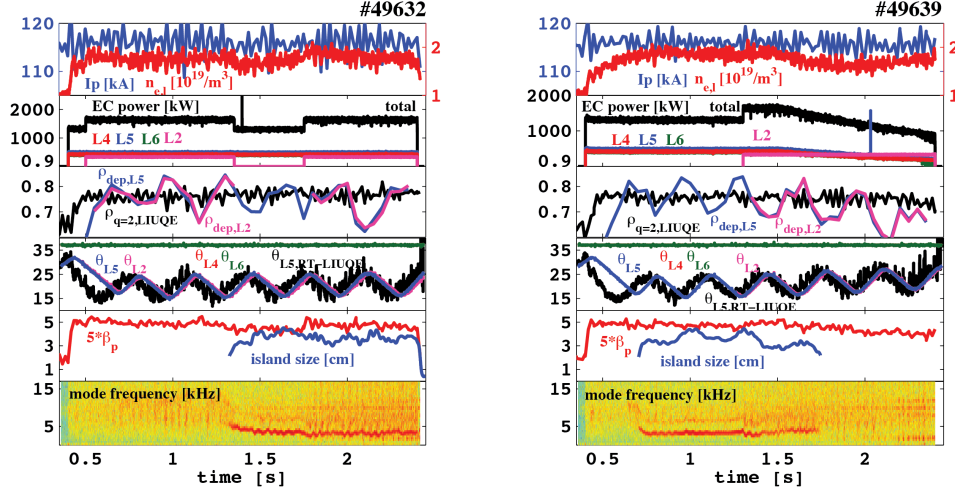


Figure 5.20: Left: the mode preemption using robust control is demonstrated. Until 1.3s, launchers 2 and 5 are sweeping around the target position (estimated with target q value of 2.0) with 0.8MW and the mode does not appear. Then launcher 2 is switched off and the preemption is unsuccessful. The mode is destabilised and once the mode is present robust stabilisation with two launchers (after 1.75s) fails. When the L2 power is switched on, the island size decreases but stays oscillating around 3cm. Right: With one launcher (L5, 0.5MW), the mode cannot be preempted. To find the required power level to completely suppress the mode, the power ramps down from 1.5s. The ratio of the central to the off-axis EC power decreases and it has been reduced by approximately 7% showing that the EC powers on the mode location for the discharge #49632 and until 1.5s for this shot are marginally too low to stabilise the mode.

5.5 Summary

In this chapter, the recent TCV experimental results on NTM control using real-time equilibrium reconstruction have been shown. The real-time version of the long-used equilibrium reconstruction code LIUQE (RT-LIUQE) has been implemented in the TCV real-time control system and has been used to provide the position of NTMs in real-time. Several initial problems, such as noise on the signal and the offset of q profile, have been found and fixed.

Using RT-LIUQE, NTM mode stabilisation has been successfully demonstrated during a number of experiments. With a given target q value, the radial mode location using the q profile estimated by RT-LIUQE has been found. The estimated mode location is converted to launcher angles via a pre-designed interpolation function. Finally, the mode location has been tracked in real-time and EC beam has been able to aim at the right position in the plasma, based on the launcher angle command, to suppress the mode.

In this experimental set, the mode has been triggered through central ECCD's influence on the current density profile. During the experiment it has been shown that a sufficient amount of current drive is required at the centre to destabilise the mode. It has

also been demonstrated that the deposition of the EC beam outside the mode location does not have a detrimental effect on the mode destabilisation. Indeed, the stabilising effectiveness can decrease but the mode does not grow due to the misalignment of EC beam.

Experiments for mode preemption have been carried out as well. Initial lessons learned from both mode stabilisation and destabilisation experiments have been subsequently applied. With sufficient ECCD, EC beams have been placed at the mode location from the beginning of the discharge and the mode has not appeared. In addition, the rise of the 3/2 mode has been observed before the growth of 2/1 mode and it has been possible to prevent the appearance of an 2/1 mode by using 3/2 mode preemption. Though analysis of mode coupling should be carried out, it seems that experimentally these two modes' behaviours are linked.

In order to enhance the control method, the uncertainties for estimating the target position has been investigated. There were uncertainties which come from the offset of both LIUQE and RT-LIUQE and the conversion between target position and launcher mirror angle. The exact value of the offset cannot be evaluated in real-time and changes in time. The conversion factor between target position and launcher angle is presently pre-determined and does not take into account any changes in the plasma. Therefore, it is not possible to guarantee that the estimated target position is close to the *real* mode location and that the stabilising EC beam is correctly driving current at the target position.

A new approach to NTM control has been introduced, named "robust" control. After evaluating the target position, a sinusoidal variation is added to the target position. The EC beam deposition oscillates around the target position increasing the probability of aiming the EC beam at the optimum position for mode stabilisation. In this way, system uncertainties can be compensated. The capability of robust control of NTMs has been experimentally demonstrated. With marginal stabilising power, robust control has a similar effect on the mode stabilisation as without robust control. With sufficient stabilising power, robust control can be more effective since the mode is immediately stabilised when the EC beam reaches the mode location during sweeping; whereas without robust control that location is perhaps never reached. As well as stabilisation of an existing mode, robust control has been applied to mode preemption. The oscillating EC beam delivered the heating and current drive around the target position and the mode appearance was prevented when ample power for preemption was available.

As a result of this work, it is possible to perform improved real-time NTM control experiments using RT-LIUQE and the robust control method. More advanced experiments will require more work on the real-time system. A real-time mode detection will be helpful to check the moment of mode appearance and the mode number. RT mode detection has been used in the past, but was not available during this work; thus linking RT detection and RT-LIUQE is left for future work. Finally, RT ray-tracing would be valuable to provide the mapping of the launcher angle to the target position in real-time.

Chapter 6

Conclusions

In this thesis, the experimental and simulation results of sawteeth and NTM control, which have been carried out in the TCV, KSTAR, AUG and ITER tokamaks, have been presented as well as the transport model for electron temperature and density profile estimation. In this chapter, the achievement of each main chapter in this work will be summarised.

6.1 Predictive electron transport modelling

For the sawtooth simulation, a simple and fast transport model has been introduced to quickly evaluate T_e and n_e profiles in TCV L-mode plasmas during sawtooth cycle. For the T_e profile, the shape of the transport coefficient χ_e has been defined as an operation-scenario-dependent constant value in the central region and to be proportional to the square of the safety factor q in the core region. It should be noted that the edge χ_e model has not yet been developed, hence there the T_e profile has been taken from experiment, providing the boundary condition. The amplitude of the χ_e profile has automatically been adjusted to have equivalent energy confinement times from simulation and the appropriate scaling law. Using the resultant χ_e profile, the T_e profile has been calculated. Although a predictive modelling is constrained by two free parameters, the T_e value at the boundary between core and edge regions and the H_e factor, thanks to the stiffness characteristic in the core region, it has been shown that a reliable T_e profile can be obtained by adjusting these parameters to have R/L_{T_e} lying in the range between [8, 14].

According to Ref. [Sauter:PoP2014], the n_e profile also shows the stiffness characteristic. Therefore, a constant R/L_{n_e} value in the core region has been used to evaluate the n_e profile, whereas R/L_{n_e} varies between zero and the constant value in the central region. The central n_e profile is modified by sawtooth activity. As in the case of T_e , in the edge region the n_e profile has been fixed from the experimental data. In this work, a fixed value of R/L_{n_e} has been used to reproduce the experimental n_e profile. Therefore, to perform a predictive simulation, a scaling law for R/L_{n_e} from a cross-tokamak study would be required.

In this thesis, we have introduced a new scaling factor which takes into account the effect of the heating deposition position on confinement. Using this new scaling factor, combined with the transport model, the temporal and spatial variations of the H_e factor

have been well reproduced as an EC beam sweeps from off-axis to the centre; as have the T_e and n_e profiles. Although this new scaling factor has been tested solely for TCV discharges #41175 and #41170 as an initial study, it has provided an acceptable starting point for later simulations, not only for EC sweeping cases but also for other simulations in which off-axis heating is used.

It has been shown that the T_e and n_e profiles of H-mode plasmas can also be evaluated using the simplified transport model. As for L-mode, χ_e , defined by the q^2 profile and rescaled by the appropriate scaling law, has been able to determine reliable T_e profiles - comparable to the experimental ones - as well as the estimated n_e profiles, using a fixed R/L_{n_e} . However, since T_e profiles of L- and H-mode plasmas have different exponential slopes, another simple method - using an inverse scaling length λ_{T_e} - has also been tested to define the χ_e profile in the core region. With this χ_e , H-mode T_e profiles have been evaluated and shown in good agreement with the experimental profiles. It may be possible to find a scaling for λ_{T_e} across tokamaks since on TCV we have seen that this parameter does not change much with other plasma parameters, due to the stiffness.

The question for edge T_e and n_e profiles evaluation still remains. As discussed in Ref. [Sauter:PoP2014], the edge profiles have linear shape and the slope can vary with the plasma parameters. If a scaling law for the linear slope were to become available, T_e and n_e profiles in the edge could be predicted and be combined with the core profiles, providing the boundary value without the need for experimental measurements.

6.2 Control of sawtooth instability

From the experiments on TCV, KSTAR and AUG, we have tested the feasibility of sawtooth pacing and locking. In TCV, control of the period of individual sawteeth has been experimentally demonstrated using sawtooth pacing, reliant on the TCV real-time control system. For sawtooth locking experiments, it has been shown that the sawtooth period locks to the EC power modulation for a range of combinations of duty cycle and period. The experimental results have been reproduced by sawtooth simulation using the simplified transport model combined with a conventional sawtooth model. For pacing, the estimated time delay between the removal of the EC power and the appearance of the next sawtooth crash for each modulation period has been matched to those observed experimentally. With various combinations of modulation period and duty cycle, the possible locking range has been scanned and the resultant locking range has shown good agreement with the experimentally determined range. From the success of sawtooth control using sawtooth pacing and locking in TCV discharges, the application of these techniques to other tokamaks under various operation conditions has begun to be tested.

For the first attempt, we have applied the sawtooth locking method to the KSTAR tokamak for sawtooth period control using modulated EC power. Since the real-time control system was not ready for sawtooth pacing, only locking was attempted. Once the optimum deposition position to stabilise sawteeth was determined by EC beam sweeping, sawtooth locking experiments were performed with different modulation periods and duty cycles. With a constant modulation period of 43ms and duty cycle of 70%, the sawtooth period was similar to the modulation period at some moments while different at other moments due to the varying integrated EC power per pulse. In the case of higher power, the evolution of sawteeth was retarded and influenced by the next pulse. Therefore,

the sawtooth period was lengthened and the phasing between the EC pulse and the sawtooth crash became irregular; the sawtooth period was governed by total input power per crash. In a second test (62.5ms and 50%), the sawtooth period was regular with two different periods. Due to the long EC-off duration, regulated short-period sawteeth occurred between the EC pulses and regulated longer-period sawteeth were influenced by each EC pulse; the sum of these two periods matched the modulation period. Although only a few cases have been tested due to the limited experimental time available, as a first try, these experiments have demonstrated the applicability of sawtooth locking to the KSTAR tokamak for sawtooth period control. More experiments should follow to complete the investigation of the capability of predictable sawtooth locking on KSTAR.

We have extended the application of sawtooth control techniques to AUG plasmas as well. As in KSTAR, the real-time control system for sawtooth pacing was not available, thus only sawtooth locking has been investigated. Again, the deposition position of the EC beam has been determined from a sweeping experiment, and based on the sweeping result, a possible locking range has been anticipated by sawtooth simulation. From two discharges for locking, sawteeth have shown similar period to the modulation period in some cases but in general sawteeth have not phase-locked to the injected EC power. Due to changes in the EC deposition position relative to the $q = 1$ surface, the maximum sawtooth periods and the size of possible locking range were different in different discharges. After normalisation of the modulation periods with the estimated maximum sawtooth period, the experimental results were mapped on the locking range from simulation. Assuming a narrower possible locking region with deposition more towards the axis, the experimental results showed some similarities to the simulation result. As for the KSTAR experiment, the experimental time was limited. Hence to further understand the sawtooth behaviour and to find the complete locking range, more experiments will be required.

Predictive simulations of sawteeth in the ITER baseline scenario have been carried out to estimate the feasibility of sawtooth pacing and locking using the present EC launcher design. Depending on the number of beams and the control parameter γ , the deposition positions of each beam from the USMs and the injected EC beam shape have been determined. In this work, we have shown that the sawtooth period in an ITER plasma can be paced by or lock to the EC modulation period with different EC beam shapes and deposition positions. From simulation, it has been demonstrated that the time delay between the removal of EC power and the moment of the next crash is of the order of seconds, thus the EC launcher mirror used for sawtooth control has sufficient time to move the EC beam to the mode resonant surface of the expected NTMs to preempt them from being triggered at the time of the sawtooth crash. Furthermore, a modified pacing scheme in which EC power has been switched on with a delay after the crash detection has been proposed and tested in simulations. Sawteeth have still been regulated by the EC pulses and this allows sufficient time for the same preempting beams to be repositioned near the $q = 1$ surface to pace the next sawtooth. From this simulation, the feasibility of sawtooth pacing and locking has been demonstrated. However, due to the simplicity of the simulation with respect to fast particle features of ITER plasmas, more detailed simulation work needs to be carried out, such as taking into account ICRH stabilisation effects for example.

6.3 Real-time control of neoclassical tearing mode

During this work, the main improvement to NTM control experiments has been the application of the real-time equilibrium code (RT-LIUQE [Moret:FED2015]), which has been implemented in the TCV real-time control system. Using RT-LIUQE, the mode location has been determined in real-time using the safety factor q profile and converting a target value to launcher angles. Using this real-time angle command, mode stabilisation and pre-emption of a 2/1 NTM have been successfully demonstrated with sufficient EC power (ECCD). During the pre-emption test, it has been shown that pre-emption of the 3/2 mode can prevent the onset of the 2/1 mode; these two modes seem to be linked, but for better understanding, more analysis of mode coupling should follow.

Due to the uncertainties in estimating the target position, a very careful choice of the target q value has been required. In order to compensate for this uncertainty, a new approach to NTM control has been introduced, which is called "robust" control. By adding a sinusoidal variation to the target position, the EC beam can be deposited at the optimum position for mode stabilisation despite uncertainties in the estimated mode position. In this set of experiments, it has been demonstrated that NTMs are triggered by central ECCD and that EC deposition outside the island location does not destabilise the mode, although the stabilising effect is smaller. Therefore, an oscillating EC beam *around* the target position can be applied to stabilise or pre-empt the mode without deleterious effect on the mode (oscillating in radial position at constant power). The capability of robust NTM control has been experimentally demonstrated. It has been shown that robust control can be more effective (given sufficient stabilising power) despite using an incorrect average target position since the mode is immediately stabilised when the EC beam reaches to the mode location during sweeping. Further study is required to investigate the effects related to the relation between the sweep rate and the speed at which NTMs stabilise as these are likely to be different in different tokamaks.

In this work, we have enhanced the capability of real-time NTM control using RT-LIUQE and a robust control scheme. In order to further improve NTM control, a real-time mode detection combined with RT-LIUQE will be required. In this way, the detection of mode appearance can trigger the real-time control and, by evaluating the mode number, an estimated target q value can automatically be given. Furthermore, using real-time ray tracing, the mapping of the target position to launcher angle can be estimated in real-time and one of the main uncertainties in the TCV application of NTM control can be removed.

Bibliography

- [Alberti:NF2005] Alberti S. et al. “Third-harmonic, top-launch, ECRH experiments on TCV tokamak”. *Nucl. Fusion*, 45(11):1224, 2005. <http://stacks.iop.org/0029-5515/45/i=11/a=002>.
- [Angioni:NF2003] C. Angioni et al. “Effects of localized electron heating and current drive on the sawtooth period”. *Nucl. Fusion*, 43:455, 2003. <http://iopscience.iop.org/0029-5515/43/6/308>.
- [Angioni:PoP2000] C. Angioni and O. Sauter. “Neoclassical transport coefficients for general axisymmetric equilibria in the banana regime”. *Phys. Plasmas*, 7:1224, 2000. <http://link.aip.org/link/?PHPAEN/7/1224/1>.
- [Angioni:PoP2005] C. Angioni et al. “Relationship between density peaking, particle thermodiffusion, Ohmic confinement, and microinstabilities in ASDEX Upgrade L-mode plasmas”. *Phys. Plasmas*, 12(4):040701, 2005. <http://link.aip.org/link/PHPAEN/v12/i4/p040701/s1&Agg=doi>.
- [Angioni:PoP2005b] C. Angioni et al. “Collisionality dependence of density peaking in quasilinear gyrokinetic calculations”. *Phys. Plasmas*, 12:112310, 2005. <http://link.aip.org/link/PHPAEN/v12/i11/p112310/s1>.
- [Angioni:Thesis] C. Angioni. “*Modelling of electron transport and of sawtooth activity in tokamaks*”. PhD thesis, École Polytechnique Fédérale de Lausanne (EPFL), Lausanne, 2001. <http://infoscience.epfl.ch/record/32945?ln=en>.
- [Arnoux:PPCF2005] Arnoux G. et al. “Third harmonic X-mode absorption in a top-launch configuration on the TCV tokamak”. *Plasma Phys. Control. Fusion*, 47(2):295, 2005. <http://stacks.iop.org/0741-3335/47/i=2/a=007>.
- [Artsimovich:NF1972] L.A. Artsimovich. “Tokamak devices”. *Nucl. Fusion*, 12(2):215, 1972. <http://iopscience.iop.org/0029-5515/12/2/012>.
- [Bae:FED2012] Y.S. Bae et al. “Commissioning of the first KSTAR neutral beam injection system and beam experiments”. *Fusion Engineering and Design*, 87(9):1597, 2012. <http://dx.doi.org/10.1016/j.fusengdes.2012.05.011>.
- [Bae:FST2014] Y.S. Bae et al. “Physics and Experimental Results of KSTAR ECH”. *Fusion Science and Technology*, 65(1):88, 2014. http://www.ans.org/pubs/journals/fst/a_35472.

BIBLIOGRAPHY

- [Baker:NF2000] D.R. Baker et al. “Particle transport phenomena in the DIII-D tokamak”. *Nucl. Fusion*, 40(5):1003, 2000. <http://iopscience.iop.org/0029-5515/40/5/301>.
- [Barnes:PoP2010] M. Barnes et al. “Direct multiscale coupling of a transport code to gyrokinetic turbulence codes”. *Phys. Plasmas*, 17(5):056109, 2010.
- [Barry:LAPD1997] S. Barry, C. Nieswand, and S.L. Prunty. “Far-infrared polarimetry on the TCV tokamak”. In *Proceedings of the 8th international symposium on Laser-aided Plasma Diagnostics (LAPD-8)*, Doorwerth, The Netherlands, 1997.
- [Bateman:MHD] G. Bateman. *MHD instabilities*. The MIT Press, 1978.
- [Bortolon:Thesis] A. Bortolon. “Plasma rotation and momentum transport studies in the TCV tokamak based on charge exchange spectroscopy measurements”. PhD thesis, École Polytechnique Fédérale de Lausanne (EPFL), Lausanne, 2009. <http://infoscience.epfl.ch/record/142212?ln=en>.
- [Bosshard:Thesis] P. Bosshard. “Confinement ionique dans le tokamak TCV mesuré par spectroscopie d’échange de charge”. PhD thesis, École Polytechnique Fédérale de Lausanne (EPFL), Lausanne, 2003. <http://infoscience.epfl.ch/record/33199?ln=en>.
- [Brennan:PoP2002] D.P. Brennan et al. “Tearing mode stability studies near ideal stability boundaries in DIII-D”. *Phys. Plasmas*, 9(7):2998, 2002. <http://scitation.aip.org/content/aip/journal/pop/9/7/10.1063/1.1481504>.
- [Budny:NF2008] R.V. Budny et al. “Predictions of H-mode performance in ITER”. *Nucl. Fusion*, 48(7):075005, 2008. <http://iopscience.iop.org/0029-5515/48/7/075005>.
- [Burdakov:PPCF2010] A.V. Burdakov, A.A. Ivanov, and E.P. Kruglyakov. “Modern magnetic mirrors and their fusion prospects”. *Plasma Phys. Control. Fusion*, 52(12):124026, 2010. <http://iopscience.iop.org/0741-3335/52/12/124026/>.
- [Bussac:PRL1975] M.N. Bussac et al. “Internal kink modes in toroidal plasmas with circular cross sections”. *Phys. Rev. Lett.*, 35(24):1638, 1975. http://www.osti.gov/energycitations/product.biblio.jsp?osti_id=4075324.
- [Buttery:PRL2002] R.J. Buttery et al. “Neoclassical Tearing Physics in the Spherical Tokamak MAST”. *Phys. Rev. Lett.*, 88(12):125005, 2002. <http://link.aps.org/doi/10.1103/PhysRevLett.88.125005>.
- [Callen:IAEA1987] J.D. Callen et al. “Neoclassical MHD equations, instabilities and transport in tokamaks”. In *Plasma Physics and Controlled Nuclear Fusion Research*, volume 2, Kyoto, Japan: IAEA, Vienna 157. http://inis.iaea.org/search/search.aspx?orig_q=RN:18091936.

-
- [Canal:NF2013] G.P. Canal et al. “Fast seeding of NTMs by sawtooth crashes in TCV and their preemption using ECRH”. *Nucl. Fusion*, 53(11):113026, 2013. <http://iopscience.iop.org/0029-5515/53/11/113026/>.
- [Carrera:PoF1986] R. Carrera, R.D. Hazeltine, and M. Kotschenreuther. “Island bootstrap current modification of the nonlinear dynamics of the tearing mode”. *Phys. Fluids*, 29(4):899, 1986. <http://link.aip.org/link/PFLDAS/v29/i4/p899/s1&Agg=doi>.
- [Chang:NF1990] Z. Chang and J.D. Callen. “Global energy confinement degradation due to macroscopic phenomena in tokamaks”. *Nucl. Fusion*, 30(2):219, 1990. <http://iopscience.iop.org/0029-5515/30/2/003>.
- [Chapman:NF2010] I.T. Chapman et al. “Empirical scaling of sawtooth period for onset of neoclassical tearing modes”. *Nucl. Fusion*, 50(10):102001, 2010. <http://stacks.iop.org/0029-5515/50/i=10/a=102001?key=crossref.22e8def570181ac87af06dca89b5e947>.
- [Chapman:NF2010b] I.T. Chapman et al. “The effect of plasma profile variation on the stability of the $n = 1$ internal kink mode in rotating tokamak plasmas”. *Nucl. Fusion*, 50(2):025018, 2010. <http://stacks.iop.org/0029-5515/50/i=2/a=025018>.
- [Chapman:NF2013] I.T. Chapman et al. “Power requirements for electron cyclotron current drive and ion cyclotron resonance heating for sawtooth control in ITER”. *Nucl. Fusion*, 53(6):066001, 2013. <http://stacks.iop.org/0029-5515/53/i=6/a=066001?key=crossref.02d8e002c531ce26e525c70a1dc7dc9b>.
- [Chapman:PPCF2011] I.T. Chapman et al. “Sawtooth control in ITER using ion cyclotron resonance heating”. *Plasma Phys. Control. Fusion*, 53(12):124003, 2011. <http://stacks.iop.org/0741-3335/53/i=12/a=124003?key=crossref.fb669aa224b6fa3577d24c0b70cd80e9>.
- [Chapman:PRL2010] I.T. Chapman et al. “Magnetic Reconnection Triggering Magneto-hydrodynamic Instabilities during a Sawtooth Crash in a Tokamak Plasma”. *Phys. Rev. Lett.*, 105(25):255002, 2010. <http://link.aps.org/doi/10.1103/PhysRevLett.105.255002>.
- [Collazos:FST2009] A. Collazos et al. “Progress on the ITER upper launcher millimeter-wave design and testing”. *Fusion Science and Technology*, 55(1):84, 2009. <http://cat.inist.fr/?aModele=afficheN&cpsidt=21204800>.
- [Coppi:SovJPP1976] B. Coppi et al. “Resistive internal kink modes”. *Soviet Journal of Plasma Physics*, 2:533, 1976.
- [Cowley:PoF1986] S.C. Cowley, R.M. Kulsrud, and T.S. Hahm. “Linear stability of tearing modes”. *Phys. Fluids*, 29(10):3230, 1986. <http://scitation.aip.org/content/aip/journal/pof1/29/10/10.1063/1.865841>.

BIBLIOGRAPHY

- [DeLazzari:Nf2009] D. De Lazzari and E. Westerhof. “On the merits of heating and current drive for tearing mode stabilization”. *Nucl. Fusion*, 49(7):075002, 2009. <http://stacks.iop.org/0029-5515/49/i=7/a=075002?key=crossref.07bc3ff65bc9ae9332f4de570c215dfa>.
- [DeLazzari:Nf2010] D. De Lazzari and E. Westerhof. “On the merits of heating and current drive for tearing mode stabilization”. *Nucl. Fusion*, 50(7):079801, 2010. <http://iopscience.iop.org/0029-5515/50/7/079801>.
- [Donne:Nf2007] A.J.H. Donn e et al. “Chapter 7: Diagnostics”. *Nucl. Fusion*, 47(6):S337, 2007. <http://stacks.iop.org/0029-5515/47/i=6/a=S07?key=crossref.7bc16f08971965dc56c3d4faea0af115>.
- [Fable:PPCF2010] E. Fable, C. Angioni, and O. Sauter. “The role of ion and electron electrostatic turbulence in characterizing stationary particle transport in the core of tokamak plasmas”. *Plasma Phys. Control. Fusion*, 52(1):015007, 2010. <http://stacks.iop.org/0741-3335/52/i=1/a=015007?key=crossref.c29f0e3bb34083486900eedfb15dac86>.
- [Fable:Thesis] E. Fable. “*Experimental and theoretical study of particle transport in the TCV tokamak*”. PhD thesis,  cole Polytechnique F d rale de Lausanne (EPFL), Lausanne, 2009. <http://infoscience.epfl.ch/record/130845?ln=en>.
- [Farina:FST2007] D. Farina. “A quasi-optical beam-tracing code for electron cyclotron absorption and current drive: GRAY”. *Fusion Science and Technology*, 52(2):154, 2007. <http://cat.inist.fr/?aModelle=afficheN&cpsid=19013894>.
- [Farina:Nf2012] D. Farina et al. “Potential of the ITER electron cyclotron equatorial launcher for heating and current drive at nominal and reduced fields”. *Nucl. Fusion*, 52(3):033005, 2012. <http://stacks.iop.org/0029-5515/52/i=3/a=033005?key=crossref.2df0e606c0dc5141240a5af3e91cfd24>.
- [Farina:private] D. Farina. personal communication, 2013.
- [Faugel:FED2005] H. Faugel et al. “The ASDEX Upgrade ICRF system: Operational experience and developments”. *Fusion Engineering and Design*, 74(1-4):319, 2005. <http://linkinghub.elsevier.com/retrieve/pii/S0920379605002838>.
- [Felici:EPS2009] F. Felici et al. “Self-consistent simulation of tearing modes during ECCD experiments on TCV”. In *Proc. 36th EPS Conference on Plasma Physics (Sofia, Bulgaria, June 2009)*.
- [Felici:FED2014] F. Felici et al. “Development of real-time plasma analysis and control algorithms for the TCV tokamak using SIMULINK”. *Fusion Engineering and Design*, 89(3):165, 2014. <http://dx.doi.org/10.1016/j.fusengdes.2013.11.010>.
- [Felici:Nf2011] F. Felici et al. “Real-time physics-model-based simulation of the current density profile in tokamak plasmas”. *Nucl. Fusion*, 51(8):083052, 2011. <http://stacks.iop.org/0029-5515/51/i=8/a=083052?key=crossref.c330df5aaf0fede3b35cd0ace44959e5>.

- [Felici:Nf2012] F. Felici et al. “Integrated real-time control of MHD instabilities using multi-beam ECRH/ECCD systems on TCV”. *Nucl. Fusion*, 52(7):074001, 2012. <http://stacks.iop.org/0029-5515/52/i=7/a=074001?key=crossref.d3101d38dcee6b7c03d9aa2ba4fc4ffe>.
- [Felici:Thesis] F. Felici. “Real-time control of tokamak plasmas: from control of physics to physics-based control”. PhD thesis, École Polytechnique Fédérale de Lausanne (EPFL), Lausanne, 2011. <http://dx.doi.org/10.5075/epfl-thesis-5203>.
- [Fitzpatrick:PoP1995] R. Fitzpatrick. “Helical temperature perturbations associated with tearing modes in tokamak plasmas”. *Phys. Plasmas*, 2(3):825, 1995. <http://link.aip.org/link/PHPAEN/v2/i3/p825/s1&Agg=doi>.
- [Franke:Thesis] S. Franke. “Application of Thomson scattering at 1.06mm as a diagnostic for spatial profile measurements of electron temperature and density on the TCV tokamak”. PhD thesis, École Polytechnique Fédérale de Lausanne (EPFL), Lausanne, 1997. <http://infoscience.epfl.ch/record/32131?ln=en>.
- [Freidberg:PlasmaPhysics] J.P. Freidberg. *Plasma Physics and Fusion Energy*. Cambridge University Press, 2007.
- [Furth:PoF1963] H.P. Furth, J. Killeen, and M.N. Rosenbluth. “Finite-Resistivity Instabilities of a Sheet Pinch”. *Phys. Fluids*, 6(4):459, 1963. <http://link.aip.org/link/PFLDAS/v6/i4/p459/s1&Agg=doi>.
- [Furth:PoF1973] H.P. Furth. “Tearing mode in the cylindrical tokamak”. *Phys. Fluids*, 16(7):1054, 1973. <http://link.aip.org/link/PFLDAS/v16/i7/p1054/s1&Agg=doi>.
- [Gantenbein:PRL2000] G Gantenbein et al. “Complete suppression of neoclassical tearing modes with current drive at the electron-cyclotron-resonance frequency in ASDEX Upgrade tokamak”. *Phys. Rev. Lett.*, 85(6):1242, 2000. <http://journals.aps.org/prl/abstract/10.1103/PhysRevLett.85.1242>.
- [Garbet:PPCF2004] X. Garbet et al. “Profile stiffness and global confinement”. *Plasma Phys. Control. Fusion*, 46(9):1351, 2004. <http://iopscience.iop.org/0741-3335/46/9/002>.
- [Gimblett:PPCF1994] C.G. Gimblett and R.J. Hastie. “Calculation of the post-crash state and 1 1/2 D simulation of sawtooth cycles”. *Plasma Phys. Control. Fusion*, 36:1439, 1994. <http://iopscience.iop.org/0741-3335/36/9/005>.
- [Glasser:PoF1975] A.H. Glasser, J.M. Greene, and J.L. Johnson. “Resistive instabilities in general toroidal plasma configurations”. *Phys. Fluids*, 18(7):875, 1975. <http://link.aip.org/link/PFLDAS/v18/i7/p875/s1&Agg=doi>.
- [Goodman:Nf2008] T.P. Goodman and the TCV Team. “Experience in integrated control of the multi-megawatt electron cyclotron heating system on the TCV tokamak: the first decade”. *Nucl. Fusion*, 48(5):054011, 2008. <http://stacks.iop.org/0029-5515/48/i=5/a=054011?key=crossref.f221119072b05a39c50d8dff80bcb0ae>.

BIBLIOGRAPHY

- [Goodman:PRL2011] T.P. Goodman et al. “Sawtooth pacing by real-time auxiliary power control in a tokamak plasma”. *Phys. Rev. Lett.*, 106(24), 2011. <http://link.aps.org/doi/10.1103/PhysRevLett.106.245002>.
- [Graves:Nature2012] J.P. Graves et al. “Control of magnetohydrodynamic stability by phase space engineering of energetic ions in tokamak plasmas”. *Nature Communications*, 3:624, 2012. <http://www.nature.com/ncomms/journal/v3/n1/abs/ncomms1622.html>.
- [Graves:PRL2004] Jonathan Graves. “Influence of Asymmetric Energetic Ion Distributions on Sawtooth Stabilization”. *Phys. Rev. Lett.*, 92(18), 2004. <http://link.aps.org/doi/10.1103/PhysRevLett.92.185003>.
- [Gude:NF1999] A Gude, S Günter, and S Sesnic. “Seed island of neoclassical tearing modes at ASDEX upgrade”. *Nucl. Fusion*, 39(1):127, 1999. <http://gateway.webofknowledge.com/gateway/Gateway.cgi?GWVersion=2&SrcAuth=mekentosj&SrcApp=Papers&DestLinkType=FullRecord&DestApp=WOS&KeyUT=000080095700008>.
- [Hegna:PoP1998] C.C. Hegna. “The physics of neoclassical magnetohydrodynamic tearing modes”. *Phys. Plasmas*, 5(5):1767, 1998. <http://link.aip.org/link/PHPAEN/v5/i5/p1767/s1&Agg=doi>.
- [Hegna:PoP1999] C.C. Hegna. “Nonlinear dynamics of pressure driven magnetic islands in low aspect ratio tokamaks”. *Phys. Plasmas*, 6(10):3980, 1999. <http://scitation.aip.org/content/aip/journal/pop/6/10/10.1063/1.873661>.
- [Hemsworth:RSI2008] R.S. Hemsworth, A. Tanga, and V. Antoni. “Status of the ITER neutral beam injection system”. *Rev. Sci. Instrum.*, 79(2):02C109, 2008. <http://scitation.aip.org/content/aip/journal/rsi/79/2/10.1063/1.2814248>.
- [Hender:NF2007] T.C. Hender et al. “Chapter 3: MHD stability, operational limits and disruptions”. *Nucl. Fusion*, 47(6):S128, 2007. <http://stacks.iop.org/0029-5515/47/i=6/a=S03?key=crossref.0b9322e42a59b955269531e35f39b3bb>.
- [Henderson:EC2006] M.A. Henderson et al. “The ITER ECH FS upper launcher design for an optimized physics performance”. In *Proceedings of the 14th Joint Workshop on Electron Cyclotron Emission and Electron Cyclotron Resonance Heating*, Santorini, Greece, 9–12 May, 2006.
- [Henderson:FED2001] M.A. Henderson et al. “Poloidally asymmetric plasma response with ECH deposition near $q = 1$ in TCV”. *Fusion Engineering and Design*, 53(1-4):241, 2001. <http://www.sciencedirect.com/science/article/pii/S0920379600004932>.
- [Henderson:NF2008] M.A. Henderson et al. “Overview of the ITER EC upper launcher”. *Nucl. Fusion*, 48(5):054013, 2008. <http://stacks.iop.org/0029-5515/48/i=5/a=054013?key=crossref.ceaaa462ebb9f0c780b10e36af1062fe>.

- [Herrmann:FST2003] A. Herrmann and O. Gruber. “Chapter 1: ASDEX upgrade introduction and overview”. *Fusion Science and Technology*, 44(3):569, 2003. <http://gateway.webofknowledge.com/gateway/Gateway.cgi?GWVersion=2&SrcAuth=mekentosj&SrcApp=Papers&DestLinkType=FullRecord&DestApp=WOS&KeyUT=000186115300003>.
- [Hinton:RMP1976] F.L. Hinton and R.D. Hazeltine. “Theory of plasma transport in toroidal confinement systems”. *Rev.Mod.Phys.*, 48:239, 1976. <http://journals.aps.org/rmp/abstract/10.1103/RevModPhys.48.239>.
- [Hofmann:NF1988] F. Hofmann and G. Tonetti. “Tokamak Equilibrium Reconstruction Using Faraday-Rotation Measurements”. *Nucl. Fusion*, 28(10):1871, 1988. <http://gateway.webofknowledge.com/gateway/Gateway.cgi?GWVersion=2&SrcAuth=mekentosj&SrcApp=Papers&DestLinkType=FullRecord&DestApp=WOS&KeyUT=A1988Q985700014>.
- [Hofmann:PPCF1994] F. Hofmann et al. “Creation and Control of Variably Shaped Plasmas in TCV”. *Plasma Phys. Control. Fusion*, 36(12B):B277, 1994. <http://gateway.webofknowledge.com/gateway/Gateway.cgi?GWVersion=2&SrcAuth=mekentosj&SrcApp=Papers&DestLinkType=FullRecord&DestApp=WOS&KeyUT=A1994QB97700024>.
- [ITER-PhysicsBasis:NF1999] ITER Physics Basis Editors. “Chapter 2: Plasma confinement and transport”. *Nucl. Fusion*, 39(12):2175, 1999. <http://iopscience.iop.org/0029-5515/39/12/302>.
- [Isayama:NF2003] A. Isayama et al. “Achievement of high fusion triple product, steady-state sustainment and real-time NTM stabilization in high- β_p ELMy H-mode discharges in JT-60U”. *Nucl. Fusion*, 43(10):1272, 2003. <http://iopscience.iop.org/0029-5515/43/10/031>.
- [Isayama:NF2009] A. Isayama et al. “Neoclassical tearing mode control using electron cyclotron current drive and magnetic island evolution in JT-60U”. *Nucl. Fusion*, 49(5):055006, 2009. <http://stacks.iop.org/0029-5515/49/i=5/a=055006?key=crossref.3dd52ffb6e2f54c2784d5ec17036c6d0>.
- [Isayama:PPCF2000] A. Isayama et al. “Complete stabilization of a tearing mode in steady state high- β_p H-mode discharges by the first harmonic electron cyclotron heating/current drive on JT-60U”. *Plasma Phys. Control. Fusion*, 42(12):L37, 2000. <http://iopscience.iop.org/0741-3335/42/12/102>.
- [JeongJH:EC2014] J.H. Jeong et al. “Demonstration of sawtooth period control with EC waves in KSTAR plasma”. In *Proceedings of the 18th Joint Workshop on Electron Cyclotron Emission and Electron Cyclotron Resonance Heating*, Nara, Japan, 22–25 April, 2014.
- [JeongSH:RSI2010] S.H. Jeong et al. “Electron cyclotron emission diagnostics on KSTAR tokamak”. *Rev. Sci. Instrum.*, 81(10):10D922, 2010. <http://scitation.aip.org/content/aip/journal/rsi/81/10/10.1063/1.3491224>.

BIBLIOGRAPHY

- [Kadomtsev:SovJPP1975] B. Kadomtsev. “On disruptive instability in tokamaks”. *Soviet Journal of Plasma Physics*, 1:710, 1975.
- [Kessel:Nf2009] C.E. Kessel et al. “Development of ITER 15 MA ELMy H-mode inductive scenario”. *Nucl. Fusion*, 49(8):085034, 2009. <http://stacks.iop.org/0029-5515/49/i=8/a=085034?key=crossref.493549f781d9b8f118233c6b9c0b9d78>.
- [Kim:EPS2012] D. Kim et al. “Simulation of the effect of ECH/ECCD on sawtooth period”. In *Proc. 39th EPS Conference on Plasma Physics (Stockholm, Sweden, July 2012)*.
- [Kim:PoP2014] D. Kim, T.P. Goodman, and O. Sauter. “Real-time sawtooth control and neoclassical tearing mode preemption in ITER”. *Phys. Plasmas*, 21(6):061503, 2014. <http://scitation.aip.org/content/aip/journal/pop/21/6/10.1063/1.4884349>.
- [Kirneva:PPCF2012] N.A. Kirneva et al. “Dependence of L-mode confinement on the electron cyclotron power deposition profile in the TCV tokamak”. *Plasma Phys. Control. Fusion*, 54(1):015011, 2012. <http://iopscience.iop.org/0741-3335/54/1/015011>.
- [Kolemen:Nf2014] E. Kolemen et al. “State-of-the-art neoclassical tearing mode control in DIII-D using real-time steerable electron cyclotron current drive launchers”. *Nucl. Fusion*, 54(7):073020, 2014. <http://stacks.iop.org/0029-5515/54/i=7/a=073020?key=crossref.e5c1ab404443aedbbd06b2a15441021d>.
- [Kotschenreuther:PoP1995] M. Kotschenreuther et al. “Quantitative predictions of tokamak energy confinement from first-principles simulations with kinetic effects”. *Phys. Plasmas*, 2(6):2381, 1995. <http://scitation.aip.org/content/aip/journal/pop/2/6/10.1063/1.871261>.
- [Kruskal:PoF1958] M.D. Kruskal and C.R. Oberman. “On the Stability of Plasma in Static Equilibrium”. *Phys. Fluids*, 1(4):275, 1958. <http://link.aip.org/link/PFLDAS/v1/i4/p275/s1&Agg=doi>.
- [Kwak:FED2010] J.G. Kwak et al. “Commissioning the ICRF system and an ICRF assisted discharge cleaning at the KSTAR”. *Fusion Engineering and Design*, 85(2):169, 2010. <http://dx.doi.org/10.1016/j.fusengdes.2009.09.002>.
- [LaHaye:Nf2005] R.J. La Haye et al. “Higher stable beta by use of preemptive electron cyclotron current drive on DIII-D”. *Nucl. Fusion*, 45(11):L37, 2005. <http://stacks.iop.org/0029-5515/45/i=11/a=L02?key=crossref.77fe8fe3d16a72a26e4e9028b7519cf5>.
- [LaHaye:Nf2006] R.J. La Haye et al. “Cross-machine benchmarking for ITER of neoclassical tearing mode stabilization by electron cyclotron current drive”. *Nucl. Fusion*, 46(4):451, 2006. <http://stacks.iop.org/0029-5515/46/i=4/a=006?key=crossref.5ef56220336fc579ba2933d5b93104ee>.

-
- [LaHaye:PoP2002] R.J. La Haye et al. “Control of neoclassical tearing modes in DIII-D”. *Phys. Plasmas*, 9(5):2051, 2002. <http://scitation.aip.org/content/aip/journal/pop/9/5/10.1063/1.1456066>.
- [LaHaye:PoP2006] R.J. La Haye. “Neoclassical tearing modes and their control”. *Phys. Plasmas*, 13(5):055501, 2006. <http://link.aip.org/link/PHPAEN/v13/i5/p055501/s1&Agg=doi>.
- [Lauret:NF2012] M. Lauret et al. “Demonstration of sawtooth period locking with power modulation in TCV plasmas”. *Nucl. Fusion*, 52(6):062002, 2012. <http://iopscience.iop.org/0029-5515/52/6/062002/>.
- [Le:FED2014] H.B. Le et al. “Distributed digital real-time control system for TCV tokamak”. *Fusion Engineering and Design*, 89(3):155, 2014. <http://dx.doi.org/10.1016/j.fusengdes.2013.11.001>.
- [Lee:NF2000] G.S. Lee et al. “The KSTAR project: An advanced steady state superconducting tokamak experiment”. *Nucl. Fusion*, 40(3Y):575, 2000. <http://gateway.webofknowledge.com/gateway/Gateway.cgi?GWVersion=2&SrcAuth=mekentosj&SrcApp=Papers&DestLinkType=FullRecord&DestApp=WOS&KeyUT=000086358500020>.
- [Lee:RSI2010] J.H. Lee et al. “Diagnostics for first plasma and development plan on KSTAR”. *Rev. Sci. Instrum.*, 81(6):063502, 2010. <http://scitation.aip.org/content/aip/journal/rsi/81/6/10.1063/1.3429942>.
- [Lennholm:PRL2009] M. Lennholm et al. “Demonstration of Effective Control of Fast-Ion-Stabilized Sawteeth by Electron-Cyclotron Current Drive”. *Phys. Rev. Lett.*, 102(11):115004, 2009. <http://link.aps.org/doi/10.1103/PhysRevLett.102.115004>.
- [Liewer:NF1985] P.C. Liewer. “Measurements of microturbulence in tokamaks and comparisons with theories of turbulence and anomalous transport”. *Nucl. Fusion*, 25(5):543, 1985. <http://iopscience.iop.org/0029-5515/25/5/004>.
- [Lindl:PoP2014] J. Lindl et al. “Review of the National Ignition Campaign 2009-2012”. *Phys. Plasmas*, 21(2):020501, 2014. <http://scitation.aip.org/content/aip/journal/pop/21/2/10.1063/1.4865400>.
- [Lister:FT1997] J.B. Lister et al. “The control of tokamak configuration variable plasmas”. *Fusion Technology*, 32(3):321, 1997. <http://gateway.webofknowledge.com/gateway/Gateway.cgi?GWVersion=2&SrcAuth=mekentosj&SrcApp=Papers&DestLinkType=FullRecord&DestApp=WOS&KeyUT=A1997YF39900004>.
- [Luce:PoP2004] T.C. Luce et al. “High performance stationary discharges in the DIII-D tokamak”. *Phys. Plasmas*, 11(5):2627, 2004. <http://scitation.aip.org/content/aip/journal/pop/11/5/10.1063/1.1704644>.
-

BIBLIOGRAPHY

- [Lutjens:CPC1996] H. Lütjens, A. Bondeson, and O. Sauter. “The CHEASE code for toroidal MHD equilibria”. *Computer Physics Communications*, 97(3):219, 1996. <http://www.sciencedirect.com/science/article/pii/001046559600046X>.
- [Lutjens:NF1992] H. Lütjens, A. Bondeson, and G. Vlad. “Ideal MHD Stability of Internal Kinks in Circular and Shaped Tokamaks”. *Nucl. Fusion*, 32(9):1625, 1992. <http://gateway.webofknowledge.com/gateway/Gateway.cgi?GWVersion=2&SrcAuth=mekentosj&SrcApp=Papers&DestLinkType=FullRecord&DestApp=WOS&KeyUT=A1992JU24900010>.
- [Lutjens:PoP2001] H. Lütjens, J-F. Luciani, and X. Garbet. “Curvature effects on the dynamics of tearing modes in tokamaks”. *Phys. Plasmas*, 8(10):4267, 2001. <http://link.aip.org/link/PHPAEN/v8/i10/p4267/s1&Agg=doi>.
- [Lyon:PPCF1990] J.F. Lyon. “Review of Recent Stellarator Results in the USA the USSR, and Japan”. *Plasma Phys. Control. Fusion*, 32(11):1041, 1990. <http://iopscience.iop.org/0741-3335/32/11/015>.
- [Maraschek:PRL2007] M. Maraschek et al. “Enhancement of the Stabilization Efficiency of a Neoclassical Magnetic Island by Modulated Electron Cyclotron Current Drive in the ASDEX Upgrade Tokamak”. *Phys. Rev. Lett.*, 98(2):025005, 2007. <http://link.aps.org/doi/10.1103/PhysRevLett.98.025005>.
- [Martynov:PPCF2005] A. Martynov, J.P. Graves, and O. Sauter. “The stability of the ideal internal kink mode in realistic tokamak geometry”. *Plasma Phys. Control. Fusion*, 47(10):1743, 2005. <http://stacks.iop.org/0741-3335/47/i=10/a=009?key=crossref.ec75ac820a25668fa3c13d0c72398d52>.
- [Matsuda:IEEE1989] K. Matsuda. “Ray Tracing Study of the Electron-Cyclotron Current Drive in DIII-D Using 60 GHz”. *IEEE Trans. Plasma Sci.*, 17(1):6, 1989. http://ieeexplore.ieee.org/xpls/abs_all.jsp?arnumber=21664.
- [Migliuolo:PoFB1991] S. Migliuolo, F. Pegoraro, and F. Porcelli. “Stabilization of collisional drift-tearing modes at the breakdown of the constant- Ψ approximation”. *Phys. Fluids B*, 3(6):1338, 1991. <http://scitation.aip.org/content/aip/journal/pofb/3/6/10.1063/1.859828>.
- [Monticello:PoF1980] D.A. Monticello and R.B. White. “Nonlinear drift tearing modes”. *Phys. Fluids*, 23(2):366, 1980. <http://scitation.aip.org/content/aip/journal/pof1/23/2/10.1063/1.862995>.
- [Moret:FED2015] J.M. Moret et al. “Tokamak equilibrium reconstruction code LIUQE and its real time implementation”. *to be published in Fusion Engineering and Design*, 2015.
- [Moret:RSI1998] J.M. Moret et al. “Magnetic measurements on the TCV Tokamak”. *Rev. Sci. Instrum.*, 69(6):2333, 1998. <http://scitation.aip.org/content/aip/journal/rsi/69/6/10.1063/1.1148940>.

- [Nave:NF1990] M.F.F. Nave and J.A. Wesson. “Mode-Locking in Tokamaks”. *Nucl. Fusion*, 30(12):2575, 1990. <http://gateway.webofknowledge.com/gateway/Gateway.cgi?GWVersion=2&SrcAuth=mekentosj&SrcApp=Papers&DestLinkType=FullRecord&DestApp=WOS&KeyUT=A1990ER72900011>.
- [Nordman:NF1990] H. Nordman, J. Weiland, and A. Jarmén. “Simulation of toroidal drift mode turbulence driven by temperature gradients and electron trapping”. *Nucl. Fusion*, 30(6):983, 1990. <http://iopscience.iop.org/0029-5515/30/6/001>.
- [Nowak:IAEA2014] Nowak. S. et al. “(N)TM Onset by Central EC Power Deposition in FTU and TCV Tokamaks”. In *Proc. 25th IAEA Fusion Energy Conference (Saint Petersburg, Russia) (Vienna:IAEA) paper EX/P2-54 2014*.
- [Nowak:JPHYS2012] S. Nowak et al. “Evidence of Neoclassical Toroidal Viscosity on the Neoclassical Tearing Modes in TCV tokamak”. *J. Phys.: Conf. Ser.*, 401:012017, 2012. <http://stacks.iop.org/1742-6596/401/i=1/a=012017?key=crossref.0572e8d90596f31b0746782b56ff24c2>.
- [Onjun:NF2009] T. Onjun and Y. Pianroj. “Simulations of ITER with combined effects of internal and edge transport barriers”. *Nucl. Fusion*, 49(7):075003, 2009. <http://iopscience.iop.org/0029-5515/49/7/075003>.
- [Ottaviani:PPCF1997] M. Ottaviani, W. Horton, and M. Erba. “The long wavelength behaviour of ion-temperature-gradient-driven turbulence and the radial dependence of the turbulent ion conductivity”. *Plasma Phys. Control. Fusion*, 39(9):1461, 1997. <http://iopscience.iop.org/0741-3335/39/9/012>.
- [Paley:PPCF2009] J.I. Paley et al. “Real time control of the sawtooth period using EC launchers”. *Plasma Phys. Control. Fusion*, 51(5):055010, 2009. <http://stacks.iop.org/0741-3335/51/i=5/a=055010?key=crossref.b0eefa9c1c981e7a18bd76197fc698ff>.
- [Paley:RTC2010] J.I. Paley et al. “Architecture and commissioning of the TCV distributed feedback control system”. In *17th IEEE-NPSS Real Time Conference (RT)*, 2010.
- [Parail:NF2013] V. Parail et al. “Self-consistent simulation of plasma scenarios for ITER using a combination of 1.5D transport codes and free-boundary equilibrium codes”. *Nucl. Fusion*, 53(11):113002, 2013. <http://stacks.iop.org/0029-5515/53/i=11/a=113002?key=crossref.742c7a8ca3bc69e3bccccf0900c556a05>.
- [Park:FST2013] S. Park et al. “Progress of KSTAR 5-GHz lower hybrid current drive system”. *Fusion Science and Technology*, 63(1):49, 2013. <http://gateway.webofknowledge.com/gateway/Gateway.cgi?GWVersion=2&SrcAuth=mekentosj&SrcApp=Papers&DestLinkType=FullRecord&DestApp=WOS&KeyUT=000314740500007>.
- [Pegoraro:PoFB1989] F. Pegoraro, F. Porcelli, and T.J. Schep. “Internal kink modes in the ion-kinetic regime”. *Phys. Fluids B*, 1(2):364, 1989. <http://scitation.aip.org/content/aip/journal/pofb/1/2/10.1063/1.859149>.

BIBLIOGRAPHY

- [Pereverzev:2002] G.V. Pereverzev and P.N. Yushmanov. “*ASTRA Automated System for Transport Analysis*”. Max-Planck-Institut für Plasmaphysik, Rep. IPP 5/98, Garching, February 2002.
- [Piras:PPCF2009] F. Piras et al. “Snowflake divertor plasmas on TCV”. *Plasma Phys. Control. Fusion*, 51(5):055009, 2009. <http://stacks.iop.org/0741-3335/51/i=5/a=055009?key=crossref.a281e046d21242eba91cedfc60587859>.
- [Piras:PRL2010] F. Piras et al. ““Snowflake” H-Mode in a Tokamak Plasma”. *Phys. Rev. Lett.*, 105(15):155003, 2010. <http://link.aps.org/doi/10.1103/PhysRevLett.105.155003>.
- [Pletzer:JCP1994] A. Pletzer, A. Bondeson, and R.L. Dewar. “Linear stability of resistive MHD modes: axisymmetric toroidal computation of the outer region matching data”. *Journal of Computational Physics*, 115(2):530, 1994. <http://www.sciencedirect.com/science/article/pii/S0021999184712150>.
- [Pletzer:PoP1999] A. Pletzer and F.W. Perkins. “Stabilization of neoclassical tearing modes using a continuous localized current drive”. *Phys. Plasmas*, 6(5):1589, 1999. <http://scitation.aip.org/content/aip/journal/pop/6/5/10.1063/1.873412>.
- [Pochelon:RF1998] Pochelon A. et al. “Preliminary confinement studies during ECRH in TCV”. In *Second Europhysics Topical Conference on Radio Frequency Heating and Current Drive of Fusion Devices*, volume 22, Brussels, Belgium.
- [Poli:CPC2001] E. Poli and G.V. Peeters, A.G. Pereverzev. “TORBEAM, a beam tracing code for electron-cyclotron waves in tokamak plasmas”. *Comput. Phys. Commun.*, 136:90, 2001. <http://www.sciencedirect.com/science/article/pii/S0010465501001461>.
- [Poli:PRL2005] E. Poli, A. Bergmann, and A. Peeters. “Role of Kinetic Effects on the Polarization Current around a Magnetic Island”. *Phys. Rev. Lett.*, 94(20):205001, 2005. <http://link.aps.org/doi/10.1103/PhysRevLett.94.205001>.
- [Porcelli:PPCF1991] F. Porcelli. “Fast Particle Stabilization”. *Plasma Phys. Control. Fusion*, 33(13):1601, 1991. <http://iopscience.iop.org/0741-3335/33/13/009>.
- [Porcelli:PPCF1996] F. Porcelli, D. Boucher, and M.N. Rosenbluth. “Model for the sawtooth period and amplitude”. *Plasma Phys. Control. Fusion*, 38:2163, 1996. <http://iopscience.iop.org/0741-3335/38/12/010>.
- [Raju:PPCF2003] D. Raju, O. Sauter, and J.B. Lister. “Study of nonlinear mode coupling during neoclassical tearing modes using bispectrum analysis”. *Plasma Phys. Control. Fusion*, 45(4):369, 2003. <http://iopscience.iop.org/0741-3335/45/4/304>.
- [Ramponi:PoP1999] G. Ramponi, E. Lazzaro, and S. Nowak. “On the stabilization of neoclassical tearing modes by electron cyclotron waves”. *Phys. Plasmas*, 6(9):3561, 1999. <http://link.aip.org/link/PHPAEN/v6/i9/p3561/s1&Agg=doi>.

- [Rebut:IAEA1989] P.H. Rebut, P.P. Lallia, and M.L. Watkins. “The critical temperature gradient model of plasma transport: applications to JET and future tokamaks”. In *Plasma Physics and Controlled Nuclear Fusion Research 1988: Proc. 12th Int. Conf (Nice, 1988)*, volume 2, IAEA, Vienna p.191.
- [Reimerdes:PRL2002] H. Reimerdes et al. “From Current-Driven to Neoclassically Driven Tearing Modes”. *Phys. Rev. Lett.*, 88(10):105005, 2002. <http://link.aps.org/doi/10.1103/PhysRevLett.88.105005>.
- [Rice:NF1999] B.W. Rice et al. “Progress towards sustainment of advanced tokamak modes in DIII-D”. *Nucl. Fusion*, 39(11Y):1855, 1999. <http://iopscience.iop.org/0029-5515/39/11Y/326>.
- [Rosenberg:PoP2002] A.L. Rosenberg et al. “Modeling of neoclassical tearing mode stability for generalized toroidal geometry”. *Phys. Plasmas*, 9(11):4567, 2002. <http://scitation.aip.org/content/aip/journal/pop/9/11/10.1063/1.1512285>.
- [Rossel:Thesis] J. Rossel. “*Edge Localized Mode Control in TCV*”. PhD thesis, École Polytechnique Fédérale de Lausanne (EPFL), Lausanne, 2012. <http://infoscience.epfl.ch/record/174678?ln=en>.
- [Rutherford:PoF1973] P.H. Rutherford. “Nonlinear growth of the tearing mode”. *Phys. Fluids*, 16(11):1903, 1973. <http://link.aip.org/link/PFLDAS/v16/i11/p1903/s1&Agg=doi>.
- [Ryter:NF2001] F. Ryter et al. “Confinement and transport studies of conventional scenarios in ASDEX Upgrade”. *Nucl. Fusion*, 41(5):537, 2001. <http://iopscience.iop.org/0029-5515/41/5/307>.
- [Saibene:IAEA2006] G. Saibene et al. “Design of the ITER electron cyclotron wave launcher for NTM control”. http://www-naweb.iaea.org/napc/physics/FEC/FEC2006/papers/it_p2-14.pdf.
- [Sauter:CPC2013] O. Sauter and S.Y. Medvedev. “Tokamak coordinate conventions: COCOS”. *Computer Physics Communications*, 184(2):293, 2013. <http://dx.doi.org/10.1016/j.cpc.2012.09.010>.
- [Sauter:IAEA2010] O. Sauter et al. “Effects of ECH/ECCD on tearing modes in TCV and link to rotation profile”. In *Proc. 23th IAEA Fusion Energy Conference (Daejeon, Korea) (Vienna:IAEA) paper EXS/P2-17, 2010*. http://www-pub.iaea.org/mtcd/meetings/cn180_papers.asp.
- [Sauter:PPCF2002] O. Sauter et al. “Marginal β -limit for neoclassical tearing modes in JET H-mode discharges”. *Plasma Phys. Control. Fusion*, 44:1999, 2002. <http://iopscience.iop.org/0741-3335/44/9/315>.
- [Sauter:PPCF2010] O. Sauter et al. “On the requirements to control neoclassical tearing modes in burning plasmas”. *Plasma Phys. Control. Fusion*, 52(2):025002, 2010. <http://stacks.iop.org/0741-3335/52/i=2/a=025002?key=crossref.f2bbdf8c8f4aa515cf363520357bda6c>.

BIBLIOGRAPHY

- [Sauter:PRL2002] O. Sauter et al. “Control of Neoclassical Tearing Modes by Sawtooth Control”. *Phys. Rev. Lett.*, 88(10), 2002. <http://link.aps.org/doi/10.1103/PhysRevLett.88.105001>.
- [Sauter:PoP1997] O. Sauter et al. “Beta limits in long-pulse tokamak discharges”. *Phys. Plasmas*, 4(5):1654, 1997. http://flw.ph.utexas.edu/linked/flw-publist_files/Papers/Sauter/1997.pdf.
- [Sauter:PoP1999] O. Sauter, C. Angioni, and Y.R. Lin-Liu. “Neoclassical conductivity and bootstrap current formulas for general axisymmetric equilibria and arbitrary collisionality regime”. *Phys. Plasmas*, 6:2834, 1999. <http://link.aip.org/link/?PHPAEN/6/2834/1>.
- [Sauter:PoP2001] O. Sauter et al. “Steady-state fully noninductive operation with electron cyclotron current drive and current profile control in the tokamak à configuration variable (TCV)”. *Phys. Plasmas*, 8(5):2199, 2001. <http://link.aip.org/link/PHPAEN/v8/i5/p2199/s1&Agg=doi>.
- [Sauter:PoP2002] O. Sauter, C. Angioni, and Y.R. Lin-Liu. “Erratum: “Neoclassical conductivity and bootstrap current formulas for general axisymmetric equilibria and arbitrary collisionality regime” [Phys. Plasmas 6, 2834 (1999)]”. *Phys. Plasmas*, 9(12):5140, 2002. <http://scitation.aip.org/content/aip/journal/pop/9/12/10.1063/1.1517052>.
- [Sauter:PoP2014] O. Sauter et al. “On the non-stiffness of edge transport in L-mode tokamak plasma”. *Phys. Plasmas*, 21(5):055906, 2014. <http://scitation.aip.org/content/aip/journal/pop/21/5/10.1063/1.4876612>.
- [Sauter:Varenna1999] O. Sauter et al. “Sawtooth period simulations of TCV discharges”. In *Proc. Joint Varenna-Lausanne Int. Workshop on Theory of Fusion Plasmas, Varenna, Italy, August, 1999*.
- [Shimada:Nf2007] M. Shimada et al. “Chapter 1: Overview and summary”. *Nucl. Fusion*, 47(6):S1, 2007. <http://stacks.iop.org/0029-5515/47/i=6/a=S01?key=crossref.9f5018b333c98316af6e827446ba6d15>.
- [Snyder:Nf2011] P.B. Snyder et al. “A first-principles predictive model of the pedestal height and width: development, testing and ITER optimization with the EPED model”. *Nucl. Fusion*, 51(10):103016, 2011. <http://stacks.iop.org/0029-5515/51/i=10/a=103016?key=crossref.334289a0972991b200871ad1b82fa95c>.
- [Stabler:FST2003] A. Stäbler et al. “Chapter 13: Current drive in ASDEX Upgrade”. *Fusion Science and Technology*, 44(3):730, 2003. <http://gateway.webofknowledge.com/gateway/Gateway.cgi?GWVersion=2&SrcAuth=mekentosj&SrcApp=Papers&DestLinkType=FullRecord&DestApp=WOS&KeyUT=000186115300015>.
- [Staebler:PoP2007] G.M. Staebler, J.E. Kinsey, and R.E. Waltz. “A theory-based transport model with comprehensive physics”. *Phys. Plasmas*, 14(5):055909, 2007. <http://scitation.aip.org/content/aip/journal/pop/14/5/10.1063/1.2436852>.

- [Stober:EPJ2012] J. Stober et al. “ECRH on ASDEX Upgrade - System Status, Feed-Back Control, Plasma Physics Results -”. *EPJ Web of Conferences*, 32:02011, 2012. <http://www.epj-conferences.org/10.1051/epjconf/20123202011>.
- [Strauss:FED2013] D. Strauss et al. “Preliminary design of the ITER ECH Upper Launcher”. *Fusion Engineering and Design*, 88:2761, 2013. <http://www.sciencedirect.com/science/article/pii/S0920379613003347>.
- [Streibl:FST2003] B. Streibl et al. “Chapter 2: Machine design, fueling, and heating in ASDEX upgrade”. *Fusion Science and Technology*, 44(3):578, 2003. <http://gateway.webofknowledge.com/gateway/Gateway.cgi?GWVersion=2&SrcAuth=mekentosj&SrcApp=Papers&DestLinkType=FullRecord&DestApp=WOS&KeyUT=000186115300004>.
- [Sushkov:RSI2008] A. Sushkov et al. “High-resolution multiwire proportional soft x-ray diagnostic measurements on TCV”. *Rev. Sci. Instrum.*, 79(2):023506, 2008. <http://scitation.aip.org/content/aip/journal/rsi/79/2/10.1063/1.2833822>.
- [Taroni:PPCF1994] A. Taroni et al. “Global and local energy confinement properties of simple transport coefficients of the Bohm type”. *Plasma Phys. Control. Fusion*, 36(10):1629, 1994. <http://iopscience.iop.org/0741-3335/36/10/003>.
- [Treutterer:SOFE2013] W. Treutterer et al. “Real time control of plasma performance on ASDEX upgrade and its implications for ITER”. In *Fusion Engineering (SOFE), 2013 IEEE 25th Symposium on*, 2013. http://ieeexplore.ieee.org/xpls/abs_all.jsp?arnumber=6635345.
- [Troyon:PPCF1984] F. Troyon et al. “MHD-limits to plasma confinement”. *Plasma Phys. Control. Fusion*, 26(1A):209, 1984. <http://iopscience.iop.org/0741-3335/26/1A/319>.
- [VanDam:PoF1982] J.W. Van Dam. “A generalized kinetic energy principle”. *Phys. Fluids*, 25(8):1349, 1982. <http://scitation.aip.org/content/aip/journal/pof1/25/8/10.1063/1.863898>.
- [Vijvers:APS2013] W.A.J. Vijvers et al. “Power exhaust in all geometric variations of the snowflake divertor on TCV”. In *Conference on Plasma Physics: 55th APS, Denver, USA*, 2013.
- [Vijvers:NFSUB] W.A.J. Vijvers et al. “First experimental demonstration of heat load mitigation with an X-divertor in a tokamak”. *To be submitted to Nucl. Fusion*, 2015.
- [VonGoeler:PRL1974] S. Von Goeler, W. Stodiek, and N. Sauthoff. “Studies of Internal Disruptions and m=1 Oscillations in Tokamak Discharges with Soft X-Ray Techniques”. *Phys. Rev. Lett.*, 33(20):1201, 1974. <http://link.aps.org/doi/10.1103/PhysRevLett.33.1201>.
- [Waelbroeck:PRL2001] F. Waelbroeck, J. Connor, and H. Wilson. “Finite Larmor-Radius Theory of Magnetic Island Evolution”. *Phys. Rev. Lett.*, 87(21):215003, 2001. <http://link.aps.org/doi/10.1103/PhysRevLett.87.215003>.

BIBLIOGRAPHY

- [WagnerD:PPCF2012] D. Wágner et al. “Understanding the core density profile in TCV H-mode plasmas”. *Plasma Phys. Control. Fusion*, 54(8):085018, 2012. <http://stacks.iop.org/0741-3335/54/i=8/a=085018?key=crossref.49a891435e79350418c75eac482b5622>.
- [WagnerF:PPCF2010] F. Wagner et al. “On the heating mix of ITER”. *Plasma Phys. Control. Fusion*, 52(12):124044, 2010. <http://stacks.iop.org/0741-3335/52/i=12/a=124044?key=crossref.4da322579bef3f7e3f454b8f500baccd>.
- [Waltz:PoP1997] R.E. Waltz et al. “A gyro-Landau-fluid transport model”. *Phys. Plasmas*, 4(7):2482, 1997. <http://w3.pppl.gov/~hammett/gyrofluid/papers/1997/Waltz-GLF23.pdf>.
- [Weisen:NF2005] H. Weisen et al. “Collisionality and shear dependences of density peaking in JET and extrapolation to ITER”. *Nucl. Fusion*, 45(2):L1, 2005. <http://iopscience.iop.org/0029-5515/45/2/L01>.
- [Wesson:Tokamaks] J. Wesson. *Tokamaks*. Oxford University Press, 4th edition, 2011.
- [Westerhof:NF1987] E. Westerhof. “Requirements on heating or current drive for tearing mode stabilization by current profile tailoring”. *Nucl. Fusion*, 27(11):1929, 1987. <http://iopscience.iop.org/0029-5515/27/11/018>.
- [Westerhof:NF1990] E. Westerhof. “Tearing mode stabilization by local current density perturbations”. *Nucl. Fusion*, 30(6):1143, 1990. <http://iopscience.iop.org/0029-5515/30/6/017>.
- [Westerhof:NF2007] E. Westerhof et al. “Tearing mode stabilization by electron cyclotron resonance heating demonstrated in the TEXTOR tokamak and the implication for ITER”. *Nucl. Fusion*, 47(2):85, 2007. <http://stacks.iop.org/0029-5515/47/i=2/a=003?key=crossref.22b3717640ed7481fdaaba8fea93ef0d>.
- [WilsonH:PoP1996] H.R. Wilson et al. “Threshold for neoclassical magnetic islands in a low collision frequency tokamak”. *Phys. Plasmas*, 3(1):248, 1996. <http://link.aip.org/link/PHPAEN/v3/i1/p248/s1&Agg=doi>.
- [WilsonJ:PoP2015] J.R. Wilson and P.T. Bonoli. “Progress on ion cyclotron range of frequencies heating physics and technology in support of the International Tokamak Experimental Reactor”. *Phys. Plasmas*, 22(2):021801, 2015. <http://scitation.aip.org/content/aip/journal/pop/22/2/10.1063/1.4901090>.
- [Witvoet:NF2011] G. Witvoet et al. “Numerical demonstration of injection locking of the sawtooth period by means of modulated EC current drive”. *Nucl. Fusion*, 51(10):103043, 2011. <http://stacks.iop.org/0029-5515/51/i=10/a=103043?key=crossref.d8fcc6ec038cb069fa7e37ec0a4a051d>.
- [Witvoet:NF2011b] G. Witvoet et al. “Systematic design of a sawtooth period feedback controller using a Kadomtsev-Porcelli sawtooth model”. *Nucl. Fusion*, 51(7):07304, 2011. <http://iopscience.iop.org/0029-5515/51/7/073024>.

- [Yun:RSI2010] G.S. Yun et al. “Development of KSTAR ECE imaging system for measurement of temperature fluctuations and edge density fluctuations”. *Rev. Sci. Instrum.*, 81(10):10D930, 2010. <http://scitation.aip.org/content/aip/journal/rsi/81/10/10.1063/1.3483209>.
- [Yushmanov:NF1990] P.N. Yushmanov et al. “Scalings for tokamak energy confinement”. *Nucl. Fusion*, 30:1999, 1990. <http://iopscience.iop.org/0029-5515/30/10/001>.
- [Zabolotsky:NF2006] A. Zabolotsky et al. “Influence of particle sources on electron density peaking in TCV and JET”. *Nucl. Fusion*, 46(5):594, 2006. <http://stacks.iop.org/0029-5515/46/i=5/a=010?key=crossref.3dc805ff01b7336dcd490b04107bf288>.
- [Zhu:PoP2000] P. Zhu, G. Bateman, A.H. Kritz, and W. Horton. “Predictive transport simulations of internal transport barriers using the Multi-Mode model”. *Phys. Plasmas*, 7(7):2898, 2000. <http://scitation.aip.org/content/aip/journal/pop/7/7/10.1063/1.874140>.
- [Zohm:EC2006] H. Zohm et al. “The physics base for NTM stabilisation by ECCD in ITER”. In *Proceedings of the 14th Joint Workshop on Electron Cyclotron Emission and Electron Cyclotron Resonance Heating*, Santorini, Greece, 9–12 May, 2006.
- [Zucca:PPCF2009] C. Zucca et al. “Current density evolution in electron internal transport barrier discharges in TCV”. *Plasma Phys. Control. Fusion*, 51(1):015002, 2009. <http://iopscience.iop.org/0741-3335/51/1/015002>.
- [Zucca:Thesis] C. Zucca. “*Modeling and control of the current density profile in tokamaks and its relation to electron transport*”. PhD thesis, École Polytechnique Fédérale de Lausanne (EPFL), Lausanne, 2009. <http://infoscience.epfl.ch/record/133631>.